Capturing Atomic and Electronic Motion with High Harmonic Generation Light Pulses

The cover displays four images of the sun recorded by NASA's Solar Dynamics Observatory (SDO). The goal of the SDO is to understand the solar variations that influence life on Earth and humanity's technological systems. To study the behavior of the sun's corona extreme ultraviolet (XUV) light, rather than visible light, is recorded in these images. In the hot plasma of the corona highly charged ions exist that emit light at XUV wavelengths. For example, the light in these images (33.5 nm) is mostly coming from Fe^{16+} ions. Although in a completely different context, XUV light is also used in the experiments that are described in this thesis. The images on the cover show the motion of the sun with a three day interval, the final image was taken on the 2^{nd} of March 2011 at 00:00:05.
For more info and images: http://sdo.gsfc.nasa.gov/

ISBN: 978-90-77209-46-2

Printed by Gildeprint Drukkerijen, Enschede
An electronic version of this thesis is available at www.amolf.nl/publications

Capturing Atomic and Electronic Motion with High Harmonic Generation Light Pulses

EEN WETENSCHAPPELIJKE PROEVE OP HET GEBIED VAN
DE NATUURWETENSCHAPPEN,WISKUNDE EN INFORMATICA

PROEFSCHRIFT

ter verkrijging van de graad van Doctor
aan de Radboud Universiteit Nijmegen,
op gezag van de rector magnificus
prof. mr. S.C.J.J. Kortmann,
volgens besluit van het college van decanen
in het openbaar te verdedigen op donderdag 23 juni 2011
om 10.30 uur precies

door

Freek Kelkensberg

Geboren op 15 mei 1981
te Zwolle

Promotor:	Prof. dr. M. J. J. Vrakking
Manuscriptcommissie:	Prof. dr. D. H. Parker Prof. dr. A. L'Huillier, Universiteit Lund, Zweden Dr. A. F. Koenderink, FOM Instituut AMOLF

The work described in this thesis was performed at the FOM Institute for Atomic and Molular Physics (AMOLF), Science Park 104, 1098 XG Amsterdam, The Netherlands. This work is part of the research programme of the 'Stichting voor Fundamenteel Onderzoek der Materie (FOM)', which is financially supported by the 'Nederlandse Organisatie voor Wetenschappelijk Onderzoek (NWO)'.).

Contents

1 Introduction

The shutter time of a camera needs to be short compared to the speed at which an object in front of the camera is moving in order to capture a clear image. In this way we can follow the motion of a wide range of objects ranging from bacteria to planets. However, the natural motion of elementary particles, like atoms and electrons, is too fast to be recorded by ordinary cameras. To resolve the dynamics of these particles in time, techniques based on ultrashort laser pulses have been developed. Optical laser pulses, rather than the electronic pulses that are used in a camera, are used for this task because the duration of a laser pulse can be several orders of magnitude shorter than the shortest electronic pulses that can be generated. Such laser pulses exist in a wide variety of frequencies, energies and pulse durations. This thesis concerns the application of laser pulses that are generated by a process called high harmonic generation (HHG) for time-resolved experiments. With HHG one can generate laser pulses in the XUV wavelength regime with pulse durations in the femtosecond (1 fs = 10^{-15} s) and attosecond (1 as = 10^{-18} s) domain, respectively allowing studies on the motion of atoms and electrons.

1.1 High harmonic generation

1.1.1 Discovery of high harmonic generation and the three-step model

Soon after the invention of the laser in 1960 [1] the second harmonic from a Ruby laser was generated by sending the fundamental laser light into a quartz crystal [2][1]. The key to this success was the high intensity of the light that could be delivered by the recently invented laser. A high intensity is needed to induce a significant non-linear polarization in the crystal which results in the emission of the second harmonic of the incoming radiation. One can also produce higher order harmonics with sufficiently high intensities, but the conversion efficiency rapidly decreases with the harmonic order. With the invention of short pulse lasers, first by Q-switching [3] and later by mode-locking [4–6], higher intensities became available to drive harmonic generation processes. Generation of the fifth and seventh harmonic of

[1] Curiously, the main observation of the paper was removed by the editor of Physical Review Letters who mistook the second harmonic spot on the image of the photographic plate for a piece of dirt.

UV laser pulses led to the generation of the first coherent radiation in the VUV and XUV region of the electromagnetic spectrum [7, 8], wavelengths at which laser action is increasingly difficult to achieve.

The development of laser amplifiers [9, 10] made it possible to study harmonic generation in gases at unprecedented intensities of $> 10^{13}$ W/cm^2 (Fig. 1.1a). This led to the surprising discovery that, after the rapid decrease of the intensity at the lowest harmonics (perturbative regime), a plateau of harmonic emission with approximately constant intensity is generated [11, 12]. The plateau ends at a sharp cut-off beyond which no harmonic emission is found (see Fig. 1.1c). Because of symmetry reasons the generation of even harmonics is not allowed in normal harmonic generation in gasses and only the odd harmonics are produced. In Fig. 1.1c an idealized HHG photon spectrum is shown which illustrates the three regions in the spectrum. The photon spectrum that results from high harmonic generation (HHG) can extend well above the ionization potential (I_p) of the atom. It was found that the cut-off position obeys a universal rule and lies at approximately $I_p + 3U_p$ for all wavelengths, atoms and intensities [13]. U_p is the ponderomotive energy which is given by the intensity and frequency of the laser field.

Numerous theoretical efforts that followed the initial experimental results have led to a thorough understanding of the process of HHG as well as the development of accurate models to simulate HHG. Quantum calculations in which the time-dependent Schrödinger equation was solved for a single electron interacting with the fundamental laser field reproduced the main observations of HHG experiments. Such calculations have helped to determine, among other things, the cut-off law for HHG [13]. Explanations were soon found in terms of a classical model for the interaction of the electron with the field [14–17]. The influential paper by Corkum [17] introduced the model that describes the HHG process in three steps. The three-step model is schematically illustrated in Fig. 1.1b. In step 1 the atom is ionized by the strong laser field launching an electron in free space. The electron is accelerated by the laser field, first away from the parent ion but when the field changes sign it is returned to the core (step 2). In the third, step the accelerated electron recombines with the parent ion and emits the energy it has acquired in the field in the form of an XUV photon. The empirical cut-off law follows naturally from this model. Furthermore, it can explain the polarization dependence of the HHG process. Harmonic emission is suppressed for circular or elliptical polarization of the driver field because such fields do not direct the electron back to the parent ion; therefore, no recombination can take place. Semi-classical theories for HHG that recover the classical picture were formulated soon after the classical model was introduced. These semi-classical models have remained the most important method for numerical simulations of HHG since their introduction [18, 19].

1.1.2 Development of HHG light sources

The HHG radiation that is typically produced in an extended medium of atoms, deviates significantly from the radiation that would be emitted by a single atom. In a macroscopic medium the radiation from the individual atoms adds up coherently leading to constructive and destructive interference between the waves [20]. The resulting emission from the medium is dominated by radiation that is the result of

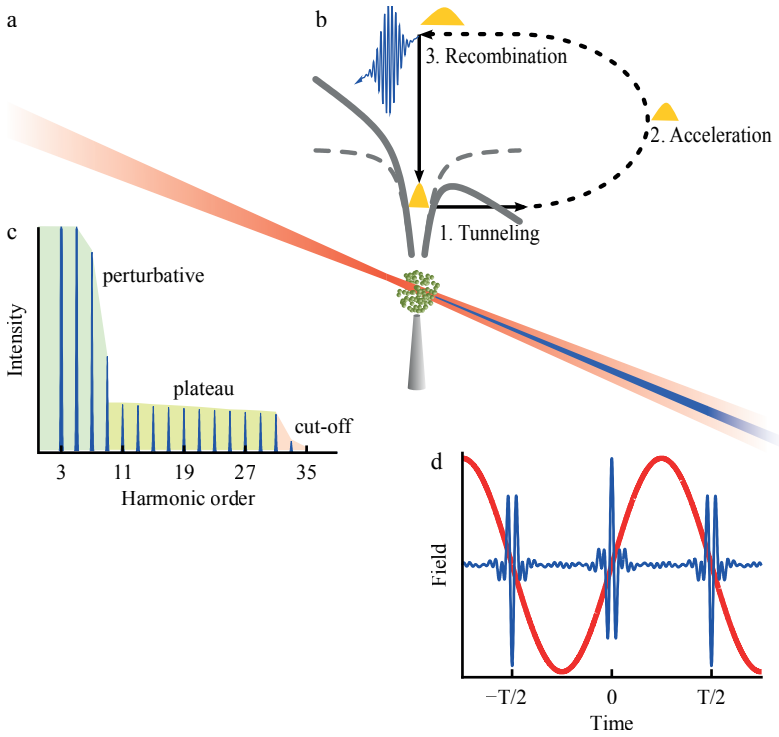

Figure 1.1: (a)High harmonic generation is performed by focussing an intense laser pulse in an atomic gas. An intuitive explanation is given by the three-step model which is schematically illustrated in (b). The laser electric field acts on the atomic potential which leads to tunnel ionization at the peak of the field. The free electron is accelerated and directed back to the parent ion by the field. When the electron subsequently recombines with the ion the excess energy that was gained in the field is released in the form of radiation. This radiation consists of the odd harmonic orders of the driver field. A rapid decline of the yield over the first few orders (perturbative regime) is followed by an extended plateau of harmonics with approximately equal intensity. The plateau ends with a sharp cut-off beyond which no harmonics are emitted. The three regions are illustrated in the idealized HHG spectrum in (c). Selecting the harmonics in the plateau and cut-off region of the spectrum in (c) leads to to the attosecond pulse train (APT) in (d) with two pulses per optical cycle of the fundamental laser field. In (d) the electric field of the APT is shown in blue together with the fundamental field in red

paths of constructive interference, i.e. paths for which phase-matching is achieved. One important consequence of phase matching is that the radiation is confined in a beam with a small divergence. Better control and understanding of the generation process have greatly improved the output of HHG sources by finding the optimal conditions for phase-matching [21, 22]. Besides that, the ongoing development of lasers, leading to shorter pulses with higher energies, has also aided in the increase of the output of HHG sources and the extension of the cut-off photon energy.

The introduction of femtosecond laser amplifiers that use Ti:Sapphire as the

gain medium, has been of vital importance in the availability of suitable laser pulses to generate high harmonics. HHG with several μJ of output energy has been demonstrated [23]. These pulses can be focused to high enough intensities to study non-linear processes in the XUV region, such as two-photon ionization [24, 25], two-photon double ionization [26, 27] and two-photon above threshold ionization [28].

The photon energy of these high intensity HHG pulses is in the region between 20 and 40 eV. Early attempts to increase the photon energies that are produced by HHG resulted in the production of radiation in the water window (centered at 400 eV) [29, 30]. The water window is the region where water is transparant for X-ray radiation while carbon atoms absorb, making it an ideal spectral region for high contrast imaging of biological tissue. A few years later high harmonic radiation at 1 keV was also demonstrated [31]. Unfortunately, the number of photons that these sources produce are extremely low because of a weak single atom response (very high non-linearity) and a lack of macroscopic phase matching. More recently, improved phase matching schemes, that use mid-IR driver lasers, have led to a significant increase in the output energy of soft X-ray high harmonics [32–35].

1.1.3 Generation and characterization of attosecond pulses

A few years after the first experimental demonstration of HHG in a gas medium, a number of proposals were put forward that suggested the formation of attosecond pulses based on HHG [36–38]. The spectral bandwidth that can be produced by HHG is large enough to support such short pulses but in order to build up to an attosecond pulse all those frequencies need to be emitted in phase. When a flat spectral phase over a number of consecutive odd harmonic orders is assumed, the result of an inverse Fourier transform of a typical HHG spectrum translates into a train of sub-cycle pulses in the time domain as is indicated in Fig. 1.1d. In other words, when the harmonics are locked in phase they form an attosecond pulse train (APT). The classical model of HHG indeed predicts that this is the case since the recombination, and hence the emission of high harmonics, occurs within a fraction of the optical cycle of the field. For a typical driver wavelength of 800 nm, corresponding to an optical cycle of 2.7 fs, this immediately leads to the conclusion that the harmonic emission takes place in attosecond bursts. Although it was long expected that HHG leads to attosecond pulses, it has taken almost a decade before it could be confirmed experimentally [39]. The reason for this long delay was the unavailability of techniques to measure pulse durations of sub-femtosecond pulses in the XUV domain. A number of theoretical and experimental contributions [40–44] led to the successful temporal characterization of an attosecond pulse train in ref. [39] by a method that is called reconstruction of attosecond bursts by interference of two-photon transitions (RABBITT)[45]. In a RABBITT experiment one combines the HHG pulse with an infrared (IR) field at the fundamental frequency. Using a copy of the generating laser pulse ensures that the phase of the IR field is locked to the pulses in the APT. The relative phase of the harmonics is determined from the interference that occurs in the photoelectron sidebands produced by an XUV and an IR photon. A close analysis of the HHG process shows that the spectral phase of the plateau harmonics is actually not flat and the attosecond pulses in an

APT have a linear chirp. This was experimentally observed using the RABBITT technique [46]. Thin metal films partially compensate the chirp, resulting in shorter attosecond pulses [47]. After the initial RABBITT measurements, attosecond autocorrelations have also confirmed the existence of attosecond pulse trains [25, 28].

Already before the experimental demonstration of attosecond pulse trains it was recognized that isolated attosecond pulses would in some cases be more attractive in attosecond pump-probe studies [38]. By now, several successful strategies have been developed that allow one to generate isolated attosecond pulses. The first demonstration of isolated attosecond pulses used the selection of harmonics in the cut-off region of HHG produced by few-cycle pulses [48]. Due to the high nonlinearity of the harmonic generation process, the harmonic radiation generated by the strongest half-cycle in the pulse can be selected by spectral selection of only the highest photon energies (cut-off). Few-cycles pulses are a prerequisite in this scheme, in order to have enough differentiation between subsequent half-cycles in the pulse. Furthermore, the carrier to envelope phase (CEP) of the laser pulses need to be stabilized and controlled [49]. Ongoing development of this way of generating isolated attosecond pulses, has enabled the production of pulses with a duration of only 80 as [50], currently the world record.

The second method to generate isolated attosecond pulses uses the ellipticity dependence of HHG [38]. An isolated attosecond pulse can be produced by modulating the polarization from circular to linear and back to circular such that only a single half cycle is linearly polarized. The circular polarization in the wings of the pulse suppresses the emission of HHG and a single attosecond pulse is generated by the linearly polarized half-cycle. In the first experiments in which such a polarization gate was used, it was demonstrated that the HHG emission could be confined to a smaller fraction of the driver pulse, although no isolated attosecond pulses were produced [51–54]. The combination of a few-cycle driver pulse and a polarization gate led to the generation of isolated attosecond pulses with a duration of 130 as [55]. More recently, polarization gating schemes have been reported that allow many-cycle laser pulses [56–58] to generate isolated attosecond pulses.

The observation and characterization of isolated attosecond pulses, for which the RABBITT technique cannot be used, is based on the the principle of *attosecond streaking*, pioneered and developed in a sequence of studies [48, 59–61]. In an attosecond streaking experiments electrons are launched by an attosecond pulse in a moderately strong IR field. The final energy of the electron, after interaction with the field, depends on the phase of the electric field at which it is born [62]. This time-to-energy mapping led to the first experimental demonstration of an isolated attosecond pulse [48, 61] and formed the basis of the technique to fully reconstruct the attosecond pulse structure [63].

1.2 Time resolved experiments to study atomic and electronic motions

1.2.1 The timescale of quantum mechanical motion

In this thesis we want to study the motion of atoms and electrons. The motion of these elementary particles is governed by the laws of quantum mechanics. The characteristic timescale at which motion occurs in quantum mechanics can be found by considering a system with two eigenstates $\varphi_{1,2}$ with eigenenergies $E_{1,2}$. The wavefunction Ψ of the system is described by:

$$|\Psi(t)\rangle = a_1 e^{-\frac{i}{\hbar}E_1 t}|\varphi_1\rangle + a_2 e^{-\frac{i}{\hbar}E_2 t}|\varphi_2\rangle \tag{1.1}$$

where $a_{1,2}$ are (complex) amplitudes that describe the coherent superposition of the two eigenstates. This analysis is general but the two states can be thought of to be two rotational, vibrational or electronic states of a molecule. The time-dependence in the wavefunction $\Psi(t)$ results from the difference in the evolution of the phases of the amplitudes in the two states. This time-dependence can be probed by a measurement of the system in which the two states are made to interfere. The (hermitian) operator $\hat{A}$ that represents such a measurement is described in the basis of the eigenvectors of the hamiltonian as follows:

$$\hat{A} = \begin{pmatrix} c_1 & c_{12} \\ c_{12}^* & c_2 \end{pmatrix} \tag{1.2}$$

Since $\hat{A}$ is hermitian c_1 and c_2 are real. The result of the measurement yields:

$$\langle\Psi|\hat{A}|\Psi\rangle = c_1|a_1|^2 + c_2|a_2|^2 + 2\Re\{c_{12}a_1^*a_2\}\cos\frac{\Delta E}{\hbar}t - 2\Im\{c_{12}a_1^*a_2\}\sin\frac{\Delta E}{\hbar}t \tag{1.3}$$

with $\Delta E = E_2 - E_1$. When $c_{12} \neq 0$ and $a_{1,2} \neq 0$, Eq. 1.3 shows that an oscillatory motion with a period of $T = h/\Delta E$ is found. This motion can be seen as the result of the beating between the two waves corresponding to the two eigenstates. The beating can be observed when there is a non-zero amplitude in both eigenstates and the eigenstates of the measurment operator $\hat{A}$ are different from the eigenstates of the hamiltonian that describe the system. From this simple analysis it can readily be deduced that rotations of a molecule occur on picosecond (1 ps = 10^{-12} s) timescales. The period that is found from the splitting of the two lowest rotational states of CO_2 (97 μeV) is 42.7 ps.

In chemical reactions it is the atomic motion in molecules that leads to the transformation from the initial to the final state. The fastest chemical reactions evolve on femtosecond timescales and can be studied in time-resolved experiments using femtosecond laser pulses [64]. An example of femtosecond nuclear motion is the vibration of a molecule. The fastest molecular vibration that exist in nature is that of a H_2^+ molecule. The energy splitting between the two lowest vibrational levels is 270 meV which corresponds to a vibrational period of 15.2 fs.

Energy splittings between electronic states are typically on the order of $\sim$ 1 eV which gives the rationale for the statement that electronic motion occurs on

attosecond timescales. For example, the splitting between the two lowest electronic states in H_2^+ is 11.9 eV (at the equilibrium internuclear distance) corresponding to a period of 350 as. The advent of attosecond laser pulses has paved the way for experimental studies of electronic motion on attosecond timescales.

Note that no time-dependences other than the phase evolution of the amplitudes were assumed, i.e. the dynamical behavior considered so far is the result of the free evolution (no perturbation besides the measurement itself) of the system. However, the period T also defines the timescales at which the system will show the strongest response to time-dependent perturbations by, for example, oscillating electric fields.

1.2.2 Applications of HHG in femtosecond time-resolved studies

Immediately after the discovery of HHG, its potential for applications and research was recognized. Early studies used HHG radiation to perform time resolved studies in atoms [65], plasmas [66] and in condensed matter [67]. HHG sources have also contributed to studies on molecular dynamics which, as mentioned before, occurs on femtosecond timescales. Femtosecond dynamics of chemical reactions has been studied extensively using femtosecond pulses in the visible (VIS) and infrared (IR) parts of the electromagnetic spectrum [64]. HHG pulses allow one to extend this work to the XUV regime. Time-resolved photoelectron spectroscopy based on HHG sources has been used to study processes like pre-dissociation of highly excited states in acetylene [68], surface chemistry dynamics of oxygen on a Pt surface [69] and the photodissociation dynamics of a Br_2 molecule [70, 71]. Furthermore, femtosecond XUV radiation produced by HHG has been used in coincident photoelectron-photoion studies of dissociative ionization of N_2 and O_2 [72, 73]. These experiments are based on the detection of charged particles that are created in the interaction with the laser pulses. The observation of time-dependent changes in the absorption spectrum of the high harmonics form an additional technique to study femtosecond dynamics in atomic and molecular systems [74].

Because the radiation produced by HHG has a high degree of spatial and temporal coherence, it is an interesting source for coherent diffraction imaging (CDI) in the XUV and soft X-ray region, a technique that was pioneered using synchrotron radiation [75]. High harmonic sources have the advantage that they are widely available and, because of the short pulse durations that can be obtained, provide a way to extend the technique to study the dynamics of a system. The first proof-of-principle experiments on diffractive imaging using HHG pulses were based on the acquisition of many laser shots [76, 77]. More recently imaging by a single shot of the laser was demonstrated [78]. These imaging techniques are even more interesting in the light of the new generation XUV/X-ray free electron lasers (FELs). With X-ray diffraction techniques one can resolve the molecular structure since the wavelength of the radiation is small compared to the inter-atomic distances in a molecule. Femtosecond X-ray FELs provide the exciting possibility to apply diffractive imaging techniques to observe time-dependent changes in the structure of a molecule. Rather than based on photons, diffraction imaging can also be performed with electron waves. A natural way to obtain a short electron pulse that

probes the molecular structure, is the generation of photoelectrons from the molecule itself by ionization with a femtosecond pulse. The diffraction of the photoelectrons on the atomic centers on their way out of the molecule encode information on the structure in the angular distribution of the photoelectron wave [79]. Because the electron wavelength is much smaller than the photon wavelength at a given energy, photoelectron diffraction requires lower photon energies than photon diffraction to achieve the same spatial resolution. Especially because soft x-ray HHG sources are becoming more efficient, it is likely that HHG will be employed for molecular imaging techniques as well.

1.2.3 Attosecond physics in atoms, molecules and condensed matter

The emergence of attosecond pulses based on HHG, has led to a number of time-resolved experiments in which electron dynamics in atoms was investigated [80, 81]. Attosecond light pulses are, with a few exceptions, not intense enough to perform attosecond-pump attosecond-probe experiments. It is for this reason that various techniques have been developed to achieve attosecond resolution in experiments where the attosecond pulses are combined with a femtosecond IR pulse. In these experiments one uses the dependence of the process under study on the sub-cycle time evolution of the electric field, rather than the much slower envelope, of the IR pulse. The electric field oscillations can be seen to act as a clock which is read out with the attosecond pulse. Examples of dynamics in atoms that has been investigated in this way include Auger decay times [82], the sub-cycle evolution of strong field ionization [83], coherent electron scattering [84] and bound electronic wavepackets [85, 86]. Furthermore, attosecond pulses were used to measure the delay between the emission of an electron from the conduction band and from an atomic core level of a tungsten surface [87].

The investigation of electron dynamics in multi-electron systems like molecules, clusters and solid matter is one of the main driving forces for the development of attosecond technology. There is a strong interest in the application of attosecond pulses in the field of chemical physics to study the motion of electrons inside molecules. Despite the general notion that chemistry takes place on femtosecond or slower timescales, recent theoretical work has unmistakeably recognized the importance of electronic responses in photochemical processes [88–90]. For example, a sudden ionization event in a glycine molecule leads to the migration of the created hole through the entire molecule on a few femtosecond timescale, as shown in Fig. 1.2a (taken from ref. [91]). This charge migration is driven by multi-electron interactions and has been predicted in a wide range of molecular complexes. So far, experimental evidence of such processes has been indirect [92, 93]. Attosecond pulses provide a way towards time-resolved experiments to investigate electron dynamics in molecules, thereby answering open questions about the role of electrons in chemical reactions and the interaction of molecules with light.

Experimental molecular attosecond science is still in its infancy with only a few experiments that have been reported to resolve electron dynamics in a molecule using attosecond pulses. Chapter 4 describes the very first of such an experiment.

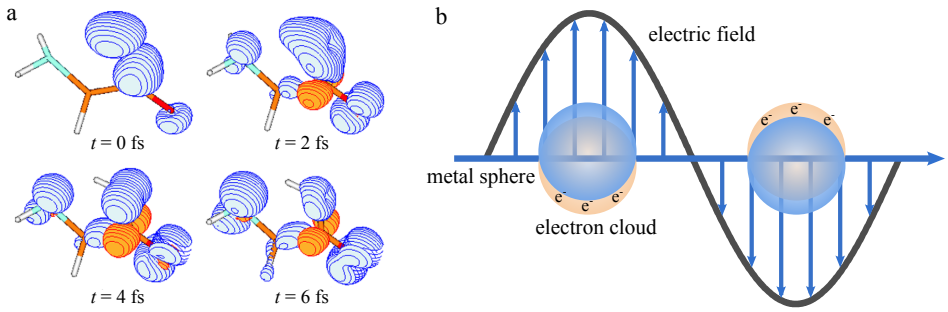

Figure 1.2: Examples of multi-electron dynamics on attosecond timescales (a) After a rapid photoionization event in a glycine molecule the created hole (blue) migrates through the molecule within a few fs. The orange color indicates an electron density. (taken from ref. [91]) (b) When a metal nanoparticle is illuminated at the surface plasmon resonance frequency a collective oscillation of the electron cloud in a metal is excited which generates a secondary enhanced field close to the metal particle.

Most likely molecular attosecond experiments will become an increasingly active field in which experimental studies will soon be extended to larger and more complex molecules.

Dynamics as the result of the collective motion of electrons occur, besides in molecules, also in solid matter. So-called plasmons are single excitations of a (quantized) collective oscillation of the free electron cloud against the positive ions of the material. The frequency of these oscillations depends on the electron density and for metals are typically in the ultraviolet range. This means that this oscillation takes place on attosecond timescales. Surface plasmon polaritons are the coupled excitation of collective electron motion and an electromagnetic wave, trapped at the interface of a metal. There is a large interest in surface plasmon polaritons in a range of applications varying from Surface Enhanced Raman Spectroscopy (SERS) [94, 95] to plasmon-based optical circuits for chips working at unprecedented frequencies [96]. Localized surface plasmons are the result of the resonant excitation of a collective motion of the electron cloud in a metal nanoparticle as is schematically illustrated in Fig. 1.2b. Attosecond pulses will enable the investigation of the underlying electron dynamics of surface plasmons in time-resolved experiments.

1.3 Background and outline of this thesis

The work that is described in this thesis was performed in the XUV physics group at the FOM Institute AMOLF in Amsterdam. At AMOLF there is a long history in HHG and, especially, in attosecond pulses. The theoretical work by AMOLF researchers H.B. Van den Linden Van den Heuvel and H.G. Muller formed a large contribution to the (semi-)classical theories of HHG [14]. In the development of techniques to characterize attosecond pulses, the research at AMOLF made important contributions [44] and the first experimental proof of attosecond pulses was

a joint effort of researchers from AMOLF and the group in Saclay (France) [39]. Shortly after this, the first attosecond experiments at AMOLF were performed in 2003 [97]. This experiment employed for the first time a velocity map imaging detector to perform a RABBITT measurement. The experiment showed that the relative phases of the harmonics are not just encoded in the yield, but also in the angular distributions of the sideband photoelectrons. More recently, experiments were carried out in collaboration with the group in Lund (Sweden). It was shown that interferences between electron wave packets created by consecutive attosecond pulses can be used to probe the dynamics, and determine the phase of the electronic wave packets in the IR field [98]. Apart from these experiments on atoms, the group at AMOLF demonstrated the phase control of electron localization in the dissociative ionization of D_2 molecules by few-cycle laser pulses [99]. This was the first time attosecond dynamics in a molecule, although indirectly, was observed and controlled.

In the first half of the 2000's, the field of attosecond science had focused primarily on the *generation* of attosecond pulses. The progress on the generation of attosecond pulses made that, when the work described in this thesis started in 2007, increasingly more attention was being paid at the *application* of attosecond pulses in time-resolved experiments on electron dynamics. In this light, the main goal of the PhD-research of this thesis was to use attosecond pulses to study electron dynamics in molecules and plasmonic systems. Following the tradition of the group at AMOLF, the research was carried out in close collaboration with other groups abroad. Most notably, an important part of the work was conducted in collaboration with the groups of Anne L'Huillier (Lund), Mauro Nisoli (Milano) and Fernando Martín (Madrid). Some of the experiments described in this thesis have also been performed in laboratories outside AMOLF.

The thesis is split into three parts. An extensive description of the XUV + IR pump probe setups that have been used in this thesis has been published elsewhere [100]. This is not reproduced here except for a short description of the experimental methods for the individual experiments. Despite the main goal being the study of electron dynamics, we have performed a number of experiments on the, somewhat slower, nuclear dynamics in molecules. Two experiments that are related to nuclear dynamics are described in Part I. Chapter 2 presents an experiment in which vibrational wavepacket dynamics in H_2^+ molecules was studied with femtosecond XUV + IR pulses. This is an example how HHG pulses can be used to study femtosecond nuclear dynamics. Part of the experiments were carried out during a very successful experimental campaign at the Politecnico in Milano in 2007. This campaign has functioned as a kick start for the rest of the thesis by generating many exciting results and new ideas. Chapter 3 describes an experiment in which photoelectron angular distributions from aligned molecules were measured. This experiment forms a first step towards experiments in which the time-dependent changes of the molecular structure in a femtosecond chemical reaction can be determined by photoelectron diffraction techniques.

In Part II attosecond electron dynamics in hydrogen molecules is studied. The experiment presented in Chapter 4 is the first experiment that shows the potential of attosecond pulses to study electron dynamics in a molecule. An isolated attosec-

ond pulse was combined with a few-cycle IR pulse to study electron localization dynamics in dissociative ionization of hydrogen. This experiment formed the major result of the previously mentioned campaign in Milano. Analyzing and interpreting the experimental results has been a demanding but stimulating task. The final outcome formed a mile-stone in attosecond science. Chapter 5 describes a semi-classical model that provides an intuitive understanding of electron localization in the dissociation of H_2^+ in the presence of an IR field. The model was developed to aid in the understanding of the experiment in chapter 4 but has a wider applicability. The development of the model formed the first step in the analysis of the experimental results of Chapter 4. The deep understanding of the physics of the problem, which came with the development of the model, was extremely rewarding. Chapter 6 describes an experiment in which an APT was used to probe IR induced dynamics by attosecond photoionization, a first step towards using attosecond pulses as the probe in a pump-probe experiment to resolve electron dynamics in molecules. This experiment was motivated by insights from the Milano campaign. Its success showed us that the new experimental setup in Amsterdam was fully functioning and provided many new opportunities.

In the last part novel attosecond experiments are investigated. Chapter 7 describes a theoretical study how attosecond pulses can be used to perform time-resolved measurements on surface plasmon fields using the concept of attosecond streaking. Resolving plasmon dynamics with attosecond pulses has been a goal of this research since the beginning. Unfortunately, to set up such an experiment has not been possible within the period of this PhD. The increased understanding of such experiments provided by the theoretical study and the evolution of the experimental techniques, will hopefully bring these experiments into reality in the coming years. In Chapter 8 the progress on the development of attosecond experiments at significantly higher repetition rates than currently possible is described. Many PhD projects start with a technical development which allows one to perform novel experiments in a later stage of the project. This thesis is different in that respect since the major technical development was done at the end and is aimed at future experiments. Nonetheless, the development of the laser has been an exciting task. The laser will, hopefully, be a source for many successful experiments in the future.

References

[1] T. H. Maiman. *Stimulated Optical Radiation in Ruby.* Nature, **187**, 493–494 (1960).

[2] P. A. Franken, A. E. Hill, C. W. Peters and G. Weinreich. *Generation of Optical Harmonics.* Phys. Rev. Lett., **7**, 118–119 (1961).

[3] F. J. McClung and R. W. Hellwarth. *Giant Optical Pulsations from Ruby.* Appl. Opt., **1**, 103–105 (1962).

[4] L. E. Hargrove, R. L. Fork and M. A. Pollack. *Locking of He-Ne laser modes induced by synchronous intracavity modulation.* Appl. Phys. Lett., **5**, 4–5 (1964).

[5] A. DeMaria, J. Glenn, W.H., M. Brienza and M. Mack. *Picosecond laser pulses.* Proceedings of the IEEE, **57**, 2 – 25 (1969).

[6] P. Smith, M. Duguay and E. Ippen. *Mode-locking of lasers.* Progress in Quantum Electronics, **3**, 107 – 229 (1974).

[7] J. Reintjes, R. C. Eckardt, C. Y. She, N. E. Karangelen, R. C. Elton and R. A. Andrews. *Generation of Coherent Radiation at 53.2 nm by Fifth-Harmonic Conversion.* Phys. Rev. Lett., **37**, 1540–1543 (1976).

[8] J. Reintjes, C. Y. She, R. C. Eckardt, N. E. Karangelen, R. A. Andrews and R. C. Elton. *Seventh harmonic conversion of mode-locked laser pulses to 38.0 nm.* Appl. Phys. Lett., **30**, 480–482 (1977).

[9] S. Szatmári. *High-brightness ultraviolet excimer lasers.* Appl. Phys. B: Lasers Opt., **58**, 211–223 (1994).

[10] M. D. Perry and G. Mourou. *Terawatt to Petawatt Subpicosecond Lasers.* Science, **264**, 917–924 (1994).

[11] A. McPherson, G. Gibson, H. Jara, U. Johann, T. S. Luk, I. A. McIntyre, K. Boyer and C. K. Rhodes. *Studies of multiphoton production of vacuum-ultraviolet radiation in the rare gases.* J. Opt. Soc. Am. B, **4**, 595–601 (1987).

[12] M. Ferray and et al. *Multiple-harmonic conversion of 1064 nm radiation in rare gases.* J. Phys. B: At., Mol. Opt. Phys., **21**, L31 (1988).

[13] J. L. Krause, K. J. Schafer and K. C. Kulander. *High-order harmonic generation from atoms and ions in the high intensity regime.* Phys. Rev. Lett., **68**, 3535–3538 (1992).

[14] H. B. van Linden van den Heuvel and H. G. Muller. *Multiphoton Processes.* In S. J. Smith and P. L. Knight, eds., *Cambridge Studies in Modern Optics.* Cambridge Univ. Press, Cambridge (1988), vol. 8.

[15] P. B. Corkum, N. H. Burnett and F. Brunel. *Above-Threshold Ionization in the Long-Wavelength Limit.* Phys. Rev. Lett., **62**, 1259–1262 (1989).

[16] K. S. K.C. Kulander and J. Krause. *Super-intense laser-atom physics.* In B. Piraux, A. L'Huillier and K. RzaZewski, eds., *NATO ASI Series B.* Plenum Press, New York (1993), vol. 316, 95.

[17] P. B. Corkum. *Plasma Perspective on Strong-Field Multiphoton Ionization.* Phys. Rev. Lett., **71**, 1994–1997 (1993).

[18] A. L'Huillier and P. Balcou. *High-order harmonic generation in rare gases with a 1-ps 1053-nm laser.* Phys. Rev. Lett., **70**, 774–777 (1993).

[19] M. Lewenstein, P. Balcou, M. Y. Ivanov, A. Lhuillier and P. B. Corkum. *Theory of High-Harmonic Generation by Low-Frequency Laser Fields.* Phys. Rev. A, **49**, 2117–2132 (1994).

[20] A. L'Huillier, P. Balcou, S. Candel, K. J. Schafer and K. C. Kulander. *Calculations of high-order harmonic-generation processes in xenon at 1064 nm.* Phys. Rev. A, **46**, 2778–2790 (1992).

[21] E. Constant, D. Garzella, P. Breger, E. Mevel, C. Dorrer, C. Le Blanc, F. Salin and P. Agostini. *Optimizing high harmonic generation in absorbing gases: Model and experiment.* Phys. Rev. Lett., **82**, 1668–1671 (1999).

[22] C. G. Durfee, A. R. Rundquist, S. Backus, C. Herne, M. M. Murnane and H. C. Kapteyn. *Phase matching of high-order harmonics in hollow waveguides.* Phys. Rev. Lett., **83**, 2187–2190 (1999).

[23] E. Takahashi, Y. Nabekawa and K. Midorikawa. *Generation of 10- μJ coherent extreme-ultraviolet light by use of high-order harmonics.* Opt. Lett., **27**, 1920–1922 (2002).

[24] Y. Kobayashi, T. Sekikawa, Y. Nabekawa and S. Watanabe. *27-fs extreme ultraviolet pulse generation by high-order harmonics.* Opt. Lett., **23**, 64–66 (1998).

[25] P. Tzallas, D. Charalambidis, N. A. Papadogiannis, K. Witte and G. D. Tsakiris. *Direct observation of attosecond light bunching.* Nature, **426**, 267–271 (2003).

[26] Y. Nabekawa, H. Hasegawa, E. J. Takahashi and K. Midorikawa. *Production of doubly charged helium ions by two-photon absorption of an intense sub-10-fs soft x-ray pulse at 42 eV photon energy.* Phys. Rev. Lett., **94**, 043001 (2005).

[27] H. Hasegawa, E. J. Takahashi, Y. Nabekawa, K. L. Ishikawa and K. Midorikawa. *Multiphoton ionization of He by using intense high-order harmonics in the soft-x-ray region.* Phys. Rev. A, **71**, 023407 (2005).

[28] Y. Nabekawa, T. Shimizu, T. Okino, K. Furusawa, H. Hasegawa, K. Yamanouchi and K. Midorikawa. *Conclusive evidence of an attosecond pulse train observed with the mode-resolved autocorrelation technique.* Phys. Rev. Lett., **96**, 083901 (2006).

[29] Z. H. Chang, A. Rundquist, H. W. Wang, M. M. Murnane and H. C. Kapteyn. *Generation of coherent soft X rays at 2.7 nm using high harmonics.* Phys. Rev. Lett., **79**, 2967–2970 (1997).

[30] C. Spielmann, N. H. Burnett, S. Sartania, R. Koppitsch, M. Schnerer, C. Kan, M. Lenzner, P. Wobrauschek and F. Krausz. *Generation of Coherent X-rays in the Water Window Using 5-Femtosecond Laser Pulses.* Science, **278**, 661 (1997).

[31] J. Seres, E. Seres, A. J. Verhoef, G. Tempea, C. Streli, P. Wobrauschek, V. Yakovlev, A. Scrinzi, C. Spielmann and F. Krausz. *Laser technology: Source of coherent kilo-electronvolt X-rays.* Nature, **433**, 596 (2005).

[32] V. S. Yakovlev, M. Ivanov and F. Krausz. *Enhanced phase-matching for generation of soft X-ray harmonics andattosecond pulses in atomic gases.* Opt. Express, **15**, 15351–15364 (2007).

[33] E. J. Takahashi, T. Kanai, K. L. Ishikawa, Y. Nabekawa and K. Midorikawa. *Coherent Water Window X Ray by Phase-Matched High-Order Harmonic Generation in Neutral Media.* Phys. Rev. Lett., **101**, 253901 (2008).

[34] T. Popmintchev, M. C. Chen, A. Bahabad, M. Gerrity, P. Sidorenko, O. Cohen, I. P. Christov, M. M. Murnane and H. C. Kapteyn. *Phase matching of high harmonic generation in the soft and hard X-ray regions of the spectrum.* Proc. Natl. Acad. Sci. U. S. A., **106**, 10516–10521 (2009).

[35] M.-C. Chen, P. Arpin, T. Popmintchev, M. Gerrity, B. Zhang, M. Seaberg, D. Popmintchev, M. M. Murnane and H. C. Kapteyn. *Bright, Coherent, Ultrafast Soft X-Ray Harmonics Spanning the Water Window from a Tabletop Light Source.* Phys. Rev. Lett., **105**, 173901 (2010).

[36] G. Farkas and C. Toth. *Proposal for Attosecond Light-Pulse Generation Using Laser-Induced Multiple-Harmonic Conversion Processes in Rare-Gases.* Phys. Lett. A, **168**, 447–450 (1992).

[37] S. E. Harris, J. J. Macklin and T. W. Hansch. *Atomic-Scale Temporal Structure Inherent to High-Order Harmonic-Generation.* Opt. Commun., **100**, 487–490 (1993).

[38] P. B. Corkum, N. H. Burnett and M. Y. Ivanov. *Subfemtosecond Pulses.* Opt. Lett., **19**, 1870–1872 (1994).

[39] P. M. Paul, E. S. Toma, P. Breger, G. Mullot, F. Auge, P. Balcou, H. G. Muller and P. Agostini. *Observation of a train of attosecond pulses from high harmonic generation.* Science, **292**, 1689–1692 (2001).

[40] V. Veniard, R. Taieb and A. Maquet. *Phase dependence of (N+1)-color (N¿1) ir-uv photoionization of atoms with higher harmonics.* Phys. Rev. A, **54**, 721–728 (1996).

[41] T. E. Glover, R. W. Schoenlein, A. H. Chin and C. V. Shank. *Observation of laser assisted photoelectric effect and femtosecond high order harmonic radiation.* Phys. Rev. Lett., **76**, 2468–2471 (1996).

[42] J. M. Schins, P. Breger, P. Agostini, R. C. Constantinescu, H. G. Muller, A. Bouhal, G. Grillon, A. Antonetti and A. Mysyrowicz. *Cross-correlation measurements of femtosecond extreme-ultraviolet high-order harmonics.* J. Opt. Soc. Am. B, **13**, 197–200 (1996).

[43] E. Constant, V. D. Taranukhin, A. Stolow and P. B. Corkum. *Methods for the measurement of the duration of high-harmonic pulses.* Phys. Rev. A, **56**, 3870–3878 (1997).

[44] E. S. Toma, H. G. Muller, P. M. Paul, P. Breger, M. Cheret, P. Agostini, C. Le Blanc, G. Mullot and G. Cheriaux. *Ponderomotive streaking of the ionization potential as a method for measuring pulse durations in the XUV domain with fs resolution.* Phys. Rev. A, **62**, 061801 (2000).

[45] H. Muller. *Reconstruction of attosecond harmonic beating by interference of two-photon transitions.* Appl. Phys. B: Lasers Opt., **74**, s17–s21 (2002). 10.1007/s00340-002-0894-8.

[46] Y. Mairesse *et al. Attosecond synchronization of high-harmonic soft x-rays.* Science, **302**, 1540–1543 (2003).

[47] R. Lopez-Martens *et al. Amplitude and phase control of attosecond light pulses.* Phys. Rev. Lett., **94**, 033001 (2005).

[48] M. Hentschel, R. Kienberger, C. Spielmann, G. A. Reider, N. Milosevic, T. Brabec, P. Corkum, U. Heinzmann, M. Drescher and F. Krausz. *Attosecond metrology.* Nature, **414**, 509–513 (2001).

[49] A. Baltuska *et al. Attosecond control of electronic processes by intense light fields.* Nature, **421**, 611–615 (2003).

[50] E. Goulielmakis *et al. Single-cycle nonlinear optics.* Science, **320**, 1614–1617 (2008).

[51] M. Kovacev *et al. Temporal confinement of the harmonic emission through polarization gating.* Eur. Phys. J. D., **26**, 79–82 (2003).

[52] O. Tcherbakoff, E. Mével, D. Descamps, J. Plumridge and E. Constant. *Time-gated high-order harmonic generation.* Phys. Rev. A, **68**, 043804 (2003).

[53] C. Altucci, C. Delfin, L. Roos, M. B. Gaarde, A. L'Huillier, I. Mercer, T. Starczewski and C. G. Wahlstrom. *Frequency-resolved time-gated high-order harmonics.* Phys. Rev. A, **58**, 3934–3941 (1998).

[54] R. López-Martens, J. Mauritsson, P. Johnsson, A. L'Huillier, O. Tcherbakoff, A. Zaïr, E. Mével and E. Constant. *Time-resolved ellipticity gating of high-order harmonic emission.* Phys. Rev. A, **69**, 053811 (2004).

[55] G. Sansone *et al. Isolated single-cycle attosecond pulses.* Science, **314**, 443–446 (2006).

[56] P. Tzallas, E. Skantzakis, C. Kalpouzos, E. P. Benis, G. D. Tsakiris and D. Charalambidis. *Generation of intense continuum extreme-ultraviolet radiation by many-cycle laser fields.* Nat. Phys., **3**, 846–850 (2007).

[57] H. Mashiko, S. Gilbertson, C. Q. Li, S. D. Khan, M. M. Shakya, E. Moon and Z. H. Chang. *Double optical gating of high-order harmonic generation with carrier-envelope phase stabilized lasers.* Phys. Rev. Lett., **100**, 103906 (2008).

[58] X. M. Feng, S. Gilbertson, H. Mashiko, H. Wang, S. D. Khan, M. Chini, Y. Wu, K. Zhao and Z. H. Chang. *Generation of Isolated Attosecond Pulses with 20 to 28 Femtosecond Lasers.* Phys. Rev. Lett., **103**, 183901 (2009).

[59] M. Drescher, M. Hentschel, R. Kienberger, G. Tempea, C. Spielmann, G. A. Reider, P. B. Corkum and F. Krausz. *X-ray pulses approaching the attosecond frontier.* Science, **291**, 1923–1927 (2001).

[60] R. Kienberger *et al. Steering attosecond electron wave packets with light.* Science, **297**, 1144–1148 (2002).

[61] R. Kienberger *et al. Atomic transient recorder.* Nature, **427**, 817–821 (2004).

[62] J. Itatani, F. Quere, G. L. Yudin, M. Y. Ivanov, F. Krausz and P. B. Corkum. *Attosecond streak camera.* Phys. Rev. Lett., **88**, 173903 (2002).

[63] Y. Mairesse and F. Quéré. *Frequency-resolved optical gating for complete reconstruction of attosecond bursts.* Phys. Rev. A, **71**, 011401 (2005).

[64] A. H. Zewail. *Femtochemistry: Atomic-scale dynamics of the chemical bond.* J. Phys. Chem. A, **104**, 5660–5694 (2000).

[65] M. Gisselbrecht, D. Descamps, C. Lyngå, A. L'Huillier, C.-G. Wahlström and M. Meyer. *Absolute Photoionization Cross Sections of Excited He States in the Near-Threshold Region.* Phys. Rev. Lett., **82**, 4607–4610 (1999).

[66] W. Theobald, R. Hassner, C. Wulker and R. Sauerbrey. *Temporally resolved measurement of electron densities ($>10^{23}$ cm^{-3}) with high harmonics.* Phys. Rev. Lett., **77**, 298–301 (1996).

[67] R. Haight and D. R. Peale. *Antibonding state on the Ge(111):As surface: Spectroscopy and dynamics.* Phys. Rev. Lett., **70**, 3979–3982 (1993).

[68] S. L. Sorensen *et al. Femtosecond pump-probe photoelectron spectroscopy of predissociative Rydberg states in acetylene.* J. Chem. Phys., **112**, 8038–8042 (2000).

[69] M. Bauer, C. Lei, K. Read, R. Tobey, J. Gland, M. M. Murnane and H. C. Kapteyn. *Direct Observation of Surface Chemistry Using Ultrafast Soft-X-Ray Pulses.* Phys. Rev. Lett., **87**, 025501 (2001).

[70] L. Nugent-Glandorf, M. Scheer, D. A. Samuels, A. M. Mulhisen, E. R. Grant, X. M. Yang, V. M. Bierbaum and S. R. Leone. *Ultrafast time-resolved soft x-ray photoelectron spectroscopy of dissociating Br_2.* Phys. Rev. Lett., **8719**, 193002 (2001).

[71] P. Wernet, M. Odelius, K. Godehusen, J. Gaudin, O. Schwarzkopf and W. Eberhardt. *Real-Time Evolution of the Valence Electronic Structure in a Dissociating Molecule.* Phys. Rev. Lett., **103**, 013001 (2009).

[72] E. Gagnon, P. Ranitovic, X. M. Tong, C. L. Cocke, M. M. Murnane, H. C. Kapteyn and A. S. Sandhu. *Soft X-ray-driven femtosecond molecular dynamics.* Science, **317**, 1374–1378 (2007).

[73] A. S. Sandhu, E. Gagnon, R. Santra, V. Sharma, W. Li, P. Ho, P. Ranitovic, C. L. Cocke, M. M. Murnane and H. C. Kapteyn. *Observing the Creation of Electronic Feshbach Resonances in Soft X-ray-Induced O-2 Dissociation.* Science, **322**, 1081–1085 (2008).

[74] Z.-H. Loh, M. Khalil, R. E. Correa, R. Santra, C. Buth and S. R. Leone. *Quantum State-Resolved Probing of Strong-Field-Ionized Xenon Atoms Using Femtosecond High-Order Harmonic Transient Absorption Spectroscopy.* Phys. Rev. Lett., **98**, 143601 (2007).

[75] J. Miao, P. Charalambous, J. Kirz and D. Sayre. *Extending the methodology of X-ray crystallography to allow imaging of micrometre-sized non-crystalline specimens.* Nature, **400**, 342–344 (1999).

[76] R. L. Sandberg *et al. Lensless Diffractive Imaging Using Tabletop Coherent High-Harmonic Soft-X-Ray Beams.* Phys. Rev. Lett., **99**, 098103 (2007).

[77] R. L. Sandberg *et al. High numerical aperture tabletop soft x-ray diffraction microscopy with 70-nm resolution.* Proceedings of the National Academy of Sciences, **105**, 24–27 (2008).

[78] A. Ravasio *et al. Single-Shot Diffractive Imaging with a Table-Top Femtosecond Soft X-Ray Laser-Harmonics Source.* Phys. Rev. Lett., **103**, 028104 (2009).

[79] A. Landers *et al. Photoelectron diffraction mapping: Molecules illuminated from within.* Phys. Rev. Lett., **8701**, 013002 (2001).

[80] P. B. Corkum and F. Krausz. *Attosecond science.* Nat. Phys., **3**, 381–387 (2007).

[81] F. Krausz and M. Ivanov. *Attosecond physics.* Rev. Mod. Phys., **81**, 163–234 (2009).

[82] M. Drescher, M. Hentschel, R. Kienberger, M. Uiberacker, V. Yakovlev, A. Scrinzi, T. Westerwalbesloh, U. Kleineberg, U. Heinzmann and F. Krausz. *Time-resolved atomic inner-shell spectroscopy.* Nature, **419**, 803–807 (2002).

[83] M. Uiberacker *et al. Attosecond real-time observation of electron tunnelling in atoms.* Nature, **446**, 627–632 (2007).

[84] J. Mauritsson, P. Johnsson, E. Mansten, M. Swoboda, T. Ruchon, A. L'Huillier and K. J. Schafer. *Coherent Electron Scattering Captured by an Attosecond Quantum Stroboscope.* Phys. Rev. Lett., **100**, 073003 (2008).

[85] E. Goulielmakis *et al. Real-time observation of valence electron motion.* Nature, **466**, 739–743 (2010).

[86] J. Mauritsson *et al. Attosecond Electron Spectroscopy Using a Novel Interferometric Pump-Probe Technique.* Phys. Rev. Lett., **105**, 053001 (2010).

[87] A. L. Cavalieri *et al. Attosecond spectroscopy in condensed matter.* Nature, **449**, 1029–1032 (2007).

[88] J. Breidbach and L. S. Cederbaum. *Migration of holes: Formalism, mechanisms, and illustrative applications.* J. Chem. Phys., **118**, 3983–3996 (2003).

[89] J. Breidbach and L. S. Cederbaum. *Universal attosecond response to the removal of an electron.* Phys. Rev. Lett., **94**, 033901 (2005).

[90] F. Remacle and R. D. Levine. *An electronic time scale in chemistry.* Proc. Natl. Acad. Sci. U. S. A., **103**, 6793–6798 (2006).

[91] A. I. Kuleff and L. S. Cederbaum. *Charge migration in different conformers of glycine: The role of nuclear geometry.* Chem. Phys., **338**, 320 – 328 (2007).

[92] R. Weinkauf, P. Schanen, D. Yang, S. Sonkara and E. W. Schlag. *Elementary Processes in Peptides - Electron-Mobility and Dissociations in Peptide Cations in the Gas-Phase.* J. Phys. Chem., **99**, 11255–11265 (1995).

[93] R. Weinkauf, P. Schanen, A. Metsala, E. W. Schlag, M. Burgle and H. Kessler. *Highly efficient charge transfer in peptide cations in the gas phase: Threshold effects and mechanism.* J. Phys. Chem., **100**, 18567–18585 (1996).

[94] M. Fleischmann, P. Hendra and A. McQuillan. *Raman spectra of pyridine adsorbed at a silver electrode.* Chem. Phys. Lett., **26**, 163 – 166 (1974).

[95] S. Nie and S. Emery. *Probing single molecules and single nanoparticles by surface-enhanced Raman scattering.* Science, **275**, 1102–1106 (1997).

[96] W. L. Barnes, A. Dereux and T. W. Ebbesen. *Surface plasmon subwavelength optics.* Nature, **424**, 824–830 (2003).

[97] S. A. Aseyev, Y. Ni, L. J. Frasinski, H. G. Muller and M. J. J. Vrakking. *Attosecond angle-resolved photoelectron spectroscopy.* Phys. Rev. Lett., **91**, 223902 (2003).

[98] T. Remetter *et al. Attosecond electron wave packet interferometry.* Nat. Phys., **2**, 323–326 (2006).

[99] M. F. Kling *et al. Control of electron localization in molecular dissociation.* Science, **312**, 246–248 (2006).

[100] F. Kelkensberg, W. Siu, P. Johnsson and M. Vrakking. *Attosecond Molecular Science.* In G. Ogurtsov and D. Dowek, eds., *Dynamical Processes in Atomic and Molecular Physics*, Bentham, Bentham eBooks (2011).

2 Molecular Dissociative Ionization and Wave-Packet Dynamics Studied Using Two-Color XUV and IR Pump-Probe Spectroscopy

We present a combined theoretical and experimental study of ultrafast wavepacket dynamics in the dissociative ionization of H_2 molecules as a result of irradiation with an extreme-ultraviolet (XUV) pulse followed by an infrared (IR) pulse. In experiments where the duration of both the XUV and IR pulses are shorter than the vibrational period of H_2^+, de-phasing and re-phasing of the vibrational wave packet that is formed in H_2^+ upon ionization of the neutral molecule by the XUV pulse is observed. In experiments where the duration of the IR pulse exceeds the vibrational period of H_2^+ (15 fs), a pronounced dependence of the H^+ kinetic energy distribution on XUV-IR delay is observed that can be explained in terms of the adiabatic propagation of the H_2^+ wave packet on field-dressed potential energy curves.

2.1 Introduction

With recent advances in laser technology, real-time imaging of ultrafast molecular phenomena has become possible. Femtosecond laser pulses have led to the development of transition state spectroscopy and femtosecond chemistry [1], and have been applied in pump-probe experiments to map out time-dependent nuclear motion in molecules [2]. The advent of attosecond pulses [3] has given rise to endeavours where it is the even faster electronic motion that is probed in a time-resolved manner [4]. The high-harmonic generation (HHG) technique that is responsible for the formation of attosecond laser pulses has been exploited as a probe of molecular structure and dynamics, both with regards to the position or motion of the constituent atoms [5–7] and that of the electrons [6, 8]. An important concern in these experiments is the question to which extent the structure and dynamics of the molecule(s) under investigation are influenced by the presence of the intense infrared (IR) laser field that drives the high-harmonic generation process [9]. Here we report experiments on the dissociative ionization of H_2 in a two-colour extreme ultra-violet (XUV) + infrared (IR) laser field, where variation of the pulse duration of the IR field affects the adiabaticity of the strong-field dissociation, as manifested in the proton kinetic energy distributions that can be measured. More specifically, we present a combined theoretical and experimental study of ultrafast wavepacket dynamics in the $1s\sigma_g^+$ potential of a H_2^+ molecular ion created by an ultrashort XUV pump pulse, with the initial H_2^+ geometry reflecting that of the neutral ground state. Subsequently, molecular dissociation by the process of bond-softening (BS) [10–12] is induced by

an IR pulse with different durations, ranging from 7 fs up to 35 fs. In the first case (experiment A, hereafter) the IR pulse is significantly shorter than the H_2^+ vibrational period, implying that the vibrational wave packet freely propagates on the H_2^+ ($1s\sigma_g^+$) potential energy curve until it finally dissociates under the influence of the IR pulse. By contrast, in experiment B, the duration of the IR laser pulse is comparable to or longer than the H_2^+ vibrational period. This implies that the IR field is present during the propagation of the wave packet before dissociation, which, depending on the XUV-IR delay, may or may not include the time at which the ionization by the XUV took place.

2.2 Experimental

In experiment A, few-cycle 750 nm laser pulses were obtained by means of hollow-core fiber compression [13] and were split into a central and an annular part. The central part (5 fs FWHM) was used to generate attosecond XUV laser pulses in a Kr gas cell. By using the polarization gating technique this resulted in isolated attosecond pulses with an estimated pulse duration of 400 as [14, 15]. The attosecond pulses, which spanned an energy range from 15 to 35 eV, were collinearly recombined with the annular part (7 fs FWHM) of the few-cycle IR pulse (with a variable time delay) and focused into the active region of a velocity map imaging spectrometer [16]. The velocity- and angular distribution of H^+ ions resulting from two-colour excitation of H_2 molecules was measured. Experiment B made use of a similar setup (previously described in ref. [17]), except for the fact that the IR laser pulse was about 35 fs long. Consequently, the XUV pulse generated by HHG then consisted of a train of attosecond pulses. This, and differences in the XUV spectrum, do not affect our observations significantly.

2.3 Results and analysis

Figure 2.1 shows a comparison of the time-dependent H^+ kinetic energy (KE) distributions measured in experiments A and B. For delays $\tau > 0$ fs, the XUV pulse precedes the IR pulse. In experiment A, the yield of fragments with energies below 1.2 eV oscillates in time with a period of about 27 fs. The results for experiment B, where the IR pulse duration is somewhat longer than the vibrational period of the H_2^+ molecule, are radically different. The time dependence of the H^+ KE distribution evolves smoothly as a function of time. The most striking feature in measurement B is that the KE release shows a pronounced decrease when the peak of the IR pulse comes after the XUV pulse.

In order to simulate the experimental results, a one-dimensional model was used. The molecular system H_2, originally in its ground vibrational and electronic state, is considered to be ionized by an XUV pulse or a pulse train at time t = 0. The ionization occurs by a single XUV pulse in the presence of a 7 fs FWHM IR laser pulse (experiment A), or by an XUV pulse train consisting of 15 attosecond pulses in the presence of a 35 fs FWHM IR laser pulse (experiment B). The centre of the laser pulse is positioned at a delay $t = \tau$ with respect to the XUV pulse(s). Based on the

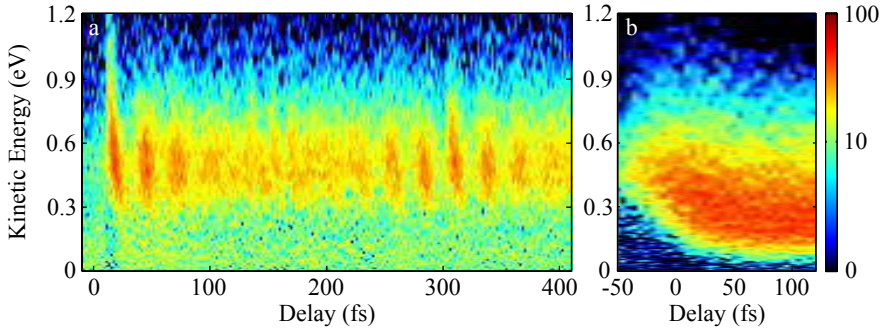

Figure 2.1: Measured time-dependent H^+ kinetic energy distributions for two-colour XUV+IR dissociative ionization of H_2, with 7 fs IR laser pulses (a) and 35 fs IR laser pulses (b). In the latter case the XUV pulse consisted of a train of attosecond laser pulses.

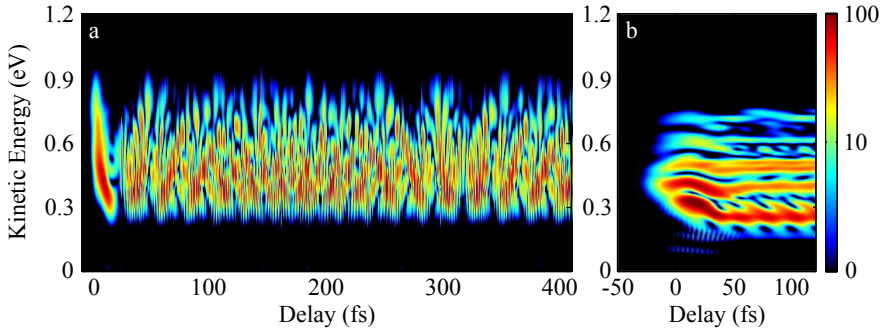

Figure 2.2: Comparison of the time-dependent kinetic energy distributions resulting from model calculations for two-colour XUV+IR dissociative ionization of H_2, making use of a 7 fs FWHM IR pulse (A) and a 35 fs FWHM IR pulse (B). In the latter case the XUV pulse consisted of a train of attosecond laser pulses

favorable Franck-Condon (FC) overlap between the neutral ground state and the ionic $|1s\sigma_g^+\rangle$ state and based on the fact that our energy-resolved detection allows us to selectively investigate the BS channel, we will consider that the attosecond pulse promotes the $v = 0$ vibrational state of the parent molecule vertically onto the $|1s\sigma_g^+\rangle$ state of the molecular ion. We consider the nuclear motion to occur on two electronic manifolds of the molecular ion H_2^+: the ground state $|1s\sigma_g^+\rangle$ and the first excited electronic state $|2p\sigma_u^+\rangle$. In the simulations, the molecule is assumed to be aligned along the laser polarization. Experimentally, the angle-resolved H^+ detection allows us to selectively observe fragments along the polarization axis. As it turns out, none of the observations reported here depend very strongly on the ejection angle of the H^+ fragment with respect to the polarization axis. The nuclear dynamics is obtained by solving the one dimensional time-dependent Schrödinger equation using a wave packet propagation procedure largely described in previous work (see [10] for complete details)). The resulting kinetic energy spectra are compared with the experimental spectra. Figure 2.2 displays the theoretical proton

KE distributions as a function of the time delay between the XUV pump and the IR probe for experiments A and B at intensities of $1{\cdot}10^{13}$ W/cm^2 and $3{\cdot}10^{12}$ W/cm^2 respectively, which corresponds to the peak intensity in the experiments. The main observations of Fig. 1 are qualitatively reproduced.

In experiment A, the XUV laser pulse prepares a coherent superposition of vibrational states of H_2^+, which evolves under essentially field-free conditions, oscillating back and forth and spreading out on the $1s\sigma_g^+$ potential before encountering the IR pulse. The short durations of the IR pulse evokes a situation, in which the laser-molecule interaction opens a "gate" to dissociation at some internuclear distance. The dissociation yield, hence, depends on a synchronization between the wave packet and the opening of this gate at the maximum of the IR field. Stated differently, the oscillations in the dissociation yield are a result of the coherence between the various vibrational components of the initial wave packet [2]. This coherence is further explored in Figure 2.3, which shows the Fourier transforms of the H^+ fragment yield integrated over the KE distribution in the range of 0-1.2 eV for the experimental (Fig. 2.3a) and the theoretical (Fig. 2.3b) results. This reveals that the oscillatory signal is composed of a series of two-level beats at frequencies that are given by the energy difference between adjacent vibrational levels centered around the level $v^+ = 9$ [18–20]. A correlation between frequency and kinetic energy is observed when the Fourier transform is shown as a function of the fragment KE (see insets in Fig. 2.3). This can be understood from the fact that higher vibrational levels, which lead to larger observed kinetic energies, have a smaller energy separation. Clearly, the calculations in Figure 2.2a contain very detailed structures which are partially washed out by the volume averaging in the experiment and which arise from the simultaneous influence of several vibrational frequencies (see Fig. 2.3) corresponding to $\Delta v = 1$ or $\Delta v = 2$ at a given fragment kinetic energy. This indicates that more than 3 vibrational states contribute at a given kinetic energy, which is a manifestation of the non-adiabatic nature of the dissociation process.

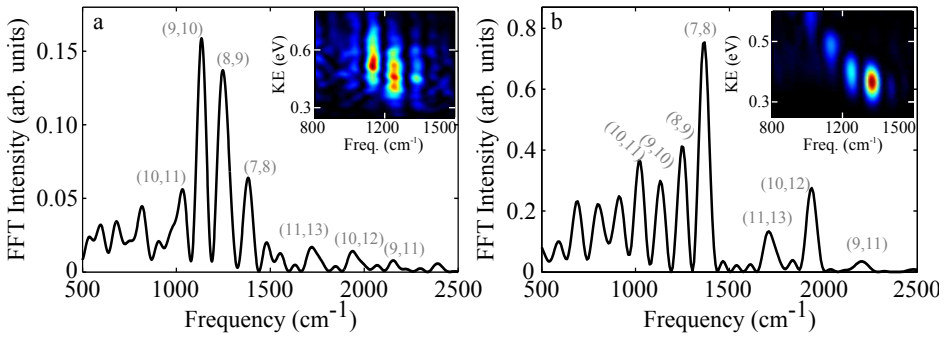

Figure 2.3: Fourier transform of the H^+ fragment yield integrated over the energy range between 0 and 1.2 eV for the experimental (a) and theoretical (b) results, in the case a 7 fs FWHM IR laser pulse. The spectra reveal the two-level beats [20] that are responsible for the observed time-dependence. The insets show an energy-resolved Fourier transformation and reveal a correlation between the fragment KE release and the vibrational level occupied prior to dissociation, observed both in the experiment and the simulations.

When the H_2^+ vibrational wave packet interacts with the longer IR pulse, as in experiment B, little or no dependence of the KE spectrum on the time delay τ is expected when the XUV pulse precedes the IR without overlapping. This is indeed what is observed for time delays $\tau > 20$ fs. In contrast, for $\tau < 20$ fs the fragment KE is strongly delay-dependent, where at near zero delay it reaches energy values similar to those encountered in experiment A.

The dependence of the H^+ kinetic energy on XUV-IR delay in experiment B can be understood in terms of the adiabaticity of the dissociation process, and the way the IR intensity affects both the preparation and the propagation of the wave packet. To understand this, it is useful to discuss the dissociation dynamics in terms of Floquet states. The probe pulse projects the various vibrational components of the wave packet onto Floquet resonances, whose widths and energies vary with the intensity of the IR pulse.

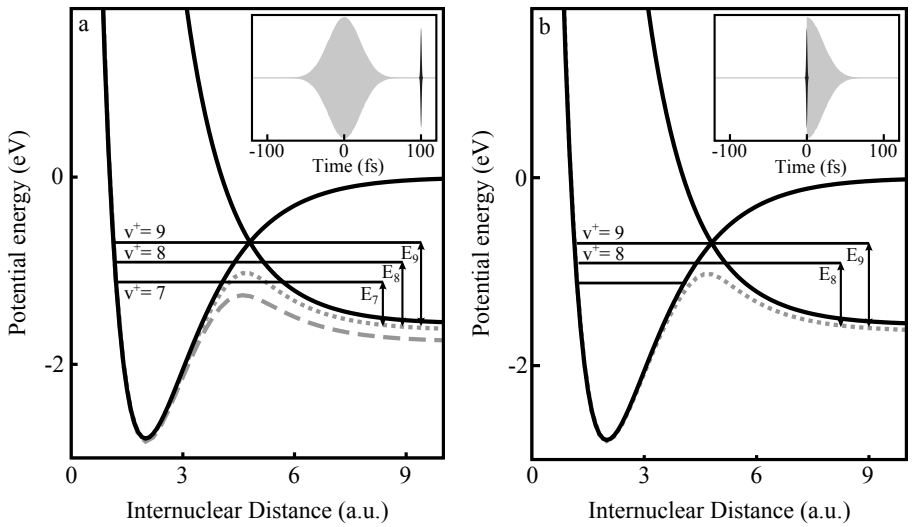

Figure 2.4: Potential energy curves of H_2^+ in a 750 nm laser-dressed diabatic representation (black solid lines). Also indicated are the lower adiabatic curves resulting from the diagonalisation of the radiative interaction for two intensities reached at the center of the pulse: $I = 3 \cdot 10^{12}$ W/cm^2 (dashed gray line) and $I = 10^{12}$ W/cm^2 (dotted gray line). E_7, E_8 and E_9 represent the kinetic energies issued from $v^+ = 7$, 8 and 9 for XUV-IR delays of 100 fs (a) and 0 fs (b).

When the IR pulse follows the XUV pulse without overlapping (i.e. $\tau > 20$ fs, situation indicated in Fig. 2.4) individual field-free vibrational states v^+ of the ion are, at first, transported adiabatically onto corresponding Floquet resonances. Each resonance gives rise to a characteristic contribution to the proton KE spectrum [18]. The magnitude of the kinetic energy is determined by the non-perturbative laser-induced modification of the dressed potential energy curves. On the way towards dissociation, the ion experiences an increasing IR pulse amplitude, lowering the BS barrier. The lowest barrier height is reached at the center of the pulse (maximum of intensity), resulting in most efficient dissociation when the lowest energy resonance

can still tunnel before the barrier rises. Most protons contributing to the spectrum have a KE of about 0.3 eV, corresponding to the resonance issued from $v^+ = 8$. Higher energy resonances are also dissociative, but are not significantly populated by the XUV ionization step (through FC mapping of the vibrationless ground state of H_2).

This situation is in contrast with the case where the IR and XUV pulses are overlapping ($\tau < 20$ fs). The vibrational states of the ion are then shaken up by the sudden intense IR excitation and transferred onto a superposition of resonances with weighting coefficients in the wave packet that can noticeably differ from those resulting from a FC ionization step. In particular higher energy resonances may temporarily be populated and play an important role in the dissociation step. Afterwards, as shown in Figure 2.4b, the ion experiences the falling edge of the IR pulse with a rising BS barrier which quenches the dissociation of low energy resonances. High energy over-the-barrier shape resonances, more populated than in the previous adiabatic case, are the ones which contribute most to the dissociation. The increasing role played by resonances issued from $v^+ = 9, 10$ explains the shift to higher energies of the proton KE distribution when the XUV pulse is close to the maximum of the IR probe. We note that at very short delays corresponding to the XUV-IR pulse overlap, the blue-shift of the kinetic energy spectrum is also observed in experiment A.

Better quantitative experiment versus theory agreement would require the relaxation of some of our model assumptions. Among these approximations are a phenomenological description of the XUV ionization step [21], the neglect of rotational degrees of freedom [22] and also of the laser focal volume averaging [22].

2.4 Conclusions

In conclusion, we have shown that the dynamics of two-colour dissociative ionization of H_2 under the influence of an XUV+IR pulse sequence depends considerably on the properties of the IR radiation and whether or not the IR laser is already present when the molecule is ionized by the XUV pulse. We have described two experimental situations where the richness of the structural determination of molecules, their imaging and possible control rest on the sudden character of the strong IR excitation and the partial breakdown of the adiabatic approximation. In this way our study represents a departure from most intense field dynamics work where, ordinarily, only adiabatic laser excitation regimes result into spectral observables with finely resolved peak structures that can be interpreted in terms of isolated, non-overlapping resonances [18]. Our experiment and numerical analysis show not only that the dynamics of a small molecule like H_2^+ is strongly dependent on the presence of a strong laser field, but moreover that the influence of the laser field is strongly dependent on its pulse duration, influencing whether any induced dynamics is adiabatic or not.

References

[1] A. H. Zewail. *Femtochemistry: Atomic-scale dynamics of the chemical bond.* J. Phys. Chem. A, **104**, 5660–5694 (2000).

[2] T. Ergler, B. Feuerstein, A. Rudenko, K. Zrost, C. D. Schroter, R. Moshammer and J. Ullrich. *Quantum-phase resolved mapping of ground-state vibrational D-2 wave packets via selective depletion in intense laser pulses.* Phys. Rev. Lett., **97**, 103004 (2006).

[3] F. Krausz and M. Ivanov. *Attosecond physics.* Rev. Mod. Phys., **81**, 163–234 (2009).

[4] M. Drescher, M. Hentschel, R. Kienberger, G. Tempea, C. Spielmann, G. A. Reider, P. B. Corkum and F. Krausz. *X-ray pulses approaching the attosecond frontier.* Science, **291**, 1923–1927 (2001).

[5] H. Niikura, P. B. Corkum and D. M. Villeneuve. *Controlling vibrational wave packet motion with intense modulated laser fields.* Phys. Rev. Lett., **90**, 203601 (2003).

[6] M. Meckel *et al. Laser-induced electron tunneling and diffraction.* Science, **320**, 1478–1482 (2008).

[7] S. Baker, J. S. Robinson, C. A. Haworth, H. Teng, R. A. Smith, C. C. Chirila, M. Lein, J. W. G. Tisch and J. P. Marangos. *Probing proton dynamics in molecules on an attosecond time scale.* Science, **312**, 424–427 (2006).

[8] J. Itatani, J. Levesque, D. Zeidler, H. Niikura, H. Pepin, J. C. Kieffer, P. B. Corkum and D. M. Villeneuve. *Tomographic imaging of molecular orbitals.* Nature, **432**, 867–871 (2004).

[9] C. C. Chirila and M. Lein. *Effect of dressing on high-order harmonic generation in vibrating H_2 molecules.* Phys. Rev. A, **77**, 043403 (2008).

[10] A. Giustisuzor, X. He, O. Atabek and F. H. Mies. *Above-Threshold Dissociation of H-2+ in Intense Laser Fields.* Phys. Rev. Lett., **64**, 515–518 (1990).

[11] P. H. Bucksbaum, A. Zavriyev, H. G. Muller and D. W. Schumacher. *Softening of the H_2^+ Molecular-Bond in Intense Laser Fields.* Phys. Rev. Lett., **64**, 1883–1886 (1990).

[12] A. D. Bandrauk. *Molecules in laser fields.* M. Dekker, New York (1993).

[13] M. Nisoli, S. DeSilvestri and O. Svelto. *Generation of high energy 10 fs pulses by a new pulse compression technique.* Appl. Phys. Lett., **68**, 2793–2795 (1996).

[14] G. Sansone *et al. Isolated single-cycle attosecond pulses.* Science, **314**, 443–446 (2006).

[15] I. J. Sola *et al. Controlling attosecond electron dynamics by phase-stabilized polarization gating.* Nat. Phys., **2**, 319–322 (2006).

[16] O. Ghafur, A. Rouzee, A. Gijsbertsen, W. K. Siu, S. Stolte and M. J. J. Vrakking. *Impulsive orientation and alignment of quantum-state-selected NO molecules.* Nat. Phys., **5**, 289–293 (2009).

[17] T. Remetter *et al. Attosecond electron wave packet interferometry.* Nat. Phys., **2**, 323–326 (2006).

[18] K. Sandig, H. Figger and T. W. Hansch. *Dissociation dynamics of H_2^+ in intense laser fields: Investigation of photofragments from single vibrational levels.* Phys. Rev. Lett., **85**, 4876–4879 (2000).

[19] M. Gruebele and A. H. Zewail. *Femtosecond Wave Packet Spectroscopy - Coherences, the Potential, and Structural Determination.* J. Chem. Phys., **98**, 883–902 (1993).

[20] G. Hunter, A. W. Yau and H. O. Pritchard. *Rotation-vibration level energies of the hydrogen and deuterium molecule-ions.* Atom. Data Nucl. Data, **14**, 11 – 20 (1974).

[21] T.-T. Nguyen-Dang, F. Chaˆteauneuf, S. Manoli, O. Atabek and A. Keller. *Tunnel ionization of H_2 in a low-frequency laser field: A wave-packet approach.* Phys. Rev. A, **56**, 2142–2167 (1997).

[22] V. Serov, A. Keller, O. Atabek, H. Figger and D. Pavicic. *Intense laser dissociation of D_2^+: From experiment to theory.* Phys. Rev. A, **72**, 033413 (2005).

3 Molecular Frame Photoelectron Angular Distributions from XUV Ionization of Aligned Molecules

Following ultra-fast chemical reactions, both in time and space, is a core-objective in the field of chemical physics. Novel XUV short pulse light sources such as high harmonic generation (HHG) and XUV/X-ray free electron lasers (FELs) like FLASH and LCLS, combined with laser-induced alignment techniques, allow the development of novel methods to make molecular movies of photochemical reactions that are based on a measurement of Molecular Frame Photoelectron Angular Distributions (MFPADs). MFPADs sensitively probe the electronic orbitals of molecules and furthermore provide information about the molecular structure when the de Broglie wavelength of the ejected electron becomes comparable to the internuclear distances in the molecule. In this context, we present experiments where CO_2 molecules were impulsively aligned using a near infrared laser and ionized using femtosecond XUV pulses obtained by HHG. The experiment reveals characteristic structures in the angular distributions for four electronic orbitals that are ionized, as well as the onset of the influence of the molecular structure on the MFPAD. The results bode well for the implementation of these methods (at higher photon energies) at FELs and in lab-scale experiments using HHG sources.

3.1 Introduction

The making and breaking of chemical bonds typically takes place on a timescale of 100 fs (1 fs = 10^{-15} s) and has motivated the development of the field of femtochemistry in the past two decades. In femtochemistry experiments, the time evolution of a molecular structure is usually probed by exploiting the relation that exists between the molecular structure and the photoabsorption spectrum [1]. Therefore, the interpretation of such experiments often hinges on a pre-existing understanding of the spectroscopy of the molecule under investigation which is increasingly difficult for more complex molecules. Novel measurement techniques are currently being developed that provide a direct probe of the molecular structure by diffraction of electron or light waves on the atomic centers. In recent years, electron diffraction experiments using short electron bunches have enabled the observation of structural changes in chemical reactions [2], crystals [3], and phase transitions [4].In these experiments the wavelength of the electrons was small compared to the internuclear distances in the system under investigation, inducing diffraction that enables one to resolve structures with sub-nanometer resolution. Although proposals exist to

reduce the duration of the electron pulses in these experiments to the attosecond domain (1 as = 10^{-18} s) [5], the creation of electron bunches shorter than a few hundred femtoseconds is a major challenge. Alternatively, one can use diffraction of ultrashort XUV or X-ray light pulses, or diffraction of electrons that are generated in photoionization of a molecule by such an XUV or X-ray light pulse. The latter approach is the topic that is explored in this paper. XUV/X-ray pulses can nowadays be generated in small-scale laboratories with a duration as short as 80 attoseconds by HHG [6], and are available with very high fluxes at new FEL facilities such as FLASH in Hamburg [7] and LCLS in Stanford [8].

Photoelectrons ejected from a molecule contain information on the molecular orbitals from which they are removed. In addition, the outgoing electrons experience the surrounding atoms in the molecule as scattering centers, endowing the photoelectron angular distribution (PAD) with a sensitivity to the underlying molecular structure [9]. The extraction of detailed information on orbitals and/or structure is possible, provided that the PAD is measured in the molecular frame, meaning in a coordinate system that is fixed with respect to the geometry of the molecule. This challenge can be met in an elegant way by measuring photoelectrons and fragment ions that are formed from the same parent molecule in coincidence [10]. Coincidence techniques have been extensively used in combination with synchrotron radiation [9, 11, 12], but are very challenging when using HHG or an XUV/X-ray FEL, since these sources are so far only available at relatively modest (10 Hz−10 kHz) repetition rates. The requirement of a rapid dissociation accompanied by an axial recoil of the fragment ions can be circumvented by using molecular alignment and orientation techniques [13–16]. These techniques allow one to control the angular distribution of a parent molecule before the ionization event takes place.

Photo-ionization of aligned molecules has previously been explored by several researchers with UV/near-IR radiation [17–19],. leading to the ejection of photoelectrons with a relatively low kinetic energy. To obtain structural information by diffraction of the ejected electrons, the electron kinetic energy needs to be sufficiently high to ensure that the de Broglie wavelength of the electron is small compared to the interatomic spacings [20, 21]. One proposed way to accomplish this is ponderomotive acceleration and subsequent re-collision of tunnel-ionized photoelectrons using an intense, low-frequency laser field. This has meanwhile been accomplished for N_2 and O_2 molecules [22] and in strong-field ionization of Xe atoms, where holographic interferences between scattered and non-scattered photoelectrons were observed [23]. An alternative method is to measure high energy photoelectrons that are ejected in single-photon ionization by XUV/X-ray photons. This is the approach followed in the current work, where we present first results for the ionization of aligned CO_2 molecules using femtosecond XUV pulses from a HHG source.

3.2 Experimental setup

In the experiment a Ti:Sapphire laser amplifier was used to generate 30 fs FWHM, 780 nm, 2 mJ laser pulses at a repetition rate of 3 kHz. The output of the laser was divided equally over two arms of a Mach Zehnder type interferometer. In one arm femtosecond XUV pulses were generated by HHG by focusing the laser in a static

gas cell filled with Ar ($\sim$ 30 mbar). The fundamental and the low order harmonics were filtered out by an aluminum filter with a thickness of 200 nm. The resulting harmonic spectrum consisted of the odd harmonics 11 (17.5 eV) up to 31 (49.3 eV). In the second arm the laser beam was sent through 2 cm of SF11 to stretch the pulse to 300 fs FWHM and subsequently used as the alignment pulse. The XUV and alignment beams were recombined on a drilled mirror and both beams were focused at the center of a velocity map imaging spectrometer by a toroidal mirror. An effusive beam of CO_2 molecules was expanded into the vacuum through a pulsed valve running at the full repetition rate of the laser [24]. The intensity of the IR field was kept low (5-15 TW/cm^2) to get a reasonable degree of alignment while limiting ionization by the alignment pulse. The 3D momentum distribution of electrons or ion fragments was projected on a position sensitive detector consisting of a set of micro-channel plates followed by a phosphor screen. A 200 ns gate was applied to the detector to select the electrons or ion fragments. Images of the 2D projection on the phosphor screen were recorded by a camera and the 3D momentum distributions were recovered by an inverse Abel transform.

3.3 Impulsive alignment of CO_2 molecules

We have used impulsive alignment of the CO_2 molecules to get access to the molecular frame. In impulsive alignment one makes use of the interaction of an intense laser pulse with the non-isotropic part of the molecular polarizability [13,15]. The interaction induces a dipole moment, which in turn leads to a torque on the molecule that aligns the molecular axis with the highest polarizability along the laser polarization axis. When the duration of the laser pulse is short compared to the rotational period (42.7 ps for CO_2, 1 ps = 10^{-12} s) of the molecules, a rotational wave packet is created. This rotational wavepacket dephases and rephases with a periodicity that is related to the rotational period. The periodic rephasing of the rotational wave packet leads to a revival of the alignment, where the molecular alignment switches between a distribution peaked along the laser polarization and an anti-alignment where the distribution is peaked perpendicular to the polarization. Impulsively aligning the molecules leads to alignment of the molecules in field-free conditions. Field-free alignment prevents interaction between the photoelectrons by the XUV and the alignment laser which will make it more difficult to extract structural information from the photoelectron angular distribution.

The alignment of the CO_2 molecules was characterized by measuring the angular distribution of O^+ ions resulting from Coulomb explosion by the XUV pulse [25]. In the axial recoil approximation, the angular distribution of the ionic fragments is directly related to the angular distribution of the molecules before ionization/dissociation takes place. Therefore, the modification of the angular distribution as a function of the delay between the alignment and dissociative pulse allows the reconstruction of the alignment dynamics.

Figs. 3.1a and 3.1b show the momentum distributions of O^+ fragments resulting from ionization of CO_2 molecules by the XUV pulse at the maximum of alignment and anti-alignment respectively. In the high kinetic energy channel, one can clearly see that the O^+ fragments peak along the laser polarization in Fig. 3.1a whereas

they are almost uniformly distributed in Fig. 3.1b. In Fig. 3.1c the expectation value $\langle\cos^2\theta_{O^+}\rangle$ of the angular distribution of the O^+ fragments is plotted as a function of delay between the two laser pulses. θ_{O^+} is the angle between the emission angle of the O^+ fragment and the laser polarization axis. The expectation value $\langle\cos^2\theta_{O^+}\rangle$ describing the fragment angular distribution is directly related to $\langle\cos^2\theta_{CO_2}\rangle$ that describes the alignment distribution of the molecules. An isotropic distribution of molecules yields an expectation value $\langle\cos^2\theta_{CO_2}\rangle = 1/3$ with higher and lower values for alignment and anti-alignment, respectively. A maximum degree of alignment is given by $\langle\cos^2\theta_{CO_2}\rangle = 1$ whereas a maximum anti-alignment is described by $\langle\cos^2\theta_{CO_2}\rangle = 0$. The evolution of $\langle\cos^2\theta_{O^+}\rangle$ exhibits alignment revivals every 10.7 ps, corresponding to a quarter of the rotational period of the molecule. The red line in Fig. 3.1c shows the calculated $\langle\cos^2\theta_{CO_2}\rangle$ that is obtained by solving the time-dependent Schrödinger equation (TDSE) for a sample of CO_2 molecules interacting with a strong laser field. With this model the expectation value $\langle\cos^2\theta_{CO_2}\rangle$ of the alignment distribution is calculated. The expectation value $\langle\cos^2\theta_{O^+}\rangle$ of the angular distribution of the O^+ fragments equals the expectation value $\langle\cos^2\theta_{CO_2}\rangle$ of the alignment distribution of the molecules plus a constant term that incorporates the effects of a geometrical alignment that results from the angular dependence of the photoionization by the XUV pulse. The experimental result was fitted with a least square method using the temperature of the molecules and the intensity of the alignment laser pulse as fitting parameters. The fitting procedure found a temperature of 140 K and an intensity of 12 TW/cm^2 which results in a maximum degree of alignment of $\langle\cos^2\theta_{CO_2}\rangle = 0.5$. The relatively high temperature was due to the effusive molecular beam which does not allow better cooling of the molecules. The intensity was kept relatively low although a higher degree of alignment could have been obtained with a higher intensity. The low intensity was used to limit ionization of the molecules by the alignment pulse and thereby we could prevent the generation of high energy above threshold ionization (ATI) electrons.

3.4 PADs from XUV ionization of CO_2 molecules

Fig. 3.2a shows the photoelectron spectrum (PES) for electrons emitted parallel ($\theta_{e^-} = 0°$) and perpendicular ($\theta_{e^-} = 90°$) to the laser polarization resulting from ionization of randomly oriented CO_2 molecules by the XUV pulse. In Fig. 1b a slice from the 3D photoelectron momentum distribution is shown from which the spectra are extracted by integrating over an acceptance angle of $\pm 20°$. The spectra contain a series of peaks, since each harmonic order can produce several ionic states that differ in their ionization potential (IP). Contributions from 4 ionization channels can be recognized, corresponding to ionization from the HOMO ($X^2\Pi_g$, IP=13.8 eV), the HOMO-1 ($A^2\Pi_u$, IP=17.6 eV), the HOMO-2 ($B^2\Sigma_u^+$, IP=18.1 eV) and the HOMO-3 ($C^2\Sigma_g^+$, IP=19.4 eV) orbitals of CO_2, as is indicated by the 4 harmonic ladders in the top part of Fig. 3.2a. The peaks from the different ionization channels are well resolved up to electron energies of about 15 eV. At the highest photoelectron kinetic energies, the resolution of the spectrometer (typically $\Delta E/E = 2\%$, [24]) is lower than the typical peak separation.

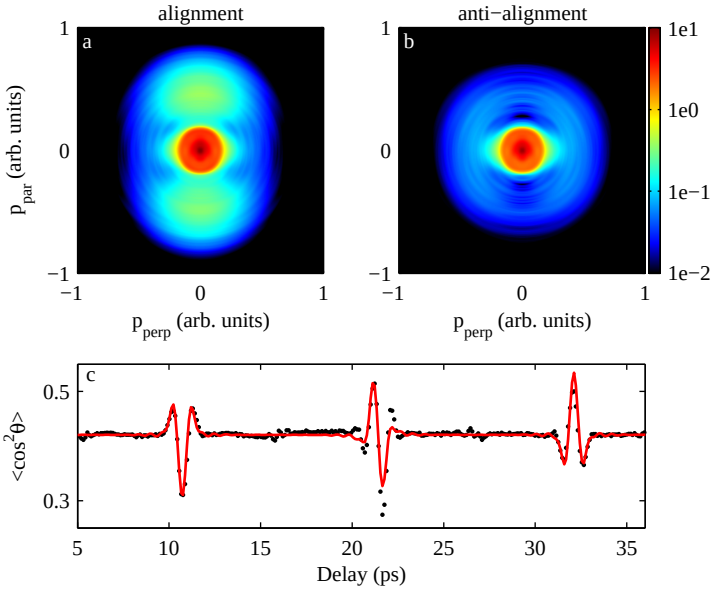

Figure 3.1: Momentum distribution of O^+ fragments from dissociative ionization and Coulomb explosion of CO_2 molecules by the XUV pulses at alignment (a) and anti-alignment (b). The angular distribution of the fragments with high momenta is directly related to the alignment distribution of the molecules. In (c) the expectation value $\langle \cos^2 \theta_{O^+} \rangle$ of the angular distribution of the (high momentum) O^+ fragments is plotted as a function of delay between the alignment pulse and the XUV pulse (black dots) along with the theoretical fit (red line). At every quarter of the rotational period, the rephasing of the rotational wavepacket created at $t = 0$ results in moments of alignment ($\langle \cos^2 \theta_{O^+} \rangle$ is high) and anti-alignment ($\langle \cos^2 \theta_{O^+} \rangle$ is low). The fit does not match the experimental data in the second revival very well probably because the experimental conditions varied during the scan.

The PAD $P(E_k, \cos\theta_{e^-})$ can be written as follows:

$$P(E_k, \cos\theta_{e^-}) = \sigma(E_k)[1 + \beta_2(E_k)P_2(\cos\theta_{e^-}) + \beta_4(E_k)P_4(\cos\theta_{e^-}) + ...] \quad (3.1)$$

where $\sigma(E_k)$ is the photoionization cross-section and $P_l(\cos\theta_{e^-})$ the l^{th} order Legendre polynomial. For single photon ionization of an isotropic sample only the β_2-parameter is nonzero while the higher order terms vanish. When the β_2-parameter is positive (negative) the electron emission predominantly takes places parallel (perpendicular) to the laser polarization. From Fig. 3.2 it can be seen that the angular distribution of the photoelectrons associated with the HOMO-1 and HOMO-3 orbitals is peaked in the direction parallel to the laser polarization (high β_2-parameter) whereas electrons from the HOMO and HOMO-2 orbitals are ejected predominantly perpendicular to the laser polarization (low β_2-parameter).

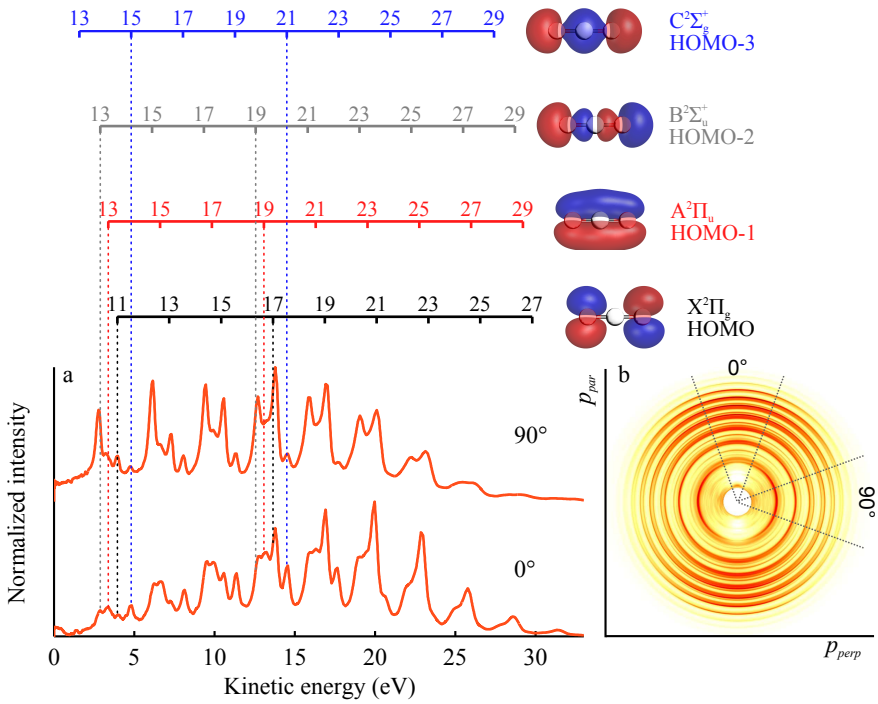

Figure 3.2: (a) Photoelectron spectra from randomly oriented CO_2 molecules for electrons emitted parallel ($\theta_{e^-} = 0°$) and perpendicular ($\theta_{e^-} = 90°$) to the polarization of the ionizing XUV pulse. (b) Photoelectron momentum distribution from which the spectra in (a) are obtained by integrating over a finite acceptance angle of ±20°. The peaks in the spectra in (a) are the result of the presence of four ionization channels corresponding to the HOMO ($X^2\Pi_g$, IP=13.8 eV), the HOMO-1 ($A^2\Pi_u$, IP=17.6 eV), the HOMO-2 ($B^2\Sigma_u^+$, IP=18.1 eV) and the HOMO-3 ($C^2\Sigma_g^+$, IP=19.4 eV) orbitals of CO_2. Each channel can be accessed by multiple harmonic orders in the XUV pulse as is indicated in the top part of the figure where the peak positions of the harmonic orders are given for the four ionization channels together with shape of the corresponding orbital.

3.5 PADs from aligned CO_2

In Fig. 3.3, it is shown that the photoelectron angular distributions undergo significant changes when the molecules are aligned. Fig. 3.3a shows $\langle \cos^2 \theta_{O^+} \rangle$ (from Fig. 3.1) as a function of the delay between the XUV pulse and the alignment pulse around the second revival of the molecular alignment ($\Delta t \approx 21$ ps). The fragment ion data is given as a reference for Figs. 3.3b and 3.3c, where the evolution of the yield (Fig. 3.3b) and the β_2-parameter (Fig. 3.3c) of electrons that correspond to ionization from the four afore-mentioned orbitals is shown for a selected set of harmonics. Note that for an aligned sample of molecules (non-isotropic) the PAD, described by Eq. 3.1, can contain higher order terms as well. The photoelectrons of

the different ionization channels show distinct behavior in both the yield and the angular distribution. The yield of electrons from the HOMO and HOMO-1 orbitals is suppressed (enhanced) when the molecules are aligned (anti-aligned), whereas the yield of electrons corresponding to the HOMO-2 and HOMO-3 orbitals shows the opposite behavior. The electron angular distribution of the HOMO channel is only slightly affected by the alignment of the molecules. The HOMO-1 and HOMO-2 become less (more) peaked along the laser polarization for alignment (anti-alignment) whereas the opposite is true for the HOMO-3 channel. The effect of the alignment on the photoelectron momentum distribution can be seen by plotting the difference between the measured photoelectron momentum distributions for aligned and anti-aligned molecules. The resulting differential photoelectron momentum distribution, shown in Fig. 3.3d, is the result of scanning back and forth between the two delays 60 times while averaging over approximately 20000 laser shots in each step. The enhancement or suppression of the photoionization yield for (anti-)aligned molecules that is observed for a given ionic state, directly relates to the parallel or perpendicular character of the transition from the Σ_g ground state of the molecule to the final molecular ion + photoelectron continuum state. The final state can have either Σ_u or Π_u total symmetry, which results in parallel and perpendicular transitions, respectively [26].The yield of ionic states that are predominantly formed by a parallel (perpendicular) transition, increases (decreases) when the molecule is aligned.

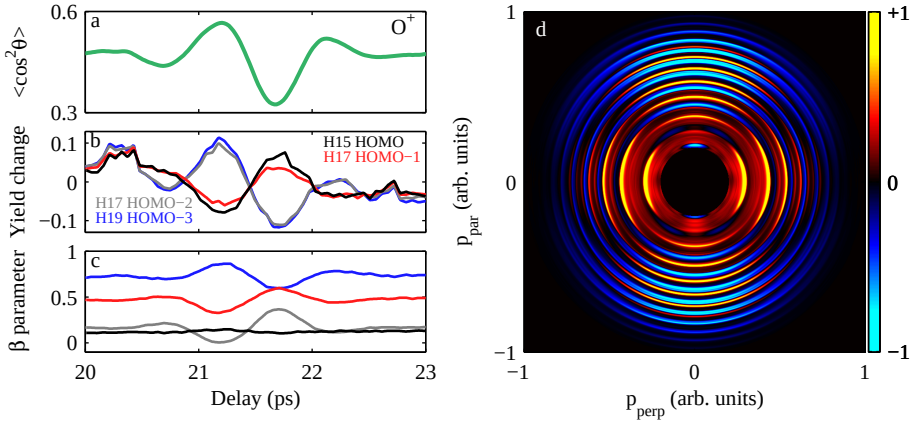

Figure 3.3: (a) $\langle \cos^2 \theta_{O^+} \rangle$ of the angular distribution of O^+ fragments (see Fig. 3.1) as a function of the delay between the alignment pulse and the XUV pulse around the second alignment revival. The expectation value $\langle \cos^2 \theta_{O^+} \rangle$ reflects the degree of alignment of the molecules ($\langle \cos^2 \theta_{CO_2} \rangle$). High values of $\langle \cos^2 \theta_{CO_2} \rangle$ are associated with alignment and low values are associated with anti-alignment. The evolution of the yield (b) and β-parameter (c) of the PAD around this revival shows that the behavior is specific for each channel. The differential momentum distribution in (d) is obtained by subtracting the momentum distributions at maximum alignment and anti-alignment. The differential PAD contains positive (red/yellow) and negative (blue) contributions, related to the symmetry (parallel or perpendicular) of the transition.

3.6 Theoretical model

To analyze the experimental results, PADs from photoionization in aligned CO_2 molecules were calculated for the four ionization channels. The calculations have been performed by Robert Lucchese and the description of the method is a summary of his report about the calculations [27]. A more detailed account can be found in refs. [28–31]. The theoretical method that is used to calculate the PADs is based on the multichannel Schwinger configuration interaction method (MCSCI) that has previously been successfully applied to calculate MFPADs that were recorded with synchrotron radiation. In this method, the initial state and final ionic states are represented as configuration interaction (CI) wave functions. All calculations were done at the experimental equilibrium geometry with R(C-O) = 1.1621 Å[32]. The one-electron basis set, used to construct the bound state wave functions, was the augmented correlation consistent polarized valence triple-ζ basis set (aug-cc-pVTZ) [33, 34]. The bound orbitals used in both the initial and final states were computed using valence complete active space self-consistent field (CASSCF) calculations [35] on the initial neutral molecule. All bound state calculations were performed using the MOLPRO quantum chemistry code [36]. The four outer valence ion states that were found to contribute to the experimental data ($X^2\Pi_g$, $A^2\Pi_u$, $B^2\Sigma_u^+$ and $C^2{\Sigma_g}^+$ of CO_2^+) were included in the MCSCI calculation. The ionization potentials of these states were adjusted, so that they corresponded to the experimental vertical ionization potential. This adjustment ensures that the photoelectron kinetic energy will have the correct asymptotic value, which is necessary since the photoelectron angular distribution is sensitive to the photoelectron kinetic energy. In the calculations the configuration interaction (CI) wave function was not the full valence CI wave function. We have limited the excitation level to at most five electrons in the weakly occupied orbitals in the initial state wave functions and four electrons in the weakly occupied orbitals in the ion state wave functions. This kept the CI wave functions from getting too large, with no more that 6852 configuration state functions in the ion state wave functions.

To simulate the PADs from aligned and anti-aligned CO_2 molecules the experimental alignment distributions have been used that were determined from the O^+ angular distribution data . For each ionization channel i and particular alignment distribution α, the differential cross sections $\sigma_i^\alpha(E_{XUV}, \theta_{e^-})$ was determined as a function of the photon energy E_{XUV} and angle of emission θ_{e^-}. To simulate the experimental results the cross-sections were transformed to an electron kinetic energy axis $E_k = E_{XUV} - IP_i$ after which the cross-section of the four ionization channels were summed:

$$PAD^\alpha(E_k, \theta_{e^-}) = \sum_i A(E_{XUV} - IP_i)\sigma_i^\alpha(E_{XUV} - IP_i, \theta_{e^-}) \tag{3.2}$$

where A is a function that represents the harmonic spectrum:

$$A(E_{XUV}) = \sum_n a_n e^{-4\ln 2\left(\frac{(E_{XUV} - nE_{ph})}{w}\right)^2} \tag{3.3}$$

In this expression, n is the harmonic order, E_{ph} the fundamental photon energy, w the spectral width (FWHM) of the individual harmonics and a_n the amplitude of

the n^{th} harmonic. The width w and amplitudes a_n were determined by projecting Eq. 3.2 onto the experimental signal for three different angles θ_{e^-}.

3.7 Comparison between experiment and theory

Fig. 3.4a shows a comparison between the experimental and calculated differential PADs as a function of the photoelectron energy and the angle θ_{e^-}. A good agreement between the experimental and numerical results is found. In Figs. 3.4b-e the experimental (dotted lines) and calculated (solid lines) differential angular distributions are plotted for the four channels separately, for a selected set of harmonics. The negative contribution to the differential photoelectron spectrum observed for the HOMO (Fig. 3.4b) and HOMO-1 (Fig. 3.4c) ionization channels indicates an enhancement in the photoelectron yield when the molecules are aligned perpendicular to the laser polarization. This indicates a predominantly perpendicular transition and a Π_u total symmetry of the final state. The positive values in the HOMO-3 (Fig. 3.4e) channel show that this is a predominantly parallel transition and that the final state symmetry is given by Σ_u. The differential photoelectron angular distribution corresponding to the HOMO-2 (Fig. 3.4d) dramatically changes around a photoelectron kinetic energy of 15 eV. At low energies only positive values are observed whereas at higher energies negatives values emerge. This shows that the symmetry of the final state changes from Σ_u to Π_u which necessarily is related to a change in the symmetry of the outgoing electron.

The differential PADs of all channels evolve with the photoelectron kinetic energy. The contribution from the HOMO (Fig. 3.4b) shows minima in the differential PAD that are centered at $\theta_{e^-} = 45°$ for low kinetic energies, and which move to $\theta_{e^-} = 0°$ and $\theta_{e^-} = 180°$ (i.e. along the laser polarization) at high kinetic energy. In the case of the HOMO-2 orbital (Fig. 3.4d), the differential angular distribution shows a pronounced maximum perpendicular to the laser polarization ($\theta_{e^-} = 90°$) at low kinetic energy. At higher energies maxima appear along the laser polarization axis, along with a minimum at $\theta_{e^-} = 45°$. Ionization from the HOMO-3 orbital (Fig. 3.4e) leads to positive values in the differential PAD at all angles for low energies while at higher energies minima develop at $\theta_{e^-} = 45°$. Previously, an energy dependence of MFPADs was observed in K-shell photo-ionization of CO and N_2 molecules [9, 37], which was related to the occurrence of shape resonances. The observations presented here could possibly be attributed to the σ^* resonance in the photo-ionization of the HOMO-3 orbital of CO_2 at a photon energy of 32 eV [38]. However, the suppression of the inter-channel couplings in the calculation revealed no significant differences in the PADs. Therefore, the evolution of the angular distribution of the ejected photoelectron may be seen as a manifestation of the influence of the molecular structure on the MFPAD, where the influence of the Coulomb field of the molecule on the trajectories of the outgoing electrons is strongly kinetic energy dependent. In this way information on the structure of the molecule finds its way into the photoelectron angular distribution.

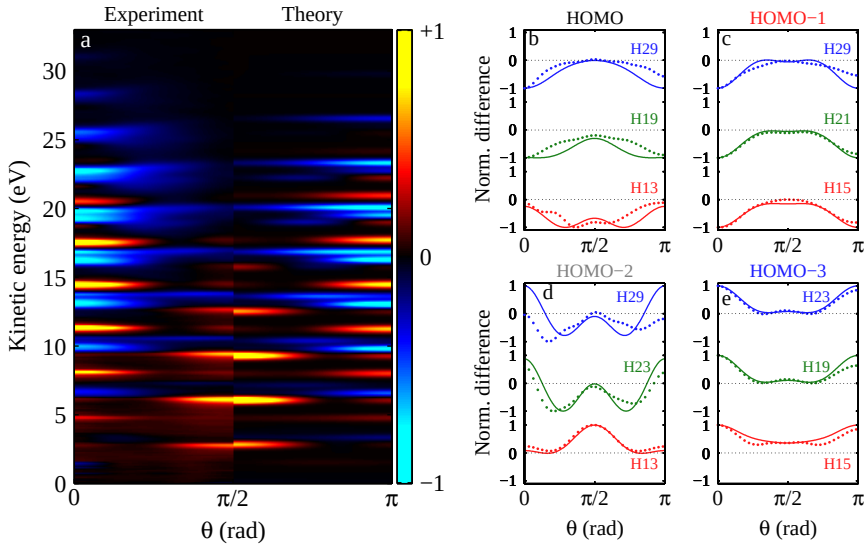

Figure 3.4: (a) Differential PADs (see Fig. 3.3d) from experimental results (left) compared to theory (right) as a function of electron kinetic energy and angle θ_{e^-} between the emission of the electron and the laser polarization. In (b-e) the experimental (dotted lines) and calculated (solid lines) differential angular distributions for a selected set of harmonics are plotted separately for the four ionization channels: HOMO $X^2\Pi_g$ (b), HOMO-1 $A^2\Pi_u$ (c), HOMO-2 $B^2\Sigma_u^+$ (d) and $C^2\Sigma_g^+$ (e). The progression of the angular distribution with the kinetic energy is the result of the interaction of the photoelectron wave with the molecular Coulomb field.

3.8 MFPADs from perfectly aligned CO_2 molecules

In the current experiment the degree of alignment allowed for the observation of the influence of the molecular alignment on the PADs, in particular by looking at the differences in the PAD between aligned and anti-aligned molecules. A higher degree of molecular alignment, which can be obtained by a better cooling of the molecular beam and/or by using a state selector [14, 39], would allow a direct determination of the MFPADs. To explore this prospect, Figs. 3.5a-h show predicted photoelectron momentum distributions for the four experimentally observed ionization channels. In these calculations the molecular axis was assumed to be perfectly aligned parallel (Figs. 3.5a-d) or perpendicular (Figs. 3.5e-h) to the vertical polarization axis. For clarity, no harmonic structure was imposed on the simulated XUV spectrum which extended from 17 to 43 eV. The symmetry of the electronic orbitals can be recognized in the MFPADs in a similar way as was observed in [39]. The photoelectron emission along the laser polarization axis is suppressed for the HOMO and HOMO-1 in the case of parallel alignment (Fig. 3.5a and 3.5b). This is due to the nodal plane in these orbitals parallel to the molecular axis (see Fig. 3.2). The HOMO and HOMO-2 orbitals have a nodal plane that is perpendicular to the molecular axis. This shows up in the MFPAD of these orbitals as a suppression of the electron

emission along the polarization when the molecule is aligned perpendicular to the laser polarization(Fig. 3.5e and Fig. 3.5g). Besides the imprint of information on the electronic structure, the influence of the molecular geometry is recognized in the evolution of the MFPADs with the electron kinetic energy. Clearly, the number of nodes in the MFPADs in Figs. 3.5a-h grows with increasing photon and photoelectron energy. The higher number of nodes in the MFPADs reflects the contributions of partial waves with higher angular momentum in the electron scattering wave packets. Figs. 3.5i-l show the decomposition of the MFPADs into partial waves as a function of electron kinetic energy, for the case of parallel alignment. For instance, Fig. 3.5i shows that ionization from the HOMO orbital leads to an electron wave packet that is mainly composed of the l=1, m=0 (p-wave) and l=3, m=0,2 partial waves (f-wave) in the photon energy range studied here. The partial wave decomposition of the electron wave packet for the HOMO-2 orbital (Fig. 3.5k) is composed of l=0,2, m=0 at low kinetic energies (i.e. s- and d-waves) and changes to l=4, m=1 (g-wave) at 15 eV. This causes the experimentally observed sign change in the differential photoelectron spectrum. The contribution of higher-l partial waves reflects the increased sensitivity of the electron to the molecular (Coulomb) field at these kinetic energies. The effect of the Coulomb field on the outgoing electron depends on its kinetic energy. This affects the coupling between the partial waves and leads to the observed evolution of the angular distribution with kinetic energy. In other words, electrons leaving the molecule are scattered and this scattering leaves its imprint on the MFPAD which can be seen as a signature of the molecular structure [20].

3.9 Conclusions and outlook

We have shown that the measured PADs from aligned molecules reflect both the orbital symmetries of the ionization channels that are accessed and the onset of an interference/diffraction pattern related to the molecular field, and consequently, the molecular structure. As such, these results pave the way towards experiments in which structural and electronic dynamics during photochemical reactions can be recorded. A natural extension of this work would be to add a third pump pulse that initiates such a photochemical reaction, for example the dissociation of a molecule. The current work demonstrates the great potential of experiments in which PADs are measured from aligned molecules using XUV and X-Ray FELs such as FLASH, LCLS and the upcoming European XFEL. Moreover, recent developments in HHG sources will make it possible to extend the current results to higher photon energies [40], which would allow photoelectron diffraction experiments to be performed on a lab-scale. An obvious advantage of HHG sources is the possibility to synchronize the ionization pulse almost perfectly to other pulses in the visible or UV range, allowing the investigation of dynamics on the few-femtosecond or even attosecond timescale. For example MFPADs that are generated by attosecond pulses can potentially be used to resolve photonionization induced charge migration processes in molecules which have been predicted to occur on attosecond timescales [41, 42].

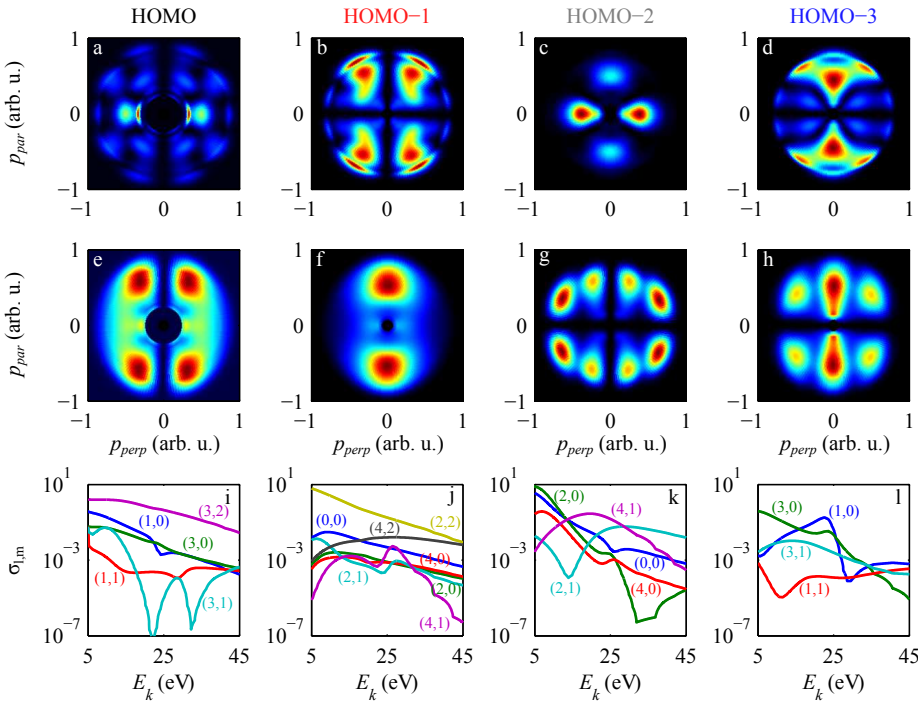

Figure 3.5: Theoretical prediction of momentum distributions for the four ionization channels leading to the $X^2\Pi_g$, $A^2\Pi_u$, $B^2\Sigma_u^+$ and $C^2\Sigma_g^+$ states of CO_2^+, for a continuous XUV spectrum (from 17 to 43 eV). The polarization axis is in the vertical direction and the molecular axis is vertical (parallel to the polarization axis) (a-d) and horizontal (perpendicular to the polarization axis) (e-h). In panels (i-l) the cross-sections $\sigma_{l,m}$ for the different partial waves (l, m) that contribute to the continuum electron wave packet are given for each ionization channel as a function of the photoelectron kinetic energy.

References

[1] A. H. Zewail. *Femtochemistry: Atomic-Scale Dynamics of the Chemical bond using ultrafast lasers - (Nobel lecture).* Angewandte Chemie-International Edition, **39**, 2587–2631 (2000).

[2] H. Ihee, V. A. Lobastov, U. M. Gomez, B. M. Goodson, R. Srinivasan, C. Y. Ruan and A. H. Zewail. *Direct imaging of transient molecular structures with ultrafast diffraction.* Science, **291**, 458–462 (2001).

[3] B. J. Siwick, J. R. Dwyer, R. E. Jordan and R. J. D. Miller. *An atomic-level view of melting using femtosecond electron diffraction.* Science, **302**, 1382–1385 (2003).

[4] N. Gedik, D. S. Yang, G. Logvenov, I. Bozovic and A. H. Zewail. *Nonequilibrium phase transitions in cuprates observed by ultrafast electron crystallography.* Science, **316**, 425–429 (2007).

[5] P. Baum and A. H. Zewail. *Attosecond electron pulses for 4D diffraction and microscopy.* Proc. Natl. Acad. Sci. U. S. A., **104**, 18409–18414 (2007).

[6] E. Goulielmakis *et al. Single-cycle nonlinear optics.* Science, **320**, 1614–1617 (2008).

[7] W. Ackermann *et al. Operation of a free-electron laser from the extreme ultraviolet to the water window.* Nat. Photonics, **1**, 336–342 (2007).

[8] P. Emma *et al. First lasing and operation of an ångstrom-wavelength free-electron laser.* Nat. Photonics, **4**, 641–647 (2010).

[9] A. Landers *et al. Photoelectron diffraction mapping: Molecules illuminated from within.* Phys. Rev. Lett., **8701**, 013002 (2001).

[10] J. Ullrich, R. Moshammer, A. Dorn, R. Dorner, L. P. H. Schmidt and H. Schniidt-Bocking. *Recoil-ion and electron momentum spectroscopy: reaction-microscopes.* Reports on Progress in Physics, **66**, 1463–1545 (2003).

[11] N. Watanabe, J. Adachi, K. Soejima, E. Shigemasa, A. Yagishita, N. G. Fominykh and A. A. Pavlychev. *Fixed-Molecule* $1s\sigma_{g,u}$ *Photoelectron Angular Distributions as a Probe of* σ_g^* *and* σ_u^* *Shape Resonances of* CO_2. Phys. Rev. Lett., **78**, 4910–4913 (1997).

[12] K. L. Reid. *Photoelectron angular distributions.* Annu. Rev. Phys. Chem., **54**, 397–424 (2003).

[13] F. Rosca-Pruna and M. J. J. Vrakking. *Experimental observation of revival structures in picosecond laser-induced alignment of* I_2. Phys. Rev. Lett., **8715**, 153902 (2001).

[14] O. Ghafur, A. Rouzee, A. Gijsbertsen, W. K. Siu, S. Stolte and M. J. J. Vrakking. *Impulsive orientation and alignment of quantum-state-selected NO molecules.* Nat. Phys., **5**, 289–293 (2009).

[15] H. Stapelfeldt. *Alignment of molecules by strong laser pulses.* Eur. Phys. J. D., **26**, 15–19 (2003).

[16] P. Johnsson *et al. Field-free molecular alignment probed by the free electron laser in Hamburg (FLASH).* J. Phys. B-At. Mol. Opt., **42**, 134017 (2009).

[17] M. Tsubouchi, B. J. Whitaker, L. Wang, H. Kohguchi and T. Suzuki. *Photoelectron imaging on time-dependent molecular alignment created by a femtosecond laser pulse.* Phys. Rev. Lett., **86**, 4500–4503 (2001).

[18] C. Z. Bisgaard, O. J. Clarkin, G. R. Wu, A. M. D. Lee, O. Gessner, C. C. Hayden and A. Stolow. *Time-Resolved Molecular Frame Dynamics of Fixed-in-Space* CS_2 *Molecules.* Science, **323**, 1464–1468 (2009).

[19] Y. Tang, Y. I. Suzuki, T. Horio and T. Suzuki. *Molecular Frame Image Restoration and Partial Wave Analysis of Photoionization Dynamics of NO by Time-Energy Mapping of Photoelectron Angular Distribution.* Phys. Rev. Lett., **104**, 073002 (2010).

[20] F. Krasniqi, B. Najjari, L. Struder, D. Rolles, A. Voitkiv and J. Ullrich. *Imaging molecules from within: Ultrafast angstrom-scale structure determination of molecules via photoelectron holography using free-electron lasers.* Phys. Rev. A, **81**, 033411 (2010).

[21] S. X. Hu, L. A. Collins and B. I. Schneider. *Attosecond photoelectron microscopy of* H_2^+. Phys. Rev. A, **80**, 023426 (2009).

[22] M. Meckel *et al. Laser-induced electron tunneling and diffraction.* Science, **320**, 1478–1482 (2008).

[23] Y. Huismans *et al. Time-Resolved Holography with Photoelectrons.* Science, **331**, 61–64 (2011).

[24] O. Ghafur, W. Siu, P. Johnsson, M. F. Kling, M. Drescher and M. J. J. Vrakking. *A velocity map imaging detector with an integrated gas injection system.* Rev. Sci. Instrum., **80**, 033110 (2009).

[25] F. Lepine *et al. Short XUV pulses to characterize field-free molecular alignment.* J. Mod. Opt., **54**, 953–966 (2007).

[26] I. Cacelli, R. Moccia and R. Montuoro. *Influence of the channel interaction on the photoabsorption and photoionization spectra of carbon dioxide.* Phys. Rev. A, **63**, 012512 (2000).

[27] R. Lucchese. *Valence Molecular Frame Photoelectron Angular Distributions in* N_2*,* CO*,* O_2*, and* CO_2 (2010). Internal report.

[28] R. R. Lucchese, K. Takatsuka and V. McKoy. *Applications of the Schwinger variational principle to electron-molecule collisions and molecular photoionization.* Physics Reports, **131**, 147 – 221 (1986).

[29] R. E. Stratmann and R. R. Lucchese. *A graphical unitary group approach to study multiplet specific multichannel electron correlation effects in the photoionization of* O_2. The Journal of Chemical Physics, **102**, 8493–8505 (1995).

[30] R. E. Stratmann, R. W. Zurales and R. R. Lucchese. *Multiplet-specific multichannel electron-correlation effects in the photoionization of NO.* The Journal of Chemical Physics, **104**, 8989–9000 (1996).

[31] R. R. Lucchese, A. Lafosse, J. C. Brenot, P. M. Guyon, J. C. Houver, M. Lebech, G. Raseev and D. Dowek. *Polar and azimuthal dependence of the molecular frame photoelectron angular distributions of spatially oriented linear molecules.* Phys. Rev. A, **65**, 020702 (2002).

[32] G. Herzberg. *Molecular spectra and molecular structure. Vol.III: Electronic spectra and electronic structure of polyatomic molecules.* Van Nostrand-Reinhold, New York (1966).

[33] R. A. Kendall, J. Thom H. Dunning and R. J. Harrison. *Electron affinities of the first-row atoms revisited. Systematic basis sets and wave functions.* The Journal of Chemical Physics, **96**, 6796–6806 (1992).

[34] J. Thom H. Dunning. *Gaussian basis sets for use in correlated molecular calculations. I. The atoms boron through neon and hydrogen.* The Journal of Chemical Physics, **90**, 1007–1023 (1989).

[35] B. O. Roos. *The Complete Active Space Self-Consistent Field Method and its Applications in Electronic Structure Calculations*, John Wiley & Sons, Inc., 399–445 (2007).

[36] H.-J. Werner, P. J. Knowles, F. R. Manby, M. Schütz *et al. MOLPRO, version 2010.1, a package of ab initio programs* (2010).

[37] R. Guillemin *et al. Nondipolar electron angular distributions from fixed-in-space molecules.* Phys. Rev. Lett., **89**, 033002 (2002).

[38] R. R. Lucchese, D. K. Watson and V. McKoy. *Iterative approach to the Schwinger variational principle for electron-molecule collisions.* Phys. Rev. A, **22**, 421–426 (1980).

[39] L. Holmegaard, J. H. Nielsen, I. Nevo, H. Stapelfeldt, F. Filsinger, J. Küpper and G. Meijer. *Laser-Induced Alignment and Orientation of Quantum-State-Selected Large Molecules.* Phys. Rev. Lett., **102**, 023001 (2009).

[40] T. Popmintchev, M. C. Chen, A. Bahabad, M. Gerrity, P. Sidorenko, O. Cohen, I. P. Christov, M. M. Murnane and H. C. Kapteyn. *Phase matching of high harmonic generation in the soft and hard X-ray regions of the spectrum.* Proc. Natl. Acad. Sci. U. S. A., **106**, 10516–10521 (2009).

[41] A. I. Kuleff and L. S. Cederbaum. *Tracing ultrafast interatomic electronic decay processes in real time and space.* Phys. Rev. Lett., **98**, 083201 (2007).

[42] F. Remacle and R. D. Levine. *Electrical transport in saturated and conjugated molecular wires.* Faraday Discuss., **131**, 45–67 (2006).

4 Electron localization following attosecond molecular photoionization

For the past several decades, we have been able to directly probe the motion of atoms that is associated with chemical transformations and which occurs on the femtosecond (10^{-15}-s) timescale. However, studying the inner workings of atoms and molecules on the electronic timescale [1–4] has become possible only with the recent development of isolated attosecond (10^{-18}-s) laser pulses [5]. Such pulses have been used to investigate atomic photoexcitation and photoionization [6, 7] and electron dynamics in solids [8], and in molecules could help explore the prompt charge redistribution and localization that accompany photoexcitation processes. In recent work, the dissociative ionization of H_2 and D_2 was monitored on femtosecond timescales [9] and controlled using few-cycle near-infrared laser pulses [10]. Here we report a molecular attosecond pump-probe experiment based on that work: H_2 and D_2 are dissociatively ionized by a sequence comprising an isolated attosecond ultraviolet pulse and an intense few-cycle infrared pulse. A localization of the electronic charge distribution within the molecule is measured that depends-with attosecond time resolution-on the delay between the pump and probe pulses. The localization occurs by means of two mechanisms, where the infrared laser influences the photoionization or the dissociation of the molecular ion. In the first case, charge localization arises from quantum mechanical interference involving autoionizing states and the laser-altered wavefunction of the departing electron. In the second case, charge localization arises owing to laser-driven population transfer between different electronic states of the molecular ion. These results establish attosecond pump-probe strategies as a powerful tool for investigating the complex molecular dynamics that result from the coupling between electronic and nuclear motions beyond the usual Born-Oppenheimer approximation.

4.1 Introduction

Following the successful development of isolated attosecond laser pulses less than a decade ago [5], their use in studying atomic photoexcitation and photoionization [6, 7] and electron dynamics in solids [8] has raised the prospects that molecular sciences may similarly benefit from the introduction of attosecond techniques. The timescale for the motion of atoms associated with chemical transformations is necessarily in the femtosecond domain, but the electronic rearrangement that accompanies the sudden removal or excitation of a selected electron is intrinsically faster.

Indeed, the removal of electrons involved in chemical bonding may result in hole dynamics on sub- or few-femtosecond timescales in systems including biomolecules and biomolecular complexes [11, 12]. Extremely fast molecular dynamics involving electron correlation can also be initiated by the excitation of doubly excited states and by subsequent autoionization processes [13, 14].

Existing experimental implementations of attosecond techniques [15–18] do not readily lend themselves to the study of intramolecular electronic rearrangement processes. We therefore measure angular asymmetries in the momentum distributions of fragments that result from dissociative ionization, as these asymmetries are directly related to charge dynamics. As a benchmark, we investigate the dissociative ionization of hydrogen molecules (H_2, D_2) and present experimental results mainly for D_2 (for which data are of higher quality). Computational results are for H_2 (for which close-coupling calculations allow a more extensive exploration of the experimental conditions), but are occasionally compared with H_2 measurements that are of lower quality but show behavior analogous to the D_2 measurements.

4.2 Experimental method

Our experiment combines an isolated attosecond extreme-ultraviolet (XUV) pulse [19], the spectrum of which extended from 20 to 40 eV, with a (time-delayed) intense infrared pulse with identical linear polarization and a full-width at half-maximum of 6 fs. To generate both beams, linearly polarized few-cycle infrared laser pulses with a controlled carrier-envelope phase were divided into a central and an annular part using a drilled mirror. The polarization state of the central part was modulated in time using two birefringent plates to obtain a short temporal window of linear polarization around the center of the pulse. This laser beam was focused in a krypton gas jet to generate an XUV continuum through high-order harmonic generation [20]. A 100-nm aluminium filter was used to eliminate low-order harmonics and the infrared radiation, and provided partial dispersion compensation of the transmitted XUV light. In this way, single attosecond pulses with a duration of between 300 and 400 as were produced [19]. The attosecond pulses were focused, using a grazing-incidence toroidal mirror, into the interaction region of a velocity-map imaging spectrometer. The annular part of the original infrared beam was focused using a spherical mirror and collinearly recombined with the attosecond pulse using a second drilled mirror. The relative time delay between the two pulses was changed with attosecond time resolution using a piezoelectric stage inserted in the interferometric set-up. The XUV and infrared laser beams were crossed with an effusive H_2 or D_2 gas jet which emerged from a 50-μm-diameter capillary that was incorporated into the repeller electrode of the velocity-map imaging spectrometer [21]. Ions generated in the two-color dissociative ionization were projected onto a dual microchannel plate plus phosphor screen detector. Two-dimensional ion images were acquired using a low-noise charge-coupled-device camera, and allowed retrieval of the three-dimensional velocity distribution of the ions.

4.3 Numerical method

Numerical calculations are done by solving the time-dependent Schrödinger equation (TDSE) for H_2 using a close-coupling method [14], taking into account all electronic and vibrational (dissociative) degrees of freedom. Because the calculations are performed in real, three-dimensional space, they therefore include the effect of electron correlation and interferences between different ionization and dissociation pathways. We focus on the detection of fragments from molecules aligned parallel to the laser polarization axis, so our calculations only include states of Σ symmetry.

Briefly, we have solved the seven-dimensional TDSE

$$\left(\hat{\mathbf{H}}^0(\mathbf{r}_1,\mathbf{r}_2,R)+V(t)-i\frac{\partial}{\partial t}\right)\Phi(\mathbf{r}_1,\mathbf{r}_2,R,t)=0 \tag{4.1}$$

where $\mathbf{r}_1$ and $\mathbf{r}_2$ are the position vectors of electrons 1 and 2, respectively (each three-dimensional), R is the internuclear distance (one-dimensional), $\hat{\mathbf{H}}^0$ is the H_2 field-free non-relativistic Hamiltonian, Φ the time-dependent wavefunction and $V(t)$ is the laser-H_2 interaction potential in the dipole approximation, which is a sum of two terms respectively corresponding to the XUV and infrared pulses separated by a peak-to-peak time delay τ, $V(t)=V_{XUV}(t)+V_{IR}(t+\tau)$, with respective frequencies ω_{XUV} and ω_{IR} and durations T_{XUV} and T_{IR}. Each pulse has a squared-cosine temporal envelope and is given by the analytical formula

$$V_k(t')=\begin{cases}\boldsymbol{p}\cdot\boldsymbol{A}_k^0\cos^2\left(\frac{\pi t'}{T_k}\right) & \text{for } -\frac{T_k}{2}<t<\frac{T_k}{2}\\ 0 & \text{elsewhere}\end{cases} \tag{4.2}$$

where $t=t'$ for the XUV pulse, $t=t'+\tau$ for the infrared pulse, $\boldsymbol{p}$ is the dipole moment and $\boldsymbol{A}_k^0$ is the vector potential of the laser. In all calculations, we used ω_{XUV}=30 eV, T_{XUV}=400 as and $I_{XUV}=|\boldsymbol{A}_{XUV}^0|^2\omega_{XUV}=10^9$ W/cm^2, where $\boldsymbol{A}_0^{XUV}$ and I_{XUV} are respectively the vector potential and the intensity of the attosecond pulse, and ω_{IR}=1.65 eV, T_{IR}=16 fs (corresponding to a pulse duration with a full-width at half-maximum of 6 fs) and $I_{IR}=|\boldsymbol{A}_{IR}^0|^2\omega_{IR}=3\times10^{12}$ W/cm^2,where $\boldsymbol{A}_{IR}^0$ and I_{IR} are respectively the vector potential and the intensity of the infrared pulse, and τ was varied from 0 to 12 fs. We solved the TDSE by expanding the time-dependent wavefunction, Φ, in a basis of fully correlated H_2 vibronic stationary states of Σ_g^+ and Σ_u^+ symmetries, which include the bound states, the non-resonant continuum states associated with the $1s\sigma_g$ and $2p\sigma_u$ ionization channels, and the lowest Q_1 and Q_2 doubly excited states. In this calculation, the TDSE was effectively six-dimensional and the results are exclusively valid for H_2 molecules oriented parallel to the polarization direction. The electronic part of the vibronic states is calculated in a sphere of radius 160 a.u. and the nuclear part in a sphere of radius 12 a.u. The sizes of these spheres are large enough to ensure that there are no significant reflections of electronic and nuclear wave packets at the sphere boundaries for propagation times less than $\tau+(T_{XUV}+T_{IR})/2$. Non-adiabatic couplings and molecular rotations were neglected.

4.4 Dissociative ionization of hydrogen molecules

The choice of hydrogen as the subject of our investigation follows a rich tradition [22, 23]. An attractive feature of H_2 is that its (intense-field) dissociative ionization can often be understood in terms of the two lowest electronic states, $^2\Sigma_g^+$ $(1s\sigma_g)$and $^2\Sigma_u^+$ $(2p\sigma_u)$, of the molecular ion (Fig. 4.1). The XUV and IR pulse dissociate hydrogen molecules to produce the ionic fragments H^+ or D^+, the velocity and angular distribution of which are then measured [24]. Fig. 4.2a shows measured kinetic energy spectra for D^+, which in the absence of the infrared beam (top trace) have a broad kinetic energy distribution consistent with earlier experimental and theoretical work [25]. Fig. 4.2c shows calculated kinetic energy spectra for H^+ using the method described above. On XUV excitation, several pathways can lead

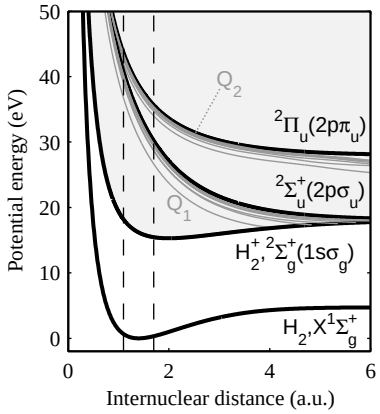

Figure 4.1: Potential energy diagram of the H_2 molecule displaying the energies of the neutral and ionic states that are relevant to the experiment as a function of internuclear distance. Photoexcitation of neutral hydrogen by XUV light leads to the excitation of the Q_1 (red) and Q_2 (blue) doubly excited states and ionization to the $1s\sigma_g$ and $2p\sigma_u$ states, which can be followed by dissociation into a neutral H atom and a H^+ ion.

to dissociative ionization. The relative weights of the observed pathways depend on the energy of the ionizing photon and on the angle between the directions of ionic fragment observation and laser polarization [25]. For photon energies up to $h\nu = 25$ eV (where h is Planck's constant and ν is the photon frequency), direct ionization forms the molecular $^2\Sigma_g^+$ $(1s\sigma_g)$state and releases a small fraction (2%) of low-kinetic-energy ionic fragments ($E_k < 1$ eV). For photon energies between $h\nu = 25$ eV and $h\nu = 36$ eV, a parallel transition preferentially excites molecules aligned along the polarization axis to the doubly excited Q_1 $^1\Sigma_g^+$ states; subsequent autoionization to the $^2\Sigma_g^+$ $(1s\sigma_g)$state produces ionic fragments with a kinetic energy that spans the range 0-10 eV but lies primarily between 2 and 7 eV (refs [26, 27]). Direct ionization to the repulsive $^2\Sigma_u^+$ $(2p\sigma_u)$state becomes possible at $h\nu = 30$ eV. At energies above $h\nu = 38$ eV, the full range of internuclear distances sampled by the ground state of H_2 can participate in this channel, leading to high-energy fragments (E_k = 5-10 eV). Above 31 eV, a perpendicular transition preferentially

excites molecules aligned orthogonally to the laser polarization axis to the $Q_2\ ^1\Pi_u$ doubly excited states. These states autoionize to both the $^2\Sigma_g^+$ $(1s\sigma_g)$state and the $^2\Sigma_u^+$ $(2p\sigma_u)$state, resulting in ionic fragments with kinetic energies of 1-5 eV and 5-8 eV, respectively [25]. Because the evaluation of the kinetic energy distributions in the experiment forces us to include ionic fragments within a 45° cone around the laser polarization axis, involvement of the $Q_2\ ^1\Pi_u$ states cannot be ruled out a priori. When the molecules furthermore interact with a few-cycle infrared pulse, the kinetic energy distributions of the ion fragments change. This is illustrated in Figs. 4.2b and 4.2d which show experimental D^+ and calculated H^+ kinetic energy distributions as functions of the relative delay, τ, between the attosecond and infrared pulses. (We note that calculations could be performed only for infrared intensities up to 3×10^{12}W cm^{-2} and for XUV-infrared delays of up to 12 fs, whereas experimental infrared intensities may have been higher by as much as a factor of two.)

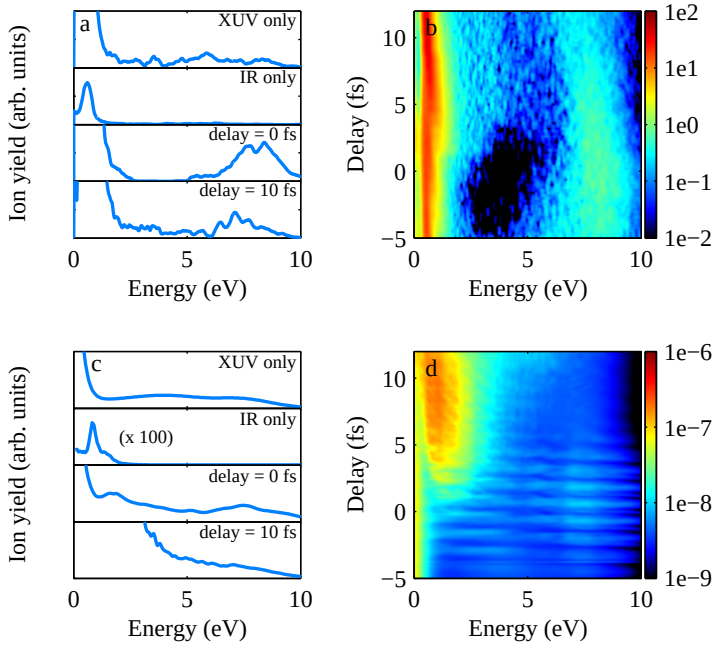

Figure 4.2: Experimental D^+ (a) and calculated H^+ (d) kinetic energy distributions with (from top to bottom) only the isolated attosecond laser pulse present, with only the few-cycle infrared (IR) laser pulse present and for two delays between the XUV and infrared pulses. Experimental D^+ (b) and calculated H^+ (d) kinetic energy distributions as functions of the delay between the attosecond pulse and the infrared pulse. The color scale shows the fragment yield in arbitrary units (b) and calculated probabilities (d).

In the low-energy regime ($E_k < 1$ eV), the infrared pulse causes bond-softening of the bound $^2\Sigma_g^+$ $(1s\sigma_g)$vibrational wave packet. The effect peaks at τ+10 fs, when the wave packet is near the outer turning point of the potential energy curve [9, 28]. When the XUV and infrared pulses overlap (τ <0 fs), the ion signal at kinetic energies of around 8 eV increases strongly and decreases at intermediate energies

(3 eV $< E_k <$ 5 eV). Guided by the close-coupling calculations, we attribute the high-energy ion signal enhancement to an increase in the excitation cross-section of the $2p\sigma_u$ continuum state caused by infrared-laser-induced mixing of the $2p\sigma_u$ and $1s\sigma_g$ states. The increase may also contain contributions from photoionization of the $Q_1\ ^1\Sigma_g^+$ doubly excited states by the infrared laser. For longer time delays ($\tau >$ 8 fs), the kinetic energy distribution above 1 eV does not change appreciably with delay and resembles the distribution obtained in the absence of the infrared field (Figs. 4.2a,b).

4.5 Laboratory frame asymmetries in two-color dissociative ionization

Dissociative ionization of H_2 lends itself to the observation of both laboratory-frame and molecular-frame asymmetries. The first corresponds to an asymmetry in the fragment ejection along the laser polarization axis, and the second corresponds to a correlation or anticorrelation in the direction of emission of the ionized electron and the ionic fragment. Laboratory-frame asymmetries were previously observed in dissociative ionization of D_2 by a carrier-envelope phase-locked infrared laser pulse [10], and symmetry-breaking in the molecular frame was observed in single-photon XUV dissociative ionization of H_2 and D_2, mediated by autoionization of the $Q_2\ ^1\Pi_u$ state [29]. We define laboratory-frame asymmetries, $A(E_k, \tau)$, as

$$A(E_k, \tau) = \frac{N_L(E_k, \tau) - N_R(E_k, \tau)}{N_L(E_k, \tau) + N_R(E_k, \tau) + \delta} \tag{4.3}$$

where $N_L(E_k, \tau)$ and $N_R(E_k, \tau)$ indicate the numbers of ions arriving within 45° of the polarization axis on the left- and, respectively, righthand sides of the detector, and δ is a small number that prevents a singularity when $N_L(E_k, \tau) + N_R(E_k, \tau)$ vanishes. Over almost the entire kinetic energy range in which D^+ and H^+ ions are formed, asymmetries are observed that oscillate as functions of τ, as shown in Fig. 4.3a (D^+) and Fig. 2c (H^+). Delaying the infrared laser by one-quarter of the infrared period (650 as) or by one-half of the infrared period (1.3 fs) leads to a disappearance or, respectively, a reversal of the electron localization. The phase of the asymmetry oscillations strongly depends on the kinetic energy of the fragment that is measured. The asymmetries can be understood by writing the two-electron wavefunction of singly ionized H_2 as

$$\begin{aligned}\Psi =& c_1[1s\sigma_g(1)\epsilon l_g(2)]_g + c_2[1s\sigma_g(1)\epsilon l_u(2)]_u \\ &+ c_3[2p\sigma_u(1)\epsilon l_u(2)]_g + c_4[2p\sigma_u(1)\epsilon l_g(2)]_u\end{aligned} \tag{4.4}$$

where, for simplicity, the wavefunction has not been antisymmetrized with respect to electrons 1 and 2, and the ionized electron 2 is described by a continuum orbital of well-defined energy ϵ and angular momentum l_g or l_u. The observation of a fragment asymmetry relies on the formation of a mixed-parity superposition state that contains contributions (at the same fragment kinetic energy and for the same angular momentum, l_u or l_g) from both the $1s\sigma_g$ state and the $2p\sigma_u$ state. This

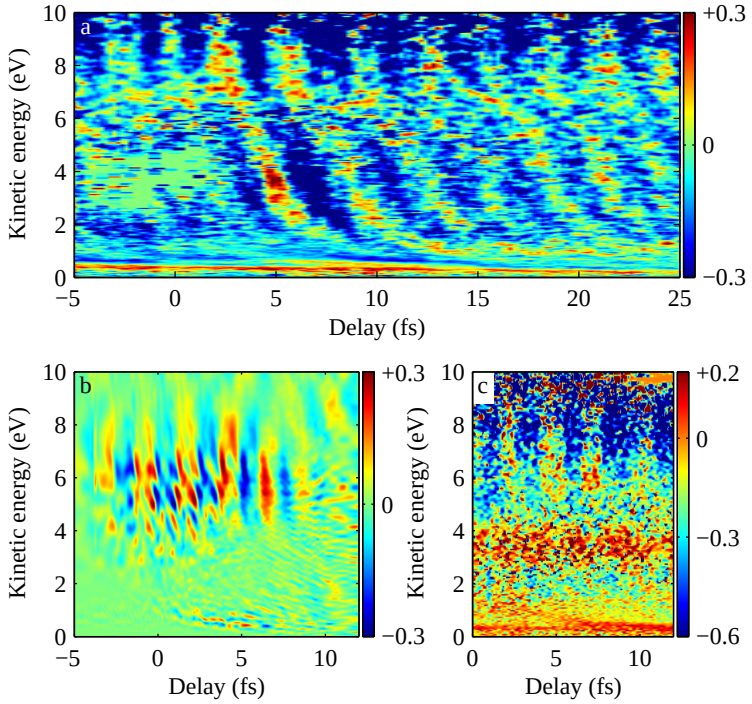

Figure 4.3: Experimentally measured asymmetry parameter (color scale) for the formation of D^+ ions in two-color (XUVinfrared) dissociative ionization of D_2, as a function of the fragment kinetic energy, E_k, and the XUVinfrared delay. A fragment asymmetry is observed that oscillates as a function of the XUVinfrared delay and that strongly depends on the kinetic energy. b, Calculated asymmetry parameter for the formation of H^+ ions in two-color XUVinfrared dissociative ionization of H_2, as a function of the fragment kinetic energy, E_k, and the XUVinfrared delay, obtained using the close-coupling method described in the text. c, Same as in a, but for H^+ ions.

can be recognized from the following expressions for wavefunctions of $H_2^+ + e^-$ that have the bound electron localized on the left (Ψ_L) or the right (Ψ_R) proton:

$$\begin{aligned}\Psi_L &= [1s\sigma_g(1) + 2p\sigma_u(1)]\epsilon l_{g,u}(2)\\ \Psi_R &= [1s\sigma_g(1) - 2p\sigma_u(1)]\epsilon l_{g,u}(2)\end{aligned} \tag{4.5}$$

From equations (1)-(3), we see that

$$N_L(E_k,\tau) - N_R(E_k,\tau) = 4\Re\{c_1 c_4^* + c_2 c_3^*\} \tag{4.6}$$

Thus, a laboratory-frame asymmetry is formed by a mixed-parity superposition in which the continuum electron has the same angular momentum, l_u or l_g, in both ionic states, with $c_1, c_4 \neq 0$ and, respectively, $c_2, c_3 \neq 0$ (ref. 10). In contrast, a molecular frame asymmetry is caused by an interference of the first and third terms in equation (2), for $c_1, c_3 \neq 0$, or the second and fourth terms, for $c_2, c_4 \neq 0$ (ref. 27).

The values of $A(E_k, \tau)$ can be accurately evaluated from the two-electron wavefunction obtained in the close-coupling calculation, and we find that they reproduce the observed oscillations in $A(E_k, \tau)$ with the periodicity of the infrared laser (Fig. 4.3b). The asymmetry oscillations are very pronounced for delays of up to 7 fs and kinetic energies above 5 eV, and decrease in amplitude for delays of more than 7 fs and kinetic energies below 5 eV.

The close-coupling calculation lends itself to a detailed analysis of the mechanisms that lead to the measurement of laboratory-frame asymmetries in the dissociative ionization of the molecule. In the absence of the infrared pulse, the XUV photoionization produces a two-electron wavefunction in which only c_2 and c_4 are non-zero, thereby precluding the observation of a laboratory-frame asymmetry. The infrared laser can cause an asymmetry either by changing the wavefunction of the continuum electron (mechanism I; Fig. 4.5a) or by changing the wavefunction of the molecular ion (mechanism II; Fig. 3c): mechanism I occurs as a result of the influence of the infrared laser during the photoexcitation process, whereas mechanism II occurs as a result of the interaction of the molecular ion with the infrared laser during the dissociation process.

Mechanism I is further explained with the help of Fig. 4.4 which shows the angular momentum and electronic state-resolved delay dependence of H^+ ions with a fragment kinetic energy in the interval 7.5 eV $< E_k <$ 8.5 eV. Angular momenta l_g and l_u respectively stand for $l_g; (1s\sigma_g \epsilon l)_g$ and $l_u; (2p\sigma_u \epsilon l)_u$ for $l = 0$ ($s_{g,u}$ wave), $l = 2$ ($d_{g,u}$ wave), ... (even l) and $l_g; (2p\sigma_u \epsilon l)_g$ and $l_u; (1s\sigma_g \epsilon l)_u$ for $l = 1$ ($p_{g,u}$ wave), $l = 3$ (f_g, u wave), ... (odd l). A (time-dependent) asymmetry is expected when for a given angular momentum a substantial population is simultaneously present in both the $1s\sigma_g$ state and the $2p\sigma_u$ state (g and u). The asymmetry oscillations in Fig. 4.3b in the region where the XUV and infrared pulses overlap ($\tau < 8$ fs) occur under conditions in which XUV-only ionization produces high-energy fragments (from excitation of the $2p\sigma_u$ state) accompanied by the emission of an s electron ($c_4 \neq 0$). However, the interaction of the infrared laser with this photoelectron redistributes the wavefunction over several angular momentum states, including the p continuum ($c_3 \neq 0$; see Fig. 4.4). At the same time, autoionization of the $Q_1\ ^1\Sigma_g^+$ state (and, to a lesser extent, direct ionization) leads to the formation of a dissociative wave packet in the $1s\sigma_g$ state that is primarily accompanied by the emission of a p electron ($c_2 \neq 0$; Fig. 4.4). Further support for the involvement of the $Q_1\ ^1\Sigma_g^+$ state is suggested by results of a close-coupling calculation in which direct excitation to the $1s\sigma_g$ state by the XUV pump was artificially suppressed (Fig. 4.5b): fringes in the region with $\tau < 7$ fs and $E_k > 5$ eV are still apparent, even though no wave packet is initially produced in the $1s\sigma_g$ state. Given these lines of evidence, we conclude that mechanism I (Fig. 4.5a) successfully explains the asymmetry oscillations observed for temporal overlap of the XUV and infrared pulses: these oscillations result from interference of one wave packet in the $1s\sigma_g$ state, predominantly formed by autoionization of the $Q_1\ ^1\Sigma_g^+$ doubly excited state, with a wave packet in the $2p\sigma_u$ state, formed through XUV photoionization and with the continuum electron absorbing one or more photons from the infrared field. Mechanism I occurs only when the XUV and infrared pulses overlap, whereas mechanism II requires only that the infrared pulse be intense during the dissociation of the molecule so it can induce

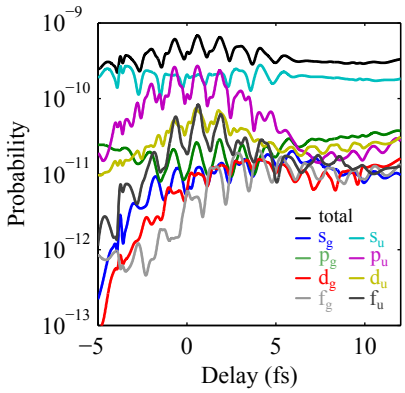

Figure 4.4: Angular momentum and electronic state-resolved delay dependence of H^+ ions with a fragment kinetic energy in the interval 7.5 eV $< E_k <$ 8.5 eV. Angular momenta l_g and l_u respectively stand for $l_g; (1s\sigma_g\epsilon l)_g$ and $l_u; (2p\sigma_u\epsilon l)_u$ for $l = 0$ ($s_{g,u}$ wave), $l = 2$ ($d_{g,u}$ wave), ...(even l) and $l_g; (2p\sigma_u\epsilon l)_g$ and $l_u; (1s\sigma_g\epsilon l)_u$ for $l = 1$ ($p_{g,u}$ wave), $l = 3$ (f_g, u wave), ... odd l)

population transfer between a wave packet dissociating in the $2p\sigma_u$ state and the $1s\sigma_g$ state (Fig. 4.5c). Because close-coupling calculations were restricted to intensities $\leq 3 \times 10^{12}$ W/cm^2 and to the excitation of states of Σ symmetry, the effects of mechanism II are only weakly visible in Fig. 4.3b. Nevertheless, it is expected to be dominant at the intensities where the experiments were performed and is clearly evident in calculations, performed by numerical integration of the one-dimensional TDSE, that describe the evolution of a vibrational wave packet initially placed in the $2p\sigma_u$ state of the H_2^+ ion (Fig. 4.5d). Moreover, under our experimental conditions the potential involvement of the $Q_2\ ^1\Pi_u$ doubly excited states implies a larger population of the $2p\sigma_u$ states than is calculated and, therefore, a reinforcement of the asymmetry at long delays in the region with $E_k > 5$ eV.

Results similar to those in Fig. 4.5d are obtained from an even simpler, semiclassical Landau-Zener model. In this model, the infrared-laser-induced population transfer during dissociation can be understood in terms of so-called quasistatic states, which are the eigenstates of the $1s\sigma_g - 2p\sigma_u$ two-level problem in the presence of a (static) electric field:

$$\begin{aligned}\Psi_1 &= \cos[\theta(t)](1s\sigma_g) + \sin[\theta(t)](2p\sigma_u)\\ \Psi_2 &= -\sin[\theta(t)](1s\sigma_g) + \cos[\theta(t)](2p\sigma_u)\end{aligned} \tag{4.7}$$

Here $\theta(t)$ is related to the splitting, $\omega_0(R)$, between the $1s\sigma_g$ and $2p\sigma_u$ states and to the infrared-laser-induced dipole coupling, $V_{g,u}(R,t) = -\mu(R)E(t)$, where $\mu(R)$ is the electronic dipole moment, by [30]

$$\tan[2\theta(t)] = \frac{-2V_{g,u}(R,t)}{\omega_0(R)} \tag{4.8}$$

Early on in the dissociation process, when $\omega_0(R) \gg \mu(R)E(t)$, the Landau-Zener transition probability is small and the nuclear wave packet remains in Ψ_2. When

$\omega_0(R) < \mu(R)E(t)$, the nuclear wave packet breaks up into a coherent superposition of the quasistatic states, which now furthermore begin to resemble the localized states Ψ_L and Ψ_R. Near the end of the dissociation, when $\omega_0(R) \approx \mu(R)E(t)$, the nuclear wave packet switches between the two quasistatic states. This merely reflects the fact that the electron is no longer able to switch from left to right, and ensures that the localization acquired in the intermediate region persists. The correlated dependence of the asymmetry on E_k and τ is caused by the dependence of the localization process on the internuclear distance at which the nuclear wave packet is launched. The semiclassical Landau Zener model is further discussed in Chapter 5.

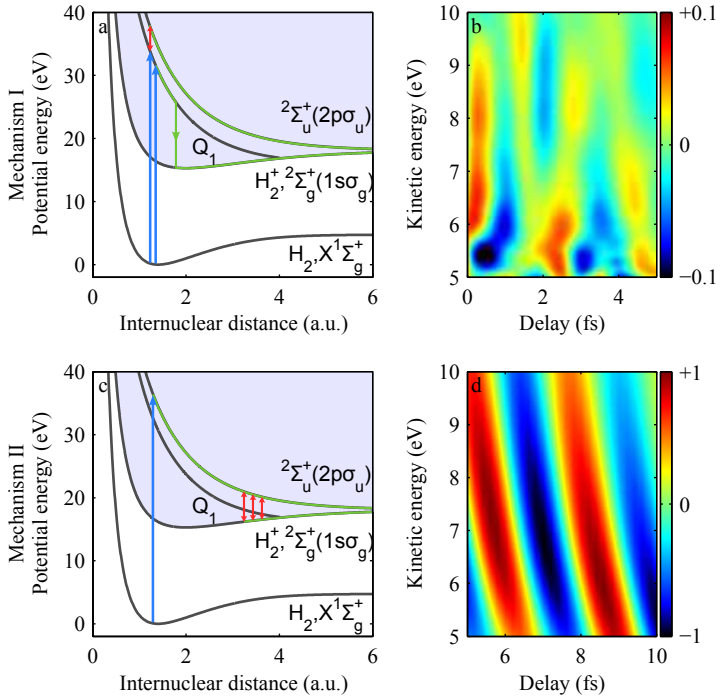

Figure 4.5: Asymmetry caused by the interference of a wave packet launched in the $2p\sigma_u$ state by direct XUV ionization or rapid ionization of the $Q_1\ ^1\Sigma_g^+$ doubly-excited states by the infrared pulse and a wave packet in the $1s\sigma_g$ state resulting from autoionization of the $Q_1\ ^1\Sigma_g^+$ states. Blue arrows indicate the effect of the XUV pulse and red arrows that of the infrared pulse; green lines and arrows signify dynamics that is intrinsic to the molecule. b, Close-coupling calculations in which direct photoexcitation to the $1s\sigma_g$ state has been excluded, supporting the notion that the Q_1 autoionizing states have an important role in the localization dynamics. c, Asymmetry caused by the interference of a wave packet that is launched in the $2p\sigma_u$ state by direct XUV ionization and a wave packet in the $1s\sigma_g$ state that results from stimulated emission during the dissociation process. d, Time-dependent asymmetry from a two-level calculation in which the wavefunction of the dissociating molecule is considered to be a coherent superposition of the $1s\sigma_g$ and $2p\sigma_u$ states.

4.6 Conclusion

Rapid electronic processes on timescales reaching into the attosecond regime define our natural environment and are at the heart of photophysical, photochemical and photobiological processes that allow and sustain life. This work has shown that combined experimental and computational efforts allow the use of attosecond pulses for the exploration of molecular systems, thereby establishing a point of departure for the direct investigation of multi-electron dynamics such as electron transfer/localization and autoionization, and of the coupling between electronic and nuclear degrees of freedom on timescales approaching the atomic unit of time.

References

[1] P. B. Corkum and F. Krausz. *Attosecond science.* Nat. Phys., **3**, 381–387 (2007).

[2] H. Kapteyn, O. Cohen, I. Christov and M. Murnane. *Harnessing Attosecond Science in the Quest for Coherent X-rays.* Science, **317**, 775–778 (2007).

[3] M. F. Kling and M. J. J. Vrakking. *Attosecond electron dynamics.* Annu. Rev. Phys. Chem., **59**, 463–492 (2008).

[4] F. Krausz and M. Ivanov. *Attosecond physics.* Rev. Mod. Phys., **81**, 163–234 (2009).

[5] M. Hentschel, R. Kienberger, C. Spielmann, G. A. Reider, N. Milosevic, T. Brabec, P. Corkum, U. Heinzmann, M. Drescher and F. Krausz. *Attosecond metrology.* Nature, **414**, 509–513 (2001).

[6] M. Drescher, M. Hentschel, R. Kienberger, M. Uiberacker, V. Yakovlev, A. Scrinzi, T. Westerwalbesloh, U. Kleineberg, U. Heinzmann and F. Krausz. *Time-resolved atomic inner-shell spectroscopy.* Nature, **419**, 803–807 (2002).

[7] M. Uiberacker *et al. Attosecond real-time observation of electron tunnelling in atoms.* Nature, **446**, 627–632 (2007).

[8] A. L. Cavalieri *et al. Attosecond spectroscopy in condensed matter.* Nature, **449**, 1029–1032 (2007).

[9] F. Kelkensberg *et al. Molecular Dissociative Ionization and Wave-Packet Dynamics Studied Using Two-Color XUV and IR Pump-Probe Spectroscopy.* Phys. Rev. Lett., **103**, 123005 (2009).

[10] M. F. Kling *et al. Control of electron localization in molecular dissociation.* Science, **312**, 246–248 (2006).

[11] F. Remacle and R. D. Levine. *An electronic time scale in chemistry.* Proc. Natl. Acad. Sci. U. S. A., **103**, 6793–6798 (2006).

[12] A. I. Kuleff and L. S. Cederbaum. *Charge migration in different conformers of glycine: The role of nuclear geometry.* Chem. Phys., **338**, 320 – 328 (2007).

[13] M. Wickenhauser, J. Burgdorfer, F. Krausz and M. Drescher. *Time resolved Fano resonances.* Phys. Rev. Lett., **94**, 023002 (2005).

[14] J. L. Sanz-Vicario, H. Bachau and F. Martin. *Time-dependent theoretical description of molecular autoionization produced by femtosecond xuv laser pulses.* Phys. Rev. A, **73**, 033410 (2006).

[15] R. Kienberger *et al. Atomic transient recorder.* Nature, **427**, 817–821 (2004).

[16] T. Uphues, M. Schultze, M. F. Kling, M. Uiberacker, S. Hendel, U. Heinzmann, N. M. Kabachnik and M. Drescher. *Ion-charge-state chronoscopy of cascaded atomic Auger decay.* New Journal of Physics, **10**, 025009 (2008).

[17] T. Remetter *et al. Attosecond electron wave packet interferometry.* Nat. Phys., **2**, 323–326 (2006).

[18] J. Mauritsson *et al. Attosecond Electron Spectroscopy Using a Novel Interferometric Pump-Probe Technique.* Phys. Rev. Lett., **105**, 053001 (2010).

[19] G. Sansone *et al. Isolated single-cycle attosecond pulses.* Science, **314**, 443–446 (2006).

[20] I. J. Sola *et al. Controlling attosecond electron dynamics by phase-stabilized polarization gating.* Nat. Phys., **2**, 319–322 (2006).

[21] O. Ghafur, W. Siu, P. Johnsson, M. F. Kling, M. Drescher and M. J. J. Vrakking. *A velocity map imaging detector with an integrated gas injection system.* Rev. Sci. Instrum., **80**, 033110 (2009).

[22] P. H. Bucksbaum, A. Zavriyev, H. G. Muller and D. W. Schumacher. *Softening of the H_2^+ Molecular-Bond in Intense Laser Fields.* Phys. Rev. Lett., **64**, 1883–1886 (1990).

[23] L. J. Frasinski, J. H. Posthumus, J. Plumridge, K. Codling, P. F. Taday and A. J. Langley. *Manipulation of bond hardening in H_2^+ by chirping of intense femtosecond laser pulses.* Phys. Rev. Lett., **83**, 3625–3628 (1999).

[24] A. T. J. B. Eppink and D. H. Parker. *Velocity map imaging of ions and electrons using electrostatic lenses: Application in photoelectron and photofragment ion imaging of molecular oxygen.* Rev. Sci. Instrum., **68**, 3477–3484 (1997).

[25] K. Ito, R. I. Hall and M. Ukai. *Dissociative photoionization of H_2 and D_2 in the energy region of 25-45 eV.* J. Chem. Phys., **104**, 8449–8457 (1996).

[26] I. Sánchez and F. Martín. *Origin of Unidentified Structures in Resonant Dissociative Photoionization of H_2.* Phys. Rev. Lett., **79**, 1654–1657 (1997).

[27] I. Sánchez and F. Martín. *Resonant dissociative photoionization of H_2 and D_2.* Phys. Rev. A, **57**, 1006–1017 (1998).

[28] A. Rudenko, T. Ergler, B. Feuerstein, K. Zrost, C. D. Schroter, R. Moshammer and J. Ullrich. *Real-time observation of vibrational revival in the fastest molecular system.* Chem. Phys., **329**, 193–202 (2006).

[29] F. Martin *et al. Single photon-induced symmetry breaking of H_2 dissociation.* Science, **315**, 629–633 (2007).

[30] P. Dietrich, M. Y. Ivanov, F. A. Ilkov and P. B. Corkum. *Two-electron dissociative ionization of H_2 and D_2 in infrared laser fields.* Phys. Rev. Lett., **77**, 4150–4153 (1996).

5 Semi-classical model of attosecond electron localization in dissociative ionization of hydrogen

In the development of attosecond molecular science, a series of experiments have recently been performed where ionic fragment asymmetries in the dissociative ionization of H_2 into $H^+ + H$, and that of D_2 into $D^+ + D$ was used to uncover electron localization processes that occur on the attosecond and few-femtosecond timescale. Electron localization was observed both in strong-field dissociative ionization using carrier envelope phase-stable few-cycle laser pulses in [Kling *et. al.*, *Science*, 2006, **312**, 246] and in a two-color extreme ultra-violet + infrared attosecond pump-probe experiment in [Sansone *et. al.*, *Nature*, 2010, **465**, 763]. Here we show that the observed electron localization can be well understood using a semi-classical model that describes the dynamics in terms of quasi-static states that take the interaction of the molecule with the laser field instantaneously into account. The electron localization is shown to be determined by the passage of the dissociating molecule through a regime where the laser-molecule interaction is neither diabatic nor adiabatic.

5.1 Electron localization in dissociative ionization of hydrogen

Since attosecond pulse trains [1] and isolated attosecond pulses [2] have become available, techniques have been developed to study attosecond electron dynamics in atoms [3, 4], molecules [5] and on surfaces [6]. As a first step towards the observation and control of charge localization in molecules, the dissociative ionization of D_2 molecules under the influence of a carrier envelope phase (CEP)-locked few-cycle laser pulse was studied [7, 8] and electron localization was observed following extreme ultra-violet (XUV) attosecond ionization of H_2 and D_2 molecules [5, 9]. In Ref. [5] the localization was the result of two mechanisms related to the interaction of a co-propagating few-cycle IR laser during the ionization process and the subsequent dissociation. In one of the mechanisms a moderately strong IR field couples the electronic and nuclear motion by driving transitions among the lowest electronic states of the molecular ion during as it is dissociating. The process is started by the attosecond pulse which creates a nuclear wavepacket in the first excited state of the molecular ion from which the dissociation follows. This mechanism is very similar to the one underlying the CEP-control in the experiments in refs [7, 8]. However in this case the dissociative wavepacket is created by recollision excitation after ionization to the ground electronic state of the molecular ion by the few-cycle pulse.

The remaining part of the pulse subsequently drives the transitions between the two electronic states. Here we show that the electron dynamics can be well understood by considering the passages of the dissociating wavepacket through a limited number of laser-induced avoided crossings that are individually well-described by a Landau-Zener formula [10, 11, 5]

Recent progress in computational methods allows the converged integration of the time-dependent Schrödinger equation (TDSE) in H_2/D_2 for a restricted range of cases, including XUV-only photoionization [12] and XUV-ionization accompanied by a moderately strong, few-cycle IR laser pulse [5]. Consideration of the full two-electron problem is important when effects involving re-collision and/or doubly-excited states play a role [7, 5]. In the present situation it suffices to consider the interaction of the IR laser with the molecular ion. Use of the Born-Oppenheimer potential energy curves as the starting point for considering the interaction of H_2^+ with an intense laser field allows the development of dressed state models where the laser coupling is explicitly taken into account [13]. Here, we will consider the application of a semi-classical model that is formulated in terms of so-called quasi-static states that result from taking the laser-induced coupling among the Born-Oppenheimer states instantaneously (i.e. on a sub-cycle time scale) into account [14, 15].

5.2 Probing electron localization by fragment asymmetries

As was explained in the previous section, our main aim is to describe the coupling of electronic and nuclear degrees of freedom that occurs in the molecular ion. Ionization of the neutral molecule is modeled as a Franck Condon projection of the neutral ground state on one of the electronic states of the molecular ion. An important advantage of the hydrogen molecule over larger and more complicated molecules, is that its behavior can often be explained while only considering the two lowest electronic states, i.e. the $1s\sigma_g$ and the $2p\sigma_u$ state of the molecular ion. These are the bonding and anti-bonding combination of 1s atomic orbitals. In a description of the laser-molecule interaction in terms of the $1s\sigma_g$ and $2p\sigma_u$ states of the molecular ion, the wavefunction $\Psi(R,t)$ is given by

$$\Psi(R,t) = \psi_g(R,t)\phi_g(\mathbf{r};R) + \psi_u(R,t)\phi_u(\mathbf{r};R) \tag{5.1}$$

where $\psi_g(R,t)$, respectively $\psi_u(R,t)$ describe nuclear wavefunctions that exist in connection with the $1s\sigma_g$ and $2p\sigma_u$ Born-Oppenheimer potential curves, which are a function of the internuclear distance R and time t, and $\phi_g(\mathbf{r};R)$ and $\phi_u(\mathbf{r};R)$ describe the wavefunctions of the single, remaining electron in H_2^+, which parametrically depend on R. The electronic coordinate $\mathbf{r}$ will be dropped in order to simplify the notation from here on. A description in terms of localized electronic states arises in a very natural way since the two electronic states $\phi_g(R)$ and $\phi_u(R)$ can be seen as a linear combination of the atomic electronic states $\phi_{left}(R)$ and $\phi_{right}(R)$ that have the electron on either the left or the right proton. With the definition $\phi_g(R) = 1/\sqrt{2}(\phi_{left}(R) + \phi_{right}(R))$ and $\phi_u(R) = 1/\sqrt{2}(\phi_{left}(R) - \phi_{right}(R))$ one

obtains for the nuclear wavefunctions $\psi_g(R,t)$ and $\psi_u(R,t)$:

$$\psi_{g,u}(R,t) = \frac{1}{\sqrt{2}}\left(\psi_{left}(R,t) \pm \psi_{right}(R,t)\right) \tag{5.2}$$

and vice versa:

$$\psi_{left,right}(R,t) = \frac{1}{\sqrt{2}}\left(\psi_g(R,t) \pm \psi_u(R,t)\right) \tag{5.3}$$

where $\psi_{left}(R,t)$ respectively $\psi_{right}(R,t)$ are defined as the nuclear wavefunctions that exist in connection with the localized electronic states $\phi_{left}(R)$ and $\phi_{right}(R)$. Measurements of ion fragment asymmetries left or right along the polarization axis directly relate to the wave functions $\psi_{left,right}(R,t)$ and hence are a convenient method to monitor electron dynamics in H_2^+. A non-zero asymmetry in the electron wavefunctions implies that the vibrational wave function consists of a coherent superposition of the $\psi_g(R)$ and $\psi_u(R)$ wavefunctions that move on the $1s\sigma_g$ and $2p\sigma_u$ electronic states, and vice versa. The electron localization within the molecule, that may be expressed by the asymmetry expression $\psi_{left}(R,t)^*\psi_{left}(R,t) - \psi_{right}(R,t)^*\psi_{right}(R,t)$ thus follows immediately from the nuclear wavefunctions. So far, this asymmetry is expressed in a spatial representation. However to make a meaningful comparison with experimental results the wavefunctions need to be transformed to a momentum space representation by a Fourier transform which then gives a momentum-dependent asymmetry $\psi_{left}(p,t)^*\psi_{left}(p,t) - \psi_{right}(p,t)^*\psi_{right}(p,t)$ with p the momentum of the nuclear wavepacket. Alternatively a kinetic energy dependent asymmetry may be considered.

In the experiments ion fragment asymmetries were measured defined by

$$A(E_k,\alpha) = \frac{I_{left}(E_k,\alpha) - I_{right}(E_k,\alpha)}{I_{left}(E_k,\alpha) + I_{right}(E_k,\alpha)} \tag{5.4}$$

where I_{left} and I_{right} are the number of ions flying out left and right with respect to the laser polarization at ion kinetic energy E_k. In Refs [7, 8], $\alpha = \phi_{CEP}$, the carrier envelope phase of a few-cycle near-IR laser pulse, and in Ref. [5, 9] $\alpha = \tau$, the delay between the attosecond laser pulse and a few-cycle near-IR laser pulse with a fixed ϕ_{CEP}. In both cases it was concluded that non-zero values of $A(E_k,\alpha)$ result from interactions of the molecule with the IR laser field in the course of the dissociation, providing a coupling of the $1s\sigma_g$ and $2p\sigma_u$ electronic states. The coupling causes population in the $2p\sigma_u$ state to be transferred to the $1s\sigma_g$ state and vice versa, thereby creating a coherent superposition state that can be accompanied by a fragment asymmetry. Importantly, the amplitudes in the coherent superposition depend on ϕ_{CEP}, resp. τ.

5.3 Semi-classical model using quasi-static states

While the description of electron localization in terms of a coherent superposition of the field-free electronic states provides a rationalization why fragment asymmetries are found experimentally and reproduced in TDSE calculations, these descriptions

do not provide insight into the dynamics and fail to explain, for example, the correlation between φ_{CEP} or τ and the fragment kinetic energy that was observed [5]. A more intuitive description is provided by using quasi-static (sometimes referred to as phase-adiabatic) states that result from diagonalization of the interaction Hamiltonian written in the basis of the field-free electronic states $\varphi_g(R)$ and $\varphi_u(R)$:

$$\hat{H}_{int}(R,t) = \begin{pmatrix} V_g(R) & V_{laser}(R,t) \\ V_{laser}(R,t) & V_u(R) \end{pmatrix} \tag{5.5}$$

where R is the internuclear distance and $V_g(R)$ and $V_u(R)$ the Born-Oppenheimer potential energy curves for the $1s\sigma_g$ and $2p\sigma_u$ states. The laser coupling term $V_{laser}(R,t)$ is given by $V_{laser}(R,t) = -\mu(R)E(t)$, where $E(t)$ is the instantaneous laser field and $\mu(R)$ the R-dependent transition dipole moment. The transition dipole moment is given by:

$$\mu(R) = \frac{R}{\sqrt{4 - 4\delta_R^2}} \tag{5.6}$$

with

$$\delta_R = e^{-R}\left(1 + R + \frac{1}{3}R^2\right) \tag{5.7}$$

The resulting quasi-static eigenvalues $V_{1,2}(R,t)$ are:

$$V_{1,2}(R,t) = \frac{V_g(R) + V_u(R)}{2} \mp \sqrt{\frac{\omega_0(R)^2}{4} + V_{laser}(R,t)^2} \tag{5.8}$$

with $\omega_0(R) = V_u(R) - V_g(R)$. The electronic quasi-static eigenstates $\varphi_1(R,t)$ and $\varphi_2(R,t)$ are given by:

$$\begin{aligned} \varphi_1(R,t) &= \cos\theta(R,t)\varphi_g(R) + \sin\theta(R,t)\varphi_u(R) \\ \varphi_2(R,t) &= -\sin\theta(R,t)\varphi_g(R) + \cos\theta(R,t)\varphi_u(R) \end{aligned} \tag{5.9}$$

where the time-dependent mixing parameter $\theta(R,t)$ is given by [15]:

$$\tan\left(2\theta(R,t)\right) = -\frac{2V_{laser}(R,t)}{\omega_0(R)} \tag{5.10}$$

Note that the electronic wavefunctions $\varphi_1(R,t)$ and $\varphi_2(R,t)$ are time-dependent and track the time evolution of the laser field. In addition to Eq. 5.9, where the quasi-static states are expressed in terms of $\varphi_g(R)$ and $\varphi_u(R)$, the quasi static states can be given in terms of the localized electronic states:

$$\begin{aligned} \varphi_1(R,t) &= \frac{1}{\sqrt{2}}\left(\varphi_{left}(R)(\cos\theta + \sin\theta) + \varphi_{right}(R)(\cos\theta - \sin\theta)\right) \\ \varphi_2(R,t) &= \frac{1}{\sqrt{2}}\left(\varphi_{left}(R)(\cos\theta - \sin\theta) - \varphi_{right}(R)(\cos\theta + \sin\theta)\right) \end{aligned} \tag{5.11}$$

The nature of the quasi-static states depends on the internuclear distance and time: early during the dissociation, for small R, the splitting between V_u and V_g is very large and generally exceeds the laser coupling, i.e., i.e. $V_{laser}(R,t) \ll \omega_0(R)$, $\theta \approx 0$, $\varphi_1 \approx \varphi_g$ and $\varphi_2 \approx \varphi_u$. Towards the end of the dissociation when the separation between the Born-Oppenheimer potential energy curves becomes negligible compared to the laser coupling, i.e. $|V_{laser}(R,t)| \gg \omega_0(R)$ and we have $\theta \approx \frac{\pi}{4}$, $\varphi_1 \approx \varphi_{left}$ and $\varphi_2 \approx -\varphi_{right}$ if $V_{laser}(R,t) < 0$ and $\theta \approx -\frac{\pi}{4}$, $\varphi_1 \approx \varphi_{right}$ and $\varphi_2 \approx \varphi_{left}$ if $V_{laser}(R,t) > 0$. In this limit the quasi-static states describe localized electronic states where the electron resides on the left, resp. right proton.

The molecular wavefunction in terms of the quasi-static states is given by:

$$\Psi(R,t) = \psi_1(R,t)\varphi_1(R,t) + \psi_2(R,t)\varphi_2(R,t) \tag{5.12}$$

From the definition of the quasi-static states (Eq. 5.9) it follows that the nuclear wavefunctions $\psi_1(R,t)$ and $\psi_2(R,t)$ that are connected to the quasi-static states $\varphi_1(R)$ and $\varphi_2(R)$ can be expressed in terms of $\psi_g(R,t)$ and $\psi_u(R,t)$ as:

$$\begin{aligned}\psi_1(R,t) &= \cos\theta(R,t)\psi_g(R) + \sin\theta(R,t)\psi_u(R)\\ \psi_2(R,t) &= -\sin\theta(R,t)\psi_g(R) + \cos\theta(R,t)\psi_u(R)\end{aligned} \tag{5.13}$$

and in terms of $\psi_{left}(R,t)$ and $\psi_{right}(R,t)$ as

$$\begin{aligned}\psi_1(R,t) &= \frac{1}{\sqrt{2}}\left(\psi_{left}(R,t)(\cos\theta + \sin\theta) + \psi_{right}(R,t)(\cos\theta - \sin\theta)\right)\\ \psi_2(R,t) &= \frac{1}{\sqrt{2}}\left(\psi_{left}(R,t)(\cos\theta - \sin\theta) - \psi_{right}(R,t)(\cos\theta + \sin\theta)\right)\end{aligned} \tag{5.14}$$

Note the similarity between the equation describing the relation between quasi-static electronic states and the localized electronic states (Eq. 5.11) on the one hand, and on the other hand Eq. 5.14 describing the relation between the nuclear wavefunctions that exist in connection with the quasi-static electronic states and the vibrational wavefunctions that exist in connection with the localized electronic states . Hence, as before, the electron localization can directly be extracted from the vibrational wavefunctions.

As pointed out previously, the quasi-static states vary with time, since they depend on the instantaneous values of the laser field and on the internuclear distance. From the definition of the quasi-static states (Eq. 5.9) it follows that:

$$\begin{aligned}\dot{\varphi}_1(R,t) &= +\dot{\theta}\varphi_2(R,t)\\ \dot{\varphi}_2(R,t) &= -\dot{\theta}\varphi_1(R,t)\end{aligned} \tag{5.15}$$

When the wavefunction in Eq. 5.12 is inserted into the Schrödinger equation, then, using Eq. 5.15 one obtains the following expression for the time-evolution of the vibrational states $\psi_1(R,t)$ and $\psi_2(R,t)$

$$i\begin{pmatrix}\dot{\psi}_1(R,t)\\ \dot{\psi}_2(R,t)\end{pmatrix} = \begin{pmatrix} V_1(R,t) & i\dot{\theta}(R,t)\\ -i\dot{\theta}(R,t) & V_2(R,t)\end{pmatrix}\begin{pmatrix}\psi_1(R,t)\\ \psi_2(R,t)\end{pmatrix} \tag{5.16}$$

This shows that $\dot{\theta}(R,t)$ acts as an effective coupling term between the two quasi-static states. $\dot{\theta}(R,t)$ can be derived from Eq. 5.10:

$$\dot{\theta}(R,t) = -\frac{\dot{V}_{laser}(R,t)\omega_0(R)}{\omega_0(R)^2 + 4V_{laser}(R,t)^2} \tag{5.17}$$

$\dot{\theta}(R,t)$, and thus the population transfer, peaks around the zero crossings of the laser field ($E(t) = 0$) when avoided crossings occur between the quasi-static states. At the crossings $\dot{\theta}(R,t) = \mu(R)E_0(t)\ \omega_l/\omega_0(R)$ where ω_l is the laser frequency and $E_0(t)$ is the envelope of the laser field. The relative strength of $\dot{\theta}$ with respect to the difference between $V_1(R,t)$ and $V_2(R,t)$ defines the dynamics that will occur at the zero crossing of the laser field. The wavepacket dynamics can be split up into three regions. In the beginning, when $\omega_0^2 \gg \mu E_0\omega_l$, the dynamics is adiabatic, i.e. populations remain in the initial quasi-static state. At the end of the dissociation when $\omega_0^2 \ll \mu E_0\omega_l$, the dynamics becomes completely diabatic and at a zero-crossing of the field the dissociating wavepacket hops from one quasi-static state to the other, leaving any existing electron localization intact. The electron localization is established in an intermediate region where the dynamics is neither adiabatic nor diabatic. In this regime, the wavepacket traverses two or three avoided crossings (see Fig. 5.1) where the degree of adiabaticity determines the extent of the localization that will asymptotically be measured. The probability that a passage through one of the avoided crossings proceeds diabatically can be evaluated by integrating the population transfer following from Eq. 5.16 between two maxima of the field. This results in a Landau-Zener formula in accordance with the treatment developed in refs. [14, 16, 17].

$$P_{diabatic}(R,t) = \ e^{-\frac{\pi\omega_0(R)^2}{4\omega_l\mu(R)E_0(t)}} \tag{5.18}$$

In Fig. 5.1b the quasi-static state energies $V_1(R,t)$ and $V_2(R,t)$ and the transition probability $P_{diabatic}(R,t)$ are displayed as a function of time for a nuclear trajectory $R(t)$ that tracks the expectation value of the internuclear distance of a Franck-Condon nuclear wavepacket that starts at $t = 0$ on the $2p\sigma_u$ potential of D_2^+ and that is exposed to the laser field shown in Fig. 5.1a. In this plot the avoided crossings in the quasi-static states can readily be recognized. The transition probability curve defines the intermediate window of a few fs long where the probability is between 0 and 1.

The interpretation of the localization dynamics in terms of quasi-static states can be further illustrated by plotting the time-dependent populations in the field free states $\int |\psi_{g,u}(R,t)|^2 \mathrm{d}R$ (Fig. 5.1c), in the quasi-static states $\int |\psi_{1,2}(R,t)|^2 \mathrm{d}R$ (Fig. 5.1d) and in the localized states $\int |\psi_{left,right}(R,t)|^2 \mathrm{d}R$ (Fig. 5.1e) for a 1D TDSE calculation where the wavepacket starts at $t = 0$ on the $\varphi_u(R,t)$ state of D_2^+ as a Frank-Condon projection of the wavefunction of the neutral ground state. The molecule is exposed to a five-cycle pulse as shown in Fig. 5.1a , with a peak intensity of $3.5 \cdot 10^{12}$ W/cm^2. The dynamics in terms of the field free states (Fig. 5.1c) is very complex and difficult to understand intuitively. By contrast, the dynamics in terms of the quasi-static states (Fig. 5.1d) is simple and readily explained in terms of the adiabaticity of a series of laser-induced curve-crossings. At early times ($t < 4$ fs) the

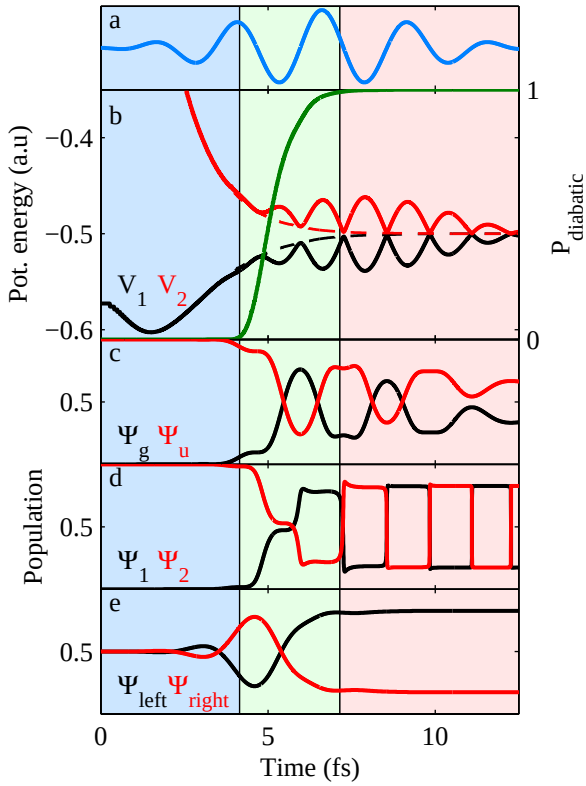

Figure 5.1: (a) 4.8 fs FWHM 800 nm laser pulse; (b) time-dependent potential energies V_1 and V_2 of the quasi-static states during molecular dissociation of D_2 in the presence of the laser field depicted in (a) with a peak intensity of $3.5 \cdot 10^{12}$ W/cm^2. The green curve shows the probability $P_{diabatic}$ for a diabatic transition given by the Landau-Zener formula, and defines three regions where the dynamics is primarily adabatic (light blue), primarily diabatic (light pink) or mixed (light green).(c-d) population dynamics during dissociation shown in (c) the field-free nuclear wavefunctions $\psi_g(R,t)$ (black) and $\psi_u(R,t)$ (red), (d) the quasi-static wavefunctions $\psi_1(R,t)$ (black) and $\psi_2(R,t)$ (red) and (e) the localized wavefunctions $\psi_{1eft}(R,t)$ (black) and $\psi_{right}(R,t)$ (red).

dynamics is adiabatic and all population stays in the upper quasi-static state. In the intermediate region (4 fs $< t <$ 7 fs) transitions between the quasi-static states are observed near zero-crossings of the laser electric field. At later times ($t >$ 7 fs) the dynamics is diabatic, and the populations of the two quasi-static states undergo a complete reversal at each zero-crossing of the laser field. The behavior in the localized states (Fig. 5.1e) can now also be understood: in the adiabatic regime the molecule is slightly polarized by the laser field and the quasi-static states acquire a limited amount of localized character. However, at every zero crossing of the laser field the localized character vanishes. In the intermediate regime the electron can no longer completely follow the field oscillations and heavy oscillations occur

in accordance with the mixing of the states. In this regime, differences between populations in left and right are present at the zero-crossings of the laser field. Finally, in the diabatic regime, the internuclear distance is too large, and therefore the internuclear barrier too high, for the electron to hop from left to right and the localization is frozen.

5.4 Results of the semi-classical model

In Fig. 5.2 calculations are presented for the asymmetry that occurs in two-color XUV+IR dissociative ionization of D_2 as a function of the kinetic energy of the fragment ions and the delay τ between the attosecond pulse and the center of a five-cycle, 800 nm pulse with a peak intensity of $3.5 \cdot 10^{12}$ W/cm^2. The zero of the delay axis τ corresponds to ionization taking place at the center of the IR pulse envelope and for positive values of the delay the IR field arrives later. A fragment kinetic energy dependence of the asymmetry in the fragment ejection is typically what is measured in an experiment and we refer to [5] for a detailed comparison between experimental results and theoretical calculations. Here we focus on a comparison between (a) 1D TDSE calculations, where a Frank-Condon projection of the neutral ground state wavefunction onto the $\psi_u(R,t)$ state is performed at t=0, and (b) the semi-classical method using the Landau-Zener formula described above. In the latter calculation, nuclear trajectories are calculated on the basis of a weighted average of the two quasi-static potential energy curves, with relative weights according to the instantaneous populations. In determining the trajectories the effect of the electric field on the nuclear dynamics is taken into account [15]. Trajectories are started from all internuclear distances within the Franck-Condon region. Since more than one crossing is relevant to the dynamics, the phase development $\Delta\varphi$ between two avoided crossings has to be taken into account, which is given by:

$$\Delta\varphi = -i \int_{t_0}^{t_0+\frac{T}{2}} \left(V_1(t') - V_2(t')\right) dt' \tag{5.19}$$

The sign of the amplitude transfer at an avoided crossing is determined from the sign of $\dot{\theta}(R,t)$ in Eq. 5.17. The two calculations show satisfactory agreement, validating the interpretation of the TDSE results in terms of non-adiabatic transitions between the quasi-static states. The observed energy correlation between the fragment kinetic energy and the time delay is due to the fact that the internuclear distance where a trajectory starts governs both the asymptotic kinetic energy and the internuclear distance where the curve-crossings take place, impacting on the Landau-Zener transition probability.

As an additional test, the intensity dependence of the 1D TDSE calculations and the semi-classical method is compared in Fig. 5.3. The fragment asymmetry for the kinetic energy corresponding to the peak of the Franck Condon wavepacket is plotted as a function of the delay τ between the attosecond pulse and a 4.8 fs FWHM, 800 nm IR field, and the peak intensity of the IR pulse [18]. The general behavior is well-reproduced which further demonstrates the applicability of the semiclassical model that is developed.

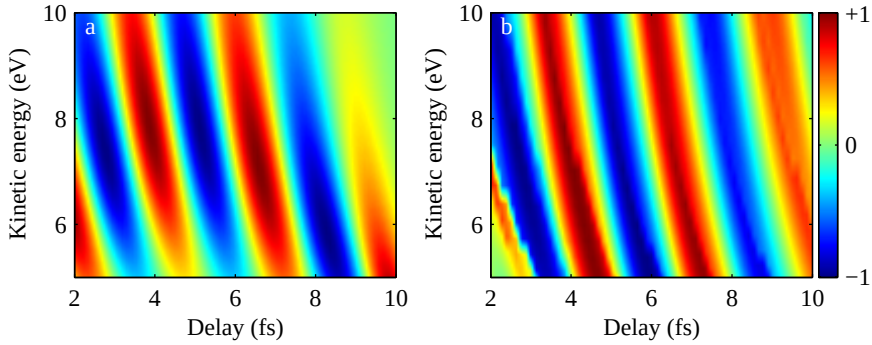

Figure 5.2: Asymmetry parameter $A(E_k, \tau)$ of D^+ fragments as a function of the delay τ between an isolated attosecond pulse that promotes a Frank-Condon wavepacket onto the $2p\sigma_u$ state at $t = 0$ and the center of a 4.8 fs FWHM, 800 nm pulse with a peak intensity of $3.5 \cdot 10^{12}$ W/cm^2 and fragment kinetic energy E_k, (a) in the 1D TDSE model and (b) in the semi-classical model.

.

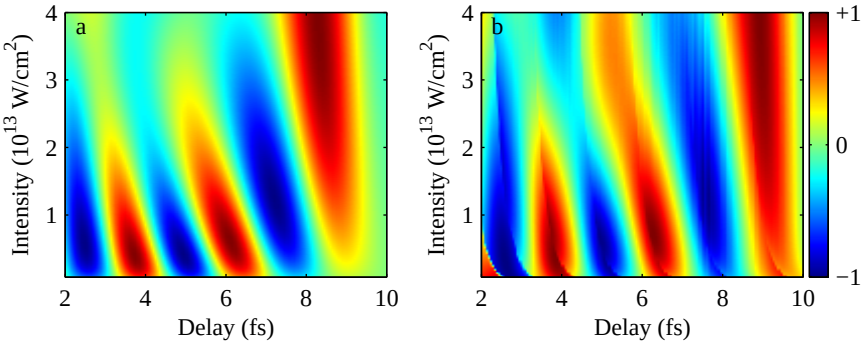

Figure 5.3: Asymmetry parameter $A(\tau)$ at fragment kinetic energy corresponding to center of the nuclear wavepacket as a function of the delay τ between the attosecond pulse and a 4.8 fs FWHM, 800 nm IR field, and the intensity of the IR pulse for the TDSE (a) and the semi-classical (b) model.

With the same model the electron localization in single-color dissociative ionization by a few-cycle CEP-stable IR pulse [7] can be described as a function of φ_{CEP}. Fig. 5.4 shows the result of calculations for a 800 nm pulse with an intensity of $1{\cdot}10^{14}$ W/cm^2 and a pulse duration of 7.3 fs FWHM. In these calculations ionization and subsequent recollision excitation to the $2p\sigma_u$ state of H_2^+ from a single half cycle close to the centre of the pulse is considered, similar to what was done in Ref. [7]. In an experiment one will in principle measure the sum of a number of consecutive half-cycles [19] and the asymmetry is conserved when the number of cycles is not too large. Although the details of the two results differ, the overall behavior is again in good agreement.

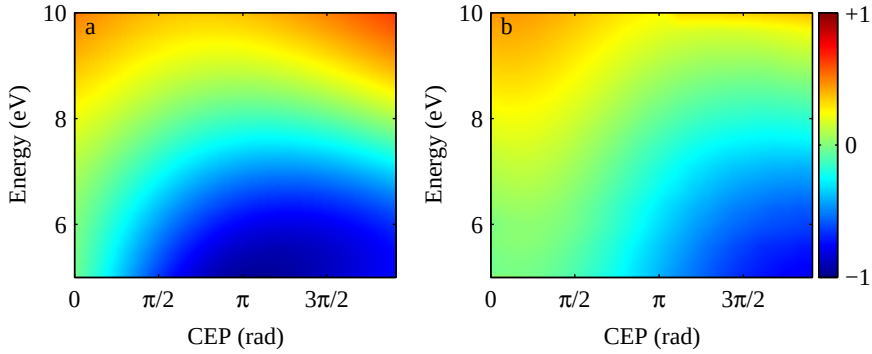

Figure 5.4: Asymmetry parameter $A(E_k, \varphi_{CEP})$ of H^+ fragments after recollision excitation to the $2p\sigma_u$ state by a selected half-cycle of the IR field as a function of φ_{CEP} and fragment kinetic energy E_k for the TDSE (a) and the semi-classical (b) model for an intensity of $1{\cdot}10^{14}$ W/cm^2 and a pulse duration of 7.3 fs FWHM

5.5 Conclusions

In conclusion, we have presented a simple model that describes electron localization during dissociation under the influence of an IR laser field. This model is relevant to two recent experiments on electron localization in dissociative ionization of H_2^+, namely an experiment on CEP-control and one applying attosecond pump-probe spectroscopy. The electron localization has its basis in the behavior of the dissociating wavepacket at a limited number of laser-induced curve-crossings that are well-described by the Landau-Zener formula. As such, this work can guide ongoing efforts to observe and control electron dynamics in more complicated molecules on attosecond time-scales. The ability of CEP-stable lasers and XUV-IR pump-probe sequences to laser-dress potential energy curves and surfaces on a sub-fs timescale allows to influence the outcome of chemical processes on electronic, rather than nuclear timescales.

References

[1] P. M. Paul, E. S. Toma, P. Breger, G. Mullot, F. Auge, P. Balcou, H. G. Muller and P. Agostini. *Observation of a train of attosecond pulses from high harmonic generation.* Science, **292**, 1689–1692 (2001).

[2] M. Hentschel, R. Kienberger, C. Spielmann, G. A. Reider, N. Milosevic, T. Brabec, P. Corkum, U. Heinzmann, M. Drescher and F. Krausz. *Attosecond metrology.* Nature, **414**, 509–513 (2001).

[3] M. Drescher, M. Hentschel, R. Kienberger, M. Uiberacker, V. Yakovlev, A. Scrinzi, T. Westerwalbesloh, U. Kleineberg, U. Heinzmann and F. Krausz. *Time-resolved atomic inner-shell spectroscopy.* Nature, **419**, 803–807 (2002).

[4] M. Uiberacker *et al. Attosecond real-time observation of electron tunnelling in atoms.* Nature, **446**, 627–632 (2007).

[5] G. Sansone *et al. Electron Localization following Attosecond Molecular Photoionization.* Nature, **465**, 763–766 (2010).

[6] A. L. Cavalieri *et al. Attosecond spectroscopy in condensed matter.* Nature, **449**, 1029–1032 (2007).

[7] M. F. Kling *et al. Control of electron localization in molecular dissociation.* Science, **312**, 246–248 (2006).

[8] M. Kremer *et al. Electron Localization in Molecular Fragmentation of H-2 by Carrier-Envelope Phase Stabilized Laser Pulses.* Phys. Rev. Lett., **103**, 213003 (2009).

[9] D. Ray *et al. Ion-Energy Dependence of Asymmetric Dissociation of D-2 by a Two-Color Laser Field.* Phys. Rev. Lett., **103**, 223201 (2009).

[10] L. Landau. *Zur Theorie der energieubertragung. II.* Physikalische Zeitschrift der Sowjetunion, **2**, 46–51 (1932).

[11] C. Zener. *Non-adiabatic Crossing of Energy Levels.* Proceedings of the Royal Society of London, Series A, **137**, 696–702 (1932).

[12] J. L. Sanz-Vicario, H. Bachau and F. Martin. *Time-dependent theoretical description of molecular autoionization produced by femtosecond xuv laser pulses.* Phys. Rev. A, **73**, 033410 (2006).

[13] A. Bandrauk and M. Sink. *Photodissociation in intense laser fields: Predissociation analogy.* J. Chem. Phys., **74**, 1110 (1981).

[14] P. Dietrich, M. Y. Ivanov, F. A. Ilkov and P. B. Corkum. *Two-electron dissociative ionization of H_2 and D_2 in infrared laser fields.* Phys. Rev. Lett., **77**, 4150–4153 (1996).

[15] I. Kawata, H. Kono and Y. Fujimura. *Adiabatic and diabatic responses of H-2(+) to an intense femtosecond laser pulse: Dynamics of the electronic and nuclear wave packet.* J. Chem. Phys., **110**, 11152–11165 (1999).

[16] M. Thachuk, M. Y. Ivanov and D. M. Wardlaw. *A semiclassical approach to intense-field above-threshold dissociation in the long wavelength limit.* J. Chem. Phys., **105**, 4094–4104 (1996).

[17] M. Thachuk, M. Ivanov and D. Wardlaw. *A semiclassical approach to intense-field above-threshold dissociation in the long wavelength limit. II. Conservation principles and coherence in surface hopping.* J. Chem. Phys., **109**, 5747–5760 (1998).

[18] F. He, A. Becker and U. Thumm. *Strong-Field Modulated Diffraction Effects in the Correlated Electron-Nuclear Motion in Dissociating H_2^+*. Phys. Rev. Lett., **101**, 213002 (2008).

[19] X. M. Tong and C. D. Lin. *Dynamics of light-field control of molecular dissociation at the few-cycle limit*. Phys. Rev. Lett., **98**, 123002 (2007).

6 Attosecond control in photoionization of hydrogen molecules

We report experiments where hydrogen molecules were dissociatively ionized by an attosecond pulse train (APT) in the presence of a near-infrared (IR) field. Fragment ion yields from distinguishable ionization channels oscillate with a period that is half the optical cycle of the IR field. For molecules aligned parallel to the laser polarization axis, the oscillations are reproduced in two-electron quantum simulations, and can be explained in terms of an interference between ionization pathways that involve different harmonic orders and a laser-induced coupling between the $1s\sigma_g$ and $2p\sigma_u$ states of the molecular ion. In the time domain this leads to a situation where the ionization probability is sensitive to the instantaneous polarization of the molecule by the IR electric field.

6.1 Introduction

The prospect of observing and being able to control ultrafast electron dynamics in molecular systems lies at the basis of the current interest to apply attosecond (1 as = 10^{-18} s) laser pulses to physical chemistry. Since the first demonstration of attosecond pulses [1, 2] pioneering experiments have demonstrated their potential in atoms [3, 4], solid state systems [5] and, most recently, molecules [6], where interest has been stimulated by numerical studies which suggest that an electronic (i.e. attosecond or few-femtosecond) timescale may be important in fundamental chemical processes [7]. For example, photoionization in glycine molecules leads to ultrafast charge rearrangements on a few-femtosecond timescale [8]. The inherent multi-electron nature of the electron dynamics in many molecular systems is a formidable challenge to theoreticians and experimentalists alike, and requires the development of novel theoretical and experimental techniques.

Attosecond pump-probe spectroscopy is based on the generation of attosecond light pulses by high harmonic generation (HHG). Presently, attosecond pulses exist in the form of attosecond pulse trains (APTs) [1] and as isolated attosecond pulses [2]. The first application of attosecond pulses to follow rapid electron dynamics in a molecule revealed that the dissociative ionization of hydrogen by a two-color extreme-ultraviolet (XUV) + infrared (IR) field results in a localization of the bound electron in the molecular ion that depends with attosecond time resolution on the time delay between the attosecond XUV pulse and the IR laser pulse [6]. This could be observed via an asymmetry of the ejected fragments in the laboratory

frame, i.e. after the dissociation was complete [9]. A similar experimental result was also obtained using an APT [10]. In these experiments the attosecond pulses initiated electron dynamics that was subsequently addressed by an IR pulse. A next challenge is to use attosecond pulses as a probe of ultrafast molecular electron dynamics. In this paper we do so by investigating how a moderately intense IR field influences the electronic states that are accessed in photoionization of hydrogen using an APT.

6.2 Experimental

In the experiment, an XUV APT (with two pulses per IR cycle) and a 30 fs FWHM 780 nm pulse (IR) with identical linear polarization were collinearly propagated and focused onto an ensemble of hydrogen or deuterium molecules. The peak intensity of the IR pulse was estimated to be $3 \cdot 10^{13}$ W/cm^2. HHG in Krypton created an XUV spectrum consisting of odd harmonics H11 up to H27. Such a spectrum allows direct ionization to the first excited ionic state ($2p\sigma_u$), but limits the excitation of higher-lying states as much as possible. The three-dimensional velocity distributions of H^+ and D^+ were measured using a velocity map imaging spectrometer (VMIS) [11] with a gas-injection system integrated into the repeller electrode [12]. The delay between the APT and the IR field was scanned with attosecond time resolution. Although only results for deuterium molecules will be presented here, hydrogen molecules show analogous behavior.

6.3 Experimental results

In Fig. 6.1a and 6.1b fragment kinetic energy spectra resulting from the interaction of D_2 with the APT only are shown for fragments ejected parallel and perpendicular to the laser polarization (black solid lines). We choose to present the measurements in this form (rather than in the form of a total fragment kinetic energy spectrum and an angular distribution), since at different angles different ionic states play a role. For these angle-specific spectra, here and in the remainder of this letter, an acceptance angle of $\pm 20°$ was used. Fig. 6.1c shows a D^+ momentum map resulting from dissociative ionization by the APT. Several contributions can be distinguished that can be related to Fig. 6.1d, where a potential energy diagram representing the relevant states is given. Direct ionization to the $1s\sigma_g$ ground state primarily leads to the production of stable D_2^+, and is accompanied by a small dissociative part ($\sim$2%) that results in a low kinetic energy peak ($E_k < 1$ eV) in Fig. 6.1a and 6.1b. The main contribution between 1 eV and 5 eV, which peaks along the laser polarization axis, comes from autoionization of the $^1\Sigma_u^+ Q_1$ doubly excited states [13] (red curves in Fig. 6.1d). Direct ionization to the $2p\pi_u$ continuum leads to fragments centered at 5 eV and peaked at 90°, however this contribution was kept very small by tuning the XUV spectrum. There are multiple dynamical pathways that contribute to the observed fragments at higher kinetic energies (7-8 eV), of which the dominant ones are direct ionization to the $2p\sigma_u$ continuum (for molecules aligned parallel to the laser polarization) and excitation of the Q_2 doubly

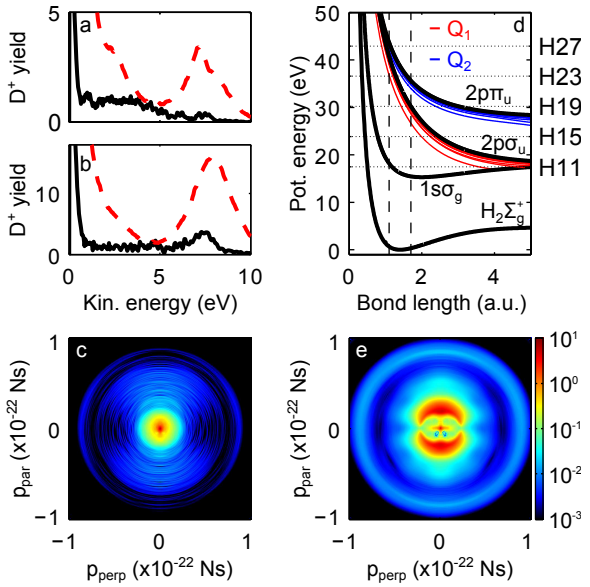

Figure 6.1: Fragment kinetic energy spectra from dissociative ionization of D_2 at 0° (a) and at 90° (b) ± 20° with respect to the laser polarization by the APT only (black solid lines) and by the APT+IR (cycle averaged) at temporal overlap (red dashed lines). Corresponding momentum maps for the APT (c) and the APT+IR (e). In (d) a potential energy diagram of D_2 is shown indicating the relevant neutral (red and blue) and ionic (black) states. The Franck-Condon region is indicated by vertical dashed lines and the position of a selection of harmonic orders present in the experiment are marked with horizontal dotted lines.

excited states (blue curves in Fig. 6.1d) (for molecules aligned perpendicular to the polarization axis). In agreement with these assignments, experiments with an XUV spectrum with a lower high energy cut-off showed a disappearance of the high energy (> 6 eV) channel, while retaining the lower energy (2-6 eV) channel due to autoionization of the $^1\Sigma_u^+ Q_1$ states.

When ionization by the APT takes place in the presence of the IR field the spectra undergo significant changes, as can been seen in Fig. 6.1a and 6.1b, which show kinetic energy spectra for parallel and perpendicular molecular alignment as red dashed lines. These curves were obtained by averaging the APT-IR time delay over one full IR cycle. Fig. 6.1e shows a corresponding momentum map. A contribution known as bond-softening appears prominently at low kinetic energies with an angular distribution that is peaked along the laser polarization axis [14, 15]. At high kinetic energies ($E_k \approx 7$ eV) a significant enhancement is observed at all angles, in agreement with our previous observations [6]. This contribution will be the main topic of this paper.

In Fig. 6.2a and 6.2b the kinetic energy spectra for fragments ejected parallel and perpendicular to the laser polarization are shown as a function of the APT-IR time delay. A strong delay dependence is observed, with different parts of the spectrum

oscillating with a period that is half the period of the IR laser. The oscillations at high kinetic energies perpendicular to the laser polarization are particularly pronounced. In Fig. 6.2c and 6.2d the ion yields from selected ionization channels are plotted as a function of delay. We note that the oscillations at high energy at 0° and 90° are out of phase. In addition, in Fig. 6.2c (parallel alignment) the oscillations at 3 eV and 7 eV are also out of phase.

6.4 Time-dependent Schrödinger model

We have performed calculations solving the time-dependent Schrödinger equation (TDSE) for a deuterium molecule interacting with an APT and IR field by using a close-coupling method [16, 6]. In these calculations all electronic and vibrational degrees of freedom were taken into account. Current computational capabilities only allow one to consider the case where the molecule is aligned parallel to the laser polarization. Moreover the pulse durations and intensities that can be explored are subject to restrictions. Therefore, in all the calculations presented here, an IR field with a with a sine squared envelop of 7.8 fs duration (2.8 fs FWHM), a central wavelength of 780 nm and an intensity of $3{\cdot}10^{12}$ W/cm^2 was combined with an APT consisting of 4 pulses, built from all the odd harmonics between H13 and H25.

In Fig. 6.3a the calculated fragment ion spectrum resulting from the interaction with the APT only is shown (black curve). This ion spectrum is dominated by the channels discussed before: direct ionization to the $1s\sigma_g$ continuum, autoionization of the $^1\Sigma_u^+ Q_1$ states to the $1s\sigma_g$ continuum and direct ionization to the $2p\sigma_u$ continuum. In Fig. 6.3b the fragment ion yield as a function of kinetic energy and delay in the two-color APT+IR field is given. The numerical results reproduce the experimentally observed oscillations in the yield at both high and low kinetic energies. Theory also predicts a significant enhancement (red dashed line in Fig. 6.3a), although less pronounced than in the experiment due to the lower intensity used in the calculations. By performing these calculations while the $^1\Sigma_u^+ Q_1$ states were excluded it was confirmed that the high energy fragments result from direct ionization to the $2p\sigma_u$ continuum, while the low energy fragments come from autoionization of the $^1\Sigma_u^+ Q_1$ states. The phase difference between the oscillations around 3 eV and at 7 eV are strongly intensity dependent. This prevents a close comparison between experiment and theory on this point.

The results reported here are reminiscent of earlier work, in which oscillations in the He^+ yield were observed as a function of the APT-IR delay [17]. The oscillations were attributed to interferences between consecutive pulses in the APT and involved the excitation of Rydberg states. By contrast, our TDSE calculations show that in D_2 the yield oscillations occur both for an APT and for isolated attosecond pulses and remain present when the neutral Q_1 states are removed from the calculation. This shows that the origin of the oscillations in the current experiment is different.

In order to arrive at a mechanistic interpretation of the observations at high fragment kinetic energies it is instructive to explore a simpler model. The TDSE for the D_2 molecule was solved in the Fixed Nuclei Approximation (FNA) with the same pulses as in the full calculation. The wavefunction in this model is described in terms of a limited number of electronic states, including those that are relevant

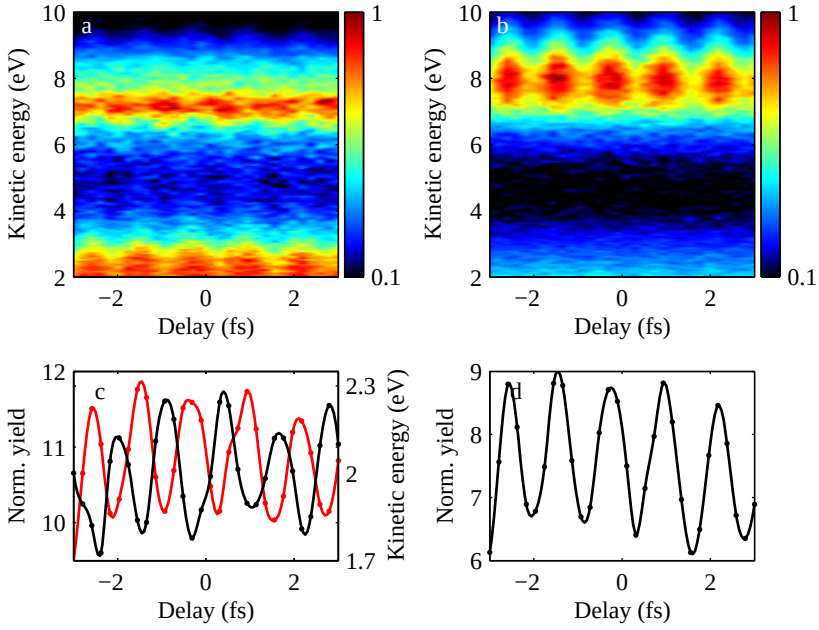

Figure 6.2: Time-dependent fragment kinetic energy spectrum as a function of delay τ between the APT and the IR pulse for fragments ejected at 0° (a) and at 90° (b) ± 20°. In (c) and (d) ion yields as a function of delay are plotted for parallel and perpendicular fragments where the signal is normalized to the yield by the APT only of that particular channel. In (c) the black (red) curve is for fragments centered at 7 (3) eV and in (d) fragments around 8 eV are shown.

for the production of the high energy fragments:

$$\Psi(t) = c_0(t)\psi_0 + \sum_l \int d\epsilon c_{g,\epsilon l}(t)\psi_{g,\epsilon l} + \sum_l \int d\epsilon c_{u,\epsilon l}(t)\psi_{u,\epsilon l} \tag{6.1}$$

where ψ_0 represents the ground state of the neutral molecule and $\psi_{g,\epsilon l}$ and $\psi_{u,\epsilon l}$ are the continuum wavefunctions of the molecular ion in the $1s\sigma_g$ and $2p\sigma_u$ states respectively plus one electron in the continuum with a partial wave l and energy ϵ. Continuum states with ungerade total symmetry Σ_u (ion + electron) are coupled with the ground state and with continuum states with gerade total symmetry Σ_g. The ground state is only coupled to Σ_g continuum states via the Σ_u states. In the full calculations, for ionization to the $2p\sigma_u$ continuum, the center of mass of the nuclear wavepacket is shifted to the right with respect to the center of the Franck Condon region (1.4 a.u.), since at an internuclear distance of 1.4. a.u. the energy gap between the ground state and the $2p\sigma_u$ continuum lies beyond the most intense part of the XUV spectrum (centered at H19). All the FNA calculations are therefore done at an internuclear distance of 1.7 a.u..

In Fig. 6.4a the simulated total ionization probability to the $2p\sigma_u$ continuum, which correlates with the formation of high energy fragments, is plotted as a function

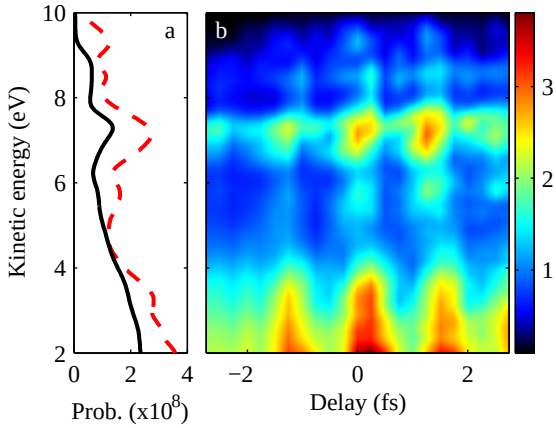

Figure 6.3: Results of the full calculations for dissociative ionization of D_2 by a 4-pulse APT and a 2.8 fs FWHM 780 nm field with a peak intensity of $3{\cdot}10^{12}$ W/cm^2. (a) Fragment kinetic energy spectra from the APT only (black solid line) and the APT+IR at τ=0 (red dashed line) (b) Fragment kinetic energy spectrum as a function of delay between the two pulses.

of the delay between the APT and the IR for three different implementations of the FNA (see Fig. 6.4b). The black dotted curve in Fig. 6.4a is the result of the full calculation (Fig. 6.3). In the first FNA calculation (blue dashed curve) only the $2p\sigma_u$ continuum is included and the couplings between states within the continuum are turned on, represented by the vertical red arrows in the green marked area in Fig. 6.4b. These couplings result in the appearance of sidebands in the photoelectron spectrum in between the photoelectron peaks that result from direct ionization by the odd harmonics in the APT. The intensity of these sidebands oscillates with the APT-IR delay as is well known from RABBITT experiments [1] but this does not lead to an oscillation in the yield of the $2p\sigma_u$ state.

A simulation including the coupling between the $1s\sigma_g$ and the $2p\sigma_u$ continua but without the couplings within the individual continua results in large oscillations of the ionization probability (red line). In Fig. 6.4b these couplings are illustrated by the diagonal red arrows. This situation again shows similarities to a RABBITT experiment, however, in the present case, the odd harmonics primarily access the $1s\sigma_g$ continuum and the sideband appears in the $2p\sigma_u$ continuum. This is furthermore illustrated in Fig. 6.4c where the delay dependence of the photoelectron spectrum corresponding to ionization to the $2p\sigma_u$ continuum is shown. Two sets of contributions can be distinguished in the plot. Direct ionization by the odd harmonics results in photoelectrons with a kinetic energy centered at 1.6 eV (H21) and 4.8 eV (H23). The sidebands that appear in between these contributions are the result of two-color APT+IR ionization to the $2p\sigma_u$ continuum via the $1s\sigma_g$ continuum mediated by the coupling between the two continua by the IR. Note that in this calculation the couplings within the individual continua has been turned off and are therefore not the reason for the sidebands. As is indicated by the diagonal red

arrows in Fig. 6.4b, there exist two pathways that lead to a specific sideband in the $2p\sigma_u$ continuum, namely absorption or emission of one IR photon from the direct photoelectron lines in the $1s\sigma_g$ continuum above and below the sideband . The production of the sideband centered at 0 eV involves harmonics H19 and H21, the sideband at 3.2 eV involves harmonics H21 and H23 and the sideband at 6.4 eV involves harmonics H23 and H25. In each sideband the two pathways interfere constructively or destructively depending on the relative phase of the IR field and the APT pulses, leading to a significant enhancement of the ionization at delays where the interference is constructive. Correspondingly, the total ionization oscillates as a function of the delay with a period of half an optical IR cycle.

This picture is modified when the couplings within the continua are turned on as well (gray dash dotted line). The yield oscillations in this result are closer to the result of the full calculation, although they show a phase difference, which is attributed to the simplicity of the FNA model, where only one internuclear distance is considered and where nuclear motion is not included. We note that the importance of coupling between the continua is greatly affected by the relative magnitudes of the cross sections for ionization by the APT. Because the cross section of the $1s\sigma_g$ continuum is much larger than that of the $2p\sigma_u$ continuum even a small IR-induced coupling can significantly affect the ionization to the $2p\sigma_u$ continuum while leaving ionization to the $1s\sigma_g$ continuum effectively unaffected. The fact that in Fig. 6.4c the sidebands are more intense than the direct ionization channels, and therefore dominate the total ionization yield, is a direct result of the difference in the ionization cross section of the two continua.

6.5 Conclusion

The frequency-domain interpretation given above can be complemented by a description in the time-domain. The APT-IR delays where a destructive interference is observed correspond to delays where the attosecond pulses in the APT are positioned at zero-crossings of the IR field, whereas delays where a constructive interference is observed correspond to delays where the attosecond pulses in the APT are positioned at (negative or positive) maxima of the IR electric field. In the presence of a strong electric field the $1s\sigma_g$ and $2p\sigma_u$ states are no longer eigenstates of the Hamiltonian. The eigenstates in the laser field are then so-called quasi-static states [18] that consist of a linear combination of the $1s\sigma_g$ and $2p\sigma_u$ basis states. In these quasi-static states the electron distribution is no longer symmetric but the molecule is polarized with the electron favoring one over the other proton. Hence an alternative way to view the experimental results is that the XUV ionization favors the production of the $2p\sigma_u$ state when - under the influence of the IR field - this state is mixed with the $1s\sigma_g$ state, with an accompanying localization of the electron within the molecule. As such, our experiment lends support to the notion that in attosecond ionization experiments changes in the charge distribution on attosecond timescales can be revealed, which is a core objective for future work in molecular attosecond physics.

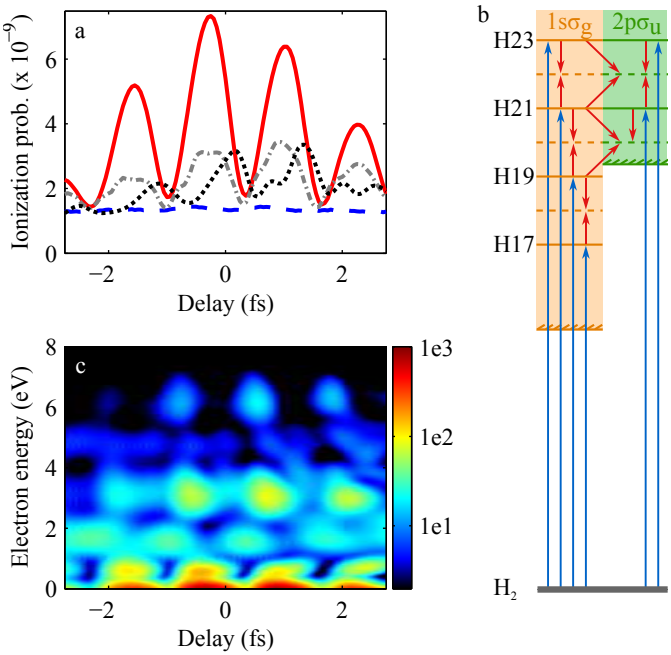

Figure 6.4: (a) Probability of ionization to the $2p\sigma_u$ continuum at an IR intensity of $3{\cdot}10^{12}$ W/cm^2. The black dotted line is the result of the full calculation including nuclear motion. The other curves are the result from the FNA model with all couplings turned on (gray, dash dotted line), only couplings within $2p\sigma_u$ continuum (blue dashed line) and only coupling between the $1s\sigma_g$ and $2p\sigma_u$ continua (red solid line) (b) Schematic illustration of APT+IR ionization to the $1s\sigma_g$ (orange) and $2p\sigma_u$ continuum (green). Vertical blue arrows represent ionization by the odd harmonic orders of the APT, red vertical arrows IR-induced couplings within the continua and red diagonal arrows the coupling between the continua.(c) Photoelectron spectrum corresponding to ionization to the $2p\sigma_u$ continuum as a function of delay for the situation in which only the coupling between the $1s\sigma_g$ and $2p\sigma_u$ continua is turned on (red line in (a)).

References

[1] P. M. Paul, E. S. Toma, P. Breger, G. Mullot, F. Auge, P. Balcou, H. G. Muller and P. Agostini. *Observation of a train of attosecond pulses from high harmonic generation.* Science, **292**, 1689–1692 (2001).

[2] M. Hentschel, R. Kienberger, C. Spielmann, G. A. Reider, N. Milosevic, T. Brabec, P. Corkum, U. Heinzmann, M. Drescher and F. Krausz. *Attosecond metrology.* Nature, **414**, 509–513 (2001).

[3] M. Drescher, M. Hentschel, R. Kienberger, M. Uiberacker, V. Yakovlev, A. Scrinzi, T. Westerwalbesloh, U. Kleineberg, U. Heinzmann and F. Krausz. *Time-resolved atomic inner-shell spectroscopy.* Nature, **419**, 803–807 (2002).

[4] M. Uiberacker *et al. Attosecond real-time observation of electron tunnelling in atoms.* Nature, **446**, 627–632 (2007).

[5] A. L. Cavalieri *et al. Attosecond spectroscopy in condensed matter.* Nature, **449**, 1029–1032 (2007).

[6] G. Sansone *et al. Electron Localization following Attosecond Molecular Photoionization.* Nature, **465**, 763–766 (2010).

[7] F. Remacle and R. D. Levine. *An electronic time scale in chemistry.* Proc. Natl. Acad. Sci. U. S. A., **103**, 6793–6798 (2006).

[8] A. I. Kuleff and L. S. Cederbaum. *Charge migration in different conformers of glycine: The role of nuclear geometry.* Chem. Phys., **338**, 320 – 328 (2007).

[9] M. F. Kling *et al. Control of electron localization in molecular dissociation.* Science, **312**, 246–248 (2006).

[10] K. P. Singh *et al. Control of Electron Localization in Deuterium Molecular Ions using an Attosecond Pulse Train and a Many-Cycle Infrared Pulse.* Phys. Rev. Lett., **104**, 023001 (2010).

[11] A. T. J. B. Eppink and D. H. Parker. *Velocity map imaging of ions and electrons using electrostatic lenses: Application in photoelectron and photofragment ion imaging of molecular oxygen.* Rev. Sci. Instrum., **68**, 3477–3484 (1997).

[12] O. Ghafur, W. Siu, P. Johnsson, M. F. Kling, M. Drescher and M. J. J. Vrakking. *A velocity map imaging detector with an integrated gas injection system.* Rev. Sci. Instrum., **80**, 033110 (2009).

[13] K. Ito, R. I. Hall and M. Ukai. *Dissociative photoionization of H_2 and D_2 in the energy region of 25-45 eV.* J. Chem. Phys., **104**, 8449–8457 (1996).

[14] P. H. Bucksbaum, A. Zavriyev, H. G. Muller and D. W. Schumacher. *Softening of the H_2^+ Molecular-Bond in Intense Laser Fields.* Phys. Rev. Lett., **64**, 1883–1886 (1990).

[15] F. Kelkensberg *et al. Molecular Dissociative Ionization and Wave-Packet Dynamics Studied Using Two-Color XUV and IR Pump-Probe Spectroscopy.* Phys. Rev. Lett., **103**, 123005 (2009).

[16] J. L. Sanz-Vicario, H. Bachau and F. Martin. *Time-dependent theoretical description of molecular autoionization produced by femtosecond xuv laser pulses.* Phys. Rev. A, **73**, 033410 (2006).

[17] P. Johnsson, J. Mauritsson, T. Remetter, A. L'Huillier and K. J. Schafer. *Attosecond Control of Ionization by Wave-Packet Interference.* Phys. Rev. Lett., **99**, 233001 (2007).

[18] P. Dietrich, M. Y. Ivanov, F. A. Ilkov and P. B. Corkum. *Two-electron dissociative ionization of H_2 and D_2 in infrared laser fields.* Phys. Rev. Lett., **77**, 4150–4153 (1996).

7 Attosecond Streaking in a Nanoplasmonic Field

Attosecond streaking spectroscopy as a technique to perform time-resolved studies on plasmonic fields is theoretically investigated. A method for simulating such experiments is developed based on the Mie-solution for the fields on spherical particles. It is shown that often the amplitude and phase of the localized field can be determined from such a streaking experiment but deviations from this are found in other cases. It is shown that in an attosecond streaking experiment the electrons are almost exclusively sensitive to the component of the field parallel to their velocity direction. This allows one to probe the different components of the field individually by resolving the angle of emission of the electrons. Finally, simulations based on fields calculated by finite-difference time-domain (FDTD), are compared to the results from the Mie-fields and are found to be in good agreement. This is a first step to extend the method to more complex structures.

7.1 Introduction

On the surface of a metal evanescent waves can exist as the result of the interaction between electromagnetic fields and collective oscillations of the conduction electrons in the metal. These excitations are commonly referred to as surface plasmons and exist in a variety of forms. The electromagnetic fields follow from the solution of Maxwell's equations on the interface between a metal ($\epsilon < 0$) and a dielectric ($\epsilon > 0$). For a planar geometry this leads to a traveling wave [1] with a corresponding dispersion curve that signifies the shorter wavelength of the surface plasmon compared to a free photon at a given frequency. The solution of Maxwell's equation for a spherical structure was first found by Mie [2]. The resulting theory has been highly successful in explaining the optical properties of metal and dielectric nanoparticles such as their scattering and absorption cross sections. The confinement of the surface plasmon wave on the sphere results in a resonance in the optical response of metal nanoparticles. The position of the resonance, largely determined by the permittivities of the metal and the surrounding, lies for metals like silver and gold in the visible spectrum.

In recent years the interest in surface plasmons has grown largely as a result of increased control in the fabrication of nanostructures. This opens up possibilities to design components such as waveguides, mirrors and beamsplitters to manipulate surface plasmons on a chip on a scale much smaller than is possible for optical cir-

cuits [3]. Another important aspect of surface plasmons is the concentration of the electromagnetic wave which leads to a higher field compared to a free-space electromagnetic wave. This field enhancement is used in a variety of sensing applications of which surface-enhanced Raman spectroscopy (SERS) is the best known example [4], which nowadays is possible at the single molecule level [5].

The electron dynamics that lie at the basis of all phenomena related to plasmons are most of the time only indirectly observed. An important parameter of this dynamics is the dephasing time, which is directly proportional to the aforementioned field enhancement. Dephasing times are predicted, and experimentally verified, to be in the range of 1-100 fs. However, the mechanisms that causes the dephasing are not well understood. Time-resolved experiments allow one to test and challenge current theoretical models, but such experiments are challenging because the fast timescales that are involved are at the limit of conventional laser pulses. The last decade techniques based on autocorrelation [6–8], frequency resolved optical gating (FROG) [9, 10] and spectral hole burning [11] have been developed for this purpose, each one of them having their own advantages. At the same time in the field of attosecond laser pulses a technique called attosecond streaking spectroscopy has been developed. This technique allowed the complete characterization of a light wave [12]. In earlier theoretical work it has been realized that this technique could potentially also form the basis of a temporal characterization of a plasmonic field [13, 14]. An important advantage of this is that in addition to the temporal resolution it is also possible to spatially resolve the fields with nanometer resolution by means of a photoemission electron microscope (PEEM). Moreover, the potential ability to resolve the absolute phase of the electric field, something which is not possible for any of the other methods, is an additional argument to develop attosecond streaking for plasmonic fields.

In an attosecond streaking experiment electrons are generated in photoionization by an attosecond pulse in the presence of a moderately strong infrared (IR) field. Since the attosecond pulse is short compared to the period of the IR field, ionization takes place at a well defined moment within that period. After the ionization the freed electrons interact with the IR field and their momentum after this interaction is dependent on the moment of ionization. This time-to-momentum mapping allows a characterization of the field by measuring the momentum (or energy) of the electrons. The outcome of an attosecond streaking experiment depends on whether or not the electron experiences a spatial variation of the field from the time it is born till it is detected. Three limiting situations are discussed that are based on the relation between the time it takes for an electron to leave the field (t_0) the period of the field T and the pulse durations t_p. The characteristic time t_0 is determined by the geometrical extension of the field r_0 and the velocity of the electron v_0 according to $t_0 = r_0/v_0$. In Fig. 7.1 a schematic representation of the three cases is given. The first case (Fig. 7.1a) occurs when the laser pulse is short compared to the time it takes the electron to leave the field ($t_0 \gg t_p$). In that situation the electron does not experience a spatial variation of the field and remains in the field from the time it is born to the end of the pulse. This is the situation generally encountered in attosecond streaking experiments in a laser field. In the second case (Fig. 7.1b) the electron can move out of the field completely during the laser pulse but it takes

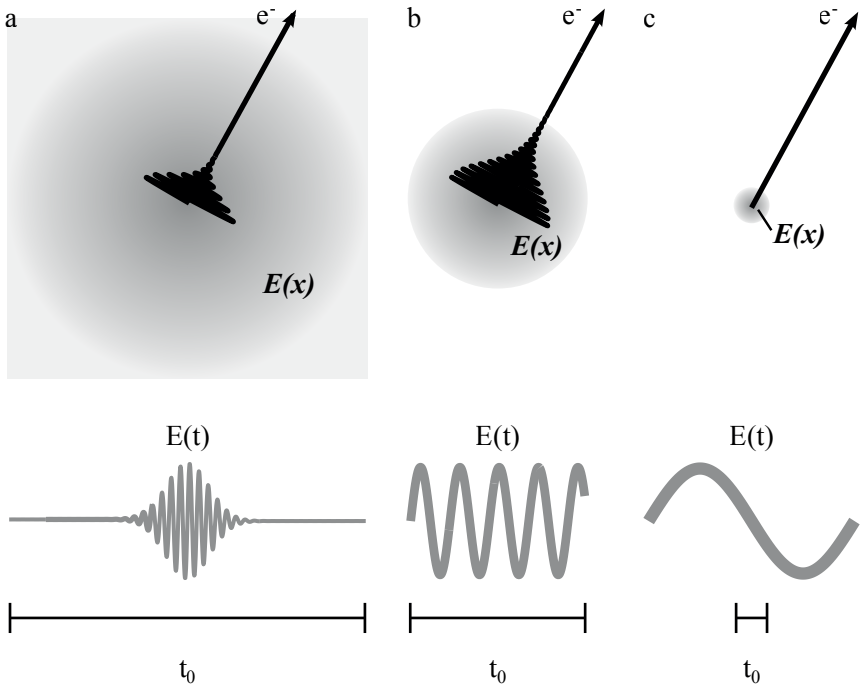

Figure 7.1: Three regimes of attosecond streaking can be distinguished by comparing the time t_0 it takes for an electron to leave field to the the pulse duration t_p and the period T of the field. In (a) ($t_0 \gg t_p$) the electron stays within the field from the time it is born to the end of the pulse. When $T \ll t_0 \ll t_p$ (b) the electron moves out of the field in a time that covers multiple optical cycles. In (c) ($t_0 \ll T$) the electron leaves the field 'instantaneously', i.e. within a fraction of an optical cycle.

many optical cycles ($T \ll t_0 \ll t_p$). The last case (Fig. 7.1c) is when the electron moves out of the field within a short period compared to the optical cycle ($t_0 \ll T$). This last condition describes the situation that was considered in ref. [13].

Streaking in a laser field

The geometrical extension of a laser field is usually much larger than the distance an electron travels from the time it is born till the end of the pulse. A classical analysis of the interaction of the electron with the field shows that for the momentum $\mathbf{p}(t)$ of the electron one can write:

$$\mathbf{p}(t) = \mathbf{p}_0 - e \int_{t_i}^{t} \mathbf{E}_L(t')\, \mathrm{d}t' = \mathbf{p}_0 + e\,(\mathbf{A}_L(t) - \mathbf{A}_L(t_i)) \tag{7.1}$$

where $\mathbf{p}_0$ is the initial momentum, e the elementary charge, $\mathbf{E}_L(t)$ and $\mathbf{A}_L(t)$ the electric field and vector potential of the laser pulse and t_i the moment of ionization. In the second equality an assumption about the electric field is made, which in its

most general form is written as:

$$\mathbf{E}_L(t) = -\nabla\Phi(t) - \frac{\partial \mathbf{A}_L}{\partial t} \tag{7.2}$$

where $\Phi(t)$ is the scalar potential of the field. For situations in which the electron does not experience a spatial variation of the field $\mathbf{E}(t)$ but only a temporal variation, the scalar potential can be neglected. At $t = \infty$ the field has vanished ($\mathbf{A}_L(t) = 0$) and it follows that the final momentum $\mathbf{p}_f$ is directly related to the vector potential at the moment of ionization:

$$\mathbf{p}_f = \mathbf{p}_0 - e\mathbf{A}_L(t_i) \tag{7.3}$$

Schematically this is illustrated in Fig. 7.2a where an idealized momentum map of photoelectrons that are initially ejected uniformly in all directions is displayed. A linearly polarized laser field displaces the circle in the momentum map by an amount equal to $-e\mathbf{A}(t_i)$. This results in a photoelectron energy W_f that depends on t_i and observation angle θ between the velocity direction of the electron and the polarization axis [15]. When a laser field of $E(t) = E_0(t)\cos\omega_l t$ is assumed, the final energy of the electrons ejected parallel ($\theta = 0°$) and perpendicular ($\theta = 90°$) to the laser polarization is given by [1]:

$$W_f(t_i, \theta = \ 0°) = W_0 + 2U_p \sin^2\omega_l t_i + \sqrt{8W_0U_p}\sin\omega_l t_i \tag{7.4}$$

$$W_f(t_i, \theta = 90°) = W_0 - 2U_p \sin^2\omega_l t_i \tag{7.5}$$

with ω_l the frequency and $E_0(t)$ the envelope of the field. $W_0 = p_0^2/2m_e$ is the starting energy of the electron with mass m_e. U_p is the ponderomotive energy which is given by $U_p = e^2E_0(t)^2/4m_e\omega_l^2$. This is the (cycle averaged) energy connected with the quiver motion of the electron in the laser field. In Fig. 7.2b the final energy W_f described by Eq. 7.4 is plotted as a function of the phase of the laser field at the moment of ionization $\omega_l t_i$ (solid black line) together with the laser field (gray line). This shows that electrons ejected parallel to the laser polarization ($\theta = 0°$) experience large positive and negative shifts in energy. Electrons ejected perpendicular to the laser polarization (Eq. 7.5) experience only energy shifts that are much smaller and only negative[16]. The dotted black line in Fig. 7.2b shows the final energy for electrons ejected perpendicular to the laser polarization.

Streaking in a continuous field

The assumption that the electron does not experience a spatial variation of the field before the field has turned off ($t_0 \gg t_p$) might not apply when attosecond streaking spectroscopy is applied to probe localized plasmon fields. If that approximations fails the relation between electric field and vector potential that was used ($\mathbf{E}_L(t) = -\frac{\partial \mathbf{A}_L}{\partial t}$) does not hold anymore and the gradient of the scalar potential of the field $\Phi(t)$ starts to be significant in Eq. 7.2. The effect of this is analyzed in the limiting situation where the field is continuous and the electron moves out of the field over

[1] Eqs. 7.4 and 7.5 are valid for the situations in which the starting energy W_0 is much larger than the ponderomotive energy U_p. This is usually the case in attosecond streaking experiments.

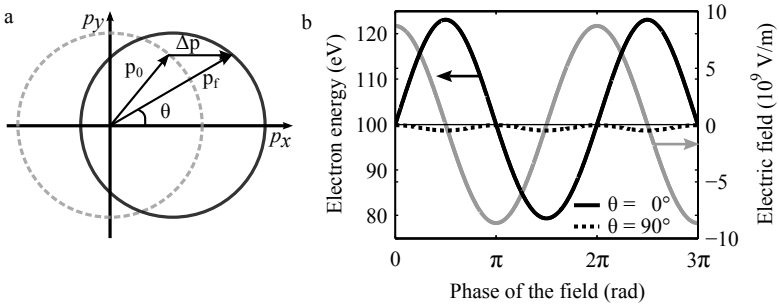

Figure 7.2: Principle of attosecond photoelectron streaking. (a) The dashed circle shows momentum distribution in the xy plane produced by the attosecond pulse which is shifted by $\Delta\mathbf{p}(t_i) = -e\mathbf{A}(\mathbf{t_i})$ through the interaction with the laser field. In (b) the resulting final energy $W_f(t_i)$ for $\theta = 0^\circ$ (solid black line) and for $\theta = 90^\circ$ (dotted black line) is plotted as a function of the phase of the laser field together with the laser field with a wavelength of 800 nm and an intensity of 10^{13} W/cm^2

.

a time covering many optical cycles ($T \ll t_0 \ll t_p$). In Fig. 7.3 the result of a 1D numerical simulation of streaking in a continuous field and a gaussian shaped field with a FWHM of 100 nm is shown. The obtained streaking curve is very close to the curve shown in Fig. 7.2b and described by Eq. 7.4. The only difference is that the electron acquires an additional (constant) offset in energy of U_p from the ponderomotive force $\mathbf{F}_p = -\nabla_\mathbf{r} U_p(r)$ when it has time to leave the field, a phenomenon well known from above threshold ionization (ATI) by long laser pulses [17]. Streaking in a continuous field with a finite size is thus described by

$$W_f(t_i) = W_0 + U_p + 2U_p \sin^2 \omega_l t_i + \sqrt{8W_0 U_p} \sin \omega_l t_i \tag{7.6}$$

Note that in practice the shift of U_p is of no importance because the relevant energy scales such as the bandwidth of the attosecond pulse and the maximum energy shift from streaking are usually much larger than U_p making it impossible to observe an energy shift of the size U_p in the streaking curve. Therefore the difference between Eqs. 7.4 and 7.6 can be neglected in practical situations. When the electron is released in a localized field it will move out of the field before the laser pulse has vanished. Eq. 7.6 suggests that a streaking measurement will have an almost identical result as in a laser field.

Streaking in highly localized fields

In the derivation of Eq. 7.6 it was assumed that the electron moves out of the field slowly and it takes the electron many optical cycles to leave the field, i.e. $t_0 \gg T$. In other words, the exit of the electron out of the field takes place adiabatically. This might however not be the case for highly localized fields for which the geometrical extension of the field becomes comparable to the distance the electron travels in an optical period ($t_0 \approx T$). For example, an electron of 100 eV travels approximately 16 nm within the optical period of the field of light with a wavelength of 800 nm.

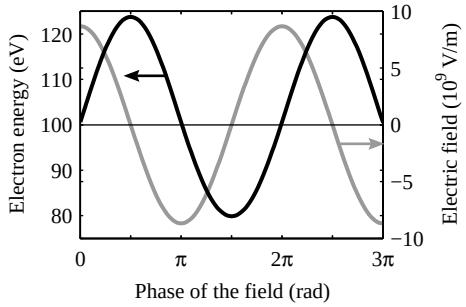

Figure 7.3: Numerical simulation of attosecond streaking in the situation of a finite sized continuous oscillating field with a wavelength of 800 nm and a peak intensity of 10^{13} W/cm^2. The spatial profile of the field is Gaussian with a FWHM of 100 nm and the initial energy of the electron is 100 eV. The final electron energy is plotted as a function of the phase of the field at which the electron is born (black curve) together with the field (gray line). The electron energy is described by Eq. 7.6 and the result is almost identical to Fig. 7.2b because U_p is only 0.6 eV.

In ref. [13] an approximation was suggested which can apply in certain cases of attosecond streaking in highly localized fields. Provided that the field extension is small enough and that the initial kinetic energy is large enough ($t_0 \ll T$), the electron can be assumed to leave the localized field 'instantaneously'. In such a situation the electron does not feel the oscillations of the field and the problem becomes (quasi-) electrostatic in nature. In this case the outcome of an attosecond streaking experiment is governed by the scalar potential in Eq. 7.2:

$$W_f(t_i) = W_0 + e\Phi_L(t_i) \tag{7.7}$$

In contrast to the previous cases the electron streaking curves oscillates in phase with the electric field (E_t). Another important difference is that the energy shift does not depend on the starting energy W_0 or angle of emission θ. Although there might be situations where the approximation $t_0 \ll T$ holds, specifically when the localized field is on the order of a few nanometer, in general there will be an intermediate regime where the approximations of both the Eqs. 7.6 and 7.7 do not hold, i.e. $t_0 \approx T$. The aim of this work is to bridge the gap between these two cases and investigate theoretically whether it is still possible to probe localized fields with attosecond pulses if one does not completely satisfy either one of the criteria discussed above.

In section 7.2 the resonant plasmon fields of spherical particles that are used in this work are presented. It gives a basic introduction to the properties of these fields and the methods to calculate them. In section 7.3 the plasmon fields are used in electron trajectory calculations to simulate attosecond streaking experiments and the results are presented. Section 7.4 and 7.5 give a discussion and conclusion on the work.

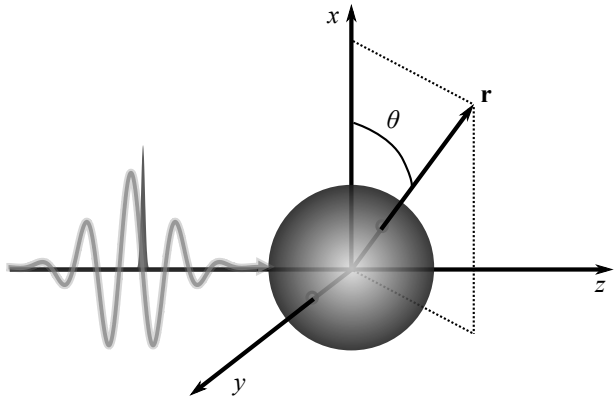

Figure 7.4: Coordinate system used throughout this work. The spherical particle with radius a is located at the origin. The two light pulses propagate along the z-axis and are polarized in the x-direction. The angle θ is defined as the angle between r and the x-axis.

7.2 Resonant plasmon fields on nanoparticles

When a metal nanoparticle is irradiated (as illustrated in Fig. 7.4), a collective oscillation of the conduction electrons is caused by the force the electric field of the radiation exerts on the electrons and the restoring Coulomb force of the nuclei. The oscillating electron cloud in turn results in a secondary field which adds coherently to the incident field. This superposition results in a total field that is modified significantly from the incident field especially for illumination at the resonance frequency. A dipole resonance is the first mode of excitation but higher modes can also be excited depending mainly on the size and shape of the particle and the wavelength of the light. The position of the resonance is determined by the permittivity of the metal and by the size and shape of the charge distribution. In the literature emphasis is often put on the far field optical properties of particles to give expressions for the scattering and extinction cross sections. These cross sections can be directly related to macroscopic properties like for example the color of the particles. For this work the near-field properties are the most relevant since the streaking occurs in the enhanced field close to the surface of the particle. The current analysis concentrates on spherical particles since it forms the simplest system in which effects of an enhanced near field can be studied. In this section three methods to describe the near-field optical properties of spherical particles are discussed. First the so-called quasi-static approximation is used in order to give an intuitive understanding of the localized field. Next, the exact solution based on the Mie-theory is given and compared to the quasi-static result. Finally a numerical solution calculated on a grid in space and time by the finite-difference time-domain method (FDTD) is presented. With FDTD geometries can be simulated for which no numerical theories exist. Streaking simulations in the next section are performed based on the fields from Mie-theory and the FDTD fields. The results based on the Mie-theory fields provide a benchmark against which the results based on FDTD field can then be checked.

7.2.1 Quasi-static approximation

For metal spherical particles with radius a much smaller than the wavelength of the incoming radiation λ_i a simple expression for the total field can be found. For a small enough particle the incoming radiation $\mathbf{E}_i$ can be considered uniform over its volume and the interaction can be described by electrostatic theory rather than electrodynamics in what is often called the quasi-static approximation. In this approximation a static electric field $\mathbf{E}_i$ is assumed although the incident field is a (plane) electromagnetic wave with an optical frequency. In the final solution the assumption is made that one can replace the static permittivities ϵ and ϵ_m by the frequency dependent permittivities at the frequency of the incident wave (see Fig. 7.5a). The solution for the field is given by solving the Laplace equation for a sphere in a homogeneous medium and an uniform static electric field. When only the first spherical harmonic in the solution of the Laplace equation is considered, the field outside the sphere is formed by the superposition of the incident field $\mathbf{E}_i$ and an ideal dipole with dipole moment $\hat{\mathbf{p}}$ [18] given by:

$$\hat{\mathbf{p}} = 4\pi\epsilon_m a^3 \frac{\epsilon - \epsilon_m}{\epsilon + 2\epsilon_m}\mathbf{E}_i \tag{7.8}$$

with ϵ and ϵ_m the permittivities of the sphere and the medium. Multipolar contributions to the field become increasingly important for particles with a larger radius but for now this analysis is restricted to the dipole contribution. Choosing the polarization of the incident field in the x-direction ($\mathbf{E}_i = E_i\hat{\mathbf{x}}$) the total (enhanced) field outside but close to the sphere is given by [19][2]:

$$\mathbf{E}_{total} = E_i\hat{\mathbf{x}} + \frac{\alpha E_i}{4\pi\epsilon_m}\left[\frac{3\cos\theta\hat{\mathbf{r}} - \hat{\mathbf{x}}}{|\mathbf{r}|^3}\right] \tag{7.9}$$

where $\alpha = 4\pi a^3 \frac{\epsilon-\epsilon_m}{\epsilon+2\epsilon_m}$ is the polarizibility of the sphere, $\hat{\mathbf{x}}$ and $\hat{\mathbf{r}}$ are the unit vectors in the x-direction and radial direction and θ is the angle between these directions (see Fig. 7.4 for an illustration of the coordinate system and angles). The field enhancement $|\mathbf{E}_{total}|^2/|\mathbf{E}_i|^2$ is wavelength dependent through the permittivity ϵ and the plasmon resonance condition is given by $\epsilon/\epsilon_m = -2$ at which point the polarizibility α blows up. The maximum field enhancement on the polarization axis ($\mathbf{r} = r\hat{\mathbf{x}}$) can be evaluated from Eq. 7.9:

$$\mathbf{E}_{total} = E_i\left(1 + \frac{\alpha}{2\pi\epsilon_m r^3}\right)\hat{\mathbf{x}} \tag{7.10}$$

From which it can be deduced that the maximum field enhancement at resonance ($\lambda_r = 354$ nm) at the surface of a silver sphere is approximately 120. The exact resonance condition ($\epsilon/\epsilon_m = -2$) is nowhere satisfied because the permittivity is complex, the imaginary component broadens the resonance and limits the field enhancement. In quasi-static approximation the maximum field enhancement at the surface is independent of the radius a (see Fig. 7.5b). In Fig. 7.5c the field

[2] Eq. 7.9 is appropriate for the field close to the surface [19], whereas far from the particle surface the radiative dipole field should be used to describe the field like is done in the derivation of the scattering and extinction cross sections of these particles [18].

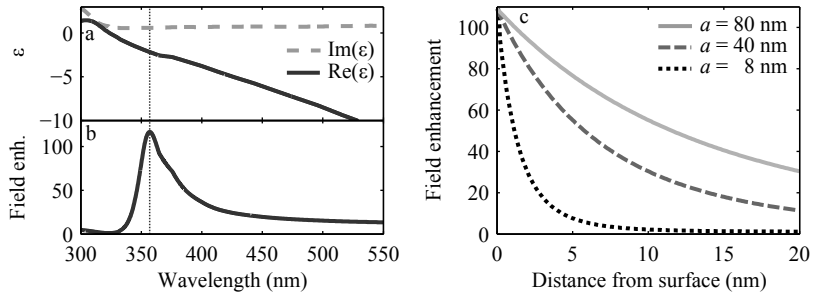

Figure 7.5: (a) Real and imaginary parts of the permittivity of silver as a function of wavelength (Palik [20]). (b) Maximum field enhancement E^2_{total}/E^2_i at the surface of a spherical particle according to the dipolar quasi-static approximation which does not depend on the radius of the particle. (c) Field enhancement for different particle radii as a function of the distance to the surface of the particle which is resonantly excited at 354 nm.

enhancement at resonance is plotted as a function of distance from the surface for different sized particles. This shows that the spatial extension of the enhanced field grows with the radius. Therefore also the time it takes an electron to leave the enhanced field, starting from the surface of the particle, increases with particle radius.

At this point it is instructive to analyze the case of attosecond streaking in the limit of an instantaneous exit of the electron from the enhanced field based on the quasi-static approximation. In this limit the energy of the electron is described by Eq. 7.7 and the time dependence is governed by the scalar potential $\Phi(t)$. The scalar potential of the metal particle at position $\mathbf{r} = a\hat{\mathbf{x}}$ is:

$$\Phi(t) = \frac{\mathbf{p}(t) \cdot \mathbf{r}}{4\pi\epsilon_m r^3} = \frac{|\mathbf{p}(t)|}{4\pi\epsilon_m a^2} \tag{7.11}$$

The dipole moment $\mathbf{p}$ is given by Eq. 7.8 and the time-dependence is inferred from $\mathbf{p}(t) = \Re\{\hat{\mathbf{p}}e^{i\omega_l t}\}$. In Fig. 7.6 the incident field E_i (solid gray line, scaled by a factor of 10 for comparison) and the enhanced field $\mathbf{E}_{total}$ (dashed gray line) are plotted for a particle with a radius of 4 nm resonantly excited by 354 nm radiation with an intensity of 10^{11} W/cm^2. The phaseshift between the incident field and the total field is due to the fact that the system is driven at the resonance. The black solid line is the resulting final photoelectron energy $W_f(t_i)$ from Eq. 7.7. As opposed to the case of attosecond streaking by a laser field, the streaking curve maps the electric field (or scalar potential) of the plasmon field rather than the vector potential. However, care must be taken in adopting Eq. 7.7 since the conditions for which it applies are rather strict. An electron with a kinetic energy of 100 eV has a velocity of approximately 6 nm/fs. In order for the electron to escape within a tenth of the optical period at a wavelength of 360 nm the field extension should be smaller than 1 nm. Even for an electron with a starting energy of 1 keV this field extension should still be less than 3 nm. Clearly, these conditions are only satisfied for particles with a radius $a \ll 10$ nm as can be seen in 7.5b. Finally it is noted that the potential $\Phi(t)$ is proportional to the radius which means that, although Eq. 7.7 only becomes

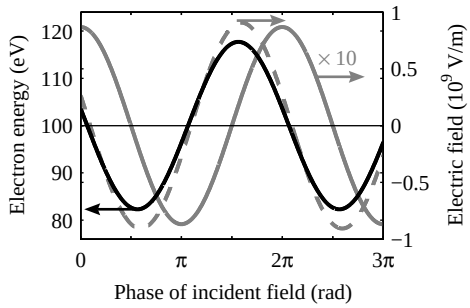

Figure 7.6: Plasmonic attosecond streaking in the instantaneous regime for a silver particle with a radius of 4 nm resonantly excited by 354 nm radiation with an intensity of 10^{11} W/cm^2. The incident field E_i (solid gray curve, scaled by factor of 10 for comparison) and enhanced field $|\mathbf{E}_{total}|$ at the surface (dashed gray curve) are plotted along with the final photoelectron energy W_f according to Eq. 7.7 (solid black curve).

valid for very small particles, the energy shift predicted by it approaches zero when the size of the particles decreases. For example the energy shift for a particle with a radius of $a = 4$ nm is about 18 eV (see Fig. 7.6), this decreases to 4.2 eV for a radius of $a = 1$ nm.

When moving to larger particles also the quasi-static approximation, although well-suited for providing a first intuition, starts to break down. As noted before, other excitations than the dipolar resonance become more important when the size of the particle increases. Although it is possible to start adding higher multipoles in the quasi-static approximation, the basic assumption on the uniformity of the incident field over the volume of the particle does not apply for larger particles and the problem becomes electrodynamic in nature. This can only be partly fixed by including corrections to the polarizibilty α that depend on the size but these approaches show deviations to the real solutions provided by Mie-theory [19]. All previous work on streaking in plasmonic fields [13, 14] was based on quasi-static fields. To extend these studies to a wider range of geometries one needs to move beyond the quasi-static approximation.

7.2.2 Mie-theory

In Mie-theory Maxwell's equations are solved for spherical particles with the appropriate boundary conditions. The exact solution is written as an infinite series of vector spherical harmonics which in practice is terminated when convergence is reached [18]. This procedure ensures that enough higher electric and magnetic multipoles are included to accurately describe the total field. In this work an implementation based on dyadic Green functions to represent the spherical harmonics is used [21]. In Fig 7.7a the dependence of the field enhancement and resonance wavelength λ_r on the particle radius a is shown. For small particles ($a < 20$ nm) the values correspond closely to the quasi-static approximation in which the field enhancement is approximately 120 and the resonance wavelength $\lambda_r = 354$ nm. For

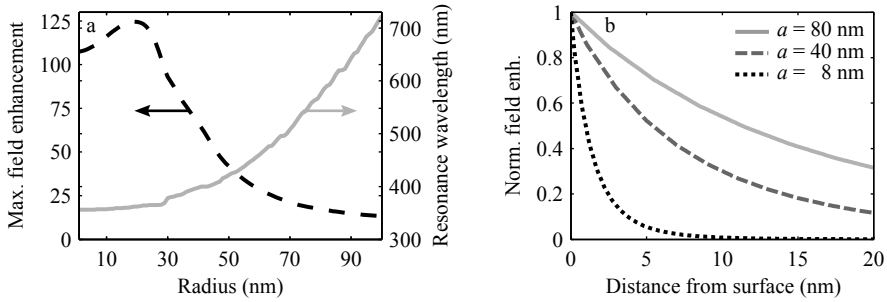

Figure 7.7: Results from a Mie-solution of the field enhancement for resonant illumination of silver spherical particles. In (a) the maximum field enhancement (dashed line) and resonant wavelength (solid line) are plotted as a function of the radius of the particle. In (b) the field enhancement is plotted as a function of the distance to the surface of the particle for three different radii. The field enhancement is normalized to the maximum field enhancement at the surface to enable comparison to Fig. 7.5b.

larger particles the Mie solution starts to deviate significantly from the quasi-static approximation due to the contribution of higher order multipoles. Fig. 7.7b shows the spatial dependence of the field enhancement for three different radii normalized to the field enhancement at the surface for comparison. This shows that the spatial dependence of the field enhancement is in good agreement with the quasi-static results in Fig. 7.5b.

In Fig. 7.8 the field enhancement in the xy-plane ($z = 0$), calculated by Mie-theory, is plotted for a spherical silver particle with a radius of 20 nm at a phase of the field where the field enhancement is maximum. The arrows that are superimposed indicate the direction of the field in the plane (z-component of the field is essentially zero). As expected, the field shows a dipole-like pattern. In figure 7.9a-b the same field is plotted but now separated into the $x-$ and y-component in the xy-plane. Fig. 7.9c shows the z-component in the xz-plane. The time-dependence of the x-component of the enhanced field at two positions on the surface of the sphere is shown in Fig. 7.10. The solid black line represents the field at $\mathbf{r} = a\hat{x}$ (referred to as pole) and the dashed black line shows the field at $\mathbf{r} = a\hat{y}$ (referred to as equator). The two fields on the two points have a phase difference close to π radians. Also plotted is the incident field (gray line), showing a phase delay between the incident and the enhanced field.

In conclusion the near field at the particle is not only localized but also highly non-uniform as compared to a laser field. The strength, direction and phase of the field all show a strong spatial dependence, a situation that is clearly very different from a laser field.

The simulations presented here, based on the Mie-solution, are all for monochromatic and thus continuous excitation. In an experiment a pulsed incident field is more likely. The response to a pulsed incident field can be constructed from the coherent superposition of a set of monochromatic results covering the bandwidth of the incident field and using the Kramers-Kronig relations to ensure causality. This has not been performed in the current work since it will not change the underlying

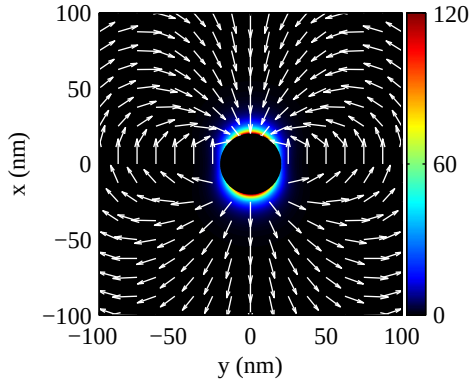

Figure 7.8: The field enhancement, shown in the xy-plane in color scale, close to the surface of a 20 nm radius spherical silver particle excited by a resonant monochromatic wave at 362 nm at a phase where the field enhancement is maximum. The arrows indicate the direction of the scattered field (no incident field) in the plane.

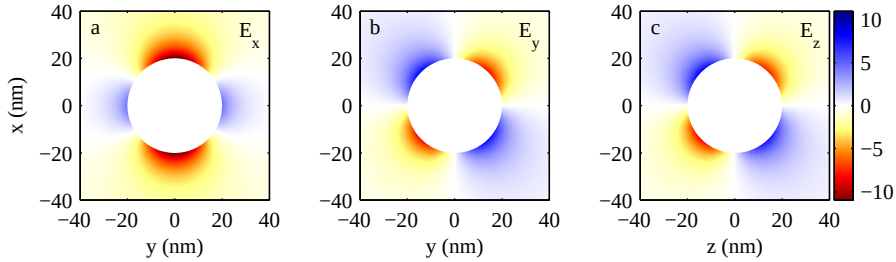

Figure 7.9: The x- (a) and y-component (b) (xy-plane) and the z-component (c) (xz-plane) of the enhanced field in the vicinity of a 20 nm radius spherical silver particle under resonant excitation by a monochromatic wave at 362 nm at a phase where the field enhancement is maximum. The values for the fields are normalized to the field amplitude of the incoming radiation.

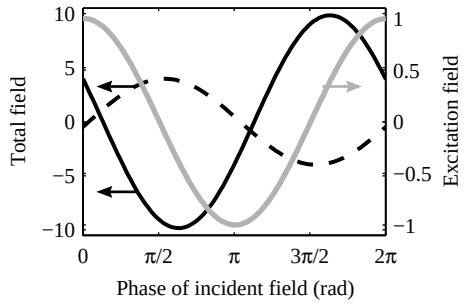

Figure 7.10: Electric fields of the incident (gray curve) and enhanced field from a Mie calculation for a silver sphere of 20 nm radius. The field at the pole ($\mathbf{r} = a\hat{x}$) (solid black curve) and at the equator ($\mathbf{r} = a\hat{y}$) (dashed black curve) show a phase difference close to π radians as well as a phase difference with the incident field.

physics. The calculations based on the continuous fields from Mie-theory can only be performed while the incident field is on. One aspect that cannot be modeled by a monochromatic theory but that is relevant to our application, is that when using exciting the system with pulsed fields, a system under resonant excitation will exhibit field oscillations even after the incident field has passed. This will be shown using the fields that are simulated by FDTD.

When moving beyond spherical particles in a homogeneous medium, analytical models become rapidly extremely complicated or simply do not exist. Analytical theories exist for the most simple structures such as a sphere or cylinder on a surface [22–24]. Numerical approaches like the discrete dipole approximation (DDA) [25, 26] and finite difference time domain (FDTD) methods [27] can be employed to simulate more complex structures. In a first step towards extending the current work to such geometries a comparison is made between results with spherical particles based on Mie-theory and FDTD.

7.2.3 FDTD simulations

For the FDTD simulations the commercial software package of Lumerical FDTD Solutions was used. A box that spanned 1 μm or 500 nm was used with a variable grid step size that was smallest (0.5 nm) at the surface of the particle. For the simulation a resonant plane wave pulse was launched from the boundary of the box along the z-direction. Figures 7.11a-c show the field enhancement from FDTD simulations of a silver particle with a radius of 20 nm that is excited by three different pulse durations with a central wavelength of 362 nm. The magnitude of the field enhancement is smaller for shorter pulses because the bandwidth of the incident field is wider than that of the resonance as can be seen in Fig. 7.11d-e. For the longest pulse duration the maximum value is still below the values obtained from Mie-calculations (Fig. 7.8) which is attributed to the finite precision of the method. Fig. 7.12a shows the x-component of the field from the simulation with a 15 fs FWHM incident field comparing reasonably well with the result from Mie-theory in Fig. 7.9a. At the surface of the particle numerical artefacts are visible that are known to occur in FDTD simulations at grid points on the interface between a metal and a dielectric medium. Avoiding this is virtually impossible but care is taken to minimize these effects as good as possible.

The three dimensional field at each point in the grid was recorded for each field components as a function of time, resulting in three (E_x, E_y, E_z) four-dimensional data sets. The amount of data that is associated with this, grows rapidly to amounts that cannot be easily handled in further calculations even when use is made of the symmetry present in the problem. Therefore, after the simulation, the field is converted to a representation in real spherical harmonics for each component of the electric field:

$$E_i(r,\theta,\phi,t) = \sum_{l=0}^{l_{max}} \sum_{m=-l}^{l} A_l^m(r,t) Y_l^m(\phi,\theta) \tag{7.12}$$

The coefficients $A_l^m(r,t)$ are retrieved from the projection of the simulated field on

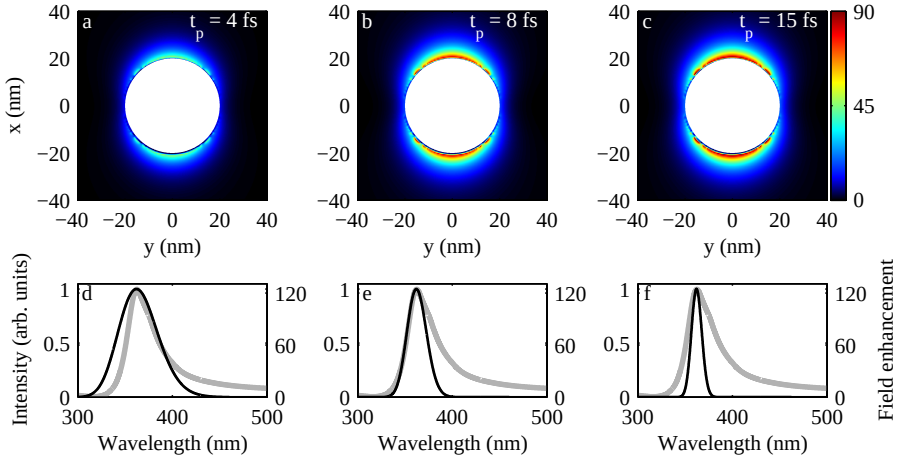

Figure 7.11: Maximum field enhancement in the xy-plane calculated by FDTD for a 20 nm spherical silver particle excited by a resonant 362 nm pulse of (a) 4 fs, (b) 8 fs and (c) 15 fs. The spectra of the incident field (black lines) of 4 fs (d), 8fs (e) and 15 fs (f) are shown compared to the wavelength dependence of the field enhancement from a Mie-calculation (gray lines).

the spherical harmonics $Y_l^m(\phi,\theta)$ which are defined as:

$$Y_l^m(\phi,\theta) = \Theta_{l|m|}(\theta)\Phi_m(\phi) \tag{7.13}$$

$$\Theta_{lm} = \sqrt{\frac{2l+1}{4\pi}\frac{(l-m)!}{(l+m)!}}P_l^m(\theta) \tag{7.14}$$

$$\Phi_m(\phi) = \begin{cases} \sqrt{2}\cos m\phi & m>0 \\ 1 & m=0 \\ \sqrt{2}\sin|m|\phi & m<0 \end{cases} \tag{7.15}$$

with $P_l^m(\theta)$ the Legendre polynomials. For the current fields $l_{max} = 5$ is sufficient to accurately describe the field. The conversion leads to a compression of two orders of magnitude. In Fig. 7.12b the same field as in 7.12a is plotted after conversion. Clearly the original field can be well represented by a description in spherical harmonics. Additionally the "hot spots" on the surface of the metal are effectively removed in the conversion since these unphysical artifacts cannot be described by only the low order spherical harmonics.

7.3 Electron streaking by plasmonic field

In this section attosecond streaking experiments on nanoparticles are simulated by numerically integrating classical electron trajectories in the enhanced field $\mathbf{E}_{total}$ of a nanoparticle under resonant excitation. The ionization step by the attosecond pulse

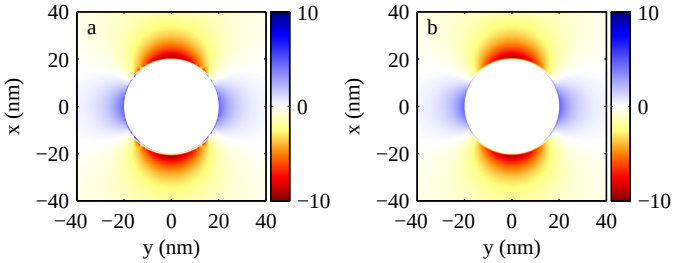

Figure 7.12: The x-component of the field in the xy-plane from the FDTD simulation with an incident field pulse duration of 11.2 fs before (a) and after (b) conversion to a representation in spherical harmonics ($l_{max} = 5$).

is assumed to produce electrons instantaneously at t_i at a certain central energy W_0 and with a bandwidth that corresponds to a Fourier limited pulse duration of a 300 as Gaussian pulse. The electrons are born on the surface of the sphere from where the interaction with the field is calculated up to a point in time and space where the electron energy is constant. By varying the moment of release of the electrons within the electric field, the delay between the attosecond pulse and the incident resonant field is simulated. The arrival time of the pulses depends on the z-coordinate, so for a fixed delay τ between two pulses, the moment of ionization is given by $t_i = \tau + z_{start}/c$ with z_{start} the z-coordinate of the starting position of the trajectory. Electrons are emitted in all directions from a uniform distribution on one half of the sphere ($z < 0$). It is assumed that the other half of the sphere ($z > 0$) is in the shadow of the attosecond pulse so no electrons are started from these positions. This is a good assumption when the wavelength of the attosecond pulse is small compared to the radius of the particle, although the results presented here will not change when electrons are started from all positions on the sphere. The electric field is obtained by interpolation of the fields discussed in the previous section that are stored on a grid. Trajectories that run into the particle are terminated while the final energy W_f of the remaining trajectories is recorded. Since a continuous incident field is used in the Mie-calculations the vector potential of this continuous field is added to the momentum of the electron at the moment when the boundary of the box is reached. In this way the electron leaves the field adiabatically despite the fact that the incident field is a (continuous) plane wave.

The situation that is considered here shows strong similarities to previous experiments and calculations on the ponderomotive acceleration of electrons by plasmon fields [28–30] which has recently been extended to few-cycle laser pulses [31–33]. In these experiments both ionization and excitation is performed by a single laser pulse, which makes it distinct from the present analysis. More specifically, in the situation considered in this work the electron starts with a relatively high kinetic energy and the ponderomotive energy is very small. Moreover, effects that are typical for strong field ionization like re-scattering, which was found to be important in ref. [33], do not play a role here.

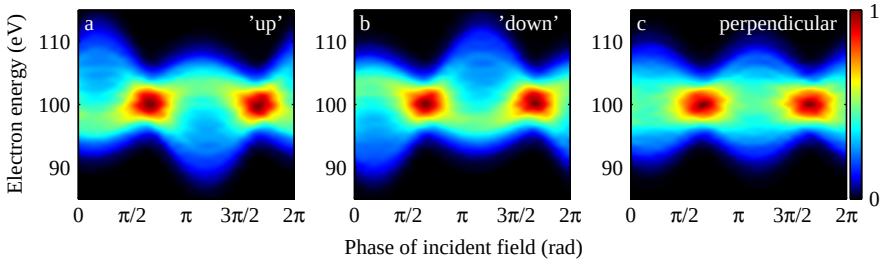

Figure 7.13: Attosecond streaking spectrograms from the enhanced field of a silver spherical particle with a radius of 20 nm from a Mie calculation resonantly driven by a monochromatic wave with a wavelength of 362 nm with an intensity of 10^{11} W/cm^2. (a) and (b) are for electrons emitted along the laser polarization in opposite direction and (c) for electrons emitted perpendicular to the incident field polarization. In all cases an acceptance angle of $\theta = \pm 40^\circ$ is used. Plotted in color scale is the normalized electron yield.

7.3.1 Streaking in plasmon field from Mie calculation

Figure 7.13 shows the result of a streaking simulation based on the field obtained with Mie-theory for a silver spherical particle with a radius of 20 nm, resonantly driven by a monochromatic wave with a wavelength of 362 nm. The photoelectron spectrum as a function of the moment of release (ionization) indicated as the phase of the incident field is plotted for three different velocity (after interaction with the field) directions. Experimentally it is possible to obtain these photoelectron spectra either by using an electron spectrometer with a narrow acceptance angle or by resolving the angle of emission in an electron spectrometer with a larger acceptance angle and post-selecting the electrons of interest. Fig. 7.13a and 7.13b show streaking spectrograms for electron that fly out parallel to the incident field polarization, in positive ('up') and negative ('down') x-direction respectively. The plots in Fig. 7.13 are obtained by integrating over an acceptance angle of $\theta = \pm 40^\circ$, the results, however, do not depend strongly on the width of this angle. The energy shift is opposite for the two directions, as it is in the case of streaking by a laser field. However, at delays where the energy shift is at its maximum, both positive and negative shifts with respect to the starting energy of 100 eV are observed in the final energy. This observation is in stark contrast to what is found in a laser field streaking experiment where an oscillating curve is obtained (Fig. 7.2). In Fig. 7.13c the result is plotted for electrons that fly out perpendicular to the incident field polarization. Because the system is cylindrically symmetric all electron spectra are independent of the angle ϕ of the velocity vector. The result in Fig. 7.13c is also different from what is observed in streaking by a laser field, in which the electron spectrum is only shifted down with a periodicity of half the optical cycle [16] (Fig. 7.2a). The origin of the differences between what is observed here and what is found in laser field streaking experiments lies in the non-uniformity of the plasmon field and will now be discussed in more detail.

Angular and spatially resolved streaking curves

In Fig. 7.14 streaking curves are plotted for electrons that are started from three specific locations on the particle: close to the pole ($\theta < 5°$) (Fig. 7.14a and 7.14d), around the equator ($85° < \theta < 95°$) (Fig. 7.14c and 7.14f) and in between these two ($40° < \theta < 50°$) (Fig. 7.14b and 7.14e). For the three locations the streaking curve is plotted for electrons that are emitted in positive x-direction ('up') (Figs. 7.14a-c) and perpendicular to the laser polarization (Figs. 7.14d-f). The results presented in Fig. 7.13a can be seen as the result of the superposition of the streaking spectrograms in Fig. 7.14a-c. The spectrogram in Fig. 7.13c corresponds to what is shown in Fig. 7.14d-f but in addition contains contributions from electron origination from positions on the sphere with $90° < \theta < 180°$.

The streaking curve in Fig. 7.14a is plotted along with the x-component of the enhanced field at the pole of the particle, demonstrating that the maximum shifts in the streaking curves occur close to the zero of the field, similar as it is expected when the momentum shift is equal to the vector potential. Note, however, that the oscillation of the enhanced field has a phase difference with the incident field (see Fig. 7.10). This shows that the oscillation in the streaking curve does not follow the vector potential of the incident field, surprisingly this seems to be different in ref. [14] in which the streaking oscillation does follow the oscillations of the vector potential of the incident field.

The energy shift in Fig. 7.14b is much smaller than in Fig. 7.14a whereas in Fig. 7.14c it is slightly larger again. In Fig. 7.14c the x-component of the enhanced field (at $r = a\hat{y}$) is plotted on top of the electron spectrogram. This shows that the maximum energy shift coincides with the zeros of the field, similar to the situation in Fig. 7.14a. The phase difference between the fields at the pole and the equator (see also Figs. 7.9a and 7.10) is reflected in the two streaking curves in Fig. 7.14a and 7.14c. This explains the negative and positive energy shifts seen in Figs. 7.13a and 7.13b. The smaller shift in Fig. 7.14b is because the x-component of the enhanced field experienced by electrons emitted from a point on the sphere around $\theta = 45°$ is smaller as can be seen in Fig. 7.9a. The y-component is largest at this position, however electrons with an initial velocity in the x-direction will only experience a small (negative) shift because of this. This can be understood by comparing this to the case of electron flying out perpendicular to the laser polarization in an attosecond streaking experiment in a laser field. The component of the field perpendicular to the direction of the electron has a much smaller effect on the energy of the electron than the component parallel to the direction of the electron (see Fig. 7.2). This is further illustrated by what is found for the electrons that are emitted perpendicular to the incident field polarization. For these electrons the energy shift is maximum for the electrons that are emitted from a point on the sphere around $\theta = 45°$ (Fig. 7.14e) whereas the energy shifts of electrons emitted close to the pole and the equator are much smaller. This can be understood by considering the spatial dependence of the enhanced field in the components perpendicular to the laser polarization in Fig. 7.9b and Fig. 7.9c, which is largest at the positions around $\theta = 45°$ and $\theta = 135°$. The streaking curve in Fig. 7.13c contains contributions from both positions and therefore is a superposition of two oscillations that are exactly out of phase. The 'residual' streaking effect in Fig. 7.14b and Fig. 7.14d is

the result of the interaction with the fields further away from the surface along the trajectory where the x and y/z-component respectively are nonzero. In conclusion: in an attosecond streaking experiment in localized fields one can probe the different components of the plasmon field individually by resolving the angular direction of the electrons.

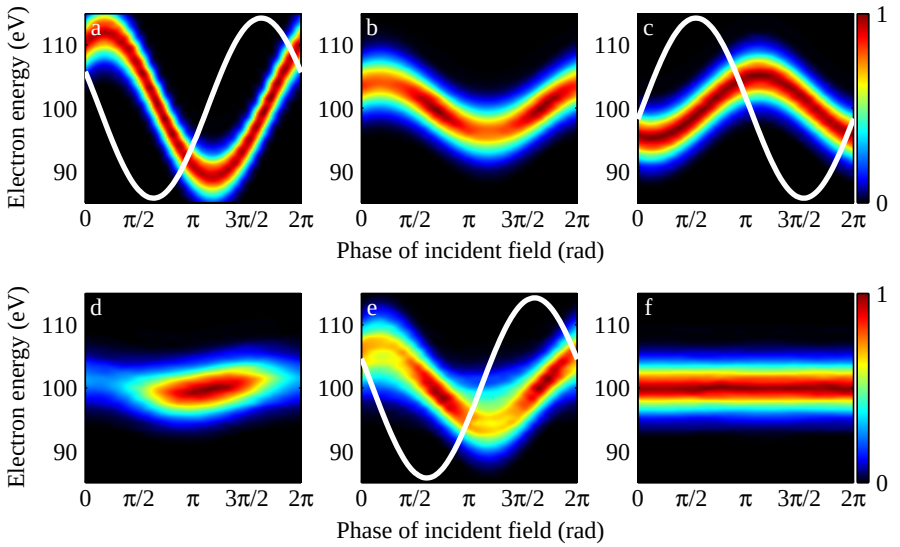

Figure 7.14: Streaking spectrogram from the same field as in Fig. 7.13 for electron emitted parallel (a-c) and perpendicular (d-f) with respect to the incident field polarization. The spectrograms show the results for electrons starting from different locations on the particle separately: for electrons that are born close to the pole of the sphere ($\theta =< 5^\circ$) (a,d), at 45 degrees (b,e) and close to the equator $85^\circ < \theta < 95^\circ$ (c,f). The white curves in (a) and (c) show the time-dependence of the x-component of the electric field where the electrons are born and in (e) it is the component that is perpendicular to the polarization.)

Intensity dependence of the streaking results

To further analyze the character of the streaking observations just presented, the dependence on the intensity of the incident field is investigated for the case of emission in positive x-direction from the pole of the particle (Fig. 7.13a). In Fig. 7.15 streaking curves are plotted for the intensities 10^{10} W/cm^2 (black line) 10^{11} W/cm^2 (dark gray line) and 10^{12} W/cm^2 (light gray line). For these curves the photoelectron spectrum at each delay is fitted to a gaussian from which the peak position is determined. In Fig. 7.15b the maximum energy is plotted as a function of U_p of the incident field. The 'plus' symbols are the result of eight separate streaking simulations and the line is a fit based on Eq. 7.6 in which the effective U_p is used as the fitting parameter. The value for U_p determined in the fit gives a factor of 98 for the field enhancement. Clearly the fit describes the intensity dependence rather well and the value for the field enhancement is not far from the

value of 120 at the surface of the sphere close to the pole. Deviations are the result of not completely fulfilling the condition of an adiabatic exit of the field, which will be illustrated later by changing the initial energy of the electron.

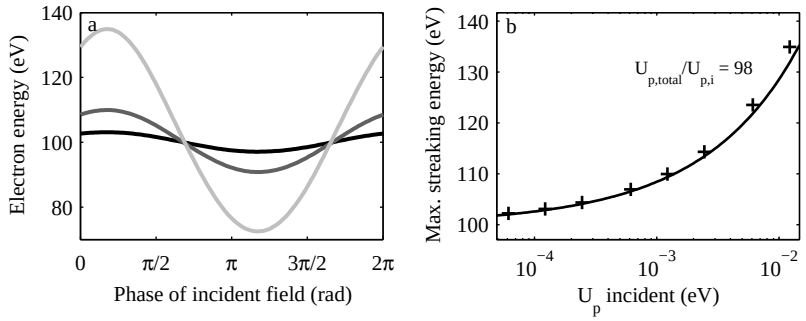

Figure 7.15: (a) Central photoelectron energy of electrons emitted from the pole of the particle emitted along the laser polarization (Fig. 7.14a) for 10^{10} W/cm^2 (black line), 10^{11} W/cm^2 (dark gray line), 10^{12} W/cm^2 (gray line). (b) Maximum energy determined from curves as in (a) for 8 different intensities plotted as a function of U_p of the incident field. The line is a fit to the data points using Eq. 7.4 from which a field enhancement is determined of 98.

Transition from the adiabatic to the instantaneous regime

In the introduction of the chapter three cases for attosecond streaking were discussed. In the second case that was discussed ($2\pi v_0/\omega \ll r_0 \ll v_0 t_p$) the electron leaves the field adiabatically whereas in the third limit ($r_0 \ll 2\pi v_0/\omega$) the electron exits "instantaneously" from the field and therefore only interacts with the field at the moment it is born. The streaking behavior in the last case is very different from the other two. The most notable is the difference in the relative phase between the streaking oscillation and the streaking field. The results presented in Fig. 7.8, 7.9 and 7.15 all indicate that for a particle with a radius of 20 nm and an initial electron energy of 100 eV the situation is best described by the adiabatic case. This is furthermore illustrated in Fig. 7.16a where the momentum shift of the electrons is plotted as a function of the phase of the incident field at the moment the electron is born for six starting energies in the range between 20 eV and 1 keV. Again the electrons emitted from the pole of the sphere emitted parallel to the laser polarization in the positive direction are selected. The curves are lying almost on top of each other, which is expected for a situation where the electron moves out of an oscillating field adiabatically since the momentum shift is independent of the initial velocity and only dependent on the properties of the field. The situation is clearly changed for a particle with a radius of 2 nm which is shown in Fig. 7.16b. The phase and amplitude of the oscillation in the momentum shift changes with the starting energy W_0. This is the result of moving from the regime of an adiabatic exit (small initial velocity) to an instantaneous exit (high initial velocity). The transition between the two regimes is gradual both in phase and amplitude (see Figs. 7.16c and

7.16d).

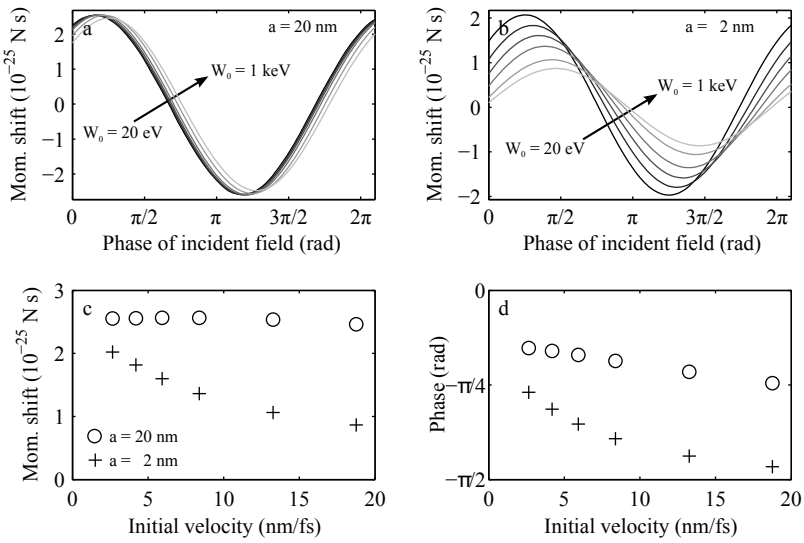

Figure 7.16: Electron momentum shift for a 20 nm (a) and 2 nm (b) particle for 6 starting energies W_0 between 20 eV and 1keV. The amplitude (c) and phase (b) of these oscillations are plotted as a function of initial velocity of the electron for 20 nm (o) and 2 nm (+) particles.

A simplified one-dimensional model is used to further explore this transition regime. In the model the field is continuous in time and has an exponential decay in space:

$$E(r,t) = E_0 \; e^{-r/r_0} \cos \omega t \tag{7.16}$$

In this field electrons are started at $r = 0$ with a certain energy. The interaction with the field is stopped when the oscillations in the electron energy have become insignificantly small. The final momentum of the electron is recorded as a function of the phase of the field at which the electron is born and the resulting oscillation is fitted to a cosine function. In Fig. 7.17a the amplitude of the oscillation in momentum is plotted as a function of initial velocity for $r_0 = 1$ nm (black line), $r_0 = 4$ nm (dark gray line) and $r_0 = 100$ nm (light gray line). The same trends as in Fig. 7.16c are observed: the amplitude decreases with initial velocity for the smallest fields. Fig. 7.17b shows the phase of the oscillation for the same calculations which shows that the phase changes with the initial velocity for the smallest field sizes. This agrees with what is found with Fig. 7.16d (with a constant phase offset). The effects that are observed here are due to the transition between two regimes, which becomes even clearer when the amplitude (Fig. 7.17c) and phase (Fig. 7.17d) are plotted as a function of the field size parameter r_0. This is done for starting energies of 20 eV (light gray line), 100 eV (dark gray line) and 1 keV (black line). The streaking behavior moves from one regime to the other when the size of the field is changed. When the field is small the phase of the streaking oscillation

approaches zero ($\cos\omega t$) meaning that it is in phase with the oscillations of the electric field whereas when the field is large the phase approaches $\pi/2$ ($\sin\omega t$) as predicted by Eq. 7.6. In the amplitude similar behavior is observed. For large field sizes the momentum shift approaches eE_0/ω and for small fields it approaches zero. This is in agreement with the observation that when the electron leaves the field instantaneously the streaking will reflect the amplitude and phase of the scalar potential $\Phi = \int E(r)dr$ of the field. This scalar potential however goes to zero for infinitesimal small fields. This is true for both the field in Eq. 7.16 as well as for the plasmon field of a spherical nanoparticle as was discussed before. In the limit of infinitesimally small particles, plasmonic field enhancements no longer play a role, and one returns to the common situation of attosecond streaking governed by the strength of the incident laser field. In the asymptotic limits of these curves the streaking behavior is well understood and the phase and amplitude are in a simple way related to the phase and amplitude of the field. In the transition regime between the asymptotic limit the streaking curve is sensitive to the geometrical extension of the field as well.

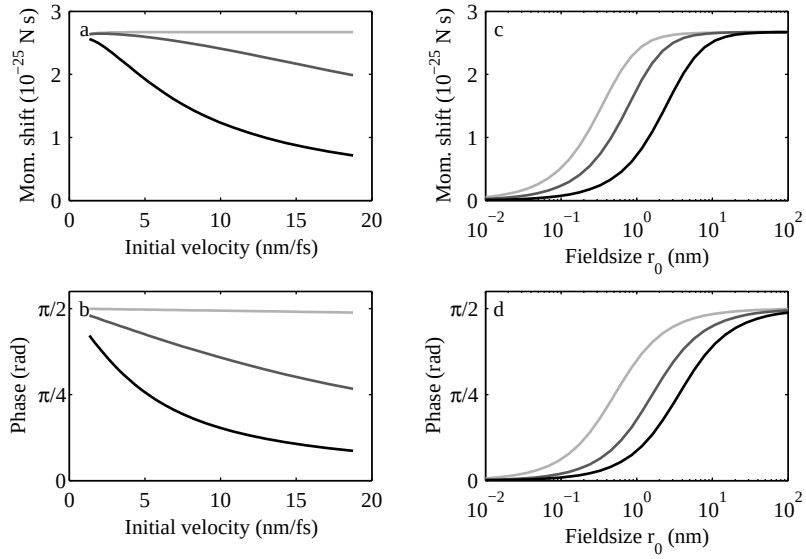

Figure 7.17: Results from model calculations for electrons released in the 1D field of Eq. 7.16. The left panels show the amplitude (a) and phase (b) of the momentum shift of the electron as a function of its initial velocity for $r_0 = 1$ nm (black line), $r_0 = 4$ nm (dark gray line) and $r_0 = 100$ nm (light gray line). The right panels show the amplitude (a) and phase (b) of the momentum shift of the electron as a function of the field size parameter r_0 for $W_0 = 1000$ eV (black line), $W_0 = 100$ eV (dark gray line) and $W_0 = 20$ nm (light gray line).

7.3.2 Streaking in plasmon field from a FDTD simulation

Figure 7.18 shows the simulated streaking spectrograms for the FDTD-fields in Figs. 7.11a-c for electrons emitted along the polarization in the positive x-direction (same as for Fig 7.13a). The zero of the delay axis is chosen such that the attosecond pulse overlaps with the center of the incoming pulse. This shows that the maximum streaking amplitudes are reached a few fs after the center of the incoming pulse has reached the particle. The first observation is that for the shortest pulse duration the energy shifts are smaller than for the other two (see Figs 7.18b,d,f). This relates to the fact that the bandwidth of the short incoming pulse is wider than the resonance (Figs. 7.11d-f), as was discussed before. This shows that in an actual experiment one might not necessarily opt for the shortest pulse durations available.

Another observation is that even after the incident field has vanished ($\tau > 10$ fs) oscillations are observed resulting from the finite lifetime of the plasmon. From this asymmetry in the streaking spectrogram the dephasing time of the plasmon can be extracted. These spectrograms would allow for a complete characterization of the incident and plasmon field including the *carrier envelope phase* (CEP) of both fields if a reference streaking spectrogram is measured in parallel that depends on the incident field rather than the plasmon field.

To compare the results from the FDTD-fields with the results obtained with a field from a Mie-calculation, the streaking spectrogram from Fig. 7.18b is separated into the contributions originating from the pole (Fig. 7.19a) and the equator (Fig. 7.19b) of the particle as was done before in Fig. 7.14. The x-component of the enhanced field at the respective locations is plotted on top of the streaking spectrograms. The maximum shifts in energy coincide with the zeros of the field, as was the case in the previous calculations based on a field from a Mie-solution. The amplitude of the oscillation is slightly smaller than in the Mie-results which is attributed to the fact that the field enhancement in the FDTD-fields is about 30% smaller than in the Mie-calculation.

7.4 Validity of the classical approximation of the interaction between the fields and the electron

Interference of electrons released at different moments in time are neglected by adopting a classical model for the interaction of the electrons with the field. This is justified when the duration of the ionization event, i.e. the attosecond pulse duration, is short compared to the optical period of the dressing field. When electrons are ejected over longer time spans interference between these electrons will result in deviations from the classical picture. When these electron wavepackets extends over more than one optical cycle in time it results in sidebands at a distance of one or multiple photon(s) from the original photoelectron peak [15, 34]. Since here the analysis is restricted to (isolated) attosecond pulses the classical approach is appropriate.

Also the ionization by the attosecond pulse is modeled in a simplified manner. An accurate simulation of the ionization process would require a quantum mechanical model. Recently theoretical models have been developed to simulate attosecond

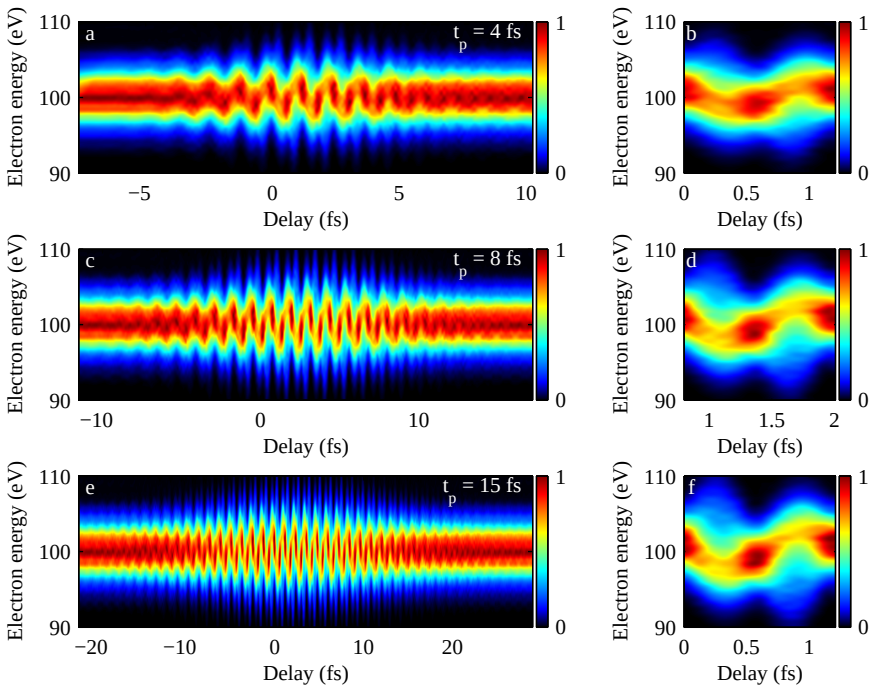

Figure 7.18: Attosecond streaking spectrograms for electrons emitted along the laser polarization in the positive x-direction within an acceptance angle of $\theta \pm 40°$. The simulations are based on the FDTD fields from Fig. 7.11 for an incident intensity of 10^{11} W/cm^2. (a,c,d) show delays covering the entire pulse duration and in (e,f,g) a zoom in over a single cycle of the field is given.

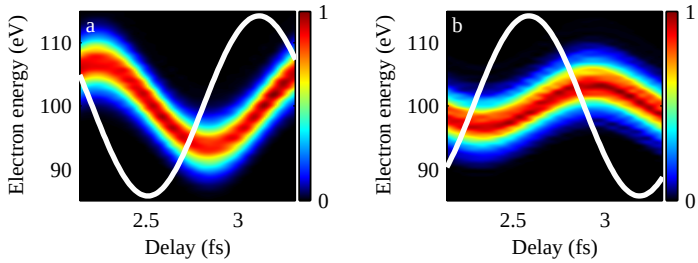

Figure 7.19: Streaking spectrogram for the same situation as in Fig. 7.18b for electrons that are started close to the pole of the particle (a) and around the equator (b). The white curves show the time-dependence of the x-component of the electric fields at the locations where the electrons are born. The delay range is chosen such that a direct comparison can be made to Figs. 7.14a and 7.14c.

XUV+IR streaking measurements on surfaces that accurately describe the ionization in the two-color field [35–37]. Such models are beyond the scope of the current analysis. This simplification leads to a photoelectron spectrum which is not realistic since in reality multiple surface and atomic states can show up in the photoelectron spectrum on top of the Fermi edge. However, for the aim of this work it is sufficient to assume that there is a distinguishable photoelectron peak that can be tracked in a delay scan. This can be a line in the photoelectron spectrum of the metal itself or from an adsorbate [38]. Furthermore, we neglect the interaction of the electron with the charge distributions in the metal other than what is causing the enhanced field. Because the energy of the electrons is relatively high the effect of the Coulomb field of the positively charged atoms in the metal will be small. The interaction of the electron with its image charge in a metal sphere was analyzed to see whether this would have a significant effect on the energy of the electrons. It was found to be negligible for distances larger than 5 Å, whereas at smaller distances the image charge concept becomes invalid.

In a practical situation ionization by the incident or total field needs to be dealt with. The workfunction of silver is 4.26 eV which means that ionization requires only two photons at the wavelengths of the resonance of these particles. With the intensities of the incident field, and definitely of the plasmon field, ionization will certainly be a strong effect. This can lead to very high energy electrons as was shown in previous experiments on ponderomotive acceleration of electron in a plasmon field [28, 29]. However in the situation of these works the ponderomotive energy U_p is much larger than in the configurations of the current work. Besides that, by using short pulses the conversion of ponderomotive energy to kinetic energy will not be complete which limits the energy of the electrons. Therefore it is expected that it will be possible to separate the electrons from ionization by the attosecond pulse from the electrons generated in ionization by the resonant field. Using an adsorbate layer with a higher ionization potential could be a possibility to limit ionization by the plasmon field.

7.5 Conclusions and outlook

Attosecond streaking spectroscopy is verified to be a useful tool in the characterization of plasmon fields. A general method to simulate such experiments is presented based on Mie-theory and FDTD simulations. Analytical theories like the Mie-theory exist only for a limited number of cases. The comparison between the results based on fields from a Mie calculation and those based on FDTD-fields show a good agreement. This shows that the method based on FDTD is reliable despite the artifacts that occur at the interface of the metal particle.

The assumptions that are valid in conventional attosecond streaking are not satisfied in a plasmon field but this does not prevent one to resolve the oscillation of the plasmon field. It is shown that in most practical situations the electron moves out of the field adiabatically allowing one to resolve the phase and amplitude from localized fields. These experiments would enable therefore to measure directly both the field enhancement and the de-phasing time independently, which can form a strong test for existing models. Moreover the potential to resolve the absolute phase (CEP) of the field oscillations is a possibility not found in any other method. When the initial velocity is increased and/or the field extension is decreased both the phase and amplitude of the streaking curves change. This signifies the transition to a regime in which the electron moves out of the fields non-adiabatically. In that regime phase and amplitude of the streaking curves are no longer related to the phase and amplitude of the field in a straightforward manner.

It is shown that the non-uniformity of the localized field has a profound effect on the results. The streaking spectrograms for localized fields contain multiple oscillations on top of each other originating from different positions on the particle, instead of a single oscillation as in the case of streaking by a laser field. Obviously spatially resolving these contributions would be desirable but will be extremely challenging. Interestingly, by resolving the angle of emission of the electron one can probe the different components of the localized fields individually.

It is realistic to expect that attosecond streaking experiments will soon be successfully applied in time-resolved studies of plasmonic fields. Metallic nanoparticles can be injected in a photoelectron spectrometer by a gas jet and the experimental conditions would closely resemble those of traditional attosecond streaking experiments [12]. The main additional complexity is the need for the incident field to match the resonance of the particles under investigation. The calculations presented here suggest that the second harmonic of a regular Ti:Sapphire laser could be used as the incident field. Besides homogeneous spherical particles so-called core-shell particles will be of interest as well. In such particles the resonance can be shifted towards longer wavelengths and potentially a higher field enhancement can be achieved.

Attosecond streaking studies on plasmonic structures on a surface would be a much more general way of studying plasmon fields. Such structures are produced by either nanofabrication methods or deposition of nanoparticles. Attosecond streaking experiments on surface emitted photoelectrons have already been performed as well [39]. Simulating such an experiment would require to extend the models to include the surface. This requires numerical techniques like FDTD, DDA or an interesting alternative based on surface integrals [40].

References

[1] H. Raether. *Surface plasmons on smooth and rough surfaces and on grattings.* Springer-Verlag, Berlin (1988).

[2] G. Mie. *Beiträge zur Optik trüber Medien, speziell kolloidaler Metallösungen.* Annalen der Physik, **330**, 377–445 (1908).

[3] W. L. Barnes, A. Dereux and T. W. Ebbesen. *Surface plasmon subwavelength optics.* Nature, **424**, 824–830 (2003).

[4] M. Fleischmann, P. Hendra and A. McQuillan. *Raman spectra of pyridine adsorbed at a silver electrode.* Chem. Phys. Lett., **26**, 163 – 166 (1974).

[5] S. Nie and S. Emery. *Probing single molecules and single nanoparticles by surface-enhanced Raman scattering.* Science, **275**, 1102–1106 (1997).

[6] B. Lamprecht, A. Leitner and F. Aussenegg. *Femtosecond decay-time measurement of electron-plasma oscillation in nanolithographically designed silver particles.* Appl. Phys. B: Lasers Opt., **64**, 269–272 (1997).

[7] B. Lamprecht, A. Leitner and F. Aussenegg. *SHG studies of plasmon dephasing in nanoparticles.* Appl. Phys. B: Lasers Opt., **68**, 419–423 (1999).

[8] B. Lamprecht, J. R. Krenn, A. Leitner and F. R. Aussenegg. *Resonant and Off-Resonant Light-Driven Plasmons in Metal Nanoparticles Studied by Femtosecond-Resolution Third-Harmonic Generation.* Phys. Rev. Lett., **83**, 4421–4424 (1999).

[9] A. Anderson, K. S. Deryckx, X. G. Xu, G. Steinmeyer and M. B. Raschke. *Few-Femtosecond Plasmon Dephasing of a Single Metallic Nanostructure from Optical Response Function Reconstruction by Interferometric Frequency Resolved Optical Gating.* Nano Lett., **10**, 2519–2524 (2010).

[10] T. Zentgraf, A. Christ, J. Kuhl and H. Giessen. *Tailoring the ultrafast dephasing of quasiparticles in metallic photonic crystals.* Phys. Rev. Lett., **93**, 243901 (2004).

[11] F. Stietz, J. Bosbach, T. Wenzel, T. Vartanyan, A. Goldmann and F. Träger. *Decay Times of Surface Plasmon Excitation in Metal Nanoparticles by Persistent Spectral Hole Burning.* Phys. Rev. Lett., **84**, 5644–5647 (2000).

[12] E. Goulielmakis *et al. Direct measurement of light waves.* Science, **305**, 1267–1269 (2004).

[13] M. I. Stockman, M. F. Kling, U. Kleineberg and F. Krausz. *Attosecond nanoplasmonic-field microscope.* Nat. Photonics, **1**, 539–544 (2007).

[14] T. Pfeifer, M. J. Abel, P. M. Nagel, A. Jullien, Z. H. Loh, M. J. Bell, D. M. Neumark and S. R. Leone. *Time-resolved spectroscopy of attosecond quantum dynamics.* Chem. Phys. Lett., **463**, 11–24 (2008).

[15] J. Itatani, F. Quere, G. L. Yudin, M. Y. Ivanov, F. Krausz and P. B. Corkum. *Attosecond streak camera.* Phys. Rev. Lett., **88**, 173903 (2002).

[16] M. Drescher, M. Hentschel, R. Kienberger, G. Tempea, C. Spielmann, G. A. Reider, P. B. Corkum and F. Krausz. *X-ray pulses approaching the attosecond frontier.* Science, **291**, 1923–1927 (2001).

[17] M. Lewenstein and A. L'Huillier. *Principles of Single Atom Physics: High-Order Harmonic Generation, Above-Threshold Ionization and Non-Sequential Ionization.* In T. Brabec, ed., *Strong Field Laser Physics*, Springer, Springer Series in Optical Sciences, 147–183 (2008).

[18] C. F. Bohren and D. R. Huffman. *Absorption and Scattering of Light by Small Particles.* Wiley-Interscience (1983).

[19] K. L. Kelly, E. Coronado, L. L. Zhao and G. C. Schatz. *The Optical Properties of Metal Nanoparticles: The Influence of Size, Shape, and Dielectric Environment.* The Journal of Physical Chemistry B, **107**, 668–677 (2003).

[20] E. Palik, ed. *Handbook of optical constants of solids.* New York: Academic Press (1985).

[21] C.-t. Tai. *Dyadic green functions in electromagnetic theory.* IEEE Press, Piscataway, NJ, 2 ed. (1994).

[22] P. A. Bobbert and J. Vlieger. *Light scattering by a sphere on a substrate.* Physica A: Statistical and Theoretical Physics, **137**, 209 – 242 (1986).

[23] F. Gonzlez, G. Videen, P. J. Valle, J. M. Saiz, J. L. de la Pea and F. Moreno. *Light scattering computational methods for particles on substrates.* Journal of Quantitative Spectroscopy and Radiative Transfer, **70**, 383 – 393 (2001).

[24] G. Videen. *Light scattering from a sphere on or near a surface.* J. Opt. Soc. Am. A, **8**, 483–489 (1991).

[25] E. M. Purcell and C. R. Pennypacker. *Scattering and Absorption of Light by Nonspherical Dielectric Grains.* Astrophys. J., **186**, 705 (1973).

[26] B. T. Draine and P. J. Flatau. *Discrete-dipole approximation for scattering calculations.* J. Opt. Soc. Am. A, **11**, 1491–1499 (1994).

[27] A. Taflove and S. C. Hagness. *Computational Electrodynamics: The Finite-Difference Time-Domain Method, Third Edition.* Artech House Publishers, 3 ed. (2005).

[28] J. Kupersztych, P. Monchicourt and M. Raynaud. *Ponderomotive acceleration of photoelectrons in surface-plasmon-assisted multiphoton photoelectric emission.* Phys. Rev. Lett., **86**, 5180–5183 (2001).

[29] S. E. Irvine, A. Dechant and A. Y. Elezzabi. *Generation of 0.4-keV Femtosecond Electron Pulses using Impulsively Excited Surface Plasmons.* Phys. Rev. Lett., **93**, 184801 (2004).

[30] S. E. Irvine and A. Y. Elezzabi. *Surface-plasmon-based electron acceleration.* Phys. Rev. A, **73**, 013815 (2006).

[31] S. E. Irvine, P. Dombi, G. Farkas and A. Y. Elezzabi. *Influence of the Carrier-Envelope Phase of Few-Cycle Pulses on Ponderomotive Surface-Plasmon Electron Acceleration.* Phys. Rev. Lett., **97**, 146801 (2006).

[32] P. Dombi *et al. Observation of few-cycle, strong-field phenomena in surface plasmon fields.* Opt. Express, **18**, 24206–24212 (2010).

[33] S. Zherebtsov *et al. Controlled near-field enhanced electron acceleration from dielectric nanospheres with intense few-cycle laser fields.* Accepted in Nature Physics (2011).

[34] M. Drescher, M. Hentschel, R. Kienberger, M. Uiberacker, V. Yakovlev, A. Scrinzi, T. Westerwalbesloh, U. Kleineberg, U. Heinzmann and F. Krausz. *Time-resolved atomic inner-shell spectroscopy.* Nature, **419**, 803–807 (2002).

[35] C. Lemell, B. Solleder, K. Tőkési and J. Burgdörfer. *Simulation of attosecond streaking of electrons emitted from a tungsten surface.* Phys. Rev. A, **79**, 062901 (2009).

[36] C.-H. Zhang and U. Thumm. *Attosecond Photoelectron Spectroscopy of Metal Surfaces.* Phys. Rev. Lett., **102**, 123601 (2009).

[37] J. C. Baggesen and L. B. Madsen. *Theory for time-resolved measurements of laser-induced electron emission from metal surfaces.* Phys. Rev. A, **78**, 032903 (2008).

[38] L. Miaja-Avila, G. Saathoff, S. Mathias, J. Yin, C. La-o vorakiat, M. Bauer, M. Aeschlimann, M. M. Murnane and H. C. Kapteyn. *Direct Measurement of Core-Level Relaxation Dynamics on a Surface-Adsorbate System.* Phys. Rev. Lett., **101**, 046101 (2008).

[39] A. L. Cavalieri *et al. Attosecond spectroscopy in condensed matter.* Nature, **449**, 1029–1032 (2007).

[40] A. M. Kern and O. J. F. Martin. *Surface integral formulation for 3D simulations of plasmonic and high permittivity nanostructures.* J. Opt. Soc. Am. A, **26**, 732–740 (2009).

8 Development of high repetition rate attosecond experiments

To date, attosecond experiments have been performed at repetition rates of several kHz or lower. A number of applications would greatly benefit by an significant increase of this repetition rate. In order to accomplish this, new methods for the generation of attosecond pulses need to be developed in which laser pulses with less pulse energy are used to generate the attosecond pulses. The first steps towards harmonic generation in the enhanced near field of a nanostructure as a source of attosecond pulses are described. A laser source that can deliver pulses with the required characteristics is not commercially available and is currently being developed. The laser system that is under construction is a non-collinear optical chirped pulse parametric amplifier (NOPCPA). The design of the system is described along with numerical simulations that support the possibility to obtain the required output characteristics. Finally, the progress on the construction of the laser is presented.

8.1 Introduction and motivation

In recent years high harmonic generation (HHG) has been established as an important source of coherent and bright extreme ultraviolet (XUV) radiation in different research areas. Most notable is the possibility to generate pulses with sub-fs pulse duration [1, 2] which form the basis of a new type of time-resolved experiments to study electron dynamics on attosecond timescales in atoms, molecules and on surfaces [3–5]. Apart from this, HHG sources have also been used to investigate molecular dynamics on femtosecond timescales such as the dissociation of a neutral molecule [6, 7] or molecular ion [8] and vibrational dynamics [9].

To obtain a good energy conversion efficiency from the fundamental laser to the XUV radiation, HHG requires intensities in the range of 10^{13}-10^{14} W/cm^2 in a loose focus [10] or hollow core waveguide [11, 12]. This requires fundamental pulse energies on the order of 1 mJ which results in XUV pulses with typically 10^6-10^8 photons per laser shot. With current laser technology this limits the maximum repetition rate of HHG sources to a few kHz. The number of photons of these kHz sources is too low to induce non-linear processes with high enough probabilities to be able to detect this in an experiment. Therefore, these pulses are unsuitable for attosecond-pump attosecond-probe experiments which have been performed with low repetition rate sources ($<$ 100 Hz) [13, 14]. However, by combining the XUV pulse with an IR laser field that is phase-locked to the attosecond pulse(s), attosecond resolution is

achieved by using the optical cycle of the IR as a subfemtosecond clock. Virtually all attosecond experiments to date use kHz HHG sources based on this idea [3, 4].

The generation of attosecond pulses by HHG in its most general form leads to the formation of attosecond pulse trains (APT) [2] with two attosecond pulses for each optical cycle of the driver pulse. However, isolated attosecond pulses [1] are often preferable in time-resolved pump-probe experiments. To generate isolated attosecond pulses, all the pulses in the APT need to be suppressed except one, which can be achieved by amplitude gating [15] or polarization gating [16–18]. Although methods exist that allow many-cycle laser pulses [19–21] to generate isolated attosecond pulses, few-cycle pulses are more efficient since fewer attosecond pulses need to be suppressed. In all cases the carrier envelope phase of the pulses needs to be stabilized and controlled [22].

Most attosecond experiments rely on the fact that each laser shot interacts with a large number of atoms or molecules, thereby averaging over the ensemble. In this way one can obtain good enough statistics with a kHz source in a reasonable amount of time. Such a configuration of the experiment does not form a limitation in many cases, although there are situations in which one would rather run the experiment at a significantly higher repetition rate, even if this happens to go at the expense of the number of photons per laser shot, by keeping the flux constant.

Experiments in which ions and electrons (or two electrons) from an ionization process are measured in coincidence would highly benefit from a high repetition rate XUV source (> 100 kHz). Coincidence techniques allow one to measure correlations between the properties of the two or more particles from an ionization event, often based on their three-dimensional velocity distribution. These experiments require a desig such that a maximum of one event per laser shot is detected, meaning that on average one detects even less than one event per shot. In this way it is ensured that the detected particles originate from the same object and false coincidences are prevented. The count rates in coincidence experiments are therefore set by the repetition rate of the experiment rather than the pulse energy of the laser. Multiple implementations of coincidence schemes are possible of which the 'reaction microscope' is particularly most widely spread [23]. At the moment, however, it is a very challenging method to perform such experiments since at the moderate repetition rates of current attosecond sources, extremely long acquisition times are required to get good enough statistics. At the same time each pulse is used rather inefficiently since often the number of photons per pulse is much larger than what is needed to get the desired ionization probability. A high repetition rate HHG source would therefore be very attractive for coincidence experiments, allowing much more detailed experimental studies than is currently possible. It is estimated that it is possible to run a coincidence experiment at repetition rates of up to a few 100 kHz before the speed at which the data acquisition can be performed is limiting the rate of the experiment.

Surface photoelectron XUV spectroscopy is another type of experiments that would benefit from a high repetition rate HHG source. Space charge effects limit the number of photons per pulse that can be used in these experiments. The current kHz HHG sources generate XUV pulses far beyond this space charge limit making it necessary to reduce the number of photons per pulse [24]. An increase of the

repetition rate would prevent the need for filtering the surplus of photons and thus make a more efficient use of the flux that is available. The chances of success for the experiments that are discussed in Chapter 7 are greatly enhanced if one could perform these at a repetition rate such that all XUV photons can be used efficiently. In these experiments there is not an upper limit for the repetition rate since most likely the detection will not be on a single-shot basis as in the case of coincidence experiments.

This chapter describes the ongoing work on the development of an attosecond XUV+IR experiment at high repetition rates in the range between 100 kHz and 1 MHz. Section 8.2 discusses the challenges of scaling HHG to higher repetition rates and lower pulse energies than currently is common in HHG sources. The first results on the method that is adopted in this work will be presented. In section 8.3 the development of a new laser source to drive the high repetition rate attosecond experiments is described. The design is discussed along with theoretical simulations and the first experimental results.

8.2 High repetition rate HHG

In HHG an intense laser field ionizes an atom in the gas medium, the free electron is accelerated by the laser field away and later towards the parent ion. Upon its return the electron has a finite chance to recombine with the ion while releasing the energy it has absorbed from the field during its trip outside the ion in the form of XUV photon [25]. Since this is a highly non-linear process, a high intensity is needed to achieve an efficient energy conversion from the fundamental to the high harmonic radiation. With the traditional methods of HHG, usually loose focussing in a gas medium [10], an increase of the repetition rate would require a proportional increase of the average power of the driver laser. This would significantly increase the complexity of the laser system. For many experiments it is also not necessary to keep the number of HHG photons per pulse constant. HHG with laser pulses with significantly lower pulse energies would thus be preferable. However, keeping a reasonable conversion efficiency is a challenge in HHG with low pulse energies.

HHG at low pulse energies

A natural way to scale the HHG process to lower pulse energies is to use a tight focus geometry. Indeed this has allowed the production of high harmonics with laser pulses of 7 μJ (100 kHz, 35 fs, 800 nm) [26]. Because of the influence of the focus conditions on the phase matching of the harmonic radiation, the conversion efficiency was low $< 10^{-9}$ compared to what can be obtained in a loose focus ($\approx 10^{-7}$) [10]. Later it was shown that the phase matching can be improved significantly by increasing the pressure at a pulse energy of 25 μJ (50 kHz, 45 fs, 800 nm) allowing a conversion efficiency of 10^{-8} [27].

Efficient HHG has also been achieved at high repetition rates (50-500 kHz) using the output of a Yb-doped fiber amplifier laser [28], and even at 1 MHz [29]. Typical pulse energies of these fiber amplifier systems are in the range between 50 and 400 μJ with pulse durations of 100-300 fs. The HHG conversion efficiencies that are

obtained are $10^{-11} - 10^{-9}$. The relatively long pulse durations makes them not an ideal source for attosecond experiments since the generation of isolated attosecond pulses will not be possible. An interesting alternative, also explored in [28], is to pump an Optical Parametric Chirped Pulse Amplifier (OPCPA) with a fiber amplifier laser to generate few-cycle pulses. With the output of the OPCPA a HHG conversion of $10^{-8} - 10^{-7}$ was obtained with a pulse energy of 53 μJ at a repetition rate of 96 kHz. Summarizing, HHG in a tight laser focus is possible with pulse energies of $> 25\mu$J but becomes more difficult at lower pulse energies. It is noted that HHG in a waveguide geometry [12] faces similar problems: phase matching becomes increasingly difficult at lower pulse energies because of the smaller mode size that is needed to reach the required intensity [27] although approaches based on hollow core photonic crystal fibers (HC-PCF) are being pursued [30, 31].

A completely different method is the use of a resonant enhancement cavity for the production of XUV light at high repetition rates [32, 33]. The XUV radiation is produced by HHG in the intra-cavity focus where a >100-fold enhancement of the intensity is reached with respect to a similar focus without a cavity. This technique has been developed for the generation of a frequency comb in the XUV at repetition rates of $>$ 100 MHz and meanwhile also demonstrated at 10.8 MHz [34]. To lower the repetition rate even further, the length of the cavity would need to be increased which will add serious experimental challenges to this already demanding technique.

A potentially simpler method to reach a similar enhancement of the intensity is to use the local field enhancement between the tips of a gold bow tie nanostructure acting as an optical antenna. Doing so resulted in HHG radiation with an efficiency of $\approx 10^{-9}$ using pulses at 80 MHz with a pulse energy of 1.3 nJ [35]. The laser intensity in the focus of 10^{11} W/cm^2 was locally enhanced by a factor of at least 100 and therefore high enough to produce high harmonics in an atomic gas injected by a needle that sprays the gas on the surface with the bow ties. These results are very promising and it is therefore chosen to investigate whether this can be a viable source for future attosecond experiments at high repetition rate. The progress on implementing this method in an attosecond XUV+IR experiment is described next.

Implementation of HHG using nanostructures

The proof-of-principle experiment in [35] was performed by focussing pulses of 1.3 nJ (75 MHz) to a spot size of 10 μm on a field of bow ties on a transparent substrate (Fig. 8.1c). The method can be scaled to higher pulse energies (at lower repetition rates) by increasing the area of the nano-structure and keeping the intensity constant. It is estimated that with a pulse energy of 1 μJ and an efficiency of 10^{-9}, sufficient XUV photons will be generated for the use in an experiment. To accommodate this pulse energy, bow tie nano-structures have been fabricated with areas of 300 $\times$ 300 μm by e-beam lithography (Fig. 8.1b). Fig. 8.1a shows a drawing of the experimental setup that was built to position the nano-structure in the laser beam and to inject the gas on the surface. The chamber will be attached to the detector chamber through a differentially pumped section to limit contamination from the HHG gas in the detector chamber.

Third harmonic generation (THG) was used as a test for the bow tie nanostructures that were fabricated. A small portion ($\approx 5\mu$J) of the output of 30 fs

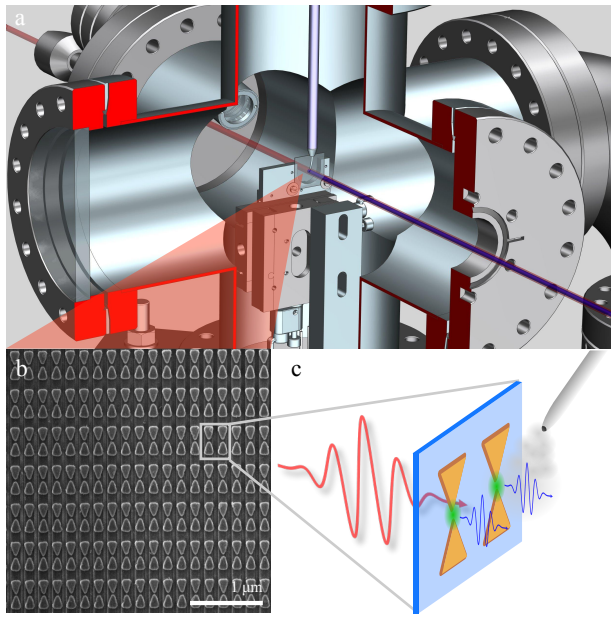

Figure 8.1: (a) Drawing of the vacuum chamber that is constructed to perform HHG on the bow tie nanostructure. The sample is positioned by two motorized translation stages. Gas is injected by the needle from the top. (b) SEM image of part of bow tie nanostructure fabricated by e-beam lithography, the entire array is 300 × 300 μm.(c) Schematic diagram showing the transparent sample illuminated from the back by the IR pulse creating high fields at the tips of the bow ties from where HHG takes place in the gas medium injected by the needle.

FWHM, 780 nm Ti:Sapphire laser amplifier at 3 kHz was focused to an intensity of 10^{11} W/cm^2 on the nanostructure which was positioned inside a static gas cell filled with Argon. By estimating the absorption cross-section an indication of the maximum heat load of found by assuming that all the absorbed power is turned into heat of the gold while it has enough time to cool down before the next pulse arrives. The extinction cross-section is assumed to be 6 times the geometrical cross-section of the gold. The ratio between the extinction and the absorption cross-section is estimated by comparing the typical bandwidth of the extinction spectrum with the width of the extinction spectrum if there would only be absorption (Drude damping). From this an absorption cross-section of σ_{abs} of $2{\cdot}10^4$ nm^2 was determined. With the used pulse characteristics this leads to a maximum temperature rise of 250 K. Although substantial, such a rise in temperature would not reach the melting point of gold. Efficient heat transfer to the substrate will alleviate the problems of thermal damage. It is also noted that for a fixed intensity shorter pulse durations will lead to a decrease in the absorbed energy and, therefore, smaller temperature effects.

The third harmonic radiation was filtered from the fundamental by dichroic mirrors and sent to a fiber coupled spectrometer. Doing these tests using the third

harmonic rather than higher order harmonics has the advantage that normal optical manipulation and detection techniques can be used that are not available for XUV radiation. In Fig. 8.2a a typical spectrum is shown and in 8.2b the polarization dependence of the third harmonic intensity is given. This polarization dependence proves that the THG is a result of the local field enhancement since the bow tie resonance is only excited when the polarization is parallel to bow tie axis. The dependence of the THG on the pressure in the cell was investigated to determine whether the THG took place in the gas medium or in the substrate or the gold. Unfortunately these tests were inconclusive because of the limited signal-to-noise ratio in the detection. Earlier experiments in a confocal geometry have demonstrated THG from a (single) bow tie antenna. In this earlier work the THG was attributed to a non-linear response of the gold [36]. However, the authors claim that this is quenched for fundamental photon energies above 1.1 eV. This suggests that the third harmonic emission in the current experiment is either from the substrate or from the gas because the fundamental photon energy was 1.56 eV (780 nm). The THG test demonstrates that the produced bow tie structures provide a field enhancement. To determine whether the higher harmonics are being generated as well, one needs to measure the spectrum with an XUV spectrometer.

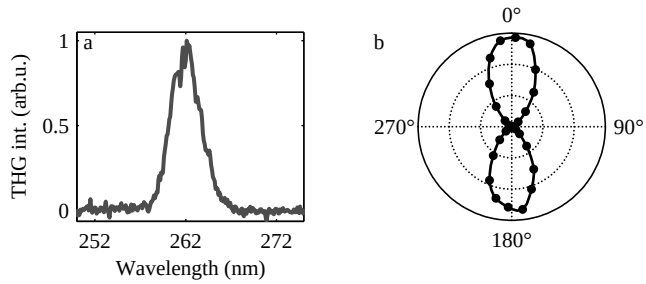

Figure 8.2: (a) Typical spectrum of THG from a bow tie nanostructure illuminated with a 780 nm, 30 fs FWHM laser pulse at an intensity of $9 \cdot 10^{10}$ W/cm^2. (b) Integrated intensity as a function of the angle between the polarization and the bow tie axis in polar plot.

8.3 Design and development of a high repetition rate laser source

8.3.1 Design considerations and targets

A schematic drawing of the two-colour attosecond setup being developed is given in Fig. 8.3. The drawing shows that the laser that will be used for the attosecond experiment at high repetition rates (100 kHz - 1 MHz) should not only be able to generate the attosecond pulses but at the same time provide enough energy for the IR pulse in an XUV+IR experiment. For the temporal characterization of the XUV pulses [37] and in experiments where attosecond electron dynamics is investigated,

the intensity of the IR pulse needs to be $> 10^{12}$ W/cm^2. With a spot size diameter on the order of 50 μm a pulse energy of approximately 1 μJ is needed for the IR pulse. To be able to generate isolated attosecond pulses the carrier-envelope-phase (CEP) of the pulses needs to be stabilized and the pulse durations should be as short as possible [15] and preferably in the few-cycle regime.

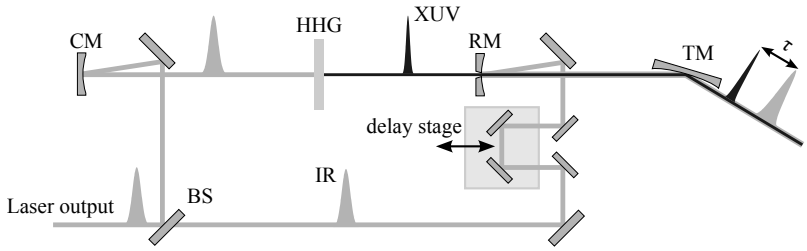

Figure 8.3: A schematic drawing of the high repetition rate XUV+IR setup that is being developed. The output of the laser is incident on a beamsplitter (BS) which splits the pulse into the two arms of a Mach-Zehnder interferometer. HHG takes place in one of the arms using the field enhancement in a nanostructure by focussing the beam with a curved mirror (CM) into the nanostructure. The XUV radiation that is produced is filtered and recombined (RM) with the other arm of the interferometer while the delay τ between the pulse is controlled by a translation stage. The beams are collinearly focused in the interaction chamber by a toroidal mirror (TM).

Laser sources commonly in use in attosecond experiments at kHz repetition rates are based on chirped pulse amplification (CPA) employing Ti:Sapphire as the gain material. Repetition rates of >100 kHz are achieved in continuously pumped regenerative amplifiers (see for example the Wyvern serie from KMLabs or the RegA serie of Coherent). These systems can deliver the required pulse energy at repetition rates of 200 kHz or more. However, the pulse duration is typically $\approx$ 50 fs and CEP stability forms a major challenge and remains unproven. Another option that was considered is the use of a long cavity oscillator (see for example the Femtosource XL from Femtolasers) but for these systems the repetition rate is typically $>$ 1 MHz and the pulse energy $<$1 μJ, although the development of a 1 MHz-1μJ version was recently accomplished by the introduction of cavity dumping [38]. However, these systems suffer from the same problems as the regenerative amplifiers: pulse durations are typically 50 fs and CEP stability is not available. These limitations do not exist for optical parametric amplifiers (OPA) [39]. In an OPA light pulses are amplified through the transfer of energy from one wavelength to another by non-linear interactions in a crystal. This has several advantages with respect to Ti:Sapphire systems where amplification is based on the storage of energy in the gain medium. For example, OPAs are usually free of thermal problems because no energy is stored in the crystal and parasitic spontaneous emission of light is typically much less of a problem in parametric amplifiers. Moreover, the principle of OPA offers great flexibility with respect to the wavelength of the amplified pulses. Systems have been designed to produce light pulses from the visible and NIR [40] to the mid-infrared [41–43]. The most important advantage for the current work is the large spectral gain bandwidths that can be obtained by adopting a non-collinear

geometry. Non-collinear OPAs (NOPA) support bandwidths large enough to allow the generation of few-cycle pulses in the visible or NIR [44, 45]. Optical parametric chirped pulse amplification (OPCPA) has been developed for the generation of high intensity laser pulses [46]. The combination of these techniques (NOPCPA) has led to the generation of few-cycle light pulses with pulse energies of >10 mJ [47–49], and, more recently, >100 mJ [50]. The Extreme Light Infrastructure (ELI) even aims to develop few-cycle pulses with pulse energies of a few J based on parametric amplification. Importantly, it has been shown that the CEP stability of the seed pulse in a parametric amplifier is preserved in the OPA [51]. More recently few-cycle OPCPA systems at high repetition rates and pulse energies of > 1 μJ have been reported [52–55]. This makes a parametric amplifier potentially an ideal candidate as the laser source for the high repetition rate attosecond experiment. The main disadvantage is that such a system is not commercially available and the ones reported in the literature have all been based on home-built pump lasers.

For the reasons mentioned above it was decided to develop the high-repetition laser based on a parametric amplifier. The basic idea for this laser is to amplify pulses from a commercial CEP-stabilized few-cycle Ti:Sapphire oscillator in a NOPCPA such that CEP-stable pulses with a duration of < 10 fs FWHM with a pulse energy of $> 1 - 2\mu$J are produced at a repetition rate of >100 kHz. In the next part of this section a more detailed introduction to OPAs is given together with simulations that support the possibility of generating the required pulse characteristics. The design of the laser system that is under construction is described and the last part shows the (preliminary) results and discusses the outlook of the system.

8.3.2 Phase matching and bandwidth considerations for a NOPCPA

This section will give a brief introduction to parametric amplifiers focussing on the phase matching conditions and the resulting gain bandwidth that can be achieved. In standard textbooks a more thorough background on non-linear optics can be found [56, 57] where also much of what is described here is covered. For a broader introduction to parametric amplifiers the reader is referred to the review by Cerullo and De Silvestri [39]. This section follows parts of the description given in the PhD-thesis by Stefan Witte [58].

In an OPA a pump pulse and a seed pulse are overlapped in a non-linear crystal in such a way that the energy of the pump pulse is transferred to two pulses at different wavelengths called the signal and idler (Fig. 8.4a) for which usually the convention is used that the wave with the shortest wavelength is the signal. Energy conservation requires that the sum of the photon energies of the signal and idler waves is equal to the photon energy of the pump ($\omega_p = \omega_s + \omega_i$) as is schematically illustrated in Fig. 8.4b.

Energy conservation allows for the generation of many possible combinations of signal and idler wavelengths. Which combination will be generated is determined by the requirement of constructive interference of the waves that are generated at different points along the propagation axis, i.e. the wave with frequency $\omega_{s,i}$

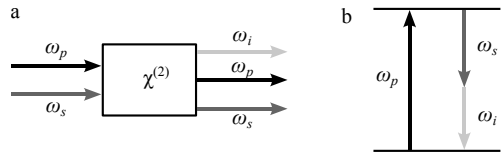

Figure 8.4: (a) Schematic illustration of parametric amplification in a non-linear medium ($\chi^{(2)}$). The energy of a strong pump wave at frequency ω_p is transferred to a weak signal wave at frequency ω_s, and the newly created third wave at frequency ω_i called the idler. (b) Energy conservation requires that the sum of the photon energies of the pump and idler waves is equal to the photon energy of the pump ($\omega_p = \omega_s + \omega_i$)

generated at $z + \Delta z$ needs to be in phase with the waves that are generated at z. Since the phase evolution upon propagation is given by $e^{-i\boldsymbol{k}\cdot\Delta\boldsymbol{z}}$ with $\boldsymbol{k}$ the wavevector, the phase mismatch in an OPA can be expressed as:

$$\Delta\boldsymbol{k} = \boldsymbol{k}_p - \boldsymbol{k}_s - \boldsymbol{k}_i \tag{8.1}$$

where $\boldsymbol{k}_p$, $\boldsymbol{k}_s$ and $\boldsymbol{k}_i$ are the wavevectors of the pump, signal and idler waves. Since the momentum of a photon is $\hbar\boldsymbol{k}$, phase matching is essentially a requirement of photon momentum conservation. Eq. 8.1 is a vector relation which simplifies when the beams are collinear, in which case the wavevectors $\boldsymbol{k}$ have the same direction as illustrated in Fig. 8.5a. The phase mismatch $\Delta\boldsymbol{k} = \Delta k\hat{\boldsymbol{z}}$ now becomes:

$$\Delta k = k_p - k_s - k_i = \frac{1}{c}\left[n(\omega_p)\omega_p - n(\omega_s)\omega_s - n(\omega_i)\omega_i\right] \tag{8.2}$$

with $n(\omega)$ the refractive index at frequency ω and c is the speed of light. This shows that phase-matching ($\Delta k = 0$) for a given set of central frequencies $\omega_{p,0}$, $\omega_{s,0}$ and $\omega_{i,0}$ puts strict constraints on the refractive indices for the three waves. Since usually the refractive index increases with frequency it is in general impossible to achieve phase-matching at arbitrary wavelengths. This is different for birefringent crystals for which the refractive index depends on the polarization of the wave. For example, in an uniaxial birefringent crystal (a crystal with a single optical axis) the refractive index depends on whether the polarization is perpendicular (ordinary wave) or parallel (extra-ordinary wave) to the plane that contains the optical axis and the propagation axis. The refractive index of the extra-ordinary wave is a function of the angle θ between the optical axis and the propagation axis $\boldsymbol{k}$. The relation is given by:

$$\frac{1}{n_e(\theta)^2} = \frac{\sin^2\theta}{\bar{n}_e^2} + \frac{\cos^2\theta}{n_o^2} \tag{8.3}$$

with $n_e(\theta)$ the effective refractive index for the extra-ordinary wave, $\bar{n}_e$ the extraordinary refractive index at $\theta = 90°$ (the quantity specified for a specific crystal) and n_o the refractive index for the ordinary wave which is independent of θ. The ellipsoid that is described by Eq. 8.3 is shown in Fig. 8.5b where $n_e(\theta)$ (gray line) and n_o (black line) are shown for an arbitrary negative uniaxial crystal ($\bar{n}_e < n_o$). The refractive index of an extraordinary wave thus can be tuned continuously between

$\bar{n}_e$ and n_o with the angle θ. For a negative uniaxial crystal an angle θ_{pm} can be found that achieves phase matching for an extraordinary narrowband pump and ordinary signal and idler (type-I eoo phase matching):

$$n_e(\omega_p, \theta_{pm})\omega_p = n_o(\omega_{s,0})\omega_{s,0} + n_o(\omega_{i,0})\omega_{i,0} \tag{8.4}$$

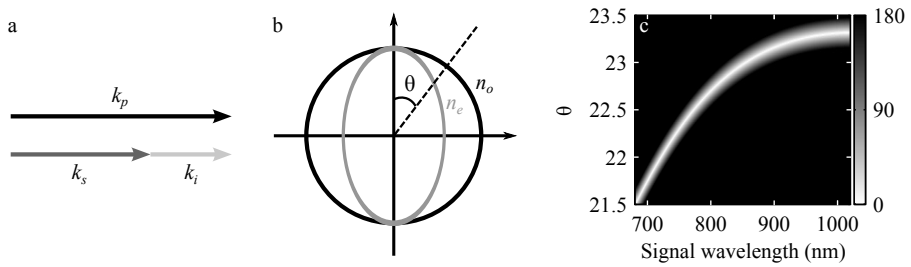

Figure 8.5: (a) Phase-matching in a collinear geometry is achieved when the wavevector of the pump has the same length as the sum of the wavevectors of the signal and idler wave. (b) Refractive index ellipse of a negative uniaxial crystal. The gray line shows the refractive index of the extraordinary wave ($n_e(\omega, \theta)$) for all values of θ which is the angle between the wavevector and the optic axis. (c) Momentum mismatch Δk (Eq. 8.4) in type-I eoo phase matching in BBO, as a function of signal wavelength and phase matching angle θ in degrees per mm crystal length. Phase matching ($\Delta k = 0$) is achieved in the white region, for a specific angle θ the bandwidth for phase matching is insufficient to support few-cycle pulses.

Since laser pulses by definition have a finite spectral bandwidth it is important to consider what the effective gain bandwidth is. Especially for few-cycle pulses large bandwidths (> 100 nm) are required. Eq. 8.4 shows that phase matching can be achieved in a collinear OPA at the central frequency, but it does not elucidate the bandwidth of the amplification. This bandwidth is limited by a non-zero momentum mismatch Δk for frequencies other than the central frequencies $\omega_{s,0}$ and $\omega_{i,0}$. This mismatch can be expanded in frequency at the signal frequency $\omega_{s,0}$:

$$\Delta k \approx \Delta k_0 + \frac{\partial \Delta k}{\partial \omega_s}\Delta\omega_s + \frac{1}{2}\frac{\partial \Delta^2 k}{\partial \omega_s^2}\Delta\omega_s^2 + ... \tag{8.5}$$

where $\Delta\omega_s = \omega_s - \omega_{s,0}$ and $\Delta k_0 = k_p - k_{s,0} - k_{i,0}$ is the momentum mismatch at the central frequencies ($k_{s,0} = n(\omega_{s,0})\omega_{s,0}/c$). Eq. 8.5 shows that in a collinear geometry the gain bandwidth is determined by the wavelength dependence of the refractive indices of the material. In Fig. 8.5c the momentum mismatch Δk is plotted as a function of signal wavelength and crystal angle θ for a pump wavelength of 515 nm. This shows that phase matching (white region) can be achieved over the entire region of wavelengths but not at a single angle θ. The phase matching bandwidth at a specific θ in a collinear OPA is not large enough to support the amplification of few-cycle pulses.

To optimize the bandwidth of phase matching, the leading term in the expansion in Eq. 8.5 ($\frac{\partial \Delta k}{\partial \omega_s}$) should be minimized since this has the largest effect on the mismatch. However, with only the phase matching angle θ_{pm} as a tuning parameter,

it is not possible to control this term without affecting Δk_0. Therefore an additional control parameter is needed with which $\frac{\partial \Delta k}{\partial \omega_s}$ can be minimized while keeping $\Delta k_0 = 0$. This can be achieved by introducing a non-collinear angle α between the signal and the pump wave as is illustrated in Fig. 8.6a and Fig. 8.6c. The two figures show the two possibilities to implement a non-collinear angle α and phase matching angle θ. The differences between the two cases will be explained later. The vector relation of the momentum mismatch in Eq. 8.1 can be written in its components parallel $\Delta k_\parallel$ and perpendicular $\Delta k_\perp$ to the signal wavevector:

$$\begin{aligned} \Delta k_\parallel &= k_p \cos\alpha - k_i \cos\beta(\omega_s) - k_s \\ \Delta k_\perp &= k_p \sin\alpha - k_i \sin\beta(\omega_s) \end{aligned} \tag{8.6}$$

where $\beta(\omega_s)$ is the frequency-dependent angle between the idler and signal. To achieve phase matching both $\Delta k_\parallel$ and $\Delta k_\perp$ should vanish. Because of the wavelength dependence of the wavevector direction of the idler there is not a unique α for which phase matching occurs. The optimum angles α and $\beta(\omega_{s,0})$ are found by minimizing the wavelength dependence of $\Delta k_\parallel$ and $\Delta k_\perp$ at the central frequencies. Doing so, leads to the minimization of the most important contribution to the phase mismatch, as expressed in Eq. 8.5. Differentiating Eq. 8.7 gives:

$$\begin{aligned} \frac{\partial \Delta k_\parallel}{\partial \omega_s} &= -\cos\beta(\omega_s)\frac{\partial k_i}{\partial \omega_s} + k_i \sin\beta(\omega_s)\frac{\partial \beta(\omega_s)}{\partial \omega_s} - \frac{\partial k_s}{\partial \omega_s} \\ \frac{\partial \Delta k_\perp}{\partial \omega_s} &= -\sin\beta(\omega_s)\frac{\partial k_i}{\partial \omega_s} - k_i \cos\beta(\omega_s)\frac{\partial \beta(\omega_s)}{\partial \omega_s} \end{aligned} \tag{8.7}$$

in which it was used that the wave vector of the pump does not depend on the frequency of the signal ($\partial k_p / \partial \omega_s = 0$). The condition for phase matching is given by:

$$\frac{\partial \Delta k_\parallel}{\partial \omega_s}|_{\omega_{s,0}} = 0, \; \frac{\partial \Delta k_\perp}{\partial \omega_s}|_{\omega_{s,0}} = 0 \tag{8.8}$$

The solution of which yields the angle $\beta(\omega_{s,0})$. This solution is found by adding the two expressions after multiplying the first equation by $\cos\beta(\omega_{s,0})$ and the second by $\sin\beta(\omega_{s,0})$, which gives:

$$\left.\frac{\partial k_s}{\partial \omega_s}\right|_{\omega_{s,0}} \cos\beta(\omega_{s,0}) + \left.\frac{\partial k_i}{\partial \omega_s}\right|_{\omega_{s,0}} = 0 \tag{8.9}$$

This can also be written in terms of the group velocities ($v_g = (\partial k / \partial \omega)^{-1}$) of the signal and idler wave:

$$v_g(\omega_{s,0}) = v_g(\omega_{i,0}) \cos\beta(\omega_{s,0}) \tag{8.10}$$

This shows that an optimal bandwidth is obtained when the group velocities of the signal and idler in the direction of the signal are matched. The group velocity is the velocity with which the pulses propagate through the crystal. The condition in Eq. 8.10 guarantees that signal and idler travel at the same speed in the direction

of the signal (no *temporal walk-off*). The absence of temporal walk-off ensures a large bandwidth over which phase matching is achieved. With the angle $\beta(\omega_{s,0})$ at the central frequency and by using Eq. 8.7 the non-collinear angle α can be found by solving for $\Delta k_{\parallel,0} = 0$ and $\Delta k_{\perp,0} = 0$. This also yields the required refractive index $n_e(\omega_p)$ for which phase matching is achieved, from which the optimized phase matching angle θ_{pm} can be determined with Eq. 8.3. The wavelength dependence of the angle between the idler and the signal ($\cos\beta(\omega_s)$) is found by solving for $k_\perp(\omega_s) = 0$ for all frequencies ω_s.

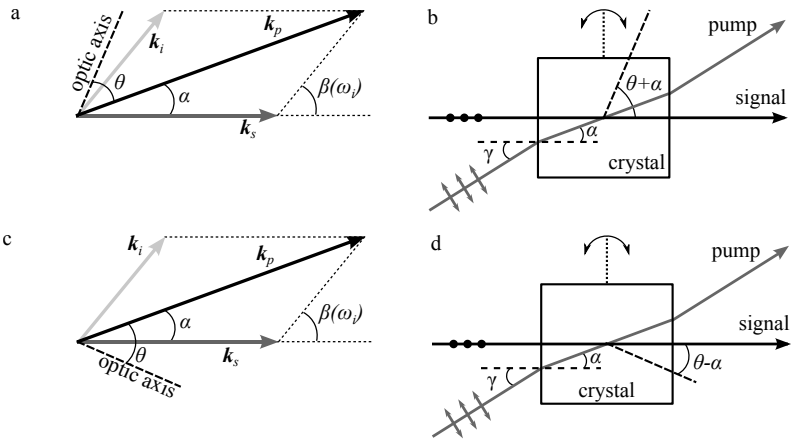

Figure 8.6: (a) Phase matching (Eq. 8.1) in the non-collinear geometry with the non-collinear angle α going from the pump away from the optic axis. (b) Non-collinear geometry from (a) implemented in type-I eoo phase matching in which the signal wave is perpendicular to the face of the crystal. The pump (signal) wave is polarized in parallel (perpendicular) to the plane of the drawing. The angle γ between the signal and pump beam is given by $\sin\gamma = n_e(\omega_p, \theta)\sin\alpha$. The crystal should be cut at $\theta + \alpha^\circ$ for this configuration. (c) Same as in (a) but with the non-collinear angle α chosen going from the pump towards the optic axis. (d) Same as in (b) but for the situation in (c). In this configuration the crystal should be cut at $\theta - \alpha$. The situation in (a,b) is preferred because of *spatial walk-off*. (see text for details).

In Fig. 8.7a the resulting momentum mismatch $k_\parallel$ is plotted as a function of signal wavelength and crystal angles θ for a non-collinear angle $\alpha = 2.5^\circ$. Comparing this to Fig. 8.5c shows that the bandwidth over which phase matching can be achieved is much larger than in the collinear case. Fig. 8.7b shows a similar plot but now as a function of the non-collinear angle α and for a crystal angle of $\theta = 24.45^\circ$.

The non-collinear angle α is the angle between the pump and the signal *inside* the crystal. In Fig. 8.6b and Fig. 8.6d the angles are drawn with respect to the crystal faces in the situation where the signal is perpendicular to the face of the crystal for the situation in Fig. 8.6a and Fig. 8.6c respectively. A signal beam that is perpendicular to the crystal face prevents angular dispersion, and consequently spatial chirp, of the broadband signal beam by refraction in the crystal. The *external* angle between the pump and the signal γ is given by $\sin\gamma = n_e(\omega_p, \theta)\sin\alpha$. This gives $\gamma = 4.1^\circ$ for type-I eoo phase matching in BBO with a pump wavelength

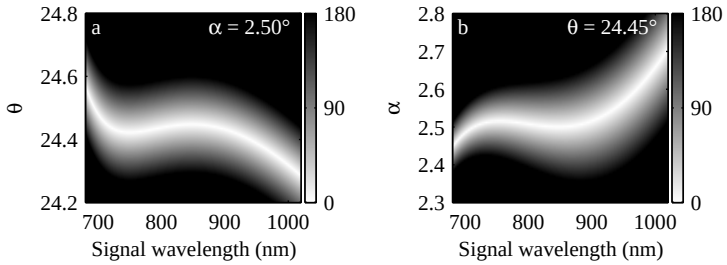

Figure 8.7: (a) Momentum mismatch $\Delta k_{\parallel}$ as a function of θ and signal wavelength in type-I eoo phase matching with a non-collinear angle of $\alpha = 2.5^{\circ}$ in units of degrees/mm crystal length. (b) Same plot as in (a) but now as a function of non-collinear angle α for $\theta = 24.45^{\circ}$. Both plots show that phase matching over a large bandwidth (700-950 nm) can be achieved in a non-collinear geometry.

of 515 nm and a signal central wavelength of 800 nm respectively ($\alpha = 2.5^{\circ}$ and $\theta = 24.45^{\circ}$).

The main difference between the cases in Fig. 8.6a and Fig. 8.6b is the way the crystal should be cut. The cutting angle is the angle between the optic axis and the face of the crystal. When the signal is perpendicular to the entrance face of the crystal, this cutting angle should be either $\theta + \alpha$ (Fig. 8.6b) or $\theta - \alpha$ ((Fig. 8.6d)). For $\alpha = 2.5^{\circ}$ and $\theta = 24.45^{\circ}$ this means 22° and 27°. The two situations are similar but not identical because of *spatial walk-off*. In a birefringent crystal there can be a small angle between the intensity distribution and the wavevector for the extraordinary wave. This walk-off angle ρ is given by:

$$\rho = -\frac{1}{n_e}\frac{\partial n_e(\theta)}{\partial \theta} \tag{8.11}$$

where the minus sign indicates that the walk-off is in the direction where the refractive index $n_e(\theta)$ decreases. In the NOPA situation considered here the walk-off angle is $\rho \approx 3.3^{\circ}$. Because it is a negative uniaxial crystal the pump beam drifts off away from its wavevector towards larger values of θ. This means that in the situation in Fig. 8.6b the walk-off is towards the signal beam whereas in Fig. 8.6d the walk-off is away from the signal beam (see Fig. 8.6b). The situation in Fig. 8.6b is therefore preferred, since the walk-off is expected to compensate for the loss of overlap between the pump and the signal beam due to the angle between the wavevectors of the beams. This will be especially important for systems with low pulse energies like the one described here where, due to tight focussing of the beams, the loss of spatial overlap is an important limitation.

The remaining mismatch in the non-collinear geometry depends on the higher order terms in Eq. 8.5. Additional degrees of freedom are necessary to minimize these terms. For example, the use of multiple pump beams [59, 60], an angularly dispersed seed [61, 62], or an angularly dispersed pump [45, 44] can all increase the bandwidth of amplification beyond what is possible in a standard NOPA geometry. However, experimentally these modifications are challenging and for the current work the potential bandwidth of a standard NOPA is considered to be sufficient.

8.3.3 Numerical simulations of a NOPCPA

In order to estimate what can be expected for the potential output of the NOPCPA system numerical simulations are performed. The model is based on what is described in refs. [63, 58, 64] where simulations are described for a low repetition rate (50 Hz) multi-stage terawatt-intensity NOPCPA. The current work aims to develop a NOPCPA with lower pulse energies and at higher repetition rates and therefore this system will necessarily need to be constructed differently from those low repetition rate systems.

A large part of this section is devoted to the derivation of the formulas describing the pulse propagation and non-linear interaction in a parametric amplification process. In the simulations a split operator method is employed to take advantage of the fact that the non-linear interaction is easier calculated in the time-domain whereas the linear propagation and dispersion operator takes its simplest form in the frequency domain. To this end the derivation presented here will finally arrive at the two operators given respectively in Eqs. 8.32 and 8.25 for the linear propagation in the frequency domain and the non-linear interaction in the time domain, both in terms of a slowly varying envelope function. The model describes the propagation in one dimension, which is chosen to be along the wavevector of the signal. Therefore, the loss of overlap because of the angles between the different beams and spatial walk-off is not included. A further discussion of this assumption is left for the end of this section. The simulation results in the second part of the section can be understood without the following derivation. The derivation is presented for completeness and it can be skipped if wanted.

Derivation of the operator equations

Optical waves are described by their electric fields $\mathbf{E}(\mathbf{r},t)$ with $\mathbf{r}$ the position- and t the time-coordinate. The equations will be given for the signal wave (indicated by a subscript s) only since often the equations describing the pump and idler are identical. Only at places where differences between the signal, pump and idler arise, all three waves will be described explicitly. Wave propagation in a medium is described by the following wave equation [56, 65] describing the electric field:

$$\nabla^2\mathbf{E}_s(\mathbf{r},t) - \frac{1}{c^2}\frac{\partial^2\mathbf{E}_s(\mathbf{r},t)}{\partial t^2} = \mu_0\frac{\partial^2\mathbf{P}_s^L(\mathbf{r},t)}{\partial t^2} + \mu_0\frac{\partial^2\mathbf{P}_s^{NL}(\mathbf{r},t)}{\partial t^2} \tag{8.12}$$

where μ_0 is the magnetic permeability of vacuum. The effect of the medium can be recognized in the right hand side where $\mathbf{P}^L(\mathbf{r},t)$ and $\mathbf{P}^{NL}(\mathbf{r},t)$ represent a linear and non-linear polarization of the medium by the electric field. These induced polarizations act as a source term for electric fields with which the incoming wave interferes. This interference results in dispersion (linear) and phase matching of new frequencies (non-linear).

The simulations are performed in one-dimension for reasons of simplicity. This means that the waves are assumed to be plane waves (no radial dependence) traveling in the z-direction for which the wave equation reads:

$$\left(\frac{\partial^2}{\partial z^2} - \frac{1}{c^2}\frac{\partial^2}{\partial t^2}\right)E_s(t,z) = \mu_0\frac{\partial^2 P_s^L(t,z)}{\partial t^2} + \mu_0\frac{\partial^2 P_s^{NL}(t,z)}{\partial t^2} \tag{8.13}$$

It is convenient to work with a complex electric field. First the Fourier transform of the real electric field is given by:

$$\tilde{E_s}(\omega_s, z) = \mathcal{F}\{E_s(t,z)\} = \int_{-\infty}^{\infty} dt\ E_s(t,z)e^{-i\omega_s t} \tag{8.14}$$

where ω_s is the angular frequency of the signal (note that ω_s is not the central frequency which will be defined later as $\omega_{s,0}$). The Fourier transform of the real electric field results in a complex field in the frequency domain $\tilde{E_s}(\omega_s, z)$ (tildes are used to denote complex quantities) for which $\tilde{E_s}(\omega_s, z) = \tilde{E_s}^*(-\omega_s, z)$ holds. The complex electric field in the time domain is obtained by the inverse Fourier transform of the complex electric field $\tilde{E_s}^+(t,z)$ at the positive frequencies:

$$\tilde{E_s}^+(t,z) = \mathcal{F}^{-1}\{\tilde{E_s}(\omega_s, z)\} = \frac{1}{2\pi}\int_0^{\infty} d\omega_s\ \tilde{E_s}(\omega_s, z)e^{i\omega_s t} \tag{8.15}$$

In the rest of the text the complex field $\tilde{E_s}^+(t,z)$ will be used but the + superscript will be dropped. The real electric field is obtained from the complex electric field by:

$$E_s(t,z) = \tilde{E_s}(t,z) + c.c. = 2\Re\{\tilde{E_s}(t,z)\} \tag{8.16}$$

which shows that the wave equation in Eq. 8.13 can be written as:

$$\left(\frac{\partial^2}{\partial z^2} - \frac{1}{c^2}\frac{\partial^2}{\partial t^2}\right)\tilde{E_s}(t,z) + c.c. = \mu_0\frac{\partial^2 P_s^L(t,z)}{\partial t^2} + \mu_0\frac{\partial^2 P_s^{NL}(t,z)}{\partial t^2} \tag{8.17}$$

The splitting of the induced polarization in a linear and non-linear term will now be used to separately derive the linear and non-linear operators used in the split-operator scheme that is used in the simulations. The full solution to the wave equations including both terms can be found in ref. [64]. First the non-linear interaction is discussed. The wave equation in Eq. 8.17 is Fourier transformed to the frequency domain using $\mathcal{F}\left\{\frac{\partial^n f(t)}{\partial t^n}\right\} = (i\omega)^n\mathcal{F}\{f(t)\}$ and first the non-linear polarization P_{NL} is included.

$$\left(\frac{\partial^2}{\partial z^2} + \frac{\omega_s^2}{c^2}\right)\tilde{E_s}(\omega_s, z) = -\omega_s^2\mu_0\tilde{P}_{NL}(\omega_s) \tag{8.18}$$

The interaction between the pump, signal and idler wave in a parametric amplifier is governed by a second order non-liner interaction ($\chi^{(2)}$). The second order non-linear polarization induced by mixing of the pump and the idler waves is given by [65, 56]:

$$P_s^{NL}(t) = \epsilon_0\int_{-\infty}^{\infty}\int_{-\infty}^{\infty}\chi^{(2)}(t-t', t-t'')E_p(t-t')E_i(t-t'')dt'dt'' \tag{8.19}$$

where $\chi^{(2)}$ is the effective second order susceptibility and ϵ_0 is the electric permittivity of vacuum. Eq. 8.19 can be written terms of the complex fields $\tilde{E_p}(t)$ and

$\tilde{E}_i(t)$ (leaving out the time-dependencies)

$$\begin{aligned} P_s^{NL}(t) &= \epsilon_0 \iint \chi^{(2)}(\tilde{E}_p + \tilde{E}_p^*)(\tilde{E}_i + \tilde{E}_i^*)dt'dt'' \\ &= \epsilon_0 \iint \chi^{(2)}\tilde{E}_p\tilde{E}_i dt'dt'' + c.c. \\ &+ \epsilon_0 \iint \chi^{(2)}\tilde{E}_p\tilde{E}_i^* dt'dt'' + c.c. \end{aligned} \tag{8.20}$$

The first term in this equation causes sum-frequency generation whereas the second term is the part that is responsible for the generation of the signal wave. This shows that the source term for the signal wave depends on the field strength of the pump E_p and idler E_i waves. The non-linear interaction is assumed to be an instantaneous response of the material. With this assumption the complex non-linear polarization term responsible for the generation of the signal, idler and pump become:

$$\begin{aligned} \tilde{P}_s^{NL}(t) &= \epsilon_0\chi^{(2)}\tilde{E}_p(t)\tilde{E}_i^*(t) \\ \tilde{P}_i^{NL}(t) &= \epsilon_0\chi^{(2)}\tilde{E}_p(t)\tilde{E}_s^*(t) \\ \tilde{P}_p^{NL}(t) &= \epsilon_0\chi^{(2)}\tilde{E}_s(t)\tilde{E}_i(t) \end{aligned} \tag{8.21}$$

The wave equation in Eq. 8.18 is Fourier transformed back to the time domain for only the positive frequencies yielding:

$$\frac{\partial^2}{\partial z^2}\tilde{E}_s(t,z) + \frac{\omega_s^2}{c^2}\tilde{E}_s(t,z) = -\omega_s^2\mu_0\tilde{P}_s^{NL}(t,z) = -\frac{\omega_s^2}{c^2}\chi^{(2)}\tilde{E}_p(t)\tilde{E}_i^*(t) \tag{8.22}$$

Next an envelope function $\tilde{\mathcal{E}}_j(t,z)$ is introduced which is slowly varying in space and time:

$$\tilde{E}_s(t,z) = \tilde{\mathcal{E}}_s(t,z)e^{-i(\boldsymbol{k}_{s,0}\cdot\boldsymbol{z}-\omega_{s,0}t)} \tag{8.23}$$

For each wave in the process one can now find an equation describing the generation (or depletion) in the propagation through the crystal in terms of their slowly varying envelopes. This is done by using the slowly varying wave approximation:

$$\left|\frac{\partial^2\tilde{\mathcal{E}}_s(t,z)}{\partial z^2}\right| \ll \left|2ik_s\frac{\partial\tilde{\mathcal{E}}_s(t,z)}{\partial z}\right| \tag{8.24}$$

The result is a system of three coupled wave equations describing the non-linear interaction between the signal, idler and pump pulses:

$$\begin{aligned} \frac{\partial\tilde{\mathcal{E}}_s(t,z)}{\partial z} &= -i\frac{\chi^{(2)}\omega_{s,0}}{2n_sc}\tilde{\mathcal{E}}_p(t,z)\tilde{\mathcal{E}}_i^*(t,z)e^{-i\Delta\boldsymbol{k}_0\cdot\Delta\boldsymbol{z}} \\ \frac{\partial\tilde{\mathcal{E}}_i(t,z)}{\partial z} &= -i\frac{\chi^{(2)}\omega_{i,0}}{2n_ic}\tilde{\mathcal{E}}_p(t,z)\tilde{\mathcal{E}}_s^*(t,z)e^{-i\Delta\boldsymbol{k}_0\cdot\Delta\boldsymbol{z}} \\ \frac{\partial\tilde{\mathcal{E}}_p(t,z)}{\partial z} &= -i\frac{\chi^{(2)}\omega_{p,0}}{2n_pc}\tilde{\mathcal{E}}_s(t,z)\tilde{\mathcal{E}}_i(t,z)e^{i\Delta\boldsymbol{k}_0\cdot\Delta\boldsymbol{z}} \end{aligned} \tag{8.25}$$

where $\Delta \boldsymbol{k}_0 \cdot \Delta \boldsymbol{z} = \Delta k_{\parallel,0} \Delta z$ is the inner product of the momentum mismatch vector and the step $\Delta \boldsymbol{z}$ in the propagation direction at the central frequencies. This momentum mismatch disappears when phase-matching conditions are chosen such that there is perfect phase-matching at the central frequencies $\omega_{s,0}$ and $\omega_{i,0}$. The non-linear nature of the process is recognized in the fact that the magnitude of the operator terms depend on the product of the field strengths of the two other waves.

The linear polarization term which is responsible for dispersion effects in the medium is given by [65]:

$$P_s^L(t,z) = \epsilon_0 \int_{-\infty}^{\infty} dt' \; \chi(t-t') E_s(t',z) \tag{8.26}$$

this time convolution is a simple product in the frequency domain. Fourier transforming yields:

$$\tilde{P}_s^L(\omega_s, z) = \epsilon_0 \chi(\omega_s) \tilde{E}_s(\omega_s, z) \tag{8.27}$$

The wave equation in Eq. 8.13 is again Fourier transformed as before but now the non-linear part is left out and only the linear polarization of Eq. 8.27 is used:

$$\left(\frac{\partial^2}{\partial z^2} + \frac{\omega_s^2}{c^2}(1 + \chi(\omega_s)) \right) \tilde{E}_s(\omega_s, z) = 0 \tag{8.28}$$

The solution of this equation can be found directly and gives an expression for the propagation of the wave in the frequency domain:

$$\tilde{E}_s(\omega_s, z) = \tilde{E}_s(\omega_s, z_0) e^{-i \boldsymbol{k}_s \cdot \Delta \boldsymbol{z}} = \tilde{E}_s(\omega_s, z_0) e^{-i \frac{\omega_s}{c} n_s(\omega_s) \Delta z} \tag{8.29}$$

where $\Delta \boldsymbol{z} = \boldsymbol{z} - \boldsymbol{z_o} = \Delta z \hat{\boldsymbol{z}}$ is the distance of travel and $\boldsymbol{k}_s$ and $n_s(\omega_s)$ are the wavelength dependent wavevector and refractive index. Note that in the second equality the z-axis is chosen along the wavevector of the signal. With that choice the angles with respect to the z-axis have to be taken into account in the corresponding expressions for the idler and pump waves. Eq. 8.29 describes wave propagation in a linear medium and includes all orders of dispersion. This is the reason that the calculation of linear dispersion is straightforward in the frequency domain whereas in the time domain it is rather involved and only a limited number of dispersion orders can be taken into account.

Again, an envelope function $\tilde{\mathcal{E}}(\omega_s, z)$ can be introduced, now in the frequency domain and slowly varying in space:

$$\tilde{E}_s(\omega_s, z) = \begin{cases} \tilde{\mathcal{E}}_s(\omega_s - \omega_{s,0}, z) e^{-i \boldsymbol{k}_{s,0} \cdot \boldsymbol{z}} & \text{for } \omega_s > 0 \\ \tilde{\mathcal{E}}_s^*(\omega_s - \omega_{s,0}, z) e^{i \boldsymbol{k}_{s,0} \cdot \boldsymbol{z}} & \text{for } \omega_s < 0 \end{cases} \tag{8.30}$$

where $\boldsymbol{k}_{s,0}$ is the signal wavevector for $\omega_s = \omega_{s,0}$. Note that the envelope function $\tilde{\mathcal{E}}_s(\Delta\omega_s, z)$ is centered around zero. The envelope functions in the frequency and time domain are connected through a Fourier transform:

$$\tilde{\mathcal{E}}_s(t,z) = \frac{1}{2\pi} \int_{-\infty}^{\infty} d\Delta\omega_s \; \tilde{\mathcal{E}}_s(\Delta\omega_s, z) e^{i(\Delta\omega_s, z)t} \tag{8.31}$$

Propagation of the envelope in a linear medium is given by:

$$\tilde{\mathcal{E}}_s(\Delta\omega_s, z) = \tilde{\mathcal{E}}_s(\Delta\omega_s, z_0)e^{-i[\boldsymbol{k}_s - \boldsymbol{k}_{s,0}]\cdot\Delta\boldsymbol{z}} = \tilde{\mathcal{E}}_s(\Delta\omega_s, z_0)e^{-i\delta\boldsymbol{k}_s\cdot\Delta\boldsymbol{z}} \tag{8.32}$$

This is the last result that is needed for the numerical simulations. Next, the implementation of the linear and non-linear operator in the split operator model is discussed.

Implementation of the split operator model

As was mentioned at the beginning of this section, linear dispersion takes a simple form in the frequency domain (Eq. 8.32) whereas the non-linear interaction is easier calculated in the time domain (Eq. 8.25). In the split operator method that is adapted in the simulations the crystal length L is divided in N slices of thickness d such that $L = Nd$. For each slice first the linear operator is applied, the envelopes in the time domain are Fourier transformed to the frequency domain using Eq. 8.31, propagation in the frequency domain is performed by Eq. 8.32 and the result is Fourier transformed back to the time domain. Next, the non-linear operator of Eg. 8.25 is used to make the step of length d through the crystal again. The set of coupled differential equations is numerically solved by a fourth-order Runga-Kutta method [66]. Convergence of the complete simulation is checked by ensuring that the outcome of the calculation does not depend on N.

Results of the simulations

Figure 8.8a shows the evolution of the spectrum of the signal during the amplification in the crystal as a function of travel distance. The pulse energy of the signal is 3.9 μJ after amplification in the 4 mm crystal and the spectrum supports a bandwidth limited pulse duration of 7.5 fs. The pump pulse parameters correspond to a 500 fs pulse of 25 μJ focused to a waist diameter of 800 μm. The modulation in the spectrum can be understood from the evolution of the temporal intensity profile of the pump pulse in Fig. 8.8b. After propagation of 2 mm in the crystal the pump pulse becomes depleted at the position where it overlaps with the part of the spectrum of the stretched pulse that corresponds to the central region of the phase matching bandwidth. These saturation effects are the origin of the modulation in the spectrum and significantly broaden the spectrum of the signal. It shows that it is important to reach into this saturation regime in order to generate bandwidths that support few-cycle pulses.

Saturation can be reached with different combinations of pump intensity and crystal length. The higher the intensity of the pump the faster the signal builds up and the pump depletes. Therefore, one can use shorter crystals with higher intensities. In Fig. 8.9 three different combinations of pump intensity and crystal length are compared. The highest intensity and corresponding shortest crystal length (black lines) leads to highest pulse energy and largest bandwidth. This shows that it is advantageous to use an intensity that is as high as possible. The B-integral and the damage threshold of the crystal are limiting the intensity that can be used [63]. The B-integral is a characteristic measure for non-linear effects due to the

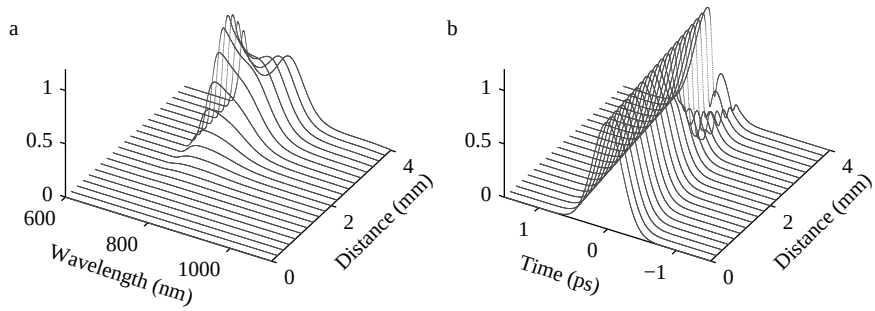

Figure 8.8: Evolution of the signal spectrum (a) and intensity profile of the pump (b) during propagation in a BBO crystal with $\theta = 45.45°$ and $\alpha = 2.5°$. The pump wavelength is 515 nm has a pulse duration of 500 fs FWHM and has a peak intensity of 9.8 GW/cm^2 with a waist of 390 μm (pulse energy is 25 μJ). The signal input is a 5 fs pulse stretched to 110 fs and has a peak intensity of $3.5{\cdot}10^6$ W/cm^2 (same waist as pump, pulse energy 2 nJ) and after 4 mm has a pulse energy of 3.9 μJ. The spectral shape of the signal is due to depletion of the pump pulse at the position where the pump overlaps with the part of the stretched seed pulse that corresponds to the central region of the phase matching bandwidth. Due to this depletion the wings of the signal spectrum are enhanced with respect to the central part and the signal spectrum becomes modulated.

non-linear refractive index n_2[1]. To prevent effects like self-focusing one normally requires the B-integral to be smaller than 1. For a BBO crystal with a length of 1 mm the B-integral equals to 1 for an intensity of 110 GW/cm^2, when the crystal is 5 mm the threshold intensity is down to 25 GW/cm^2.

The combination of a high intensity >10 GW/cm^2 and a low pulse energy (because of the high repetition rate) demand a short pulse duration ($\approx$ 1 ps). This has important consequences for the synchronization of the seed and pump laser as will be discussed in the next section.

The stretch factor of the signal input also has an important influence on the properties of the output of the amplifier. The optimum ratio between the pulse duration of the seed and the pump, forms a trade-off between gain and gain bandwidth. The pulse duration of the seed necessarily needs to be shorter than that of the pump. If this is not the case the wings of the signal pulse will not be overlapped with the pump pulse and therefore they will not be amplified. Similarly, when the pulse duration of the signal is comparable to the pulse duration of the pump the wings of the seed will experience a significantly lower gain that the central part. The seed pulses are stretched which means that the wings of the temporal profile correspond to the wings of the spectral profile. When the wings of the seed overlap with the wings of the pump pulse this results in a substantial lower gain for the (spectral) wings compared to the center and therefore a substantial narrowing of the bandwidth. On the other hand, when the duration of the seed pulses is only a fraction of the pump pulse duration, the gain is more constant over the spectrum. However, in this situation the energy of the pump pulse is used less efficiently because

[1] n_2 of BBO for 532 nm light is 7.4 $\cdot 10^{-16}$ cm^2/W [67]

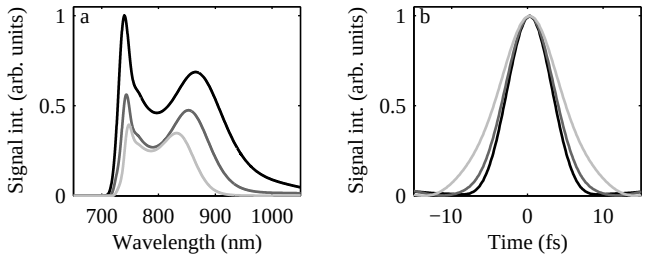

Figure 8.9: Spectrum (a) and fully compressed temporal profile (b) of the signal after amplification for three scenarios. The black, dark gray, light gray lines correspond to pump intensities of 15.5, 9.8, 6.3 GW/cm^2 and a crystal length of 3, 4, 5 mm. The signal input is a 2 nJ pulse of 5 fs FWHM stretched to 110 fs. In all three cases the signal reaches similar saturation levels but the highest intensity result has the largest bandwidth and gain. The resulting pulse energies are 4.7 μJ, 3.9 μJ and 3.8 μJ and the corresponding bandwidth limited pulse durations are 6.8 fs, 7.5 fs and 9.5 fs.

only a small part of the pump pulse contributes to the amplification which results in a lower gain. This trade-off is illustrated in Fig. 8.10 where simulation results are shown for four different seed pulse durations while keeping all other parameters constant (constant seed pulse energy is assumed at a fixed beam waist size). The plots show that the shorter the seed input the larger the spectral bandwidth of the output but the lower the pulse energy.

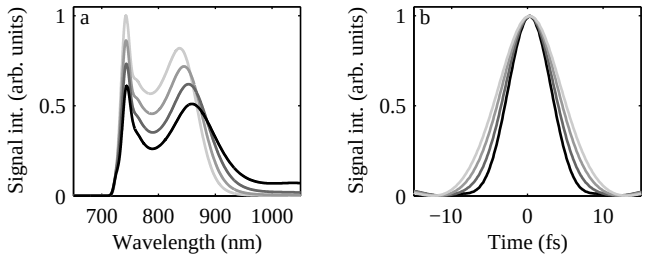

Figure 8.10: Spectrum (a) and fully compressed temporal profile (b) of the signal after amplification for different stretch factors of the signal input. The pump intensity is 9.8 GW/cm^2 with a pulse duration of 500 fs. The crystal length is 4 mm. The signal input is a 2 nJ pulse of 5 fs FWHM stretched to pulse durations of 50, 110, 180 and 280 fs with the darkest lines corresponding to the shortest input pulse. The plots show the trade-off between gain and bandwidth in the choice of the stretching factor, the larger the stretching factor the higher the gain but the smaller the bandwidth. The resulting pulse energies are 3.6 μJ, 3.9 μJ, 4.3 μJ and 4.7 μJ and the corresponding bandwidth limited pulse durations are 6.6 fs, 7.5 fs, 8.6 fs and 9.7 fs.

Discussion on the validity of the model and conclusions

The model that is employed neglects effects caused by the finite size of the beams. Because of the non-collinear angles α and β between the beams and spatial walk-off of the pump, the centers of the beams move away from each other during propagation. For the angles that are needed for broadband phase-matching this is about 40 μm/mm for the pump and 125 μm/mm for the idler relative to the signal beam. In refs. [58, 64] effects like these were not important because the sizes of the beams on the crystal were large (1 and 10 mm). However, in the OPA that is described in this chapter, the pulse energies are much lower and therefore the size of the beams needs to be smaller in order to reach the intensity at which an efficient non-linear interaction takes place. This makes the loss of spatial overlap much more critical. To include the effects of the loss of spatial overlap of the beams it might be possible to implement an artificial decay of the intensities of the beams that move away from the signal wave. It would, however, be more desirable to perform real three dimensional simulations, which would make the calculations a lot more demanding but not impossible.

Although the simulations presented do not include some of the effects that will be important in the experimental situation, the results show that the design goals are realistic. With a pump pulse energy of 25 μJ with a short enough duration it is possible to generate a sub-10 fs pulse with a pulse energy of a several μJ. Besides these general predictions, the simulations can be used to test the influence of parameters such as the pump intensity and seed pulse duration on the output of the system.

8.3.4 Experimental implementation and results

In Fig. 8.11 a schematic drawing of the NOPCPA is shown. The Ti:Sapphire seed and the Yb fiber pump laser are focused in the BBO crystal with a small non-collinear angle with respect to each other, as was discussed above. An essential requirement for a parametric amplifier is to temporally overlap the two laser pulses. This requires that the repetition rates of the pump and seed lasers are synchronized with an accuracy that is much higher than the pulse durations in the crystal. This can be achieved by either passive or active methods. In active methods the repetition rate of one of the lasers is locked to (a harmonic of) the repetition rate of the other by a phase locked loop, or both lasers are locked to a common high frequency reference [47, 68, 48]. By purely electronic means, synchronization with a residual timing jitter of 150 fs - 250 fs can be achieved. This satisfies the demand for synchronization in systems with pulse durations of $>$ 20 picosecond (ps) but is insufficient when the pulse durations are on the (sub-)ps timescale. The jitter can be reduced to the sub-fs level by a combination of electronic and optical techniques, in the form of a balanced cross-correlator, to provide an error signal for the feedback loop [69]. However such schemes are complicated and use expensive high frequency locking electronics.

Passive synchronization is based on deriving the seed for the amplifier of the pump laser and for the parametric amplifier from a single oscillator. When the amplifier uses a different gain material than the oscillator it is necessary to obtain a

seed for the amplifier in a spectral region outside the central region of the spectrum of the oscillator. For example, the seed for an Yb-based laser needs to be centered at 1030 nm, far away from the center wavelength of a Ti:Sapphire oscillator (780 nm). Conversion of the central wavelength of a pulse can be achieved by soliton frequency conversion in a photonic crystal fiber [70]. The technique is however known to be sensitive to instabilities because of the non-linear nature of the frequency conversion process. A potentially simpler method is to derive the seed directly from the spectrum of an ultra-broadband octave spanning oscillator. When possible, directly seeding the pump laser amplifier is superior over the other methods in terms of stability and simplicity. This method has therefore been adopted in the OPCPA system that is presented here. The implementation was done in close collaboration with Venteon and Amplitude Systems, the manufacturers of the few-cycle oscillator and amplifier respectively.

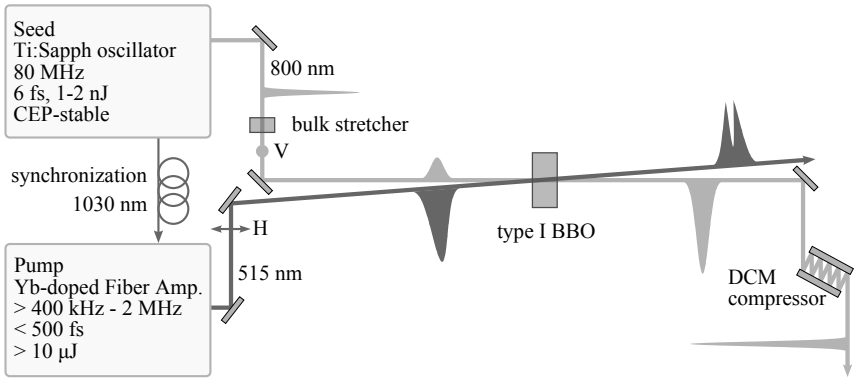

Figure 8.11: Design of the high repetition rate NOPCPA. The Ti:Sapphire oscillator delivers the seed through a fiber to the Yb:doped fiber amplifier to passively synchronize the timing of the two lasers. The seed for the OPCPA from the Ti:Sapphire oscillator is stretched by dispersion in air and optionally additional material. The output from the fiber amplifier at 1030 nm is frequency doubled to 515 nm. The two pulses are spatially and temporally overlapped in the BBO crystal with a non-collinear angle between the two beams. The output after amplification is compressed by double-chirped mirrors (DCM).

Oscillator

The few-cycle Ti:Sapphire oscillator (Venteon Pulse : ONE-IP UB) has a bandwidth that extends from 550-1200 nm (450 nm at -10 dBc). The bandwidth is large enough to use it without additional broadening in a self-referenced *f-2f* interferometer to lock the CEP of the pulses [71, 72]. The wings of the spectrum of the oscillator cavity are filtered by a dichroic mirror (DM1 in Fig. 8.12) and sent into the *f-2f* interferometer. In addition, the remaining part of the spectrum (600-1100 nm) has an overlap with the gain bandwidth at 1030 nm of the Yb based amplifier. The seed for the Yb-doped fiber amplifier is obtained by selecting the spectral region around 1030 nm, using a filter which transmits (partially) above 1000 nm (DM2) and a narrow bandpass filter with a bandwidth of 10 nm FWHM (BPF) to select

the spectral region around 1030 nm. Approximately 1 μW of power is coupled in a polarization maintaining (PM) single mode fiber, sufficient to seed the pre-amplifier of the fiber laser. The central part of the spectrum (600-1000 nm) with a pulse energy of approximately 2 nJ is used to seed the parametric amplifier.

Fiber amplifier pump laser

The fiber amplifier is a customized version of the Amplitude Tangerine fiber amplifier. It is adapted to amplify the relatively weak seed that is derived from the broadband Ti:Sapphire oscillator rather than a stand-alone Yb-based oscillator. The 1030 nm seed input from the Ti:Sapphire oscillator is amplified in the first pre-amplifier after which the pulses are stretched in a fiber based stretcher. The repetition rate is brought down by selecting pulses with an AOM pulse picker and further amplified in two pre-amplifiers. The main amplifier is a rod-type Yb-doped photonic crystal fiber (PCF). Both the pump and seed make two passes through the rod and subsequently the amplified pulses are compressed in a transmission grating compressor to a pulse duration of 300-400 fs FWHM. The average power after compression is approximately 20 W at repetition rates between 400 kHz and 2 MHz, resulting in a maximum pulse energy of 50 μJ. After frequency-doubling the infrared in a second harmonic crystal with an efficiency of approximately 50%, a pulse with a wavelength of 515 nm and pulse energy of 25 μJ at 515 nm is obtained that is used to pump the parametric amplifier.

NOPCPA

The layout of the NOPCPA is shown in Fig. 8.13. The polarization of the pump is set to horizontal by a waveplate whereas the horizontal polarization of the Ti:Sapphire oscillator is turned 90° by a polarization changing periscope. With these polarization settings the crystal tuning axis is in the horizontal plane (Fig. 8.6b). The seed beam is collimated by a concave mirror with a radius of 2 m and focused with a mirror with a radius of 1 m to a spot with a diameter of $\approx 200\mu$m on the crystal. The pump pulse is collimated, re-sized and finally focused by a system of four lenses on the crystal to a spot with a diameter of $\approx 250\mu$m. An imaging system is used to check the spatial overlap of the beams in the crystal.

The path length of the pump and the seed arm have to be adjusted such that the two pulses overlap temporally in the crystal. Fine control of the timing between the pulses is achieved by a motorized translation stage in the arm of the pump laser. To compensate for the path length in the fiber amplifier, a Herriot cell delay line [73], previously used in long-cavity oscillators [74], is implemented to ensure that the seed and the pump are derived from the same pulse of the Ti:Sapphire oscillator. Since the path length in the fiber amplifier is significant ($\approx$ 15 m) it is possible to use separate pulses from the oscillator pulse train for the seed of the fiber amplifier and the seed of the NOPCPA in principle. However, in that way the system will become sensitive to drifts in the repetition rate of the oscillator. Obviously a delay line of 15 m is a potential source of temporal drifts as well and at the moment it is being investigated which configuration yields the best results.

No additional stretching of the seed pulses is needed besides the dispersion in

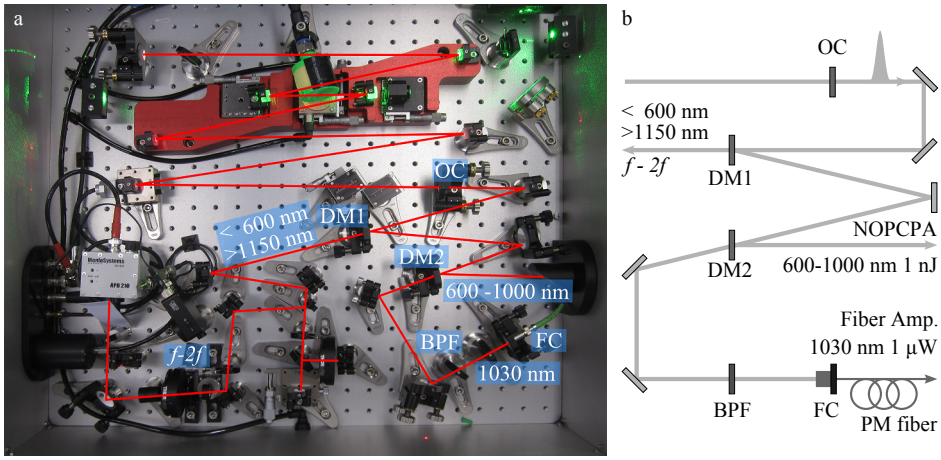

Figure 8.12: (a) Photograph of the laser cavity and filtering setup in the oscillator box. In the upper part of the picture the laser cavity can be seen with the crystal and focussing mirrors on the red centerpiece. After the output coupler (OC) the beam is distributed over the *f-2f* CEP stabilitization, the Yb fiber amplifier seed and the seed for the NOPCPA. (b) Schematic diagram of the filtering scheme that produces the three-fold output of the oscillator (see text for details).

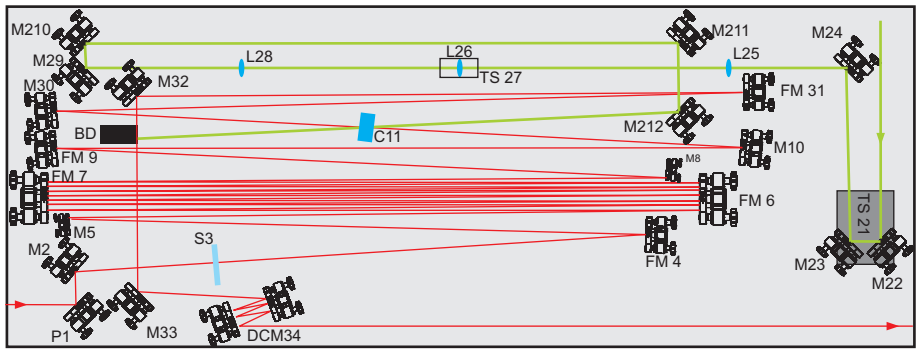

Figure 8.13: Layout of the NOPCPA with the beampaths of the pump (green) and seed (red). The seed goes through the Herriott cell delay line (FM6 and FM7) and is focused (FM9) on the crystal (C11). The amplified beam is re-collimated (FM31) and the pulses are compressed by chirped mirrors (DCM34). The relative timing of the two pulses can be adjusted with the translation stage in the pump path (TS21). The pump beam is focused on the crystal by a sequence of lenses that allow precise control over the size of the focus of the pump. After the crystal the pump beam is send into a beamdump (BD).

air and in the crystal itself. For the compression of the pulses after amplification multiple bounces on chirped mirrors will be used.

8.3.5 Results

In Fig. 8.14a a typical spectrum of the output of the NOPCPA at 400 kHz is shown. For this result a BBO crystal of 4 mm length was used. The pump pulse energy was 19 μJ which was focused on the crystal to a spot with a diameter of approximately 200 μm FWHM. The pump pulses are not fully compressed because it was noted that the pump pulses were too short relative to the pulse duration of the seed. The Herriot cell in the seed arm is bypassed and the seed is focused to a spot with a diameter of approximately 100 μm FWHM. The conversion efficiency is 13% which results in a pulse energy of 2.5 μJ. The spectrum of the output of the amplifier supports a transform limited pulse duration of 7 fs FWHM.

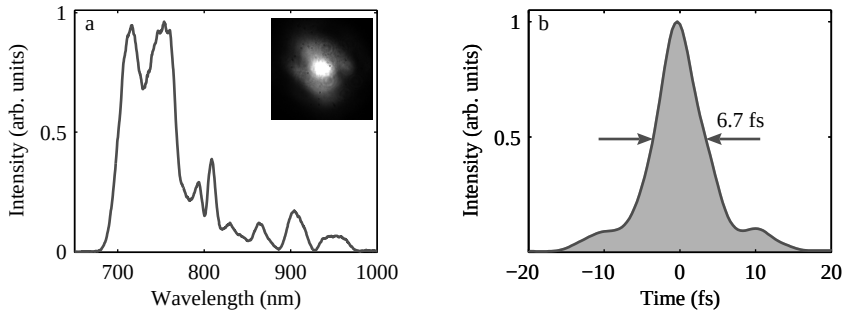

Figure 8.14: (a)Spectrum after amplification at 400 kHz in a BBO crystal with a thickness of 4 mm and a pump pulse energy of 19 μJ. The conversion efficiency is 13% which results in an output energy of the amplified pulses of 2.5 μJ. The inset shows the beam profile of the amplified beam. (b) The inverse Fourier transform of the spectrum in (a) assuming a flat spectral phase showing that the spectrum supports a 7 fs FWHM pulse.

Pulse durations of the pump and the seed

It was found that the bandwidth of the output was improved by detuning the pump laser compressor. This means that the pump pulses, when fully compressed, are too short with respect to the seed pulses. For this reason the Herriott cell delay line was bypassed in order to prevent the dispersion by the air in the long delay line. An auto-correlator for the pump pulses is under construction and it is investigated if the pump pulses can be stretched in the second harmonic generation process in the pump laser by using a longer second harmonic crystal.

Spatial chirp

Another problem that was found is a significant variation of the spectrum over the beam profile (*spatial chirp*). This is a known problem in NOPAs with small beam diameters [75]. It results from the angular dispersion of the seed in the crystal. The

spatial chirp can be reduced by focussing the beams less tightly, a more narrowband pump pulse and improvements in the alignment of the non-collinear angle.

8.3.6 Further developments

Clearly the system described here is 'work in progress'. The first results are promising and suggest that the design goals will be realized in the near future. Further developments that are planned are now briefly discussed.

Compression and temporal characterization

Compression by the double chirped mirrors will be the next after the amplification itself leads to a satisfactory result. Temporal characterization will be done with an auto-correlator and a spider. To obtain the shortest possible pulses it is necessary to not only compensate the second order dispersion (GVD) but also the third order. Different chirped mirrors will be tested and possibly a customized set of mirrors needs to be developed.

CEP stabilization

The CEP-stability of the Ti:Sapphire oscillator is routinely operated without problems. Achieving CEP-stability and sufficient seed power at 1030 nm simultaneously is a small complication since a trade-off between energy at 1030 nm and 1200 nm (for the *f-2f* interferometer) needs to be found by tuning the dispersion management wedges in the cavity of the oscillator. Although this has not been proven yet, it is not expected that this will form a severe limitation.

CEP-stability of the amplified pulses will need to be confirmed using an *f-2f* interferometer similar to the ones that are often used in Ti:Sapphire laser amplifiers [15]. CEP-stability in a parametric amplifier has been shown previously [51] and meanwhile has been tested in very similar systems as the one discussed here [55, 53]. The results show that indeed CEP-stability is preserved, however the r.m.s. deviations and the timespan over which the system is stable need to be improved. In case improvements do not lead to the required level of stability, an additional feedback loop will need to be implemented. This can be done in the same way as is common in CEP-stable Ti:Sapphire amplifiers [15] or via the recently introduced scheme based on feed-forward stabilization [76]. The disadvantage of introducing additional stabilization methods is that part of the pulse energy will be used in the CEP stabilization. In order to have the full pulse energy available in the experiment it is possible to implement an *f-2f* interferometer after the exit of the beam from an experiment.

Second amplification stage

In both of the previously mentioned references [55, 53] a second NOPA stage is implemented in which the pump pulse is reused. This led to a significant increase of the pulse energy and spectral bandwidth of the amplified pulses. Potentially, it is possible to make a second pass through the same crystal by sending both beams

back on themselves. After the single stage version of the OPCPA is optimized it will be investigated whether a second amplification stage has similar benefits for the system described here.

Increase of pump energy

The current fiber amplifier pump laser is specified to deliver a maximum pulse energy at 515 nm of 25 μJ and has in practice delivered more than 30 μJ. In optimum conditions this would allow for a pulse energy in the output of the OPA of up to 5 μJ which will be sufficient for experiments along the lines of what was discussed in the introduction. However, it will still be worthwhile to increase the pulse energy beyond what is possible with the current pump laser source. The higher the pulse energy, the more efficient the HHG process will become and the more energy will be available for the other arm in the experiment (Fig. 8.3). The current fiber amplifier can be upgraded with a more powerful laser diode to pump the rod fiber to achieve higher pulse energies at the same repetition rate. The main challenge is to keep non-linearities in the fiber under control [77]. In the research and development labs of Amplitude Systems it has already been demonstrated that pulse energies beyond 100 μJ are possible. With more pump power and higher pump pulse energies available it is likely that the parametric amplifier would need to be equipped with several stages of amplification and possibly with two pump lasers.

8.4 Conclusion

In this chapter the progress on the development of a high repetition rate (>100 kHz) source of attosecond pulses has been described. The bow tie nanostructures that have been fabricated show promising results in a test experiment in which THG is detected from the enhanced field of the bow ties. The next step will be to perform an experiment in which high harmonic generation can be detected and characterized.

A new NOPCPA laser has been designed and is under construction which will be able to deliver CEP-stable few-cycle pulses around 800 nm at repetition rates between 400 kHz and 2 MHz with a pulse energy of several μJ. This laser is being developed in close collaboration with two laser companies. The first results are promising and suggest that the design goals will be realized in the near future. The laser that is under construction will be interesting for other applications as well.

References

[1] M. Hentschel, R. Kienberger, C. Spielmann, G. A. Reider, N. Milosevic, T. Brabec, P. Corkum, U. Heinzmann, M. Drescher and F. Krausz. *Attosecond metrology.* Nature, **414**, 509–513 (2001).

[2] P. M. Paul, E. S. Toma, P. Breger, G. Mullot, F. Auge, P. Balcou, H. G. Muller and P. Agostini. *Observation of a train of attosecond pulses from high harmonic generation.* Science, **292**, 1689–1692 (2001).

[3] P. B. Corkum and F. Krausz. *Attosecond science.* Nat. Phys., **3**, 381–387 (2007).

[4] F. Krausz and M. Ivanov. *Attosecond physics.* Rev. Mod. Phys., **81**, 163–234 (2009).

[5] G. Sansone *et al. Electron Localization following Attosecond Molecular Photoionization.* Nature, **465**, 763–766 (2010).

[6] L. Nugent-Glandorf, M. Scheer, D. A. Samuels, A. M. Mulhisen, E. R. Grant, X. M. Yang, V. M. Bierbaum and S. R. Leone. *Ultrafast time-resolved soft x-ray photoelectron spectroscopy of dissociating Br_2.* Phys. Rev. Lett., **8719**, 193002 (2001).

[7] P. Wernet, M. Odelius, K. Godehusen, J. Gaudin, O. Schwarzkopf and W. Eberhardt. *Real-Time Evolution of the Valence Electronic Structure in a Dissociating Molecule.* Phys. Rev. Lett., **103**, 013001 (2009).

[8] E. Gagnon, P. Ranitovic, X. M. Tong, C. L. Cocke, M. M. Murnane, H. C. Kapteyn and A. S. Sandhu. *Soft X-ray-driven femtosecond molecular dynamics.* Science, **317**, 1374–1378 (2007).

[9] F. Kelkensberg *et al. Molecular Dissociative Ionization and Wave-Packet Dynamics Studied Using Two-Color XUV and IR Pump-Probe Spectroscopy.* Phys. Rev. Lett., **103**, 123005 (2009).

[10] E. Constant, D. Garzella, P. Breger, E. Mevel, C. Dorrer, C. Le Blanc, F. Salin and P. Agostini. *Optimizing high harmonic generation in absorbing gases: Model and experiment.* Phys. Rev. Lett., **82**, 1668–1671 (1999).

[11] A. Rundquist, C. G. Durfee, Z. H. Chang, C. Herne, S. Backus, M. M. Murnane and H. C. Kapteyn. *Phase-matched generation of coherent soft X-rays.* Science, **280**, 1412–1415 (1998).

[12] C. G. Durfee, A. R. Rundquist, S. Backus, C. Herne, M. M. Murnane and H. C. Kapteyn. *Phase matching of high-order harmonics in hollow waveguides.* Phys. Rev. Lett., **83**, 2187–2190 (1999).

[13] P. Tzallas, D. Charalambidis, N. A. Papadogiannis, K. Witte and G. D. Tsakiris. *Direct observation of attosecond light bunching.* Nature, **426**, 267–271 (2003).

[14] Y. Nabekawa, T. Shimizu, T. Okino, K. Furusawa, H. Hasegawa, K. Yamanouchi and K. Midorikawa. *Conclusive evidence of an attosecond pulse train observed with the mode-resolved autocorrelation technique.* Phys. Rev. Lett., **96**, 083901 (2006).

[15] A. Baltuska *et al. Attosecond control of electronic processes by intense light fields.* Nature, **421**, 611–615 (2003).

[16] P. B. Corkum, N. H. Burnett and M. Y. Ivanov. *Subfemtosecond Pulses.* Opt. Lett., **19**, 1870–1872 (1994).

[17] O. Tcherbakoff, E. Mével, D. Descamps, J. Plumridge and E. Constant. *Time-gated high-order harmonic generation.* Phys. Rev. A, **68**, 043804 (2003).

[18] G. Sansone *et al. Isolated single-cycle attosecond pulses.* Science, **314**, 443–446 (2006).

[19] P. Tzallas, E. Skantzakis, C. Kalpouzos, E. P. Benis, G. D. Tsakiris and D. Charalambidis. *Generation of intense continuum extreme-ultraviolet radiation by many-cycle laser fields.* Nat. Phys., **3**, 846–850 (2007).

[20] H. Mashiko, S. Gilbertson, C. Q. Li, S. D. Khan, M. M. Shakya, E. Moon and Z. H. Chang. *Double optical gating of high-order harmonic generation with carrier-envelope phase stabilized lasers.* Phys. Rev. Lett., **100**, 103906 (2008).

[21] X. M. Feng, S. Gilbertson, H. Mashiko, H. Wang, S. D. Khan, M. Chini, Y. Wu, K. Zhao and Z. H. Chang. *Generation of Isolated Attosecond Pulses with 20 to 28 Femtosecond Lasers.* Phys. Rev. Lett., **103**, 183901 (2009).

[22] I. J. Sola *et al. Controlling attosecond electron dynamics by phase-stabilized polarization gating.* Nat. Phys., **2**, 319–322 (2006).

[23] J. Ullrich, R. Moshammer, A. Dorn, R. Dorner, L. P. H. Schmidt and H. Schniidt-Bocking. *Recoil-ion and electron momentum spectroscopy: reaction-microscopes.* Reports on Progress in Physics, **66**, 1463–1545 (2003).

[24] A. Mikkelsen *et al. Photoemission electron microscopy using extreme ultraviolet attosecond pulse trains.* Rev. Sci. Instrum., **80**, 123703 (2009).

[25] P. B. Corkum. *Plasma Perspective on Strong-Field Multiphoton Ionization.* Phys. Rev. Lett., **71**, 1994–1997 (1993).

[26] F. Lindner, W. Stremme, M. G. Schätzel, F. Grasbon, G. G. Paulus, H. Walther, R. Hartmann and L. Strüder. *High-order harmonic generation at a repetition rate of 100 kHz.* Phys. Rev. A, **68**, 013814 (2003).

[27] M.-C. Chen, M. R. Gerrity, S. Backus, T. Popmintchev, X. Zhou, P. Arpin, X. Zhang, H. C. Kapteyn and M. M. Murnane. *Spatially coherent, phase matched, high-order harmonic EUV beams at 50 kHz.* Opt. Express, **17**, 17376–17383 (2009).

[28] S. Hädrich, J. Rothhardt, M. Krebs, F. Tavella, A. Willner, J. Limpert and A. Tünnermann. *High harmonic generation by novel fiber amplifier based sources.* Opt. Express, **18**, 20242–20250 (2010).

[29] J. Boullet, Y. Zaouter, J. Limpert, S. Petit, Y. Mairesse, B. Fabre, J. Higuet, E. Mével, E. Constant and E. Cormier. *High-order harmonic generation at a megahertz-level repetition rate directly driven by an ytterbium-doped-fiber chirped-pulse amplification system.* Opt. Lett., **34**, 1489–1491 (2009).

[30] O. Heckl *et al. High harmonic generation in a gas-filled hollow-core photonic crystal fiber.* Appl. Phys. B: Lasers Opt., **97**, 369–373 (2009).

[31] H. Ren, A. Nazarkin, J. Nold and P. S. Russell. *Quasi-phase-matched high harmonic generation in hollow core photonic crystal fibers.* Opt. Express, **16**, 17052–17059 (2008).

[32] C. Gohle, T. Udem, M. Herrmann, J. Rauschenberger, R. Holzwarth, H. A. Schuessler, F. Krausz and T. W. Hansch. *A frequency comb in the extreme ultraviolet.* Nature, **436**, 234–237 (2005).

[33] R. J. Jones, K. D. Moll, M. J. Thorpe and J. Ye. *Phase-Coherent Frequency Combs in the Vacuum Ultraviolet via High-Harmonic Generation inside a Femtosecond Enhancement Cavity.* Phys. Rev. Lett., **94**, 193201 (2005).

[34] A. Ozawa *et al. High Harmonic Frequency Combs for High Resolution Spectroscopy.* Phys. Rev. Lett., **100**, 253901 (2008).

[35] S. Kim, J. H. Jin, Y. J. Kim, I. Y. Park, Y. Kim and S. W. Kim. *High-harmonic generation by resonant plasmon field enhancement.* Nature, **453**, 757–760 (2008).

[36] T. Hanke, G. Krauss, D. Träutlein, B. Wild, R. Bratschitsch and A. Leitenstorfer. *Efficient Nonlinear Light Emission of Single Gold Optical Antennas Driven by Few-Cycle Near-Infrared Pulses.* Phys. Rev. Lett., **103**, 257404 (2009).

[37] F. Quere, Y. Mairesse and J. Itatani. *Temporal characterization of attosecond XUV fields.* J. Mod. Opt., **52**, 339–360 (2005).

[38] M. Siegel, N. Pfullmann, G. Palmer, S. Rausch, T. Binhammer, M. Kovacev and U. Morgner. *Microjoule pulse energy from a chirped-pulse Ti:sapphire oscillator with cavity dumping.* Opt. Lett., **34**, 740–742 (2009).

[39] G. Cerullo and S. De Silvestri. *Ultrafast optical parametric amplifiers.* Rev. Sci. Instrum., **74**, 1–18 (2003).

[40] E. Riedle, M. Beutter, S. Lochbrunner, J. Piel, S. Schenkl, S. Sprlein and W. Zinth. *Generation of 10 to 50fs pulses tunable through all of the visible and the NIR.* Appl. Phys. B: Lasers Opt., **71**, 457–465 (2000).

[41] V. Petrov and F. Noack. *Tunable femtosecond optical parametric amplifier in the mid-infrared with narrow-band seeding.* J. Opt. Soc. Am. B, **12**, 2214–2221 (1995).

[42] D. Brida, C. Manzoni, G. Cirmi, M. Marangoni, S. D. Silvestri and G. Cerullo. *Generation of broadband mid-infrared pulsesfrom an optical parametric amplifier.* Opt. Express, **15**, 15035–15040 (2007).

[43] P. Hamm, R. A. Kaindl and J. Stenger. *Noise suppression in femtosecond mid-infrared light sources.* Opt. Lett., **25**, 1798–1800 (2000).

[44] A. Shirakawa, I. Sakane, M. Takasaka and T. Kobayashi. *Sub-5-fs visible pulse generation by pulse-front-matched noncollinear optical parametric amplification.* Appl. Phys. Lett., **74**, 2268–2270 (1999).

[45] A. Baltuska, T. Fuji and T. Kobayashi. *Visible pulse compression to 4 fs by optical parametric amplification and programmable dispersion control.* Opt. Lett., **27**, 306–308 (2002).

[46] I. N. Ross, P. Matousek, M. Towrie, A. J. Langley and J. L. Collier. *The prospects for ultrashort pulse duration and ultrahigh intensity using optical parametric chirped pulse amplifiers.* Opt. Commun., **144**, 125 – 133 (1997).

[47] S. Witte, R. T. Zinkstok, W. Hogervorst and K. S. E. Eikema. *Generation of few-cycle terawatt light pulses using optical parametric chirped pulse amplification.* Opt. Express, **13**, 4903–4908 (2005).

[48] N. Ishii *et al. Multimillijoule chirped parametric amplification of few-cycle pulses.* Opt. Lett., **30**, 567–569 (2005).

[49] S. Witte, R. T. Zinkstok, A. L. Wolf, W. Hogervorst, W. Ubachs and K. S. E. Eikema. *A source of 2 terawatt, 2.7 cycle laser pulses based on noncollinear optical parametric chirped pulse amplification.* Opt. Express, **14**, 8168–8177 (2006).

[50] D. Herrmann, L. Veisz, R. Tautz, F. Tavella, K. Schmid, V. Pervak and F. Krausz. *Generation of sub-three-cycle, 16 TW light pulses by using noncollinear optical parametric chirped-pulse amplification.* Opt. Lett., **34**, 2459–2461 (2009).

[51] C. P. Hauri, P. Schlup, G. Arisholm, J. Biegert and U. Keller. *Phase-preserving chirped-pulse optical parametric amplification to 17.3 fs directly from a Ti:Sapphire oscillator.* Opt. Lett., **29**, 1369–1371 (2004).

[52] F. Tavella *et al. Fiber-amplifier pumped high average power few-cycle pulse noncollinear OPCPA.* Opt. Express, **18**, 4689–4694 (2010).

[53] J. Rothhardt *et al. High average and peak power few-cycle laser pulses delivered by fiber pumped OPCPA system.* Opt. Express, **18**, 12719–12726 (2010).

[54] M. Schultze, T. Binhammer, A. Steinmann, G. Palmer, M. Emons and U. Morgner. *Few-cycle OPCPA system at 143 kHz with more than 1 mu J of pulse energy.* Opt. Express, **18**, 2836–2841 (2010).

[55] M. Schultze, T. Binhammer, G. Palmer, M. Emons, T. Lang and U. Morgner. *Multi-μJ, CEP-stabilized, two-cycle pulses from an OPCPA system with up to 500 kHz repetition rate.* Opt. Express, **18**, 27291–27297 (2010).

[56] R. W. Boyd. *Nonlinear Optics.* Academic Press / Elsevier, 3 ed. (2008).

[57] Y. Shen. *The principles of nonlinear optics.* Wiley-Interscience, New York (1984).

[58] S. Witte. *Terawatt-intensity few-cycle laser pulses.* Ph.D. thesis, Vrije Universiteit Amsterdam (2007).

[59] E. Zeromskis, A. Dubietis, G. Tamosauskas and A. Piskarskas. *Gain bandwidth broadening of the continuum-seeded optical parametric amplifier by use of two pump beams.* Opt. Commun., **203**, 435 – 440 (2002).

[60] C. Wang, Y. Leng, B. Zhao, Z. Zhang and Z. Xu. *Extremely broad gain spectra of two-beam-pumped optical parametric chirped-pulse amplifier.* Opt. Commun., **237**, 169 – 177 (2004).

[61] L. Cardoso and G. Figueira. *Bandwidth increase by controlled angular dispersion of signal beam in optical parametric amplification.* Opt. Express, **12**, 3108–3113 (2004).

[62] G. Arisholm, J. Biegert, P. Schlup, C. Hauri and U. Keller. *Ultra-broadband chirped-pulse optical parametric amplifier with angularly dispersed beams.* Opt. Express, **12**, 518–530 (2004).

[63] I. N. Ross, P. Matousek, G. H. C. New and K. Osvay. *Analysis and optimization of optical parametric chirped pulse amplification.* J. Opt. Soc. Am. B, **19**, 2945–2956 (2002).

[64] S. Witte, R. Zinkstok, W. Hogervorst and K. Eikema. *Numerical simulations for performance optimization of a few-cycle terawatt NOPCPA system.* Appl. Phys. B: Lasers Opt., **87**, 677–684 (2007).

[65] J. C. Diels and W. Rudolph. *Ultrashort Laser Pulse Phenomena.* Academic Press, New York, 2nd. ed. (2006).

[66] H. J. Bakker, P. C. M. Planken and H. G. Muller. *Numerical calculation of optical frequency-conversion processes: a new approach.* J. Opt. Soc. Am. B, **6**, 1665–1672 (1989).

[67] R. A. Ganeev, I. A. Kulagin, A. I. Ryasnyansky, R. I. Tugushev and T. Usmanov. *Characterization of nonlinear optical parameters of KDP, LiNbO3 and BBO crystals.* Opt. Commun., **229**, 403 – 412 (2004).

[68] R. T. Zinkstok, S. Witte, W. Hogervorst and K. S. E. Eikema. *High-power parametric amplification of 11.8-fs laser pulses with carrier-envelope phase control.* Opt. Lett., **30**, 78–80 (2005).

[69] T. R. Schibli, J. Kim, O. Kuzucu, J. T. Gopinath, S. N. Tandon, G. S. Petrich, L. A. Kolodziejski, J. G. Fujimoto, E. P. Ippen and F. X. Kaertner. *Attosecond active synchronization of passively mode-locked lasers by balanced cross correlation.* Opt. Lett., **28**, 947–949 (2003).

[70] C. Teisset, N. Ishii, T. Fuji, T. Metzger, S. Köhler, R. Holzwarth, A. Baltuška, A. Zheltikov and F. Krausz. *Soliton-based pump-seed synchronization for few-cycle OPCPA*. Opt. Express, **13**, 6550–6557 (2005).

[71] H. R. Telle, G. Steinmeyer, A. E. Dunlop, J. Stenger, D. H. Sutter and U. Keller. *Carrier-envelope offset phase control: A novel concept for absolute optical frequency measurement and ultrashort pulse generation*. Appl. Phys. B: Lasers Opt., **69**, 327–332 (1999).

[72] D. J. Jones, S. A. Diddams, J. K. Ranka, A. Stentz, R. S. Windeler, J. L. Hall and S. T. Cundiff. *Carrier-envelope phase control of femtosecond mode-locked lasers and direct optical frequency synthesis*. Science, **288**, 635–639 (2000).

[73] D. Herriott, H. Kogelnik and R. Kompfner. *Off-Axis Paths in Spherical Mirror Interferometers*. Appl. Opt., **3**, 523–526 (1964).

[74] S. Dewald, T. Lang, C. D. Schröter, R. Moshammer, J. Ullrich, M. Siegel and U. Morgner. *Ionization of noble gases with pulses directly from a laser oscillator*. Opt. Lett., **31**, 2072–2074 (2006).

[75] J. Bromage, C. Dorrer and J. D. Zuegel. *Angular-dispersion-induced spatiotemporal aberrations in noncollinear optical parametric amplifiers*. Opt. Lett., **35**, 2251–2253 (2010).

[76] S. Koke, C. Grebing, H. Frei, A. Anderson, A. Assion and G. Steinmeyer. *Direct frequency comb synthesis with arbitrary offset and shot-noise-limited phase noise*. Nat. Photonics, **4**, 462–465 (2010).

[77] J. Limpert, F. Roser, D. Schimpf, E. Seise, T. Eidam, S. Hadrich, J. Rothhardt, C. Misas and A. Tunnermann. *High Repetition Rate Gigawatt Peak Power Fiber Laser Systems: Challenges, Design, and Experiment*. Selected Topics in Quantum Electronics, IEEE Journal of, **15**, 159 –169 (2009).

Summary

This thesis describes the development of methods to follow the motion of atoms and electrons in molecules and other systems, by using light pulses created through a process called high harmonic generation (HHG). The movements of atoms and electrons cannot be recorded by ordinary cameras because the shutter time of even the fastest camera is too long. This has led to the development of time-resolved techniques with ultrashort laser pulses. The pulse duration of lasers can be made orders of magnitude shorter than the shortest electronic pulses, making it possible to 'freeze' even the fastest dynamics. Famously, the emergence of femtosecond (1 fs = 10^{-15} s) laser pulses has led to techniques that can follow the fastest chemical reactions in time. These reactions take place on a few-picosecond (1 ps = 10^{-12} s) or even a sub-ps timescale. HHG has led to a novel source of ultrashort pulses which can extend these traditional femtochemistry experiments in two ways.

In HHG an intense infrared (IR) femtosecond laser pulse is used to generate light at the odd harmonic frequencies of the IR laser through a nonlinear interaction of the laser pulse with an atomic medium. The wavelength of the light that can be created in this way, extends into the extreme ultraviolet (XUV) or even soft X-ray regime. In the experiments described in this thesis wavelengths of typically 25-75 nm (15-50 eV) have been used. The short wavelength, and the correspondingly high photon energies, provide new ways of probing nuclear dynamics in molecules on femtosecond timescales. Additionally, with HHG it is possible to produce light pulses with a duration shorter than 1 fs. These are the shortest light pulses that exist and are referred to as attosecond (1 as = 10^{-18} s) pulses. The emergence of attosecond pulses has led to a whole new field of research in which one tries to resolve electronic dynamics that occur on a few-fs or even sub-fs timescale.

In the first two parts in this thesis a collection of experiments is described in which the potential of HHG pulses is explored for the study of femtosecond and attosecond dynamics in molecules. The last part explores an attractive future direction for attosecond time-resolved experiments.

Molecular nuclear dynamics The constituent atoms of a molecule are not fixed with respect to each other but move in space and time. Examples of such motion are the vibration of a molecule and the breaking of a bond in a chemical reaction. The fastest of such events typically take place within tens of femtoseconds. The H_2^+ molecule is the smallest molecule in nature and therefore it's vibrations are the fastest that exist. This vibration was the subject of the first experiment that is described in this thesis (Chapter 2), where we have looked at how the dynamics of the vibrational motion is influenced by the presence of a moderately strong laser field. Two separate experiments are described in which an XUV pulse (15-40 eV) was used to photoionize neutral hydrogen molecules creating a vibrational wavepacket ('vibration') in the molecular ion H_2^+. An IR pulse, with a certain time delay with

respect to the XUV pulse, was used to dissociate the vibrating molecule through a process called bond-softening. The energy of the resulting charged fragments was measured. The main difference between the two experiments was the duration of the dissociation pulse. When this pulse was short (7 fs) compared to the vibrational period (15 fs), the fragment yield oscillated as a function of the delay between the pulses, reflecting the vibrational dynamics. In that experiment the initial ionization by the XUV pulses took place in the absence of the dissociation pulse, which was in stark contrast to the situation where the dissociation pulse was longer (35 fs) than the vibrational period. In that experiment we observed how the molecule adapted to the field depending on whether the field was turned on gradually ('adiabatic case') or suddenly ('non-adiabatic case'). The result demonstrated how experimental methods that use strong laser fields to determine molecular structure will be sensitive not only to the intensity of the field but also to the pulse duration.

The experiment that is described in Chapter 3 forms an important step in the development of a new technique to record nuclear dynamics of a molecule with high enough spatial and temporal resolution to make a molecular movie of a chemical reaction. Traditional femtochemistry experiments, as well as the aforementioned experiment, use indirect methods to determine changes in the structure of a molecule. By contrast, the measurement of photoelectron angular distributions potentially allows a direct measurement of the structure without the need of any prior knowledge of the molecule or its dynamics. This could lead to a powerful method which is more widely applicable than the current state-of-the-art femtochemistry techniques. Structural determination from PADs relies on the fact that the electrons that are created by photoionization, scatter on the atomic centers and in this way carry information on the positions of these atoms. The success of this technique hinges on two requirements: first the wavelength of the electrons needs to be be short compared to the internuclear distance. Secondly, the electron angular distribution needs to be measured in a frame that is defined by the orientation of the molecule (molecular frame). This condition was met by using a laser pulse which aligned an initially isotropic ensemble of CO_2 molecules with respect to the laboratory frame. The aligned molecules where subsequently ionized by the XUV pulse from a HHG source to generate 'high' energy photoelectrons. The experimental PADs showed a satisfactory comparison with theoretical calculations. The theoretical calculations enabled us to determine that information both on the electronic, as well as the atomic structure, was imprinted in the PADs. The experiment provides strong support for further attempts to resolve nuclear dynamics based on diffraction of photoelectrons generated by either HHG or XUV/X-ray free electron lasers (FELs).

Molecular electron dynamics The attosecond domain is the natural timescale for electron motion. The advent of attosecond pulses, therefore allowed one to resolve such electron dynamics in time. The very first experiments in which this was pursued, have looked at electron dynamics in atoms and, somewhat later, in condensed matter. Chapter 6 describes the first experiment in which electron dynamics in a molecule was revealed using attosecond pulses. Deuterium (D_2) molecules were exposed to a sequence of an isolated attosecond pulse and a few-cycle IR pulse with a delay that was controlled with attosecond precision. A part of the photoionized

molecules dissociated, resulting in a neutral D and a D^+ fragment. The final position of the electron was monitored by detecting the (energy-resolved) direction of the D^+ fragment with respect to the laser polarization. The number of ions flying to the 'left' and to the 'right' was the same in the absence of the IR field. However, when the IR field was present, the electron could be localized to one side of the molecule. The outcome of this localization depended on the delay between the two pulses with attosecond resolution. Two mechanisms for this localization could be identified by analyzing theoretical models of the experiment. In the first mechanism the localization results from a quantum mechanical interference that involves autoionization from a doubly excited state and the interaction of the free electron with the laser field. In the second mechanism the dissociation starts from the first excited state of the molecular ion. During the dissociation the IR field drives transitions between this state and the ground state resulting in a coherent superposition of the two states. While the electronic wavefunction of both states are fully delocalized, the coherent superposition of the two states that resulted from the interaction with the laser field corresponds to a localized electron. The dynamics of the localization was furthermore explored with the help of a semiclassical model. In this model the molecule is described in terms of so-called quasi-static states. In these states the interaction of the molecule with the IR field is taken instantaneously into account (Chapter 5). The electron localization during dissociation is described by a semiclassical trajectory on the quasi-static states through a number of passages through laser-induced avoided crossings. The results of this model approximate the exact solution very well, supporting the underlying interpretation of the dynamics. The experimental results establish attosecond pump-probe strategies as a powerful tool for the investigation of complex electron dynamics in molecules.

While the role of the attosecond pulse in the electron localization experiment is best described by a 'pump' pulse that forms the onset of the chain of events, it is equally interesting to explore the role of attosecond pulses as a 'probe' of electron dynamics. This has been the aim of the experiment described in chapter 6. We have used an attosecond pulse train (APT) with two pulses per cycle of the IR field, rather than an isolated attosecond pulse, in combination with a moderately strong IR field to dissociative ionize deuterium molecules. Different dissociative ionization channels could be distinguished based on the energy and direction of the resulting charged fragments with respect to the laser polarization. We observed oscillations of the yield of the ion fragments of some of these channels as a function of the delay between the two pulses. Quantum mechanical 2-electron calculations where found to be in agreement with the experimental results. A mechanistic interpretation was provided by a simplified model of the two-color ionization. In this model the neutral ground state is ionized by the attosecond pulses to the two lowest ionic states, which are coupled by the IR field. This coupling leads to time-dependent changes in the ionization probability of the two ionic states, detected as an oscillation of the yield in the corresponding fragment channel. The coupling can alternatively be seen as a time-dependent polarization of the ionic states which is probed by the attosecond ionization. The oscillations in the fragment ion yield therefore directly reflect the IR-induced dynamics.

Future directions of attosecond physics In the experiments that are described in the previous part, we have successfully extended attosecond pump-probe spectroscopy to the field of molecular science. The use of attosecond pulses to resolve collective electron motion in metal nanoparticles is explored in a theoretical study in Chapter 7. There is a wide interest in surface plasmons, as these collective oscillations are called, due to their potential to manipulate light on lengthscales below the photon wavelength. Although the underlying electron dynamics is always implicitly assumed in the interpretation of plasmonic effects, it is hardly ever explicitly observed. Attosecond pulses potentially provide a way to resolve the oscillations of the plasmonic field by employing a technique called attosecond streaking. In attosecond streaking the attosecond pulse generates a short bunch of electrons by ionization which subsequently interacts with the electric field of an electromagnetic wave, in this case the surface plasmon field. The final energy of the electron depends on the phase of the electric field at the time it is born. We have developed a classical model to simulate the interaction of the electrons with the plasmonic field. With this model we have studied how attosecond streaking is affected by the localized character of the field. We found that both the phase and the amplitude of the streaking oscillation become dependent on the spatial extension of the plasmon field at very small fieldsizes. Furthermore it was found that a specific spatial component of the plasmon field can be probed selecting electrons that are emitted parallel to that component.

Many novel attosecond experiments, such as the one just discussed, would highly benefit from an attosecond source at higher repetition rates than currently available. Current state-of-the-art attosecond sources have repetition rates of typically a few kHz, limited by the laser sources that can provide the required pulse energies to drive the HHG process. An attosecond source that runs at a repetition rate of 100 kHz - 1 MHz requires the combination of the development of a new laser source and a HHG technique that is able to generate attosecond pulses with lower pulse energies than currently needed. The status of our work on both developments is presented in Chapter 8. HHG generation using arrays of nanometer sized bowtie optical antennas is explored as an alternative for traditional HHG in a loose laser focus. The local field enhancement of a factor of 100-1000 at the tips of the bowties makes it possible to generate high harmonics with laser pulses with significantly lower pulse energies. Bowtie-arrays have been developend that are fabricated by electron lithography. A first test experiment was performed on third harmonic generation (THG) in which it was experimentally verified that the THG was indeed due to the field enhancement of the bowtie antennas. The next step is the demonstration of the production of higher order harmonics. Simultaneously a new laser source is being developed for future attosecond experiments at high repetition rates. The design of the laser is based on a non-collinear optical parametric chirped pulse amplifier (NOPCPA) which allows for the amplification of broadband pulses. The laser system under development is expected to deliver pulses with a pulse duration of < 10 fs FWHM, a pulse energy of > 2 μJ at a repetition rate of 400 kHz and with carrier-envelope-phase (CEP) stability. The amplification of a large spectrum with the required pulse energy has been achieved, while compression and CEP-stability is currently being worked on.

Samenvatting

Het doel van het onderzoek dat staat beschreven in dit proefschrift is het bestuderen van de bewegingen van atomen en elektronen in moleculen en andere systemen. Hiervoor hebben we experimentele technieken ontwikkeld om deze bewegingen te volgen met behulp van lichtpulsen die zijn geproduceerd door hoge harmonische generatie (HHG). Bewegingen van atomen en elektronen kunnen niet vastgelegd worden door middel van conventionele camera's, omdat de sluitertijd van zelfs de allersnelste camera's te lang is om een scherp beeld van de beweging te maken. Om deze reden zijn technieken ontwikkeld op basis van ultrakorte laserpulsen, waarbij gebruik wordt gemaakt van het feit dat laserpulsen vele malen korter kunnen zijn dan de kortste elektronische pulsen. Met deze laserpulsen is het mogelijk om zelfs de allersnelste bewegingen van atomen en elektronen te volgen in de tijd. Door de ontwikkeling van femtoseconde (1 fs = 10^{-15} s) laserpulsen in de jaren '90 van de vorige eeuw, was het bijvoorbeeld voor het eerst mogelijk om moleculen te volgen tijdens een chemische reactie. Zo'n reactie kan plaatsvinden op een tijdschaal van slechts een paar picoseconden (1 ps = 10^{-12} s) of zelf sub-ps. Lichtpulsen gemaakt door middel van HHG hebben de afgelopen jaren geleid tot nieuwe methoden waarmee de bestaande technieken in de femtochemie aangevuld en uitgebreid kunnen worden.

In HHG wordt een hoge intensiteit infrarode (IR) laserpuls gedeeltelijk omgezet in licht met de (oneven) harmonische frequenties van de IR laser. Dit gebeurt door middel van een niet-lineaire interactie van de laserpuls met een atomair medium. Op deze manier kan extreem ultraviolet (XUV) licht worden gemaakt of zelfs zachte Röntgenstraling. Dit proces is door de hoge niet-lineariteit echter niet erg efficiënt: in het beste geval genereren we voor iedere miljoen IR fotonen slechts 1 XUV foton en soms is dit nog een factor 10 of 100 minder. In de experimenten in dit proefschrift zijn XUV golflengtes van typisch 25-75 nm (15-50 eV) gebruikt. Ondanks de lage opbrengst, levert HHG toch een bijzonder interessante lichtbron op met vele nieuwe mogelijkheden. Door de korte golflengtes, en de bijbehorende hoge foton energieën, is het mogelijk op nieuwe manieren nucleaire dynamica in moleculen tijdsopgelost te bestuderen met femtoseconde resolutie. Bovendien is het mogelijk HHG lichtpulsen te maken die korter zijn dan 1 fs. Dit zijn de kortste lichtpulsen die bestaan en worden attoseconde (1 as = 10^{-18} s) pulsen genoemd. De uitvinding van attoseconde pulsen heeft geleid tot een nieuw onderzoeksveld dat als doel heeft elektronbewegingen te bestuderen. Elektronen bewegen op een tijdschaal van enkele femtoseconden of zelfs sub-femtoseconde en zijn daarmee dus nog een stap sneller de atomen in een molecuul.

In de eerste twee delen van dit proefschrift is een verzameling experimenten beschreven waarin de mogelijkheden verkend worden om met behulp van HHG lichtpulsen femtoseconde - en attoseconde dynamica in moleculen te bestuderen. Het laatste deel van dit proefschrift beschrijft een aantrekkelijke nieuwe richting voor

toekomstige attoseconde experimenten.

Moleculaire nucleaire dynamica De atomen van een molecuul staan niet stil ten opzichte van elkaar, maar zijn juist continu in beweging. Voorbeelden van dergelijke bewegingen zijn de vibraties van een molecuul en het breken van een binding tussen atomen tijdens een chemische reactie. De snelste van dergelijke bewegingen duren typisch enkele tientallen femtoseconden. Het H_2^+ molecuul is het kleinste molecuul in de natuur en daarom zijn de vibraties van dit molecuul de snelste die er bestaan. In het experiment dat is beschreven in hoofdstuk 2 hebben we gekeken naar deze vibraties. We hebben daarin bestudeerd hoe het vibrerende molecuul wordt beïnvloed door een gematigd sterk IR laserveld. Er worden twee afzonderlijke experimenten beschreven waarin een XUV puls (15-40 eV) gebruikt werd om waterstofmoleculen te ioniseren waardoor een vibrerend H_2^+ molecuul ontstond. Vervolgens gebruikten we een IR puls met een gecontroleerde tijdsvertraging ten opzichte van de XUV puls, om het vibrerende molecuul te laten dissociëren ('breken') door een process met de naam 'bond-softening'. We hebben hierbij de energie van de geladen fragmenten die bij de dissociatie ontstonden gemeten. De twee experimenten verschillen van elkaar in de pulsduur van de IR laser. Wanneer deze puls kort (7 fs) was ten opzichte van de periode van de vibraties (15 fs), oscilleerde de hoeveelheid fragmenten als functie van de tijdsvertraging tussen de XUV en de IR pulsen. Deze oscillaties in de fragment opbrengst waren het directe gevolg van de vibraties van het molecuul. In het experiment met de korte IR puls vond de ionisatie door de XUV puls plaats bij afwezigheid van de IR puls. Dit veranderde in de situatie met een IR puls met een pulsduur die langer was (35 fs) dan de periode van de vibratie. In dat experiment konden we waarnemen hoe het molecuul zich aanpaste aan het veld. Dit bleek ervan af te hangen of het vibrerende molecuul plotseling of juist meer geleidelijk aan de IR laser werd blootgesteld. Het laat zien dat in experimenten waarin de structuur van moleculen bepaald wordt met behulp van sterke laservelden, de pulsduur van deze lasers een grote invloed kunnen hebben op het resultaat van het experiment. Het experiment dat beschreven staat in hoofdstuk 3 vormt een belangrijke stap in de ontwikkeling van een nieuwe methode om een moleculair filmpje van een chemische reactie te maken met voldoende resolutie in zowel plaats als tijd. Momenteel worden hier indirecte methoden voor gebruikt, zoals ook in het hierboven beschreven experiment. Het nadeel van deze methode is dat veel voorkennis over het molecuul is vereist voor de interpretatie van de data. Het zou daarom een grote verbetering zijn om met een directe meting de relatieve posities van de atomen in een molecuul te bepalen. Het meten van de hoekverdeling van fotoelektronen biedt in potentie deze mogelijkheid. Een elektron dat ontstaat door fotoionisatie wordt op zijn weg naar buiten verstrooit door de interactie met de atomen van het molecuul. Deze verstrooiing beïnvloedt dus de manier waarop het elektron uit het molecuul tevoorschijn komt, hetgeen waargenomen kan worden door de hoekverdeling van de fotoelektronen te meten. Voor het succes van deze methode bestaan echter twee voorwaarden. Ten eerste moet de golflengte van het elektron kort zijn ten opzichte van de afstand tussen de atomen. Ten tweede is het noodzakelijk om de hoekverdelingen te meten in een frame dat is gedefinieerd door de stand van het molecuul (moleculaire frame). In ons experiment hebben

we dit gedaan door een verzameling willekeurig georiënteerde CO_2 moleculen met een laserpuls uit te lijnen ten opzichte van het laboratorium frame. De uitgelijnde moleculen hebben we vervolgens geïoniseerd met een XUV puls waardoor fotoelektronen ontstonden met een relatief hoge kinetische energie. De hoekverdelingen van de elektronen die we hierbij hebben gemeten konden we reproduceren met een theoretisch model. Vervolgens konden we met dit model vaststellen dat de gemeten hoekverdelingen zowel door de structuur van de elektronen als de structuur van de atomen werden beïnvloed. Deze resultaten zijn een aanmoediging voor de verdere ontwikkeling van deze methode om hiermee in de toekomst daadwerkelijk chemische reacties te kunnen 'filmen'.

Moleculaire elektronen dynamica Het attoseconde domein is de natuurlijke tijdschaal voor de beweging van elektronen. De ontwikkeling van attoseconde lichtpulsen heeft daarom geleid tot experimenten waarin die beweging kon worden gevolgd in de tijd. In de eerste experimenten waarin attoseconde pulsen werden gebruikt keek men naar elektronen dynamica in atomen en, enige tijd later, in vaste stof. Hoofdstuk 4 beschrijft ons eigen experiment waarin voor het eerst elektron bewegingen in een molecuul werden waargenomen met attoseconde pulsen. In dit experiment hebben we deuterium (D_2) moleculen blootgesteld aan een geïsoleerde attoseconde puls en een *few-cycle* IR puls, met een onderlinge tijdsvertraging die we controleerden met attoseconde precisie. Een gedeelte van de fotogeïoniseerde moleculen dissociëerde, hetgeen resulteerde in een neutraal D en een D^+ fragment. De uiteindelijke positie van het overgebleven elektron op het D-atoom konden we volgen door de detectie van de (energie opgeloste) richting van het D^+ fragment ten opzichte van de polarisatie van de laser. Wanneer er geen IR puls was, was de kans dat het elektron links dan wel rechts eindigde gelijk. Met de IR puls kon het elektron naar links of rechts worden gestuurd, waarbij de uitkomst met attoseconde precisie afhankelijk was van de tijdsvertraging tussen de attoseconde puls en de IR puls. Door theoretische modellen van het experiment te analyseren konden we twee mechanismen voor deze lokalisatie identificeren. In het eerste mechanisme is de lokalisatie het resultaat van een quantummechanische interferentie, waarbij autoionisatie van een dubbel-geëxciteerde toestand en de interactie van het vrije elektron met het laserveld een rol spelen. Het tweede mechanisme begint met de dissociatie van het molecuul vanaf de eerste geëxciteerde toestand in het ion. Tijdens de dissociatie vinden transities plaats tussen de grondtoestand en de eerste geëxciteerde toestand onder invloed van de IR puls, hetgeen resulteert in een coherente superpositie van deze twee toestanden. De elektron golffunctie van beide toestanden is gelijk verdeeld over de twee kanten van het molecuul, terwijl de coherente superpositie van de twee toestanden correspondeert met een gelocaliseerd elektron. De dynamica die leiden tot de totstandkoming van de lokalisatie hebben we verder onderzocht met behulp van een semi-klassiek model. In dit model wordt het molecuul beschreven door middel van zogenaamde quasi-statische toestanden. In deze toestanden wordt de interactie met het veld instantaan meegenomen (hoofdstuk 5). De complexe elektronen dynamica konden met dit model worden worden gereduceerd tot een simpele formule die slechts op enkele cruciale momenten tijdens de dissociatie hoefde te worden toegepast. Het succes van het semi-klassieke model in het

reproduceren van resultaten van een completer model was een bevestiging van de interpretatie die aan het semi-klassieke model ten grondslag lag. De experimentele resultaten bevestigen dat attoseconde pulsen waardevol zijn voor het onderzoeken van complexe elektronen dynamica in moleculen.

In het hiervoor beschreven experiment kan de rol van de attoseconde puls het beste worden omschreven als de 'pomp' puls waarmee de dynamica in gang werden gezet. Het is echter evenzeer interessant om de attoseconde puls in de rol van 'probe' puls te onderzoeken. Dit was het doel van het experiment dat beschreven is in hoofdstuk 6. In dit experiment hebben we een attoseconde puls trein (APT) gebruikt met 2 pulsen per optische periode van het IR veld, in combinatie met een gematigd sterk IR veld. Met de APT en de IR puls hebben we D_2 moleculen dissociatief geïoniseerd. Op basis van de energie en de richting (ten opzichte van de polarisatie van de laser) van de D^+ fragmenten konden verschillende kanalen worden geïdentificeerd. De hoeveelheid fragmenten in verscheidene kanalen oscilleerde als functie van de tijdsvertraging tussen de twee pulsen. Deze experimentele resultaten konden worden gereproduceerd met een zeer complete quantum mechanische 2-elektron berekening, terwijl een versimpeld model een intuïtief beeld opleverde dat de waarnemingen kon verklaren. In het simpele model wordt aangenomen dat de ionisatie plaatsvindt door de XUV puls, vanaf de neutrale grondtoestand naar de laagste twee toestanden in het ion. De toestanden in het ion worden gekoppeld door het IR veld. Deze koppeling heeft een tijdsafhankelijke ionisatie-waarschijnlijkheid voor ieder van de twee toestanden tot gevolg. In het experiment hebben we dit waargenomen als oscillaties in de hoeveelheid fragmenten behorend bij een specifiek dissociätie kanaal. Het resultaat van de koppeling kan ook gezien worden als een tijdafhankelijke polarisatie van de toestanden in het ion. Met behulp van attoseconde pulsen konden we deze veranderende polarisatie zichtbaar maken.

Ontwikkeling van nieuwe attoseconde experimenten Met de experimenten die in dit proefschrift worden beschreven hebben we het attoseconde veld met succes naar de molecuulfysica uitgebreid. Er is nog veel onderzoek nodig om de volledige potentie van attoseconde pulsen voor elektronen dynamica in moleculen te benutten. Daarnaast is het interessant om verder te kijken naar andere systemen die mogelijk interessante studieobjecten zijn voor attoseconde onderzoek. In hoofdstuk 7 wordt daarom een theoretische studie gepresenteerd naar het gebruik van attoseconde pulsen om de collectieve elektron bewegingen in een metalen nanodeeltje te bestuderen. Er is momenteel veel aandacht voor oppervlakte plasmonen, zoals deze collectieve excitaties worden genoemd, vanwege de mogelijkheden die zij bieden om licht te manipuleren op lengteschalen die kleiner zijn dan de foton golflengte. Alhoewel de onderliggende elektronen dynamica altijd impliciet worden aangenomen in de interpretatie van plasmon effecten, worden ze vrijwel nooit direct waargenomen. Attoseconde pulsen bieden de mogelijkheid om de oscillaties van een plasmonveld zichtbaar te maken met behulp van de attoseconde streaking techniek. In attoseconde streaking creëert een attoseconde puls 'instantaan' een wolkje van elektronen die vervolgens interactie hebben met het oscillerende elektrische veld van - in dit geval - de surface plasmon excitatie. De uiteindelijke energie van het elektron hangt af van de fase van het veld op het moment dat het elektron 'geboren' wordt. Om beter

te begrijpen hoe een dergelijk experiment zou verlopen, hebben we een simulatieprogramma geschreven waarin we de interactie van het elektron met het plasmonveld (klassiek) berekenen. Met het model hebben we onderzocht in hoeverre de uitkomst van het experiment gevoelig is voor de afmetingen van het plasmonveld. We hebben vastgesteld dat de elektron energie na interactie met het plasmonveld alleen afhangt van de afmeting van het veld wanneer het veld extreem klein wordt gemaakt. Verder bleek dat het mogelijk is de verschillende richtingen van het plasmonveld afzonderlijk van elkaar te observeren, door elektronen te selecteren die wegvliegen in een bepaalde richting.

Veel nieuwe attoseconde experimenten, zoals een plasmon streaking experiment, zouden enorm gebaat zijn bij een bron van attoseconde pulsen met een hogere herhalingsfrequentie dan momenteel gebruikelijk is. De huidige attoseconde bronnen hebben een herhalingsfrequentie van typisch een aantal kHz, gelimiteerd door de laserbronnen die voldoende hoge pulsenergieën kunnen leveren om het HHG proces efficiënt te kunnen laten verlopen. Voor een bron van attoseconde pulsen met een herhalingsfrequentie van 100 kHz - 1 MHz is het noodzakelijk methoden te ontwikkelen die het mogelijk maken met lagere pulsenergieën HHG licht te maken. Tevens moeten lasers voor dergelijke hoge herhalingsfrequentie HHG bronnen worden ontwikkeld. In hoofdstuk 8 wordt de status van ons werk op dit gebied beschreven. Om HHG bij een lage pulsenergie mogelijk te maken, willen we nanometer bow tie arrays gebruiken. Deze bow ties werken als kleine optische antennes die lokaal het elektrisch veld van inkomend (resonant) licht met een factor 100-1000 kunnen versterken. Door deze versterking is het mogelijk met relatief lage pulsenergieën een hoge veld intensiteit te verkrijgen. Deze hoge intensiteit is nodig voor een redelijke efficiëntie van het HHG proces. We hebben deze bow tie arrays gefabriceerd en er een test experiment mee uitgevoerd waarin we hebben gekeken naar derdeharmonische generatie. Op basis van dit hiervan konden we inderdaad concluderen dat er (derde-)harmonische generatie plaatsvond in het versterkte veld van de bow ties. De volgende stap is te onderzoeken of er ook HHG licht wordt geproduceerd. Gelijktijdig is de ontwikkeling van een nieuwe laser gestart die als basis kan dienen van toekomstige attoseconde experimenten bij een 'hoge' herhalingsfrequentie. Het ontwerp van de laser is gebaseerd op een niet-collineaire optische parametrische *chirped* puls versterking (NOPCPA). Met een dergelijk systeem is het mogelijk pulsen met een grote bandbreedte te versterken teneinde zeer korte laserpulsen te produceren. De verwachting is dat de laser die ontwikkeld wordt pulsen zal genereren met een pulsduur van < 10 fs, met een pulsenergie van > 2 μJ bij een herhalingsfrequentie van 400 kHz. Verder is het de bedoeling om de *carrier-envelope-phase* (CEP) te stabiliseren, hetgeen nodig is voor het maken van van geïsoleerde attoseconde pulsen. De beoogde pulsenergie is inmiddels behaald en de pulsen hebben voldoende bandbreedte om korte pulsen mogelijk te maken. Momenteel wordt er gewerkt aan de pulsduur en de CEP-stabiliteit.

Dankwoord

In tegenstelling tot het stereotype beeld van een onderzoeker is een promotie niet iets wat je in je eentje doet. Op professioneel en op persoonlijk vlak zijn er veel personen die een rol hebben gespeeld in de totstandkoming van dit proefschrift.

Als eerste wil ik mijn begeleider Marc bedanken voor alles wat er nodig was om deze promotie mogelijk te maken. Bedankt dat je mij mee hebt genomen op een stukje van jouw ontdekkingsreis in de wetenschap. Je ambitie als wetenschapper in combinatie met je diepe begrip van de natuurkunde hebben voor mij deze reis meer dan de moeite waard gemaakt. Ik ben je dankbaar voor de uitstekende mogelijkheden die je hebt gecreëerd om dit onderzoek te doen en voor alles wat je me hebt bijgebracht om dit goed uit te voeren. Bedankt voor de vele gezamenlijke buitenlandse reizen die we in de loop van de tijd gemaakt hebben waarop ik de gezamenlijke etentjes en borrels altijd erg heb gewaardeerd. Maar boven alles wil ik je bedanken voor de ontelbare, vaak lange, discusses die we gehad hebben over natuurkunde. Ik ben bij voorbaat trots op het fantastische attoseconde instituut dat MBI gaat worden en wens je daar veel succes en plezier.

Het is al vaak gezegd maar daarom niet minder waar: de technische staf is een bijzonder goede reden om een promotie op AMOLF te willen doen. Naast dat het stuk voor stuk vakmensen zijn is de samenwerking ronduit geweldig. Rob, jij bent hiervan het voorbeeld bij uitstek, bedankt voor al je hulp, voor geen vraag te gek vinden en voor je persoonlijke aandacht. Waar nodig konden we altijd dankbaar gebruik maken van de andere excellente technici. Hinco en Ad, bedankt voor het altijd willen meedenken en alle 'tussendoor' klusjes. Voor de ontwikkeling van onze apparatuur konden we rekenen op Iliya en Dirk-Jan, om mee te denken over ons probleem en om vervolgens met de beste oplossing te komen. Een prachtig ontwerp is niets zonder Wim en zijn mannen van de mechanische werkplaats. Wim, Jan, Henk, Niels, Menno, Ricardo en Wouter, bedankt voor jullie vakmanschap, inzet en de prettige samenwerking. Duncan, Ronald en Idsart wil ik bedanken voor de gedegen homebuilt elektronica maar ook de ad-hoc hulp op momenten dat er weer eens iets was opgeblazen. Een speciaal bedankje wil ik richten tot Huub, André, Iwan en Tarik voor alle moeite die ze hebben gestoken in de inrichting van ons nieuwe lab.

Our research has benefited from many international collaborators. Many thanks to Mauro Nisoli and Anne L'Huillier for, together with Marc, setting up the joint venture which has culminated in the 'Milano campaigns'. These campaigns have had an enormous positive impact on the course of my PhD. I am very thankful to Mauro for hosting these experiments. A special thanks goes to Anne for being in my committee and carefully proofreading this thesis. In the lab of Milano Giuseppe Sansone was without doubt the most important person. Giuseppe, your talent for experiments and physics was a great example, thanks for sharing this in the lab, during the discussions afterwards and the occasional beers we have had together.

Let me also thank all the other people which who I had the pleasure to work with in the lab in Milano: Matthias, Franck, Enrico, Federico, Thomas, Sergey and Marko.

In practically all our projects we are lucky to work together with the best theoreticians in the world. The results on attosecond dynamics in hydrogen molecules have only been possible through the fruitful collaboration with Fernando Martín and his students Jhon Fredy and Felipe. Many thanks for all the stimulating discussions in Madrid or through skype, it has been a pleasure to work with you. The ECAMP conference in Salamanca was a highlight of my PhD, thank you for that opportunity. I am grateful to Misha Ivanov for inviting me to come to Ottawa and for teaching me everything I needed to know to develop the semi-classical model. I am also indepted to Catherine Lefebvre, Osman Atabek and Thanh-Tung Nguyen-Dang for our joint work on the vibrational dynamics project. I want to thank Ken Shafer and Mette Gaarde for my visit to Baton Rouge and for joining our harmonic seeding project. I thank Robert Lucchese for his contributions to the project of chapter 3. On the same project we have also benefited from fruitful discussions with Olga Smirnova and Alex Harvey. Building our new 'MHz' laser was made possible with the help of two innovative laser companies: Amplitude Systemes and Venteon. I would like to thank Yoann Zaouter and Vincent Rouffiange from Amplitude and Thomas Binhammer from Venteon for their work on this joint project and the support they have provided. I gratefully acknowledge financial support of Amplitude for the realization of this thesis.

Over the years we have had the pleasure to host many visitors in our lab in Amsterdam. First of all, the people from Milano: Matteo, Francesca and Kyungseung; thank you for your contributions in our lab but also for the fun we have had together in Amsterdam and Milano. I want to thank Paris Tzallas for his efforts in our joint project, his stay in Amsterdam and the good time I had in Crete.

Wat dichter bij huis zijn er ook tal van mensen die van groot belang zijn geweest in ons onderzoek. Femius Koenderink is onmisbaar geweest bij het doen van de plasmon streaking simulaties. Tevens wil ik hem bedanken voor het zitting nemen in mijn promotiecommissie en het zorgvuldig lezen van mijn proefschrift. Stefan Witte en Huib Bakker wil ik bedanken voor hun hulp met het opzetten van de simulaties van het OPA systeem. Ik bedank Chris Rétif voor de fabricage van de bow tie arrays en de inspectie van de samples na de vaak destructieve werking van onze laser. Dave Parker ben ik dankbaar voor zijn inspanningen omtrent de goedkeuring van mijn proefschrift en de organisatie van de verdediging.

Mijn promotie ben ik met veel plezier en enthousiasme begonnen en nu aan het eind van deze periode is dat niet anders. Er zijn veel mensen geweest die hierbij belangrijk zijn geweest.

My enthusiasm for doing research got started during the year I did my master thesis research at the QT group in Delft. I had the chance to work with many nice people on an exciting project. Specifically, I want to thank Ethan Minot for his support and stimulation during this year.

Op AMOLF heb ik samen kunnen werken met veel fijne collega's die ik wil bedanken voor de goede sfeer tijdens het werk maar ook daarbuiten. Per, thanks for being a beacon of knowledge for me, you have taught me all I needed to know to

get going and more. Most importantly, I want to thank you for your kindness and for always finding a moment for your great humor. The parties at your place are still legendary and I hope to visit you, Maria and the kids once again in Sweden or welcome you in the Netherlands. Mijn generatiegenoten Wing Kiu, Georg en Ymkje wil ik in het bijzonder bedanken voor de vele etentjes, feestjes en borrels die we samen hebben gehad. Wing Kiu wil ik daarnaast bedanken voor de vele (nachtelijke) uren in het lab, het was een plezier om met je samen te werken. Bedankt ook voor je steun en kritische blik tijdens het schrijven van onze proefschriften. De bijzondere vriendschap die we hebben opgebouwd in het afgelopen jaar is me erg dierbaar. Georg, ik wil je bedanken voor het brengen van een 'gezonde' dosis *deutsche gründlichkeit* in het lab. Bedankt voor het delen van je enthousiasme over eten (behalve over brood), drinken, muziek en reizen; het is altijd inspirerend om je hierin te volgen. Ymkje, bedankt voor de vrolijkheid die je in de groep hebt gebracht en voor het organiseren van zo vele groepsactiviteiten. Bedankt ook voor het samen ontvluchten van AMOLF voor de schaatstochtjes op de Botshol. I owe a lot to Federico for his efforts on the MHz system, and for his help with that part of my thesis. Fede, thanks for joining the group and bringing along a fresh vibe, introducing us to new words and music and a lot of Southpark. Arnaud, you are the master of data tweaking, thanks for teaching me some of it. Many thanks for all the great wines you brought from France and for sharing not only the wine but also your passion for it. Aneta, bedankt voor de pit die je in de groep hebt brengt. Julia, bedankt voor de persoonlijke aandacht die je voor iedereen hebt in de groep. Ik wil Arjan bedanken voor het delen van zijn ervaring en technische know-how. I thank Omair for his efforts in getting things started in Milano and for his dark humor. Many thanks to Axel for his enthusiasm and hard work on the bowtie project. The new team that will continue the attosecond work I thank for their enthusiasm and fresh energy: Jesse and Christian ('the cronies'), Chung-Hsin, Truong and Florian.

Het plezier dat ik in mijn werk heb gehad was alleen mogelijke door voldoende plezier daarbuiten. Ik wil al mijn lieve vrienden en vriendinnen bedanken voor hun interesse in mijn promotie maar vooral voor de afleiding daarvan in de vorm van etentjes, borrels, feestjes en vakanties. In het bijzonder wil ik mijn paranimf en goede vriendin Karin noemen, bedankt dat ik altijd op je steun kan rekenen.

Wilbert en Selma bedankt voor de gezelligheid tijdens onze familieweekenden. Geweldig dat we samen ons 'afstuderen' kunnen gaan vieren. Lianne, bedankt voor je luisterend oor en je begrip in de afgelopen periode. De eerste maanden van Fedde waren fantastisch om mee te maken, daar ben ik jou en Casper erg dankbaar voor. Ik kan niet wachten om Fedde mijn thesis voor te lezen. Papa en mama, deze is voor jullie! Bedankt voor al jullie wijze lessen en voor de materiële en morele steun waar ik altijd op kan bouwen.

Lieve Kiona, ik bedank je voor je eindeloze geduld, je rotsvaste vertrouwen en onvoorwaardelijke liefde. Bedankt voor alles wat we samen gedeeld hebben in goede en mindere tijden. Het is fijn om allebei weer naar een mooie toekomst uit te kijken.

Freek Kelkensberg
Amsterdam, mei 2011

List of publications

Publications covered in this thesis:

Molecular dissociative ionization and wave-packet dynamics studied using two-color XUV and IR pump-probe spectroscopy, F. Kelkensberg, C. Lefebvre, W. Siu, O. Ghafur, T.T. Nguyen-Dang, O. Atabek, A. Keller, V. Serov, P. Johnsson, M. Swoboda, T. Remetter, A. L'Huillier, S. Zherebtsov, G. Sansone, E. Benedetti, F. Ferrari, M. Nisoli, F. Lépine, M.F. Kling, and M.J.J. Vrakking, Phys. Rev. Lett. **103**, 123005 (2009)

Electron localization following attosecond molecular photoionization, G. Sansone, F. Kelkensberg, J.F. Pérez-Torres, F. Morales, M.F. Kling, W. Siu, O. Ghafur, P. Johnsson, M. Swoboda, E. Benedetti, F. Ferrari, F. Lépine, J.L. Sanz-Vicario, S. Zherebtsov, I. Znakovskaya, A. L'Huillier, M. Yu. Ivanov, M. Nisoli, F. Martín and M.J.J. Vrakking, Nature **465**, 763 (2010)

A semi-classical model of attosecond electron localization in dissociative ionization of hydrogen, F. Kelkensberg, G. Sansone, M. Yu. Ivanov and M.J.J. Vrakking, Phys. Chem. Chem. Phys., **13**, 8647 (2011)

Attosecond control in photoionization of hydrogen molecules, F. Kelkensberg W. Siu, J.F. Pérez-Torres, F. Morales, G. Gademann, A. Rouzée, P. Johnsson, M. Lucchini, F. Calegari, J.L. Sanz-Vicario, F. Martín and M.J.J. Vrakking, Phys. Rev. Lett. *accepted*

Molecular frame photoelectron angular distributions from EUV ionization of aligned molecules, F. Kelkensberg, A. Rouzée, W. Siu, G. Gademann, P. Johnsson, M. Lucchini, R.R. Lucchese and M.J.J. Vrakking, *submitted*

Attosecond streaking in a nanoplasmonic field, F. Kelkensberg, A.F. Koenderink and M.J.J. Vrakking, *manuscript in preparation*

Other related publications:

Attosecond ionization of O_2 molecules in the presence of an IR laser Field, W. Siu, F. Kelkensberg, G. Gademann, A. Rouzée, P. Johnsson, D. Dowek, M. Lucchini, F. Calegari, R.R. Lucchese, H. Kono, F. Lépine and M.J.J. Vrakking, *manuscript in preparation*

Attosecond control of electronion recollision in high harmonic generation, G. Gademann, F. Kelkensberg, W.K. Siu, P. Johnsson, M.B. Gaarde, K.J. Schafer and M.J.J. Vrakking, New J. Phys. **13**, 033002 (2011)

Attosecond molecular science, F. Kelkensberg, W. Siu, P. Johnsson and M.J.J. Vrakking, in: Dynamical Processes in Atomic and Molecular Physics, Bentham e-books (2011)

Attosecond time-resolved electron dynamics in the hydrogen molecule, G. Sansone, F. Kelkensberg, F. Morales, J.F. Pérez-Torres, F. Martín and M.J.J. Vrakking, IEEE J. Sel. Top. Quant. *accepted*

Attosecond electron spectroscopy using a novel interferometric pump-probe technique, J. Mauritsson, T. Remetter, M. Swoboda, K. Klünder, A. L'Huillier, K.J. Schafer, O. Ghafur, F. Kelkensberg, W. Siu, P. Johnsson, M.J.J. Vrakking, I. Znakovskaya, T. Uphues, S. Zherebtsov, M.F. Kling, F. Lépine, E. Benedetti, F. Ferrari, G. Sansone and M. Nisoli, Phys. Rev. Lett. **105**, 053001 (2010)

About the author

Freek Kelkensberg was born in Zwolle in 1981 and lived in Dedemsvaart during his childhood. In 1999 he received his 'Gymnasium' diploma from the R.S.G. De Nieuwe Veste in Coevorden. He moved to Delft in September 1999 to study Applied Physics at the Delft University of Technology. Starting in September 2002, he spent one year in the board of the student association of Applied Physics in Delft. In 2004 he received his BSc degree while he continued his studies in a master programme at the same faculty. During this programme he spent one year studying business administration at the Rotterdam School of Management of the Erasmus University. The research for his Master thesis he performed in the group of Prof. L.P. Kouwenhoven at the Kavli Institute for Nanoscience in Delft. He worked on the development of an electrically driven single photon source for quantum optics applications. In 2006 he received his MSc degree with honours. After graduating, he did an internship at MagiQ Technologies in Boston (US), where he worked on single photon detectors for the application in quantum cryptography systems. In 2007 he started his PhD research at the FOM institute AMOLF in Amsterdam as a member of the XUV-physics group of Prof. M.J.J. Vrakking. His research focused on the application of attosecond pulses to study electron motion at its natural timescale.